HEAT AND MASS TRANSFER OF MICROPOLAR AND CASSON NANOFLUID FLOW OVER AN INCLINED STRETCHING SURFACE

KHURAM RAFIQUE

DOCTOR OF PHILOSOPHY
UNIVERSITY UTARA MALAYSIA
2020

Awang Had Salleh
Graduate School
of Arts And Sciences

Universiti Utara Malaysia

PERAKUAN KERJA TESIS / DISERTASI
(Certification of thesis / dissertation)

Kami, yang bertandatangan, memperakukan bahawa
(We, the undersigned, certify that)

KHURAM RAFIQUE

calon untuk Ijazah
(candidate for the degree of) **PhD**

telah mengemukakan tesis / disertasi yang bertajuk:
(has presented his/her thesis / dissertation of the following title):

"HEAT AND MASS TRANSFER OF MICROPOLAR AND CASSON NANOFLUID FLOW OVER AN INCLINED STRETCHING SURFACE"

seperti yang tercatat di muka surat tajuk dan kulit tesis / disertasi.
(as it appears on the title page and front cover of the thesis / dissertation).

Bahawa tesis/disertasi tersebut boleh diterima dari segi bentuk serta kandungan dan meliputi bidang ilmu dengan memuaskan, sebagaimana yang ditunjukkan oleh calon dalam ujian lisan yang diadakan pada : ***27 April 2020.***
That the said thesis/dissertation is acceptable in form and content and displays a satisfactory knowledge of the field of study as demonstrated by the candidate through an oral examination held on: ***April 27, 2020.***

Pengerusi Viva: *(Chairman for VIVA)*	**Assoc. Prof. Dr. Rahela Abdul Rahim**	Tandatangan *(Signature)*
Pemeriksa Luar: *(External Examiner)*	**Prof. Dr. Mohd Zuki Salleh**	Tandatangan *(Signature)*
Pemeriksa Dalam: *(Internal Examiner)*	**Dr. Azizah Mohd Rohni**	Tandatangan *(Signature)*
Nama Penyelia/Penyelia-penyelia: *(Name of Supervisor/Supervisors)*	**Dr. Masnita Misiran @ Bakun**	Tandatangan *(Signature)*
Nama Penyelia/Penyelia-penyelia: *(Name of Supervisor/Supervisors)*	**Assoc. Prof. Dr. Muhammad Imran Anwar**	Tandatangan *(Signature)*

Tarikh:
(Date) ***April 27, 2020***

Permission to Use

In presenting this thesis in fulfilment of the requirements for a postgraduate degree from Universiti Utara Malaysia, I agree that the Universiti Library may make it freely available for inspection. I further agree that permission for the copying of this thesis in any manner, in whole or in part, for scholarly purpose may be granted by my supervisor or, in their absence, by the Dean of Awang Had Salleh Graduate School of Arts and Sciences. It is understood that any copying or publication or use of this thesis or parts thereof for financial gain shall not be allowed without my written permission. It is also understood that due recognition shall be given to me and to Universiti Utara Malaysia for any scholarly use which may be made of any material from my thesis.

Requests for permission to copy or to make other use of materials in this thesis, in whole or in part, should be addressed to:

Dean of Awang Had Salleh Graduate School of Arts and Sciences
UUM College of Arts and Sciences
Universiti Utara Malaysia
06010 UUM Sintok

Abstrak

Bendalir nano merupakan suatu kelas moden pemindahan haba bagi bendalir asas yang mengandungi zarah bersaiz nanometer. Pemindahan haba dan jisim dalam aliran lapisan sempadan pada permukaan bendalir nano tak Newtonan melalui permukaan regangan condong adalah signifikan dalam pelbagai aplikasi kejuruteraan. Justeru, tesis ini mengkaji pemindahan haba dan jisim bagi aliran bendalir nano tak Newtonan mikro kutub dan Casson melalui permukaan regangan condong. Permasalahan yang dipertimbangkan melibatkan permukaan linear, tak linear, dan condong telap. Penjelmaan kesetaraan digunakan bagi mengubah persamaan pembezaan separa tak linear kepada persamaan pembezaan biasa tak linear. Penyelesaian berangka diperoleh dengan menggunakan kaedah Keller-box. Kuantiti fizikal seperti geseran kulit, nombor Sherwood, nombor Nusselt, halaju, suhu, dan kepekatan dengan kesan pelbagai parameter bahan diperiksa. Hasil kajian mendapati dalam permasalahan aliran bendalir nano mikro kutub, pelbagai parameter bahan telah meningkatkan nombor Nusselt, nombor Sherwood, dan geseran kulit. Selanjutnya, profil halaju meningkat dengan peningkatan pada parameter bahan. Telatah yang serupa juga telah dilihat dalam kes halaju sudut terhadap parameter bahan. Sementara itu, nombor Nusselt dan nombor Sherwood menurun manakala geseran kulit meningkat dengan peningkatan kecondongan permukaan dan parameter magnetik. Halaju bendalir nano menurun, manakala suhu dan kepekatan meningkat dengan peningkatan parameter Casson. Profil halaju didapati meningkat dengan peningkatan nombor Grashof setempat dan nombor Grashof setempat terubah. Dapatan kajian ini disahkan dan menepati keputusan dalam literatur.

Kata kunci: Pemindahan haba dan jisim, bendalir nano mikro kutub, bendalir nano Casson, permukaan condong, permukaan regangan.

Abstract

Nanofluid is a modern class of heat transfer fluids made of a base fluid containing nanometer-sized particles. Heat and mass transfer in boundary layer flow of non-Newtonian nanofluid over a stretching surface is of significant concern in various engineering applications. Hence, this thesis studied the heat and mass transfer of non-Newtonian micropolar and Casson nanofluids flow over an inclined stretching surface. The considered problems involved linear, nonlinear, and permeable inclined surfaces. Similarity transformations are employed to transform the nonlinear partial differential equations into nonlinear ordinary differential equations. The numerical solutions are obtained by using Keller-box method. The physical quantities such as skin friction, Sherwood number, Nusselt number, velocity, temperature, and concentration profiles with different effects of material parameters are examined. This study found that in micropolar nanofluid flow problems, the material parameters enhanced Nusselt number, Sherwood number and skin friction. Further, velocity profile increases with increase in material parameter. Similar behavior also observed in the case of angular velocity profile against material parameter. Meanwhile, Nusselt number and Sherwood number decrease whereas skin friction increases with increasing surface inclination and magnetic parameter. Nanofluid velocity decreases whereas temperature and concentration increase with increasing Casson parameter. Velocity profile is found to increase by increasing local Grashof number and modified local Grashof number. The present results are validated and in good agreement with published results in literature.

Keywords: Heat and Mass Transfer; Micropolar nanofluid; Casson nanofluid; Inclined surface, stretching surface

Acknowledgements

BISMILLAHIRRAHMANIRRAHIM

All praise and glory is to almighty Allah (Subhanahu Wa Taalaa) the Most Gracious, the Most Merciful. Peace and blessings be upon the Messenger of Allah. First and foremost I thank Allah, the Lord of the worlds, the Generous, for blessing me the ability, strength and patience to accomplish this effort.

I express my deep sense appreciation to my supervisor Dr Masnita Misiran for her chief encouragement, keen interest, inspiring suggestions and so kind help throughout my PhD study. Also, I would like to acknowledge with much appreciation to my co-supervisor Assoc. Prof. Dr. Muhammad Imran Anwar for his valuable guidance and constructive comments to improve the quality of my research work.

Thanks to all my colleagues and friends especially to Dr Faiza Malik who have provided helpful comments and encourage me in the preparation of my PhD thesis. Last but not least, thanks to my beloved brother, sisters, aunt, Nephew (Zayan Ahmad) and my little sweet niece (Harram Fatima) for their unconditional love, unrestricted prays and encouragement in the process of completion to my PhD studies here at Universiti Utara Malaysia (UUM) Malaysia.

I would like to express my sincere gratitude to Universiti Utara Malaysia (UUM) for providing me best facilities to conduct this research work. I would like to thank to staff at School of Quantitative Sciences who have been very supportive and helpful during my study here.

Table of Contents

List of Tables

List of Figures

List of Appendices

List of Symbols

B	Magnetic Field Vector
$B(x)$	Non-Uniform Transverse Magnetic Field
B_0	the uniform magnetic field strength
$\bar{C}$	nanoparticle fraction
C	non-dimensional nanoparticle fraction
$\mathbf{C}$	couple stress tensor
C_f	skin-friction
$C_{fx}(0)$	skin-friction coefficient
C_p	nanoparticle specific heat
C_w	nanoparticle fraction at surface
C_∞	ambient nanoparticle fraction
$\triangle C$	concentration difference
D_B	Brownian diffusion coefficient
D_T	thermophoresis diffusion coefficient
$\mathbf{F}$	body forces
$\mathbf{F}_T otal$	total force
f	dimensionless stream function
g	acceleration due to gravity
h	angular velocity
h_f	heat transfer coefficient
h_p	nanoparticle specific enthalpy
$\mathbf{I}$	identity vector
$\mathbf{j}_p$	nanoparticle mass flux
j_B	mass flux due to Brownian diffusion
j^*	micro inertia per unit mass
j_T	mass flux due to thermophoresis
K	dimensionless vortex viscosity called the material parameter
k	thermal conductivity
k^*	mean absorption coefficient

$k_1{}^*$	vortex viscosity
L^*	characteristic length
Le	Lewis number
m	velocity exponent parameter
m^*	mass
m_0	constant
M	Hartmann number
$\mathbf{n}$	unit normal
N	radiation parameter
$\bar{N}^*$	microrotation or angular velocity
N^*	non-dimensional microrotation or angular velocity
Nb	Brownian motion parameter
Nt	thermophoresis parameter
Nu	Nusselt number
$\bar{p}$	external pressure on the fluid in x direction
p	non-dimensional external pressure on the fluid in x direction
pr	Prandtl number
$\mathbf{q}$	energy flux
q_m	wall mass flux
q_w	wall heat flux
q_r	radiation flux
Q_0	heat generation or absorption coefficient
R^*	reaction rate
R	chemical reaction rate parameter
Re_x	local Reynolds number based on the stretching velocity
S	suction or injection parameter
S_1	surface
dS_1	differential surface area
Sh	Sherwood number
$\bar{t}$	time
t	non-dimensional time
$\bar{T}$	fluid temperature

T	non-dimensional fluid temperature
$\mathbf{T}$	stress tensor
$\mathbf{T}_x$	vector
T_f	convective heating temperature
T_w	surface temperature
T_∞	ambient temperature
$\triangle T$	temperature difference
u_w	stretching velocity
u_∞	free stream velocity
$\bar{u}, \bar{v}$	velocity components in x and y directions
u, v	non-dimensional velocity components in x and y directions
V	arbitrary control volume
$\mathbf{V}$	velocity vector
v_w	suction or injection velocity
$\bar{x}, \bar{y}$	Cartesian coordinate axis
x, y	non-dimensional Cartesian coordinate axis
Gr	local Grashof number
Gc	local modified Grashof number

Greek Letters

α	thermal diffusivity parameter
γ^*	spin gradient viscosity
γ	inclination parameter
θ	temperature
$-\theta'(0)$	reduced Nusselt number
$-\phi'(0)$	reduced Sherwood number
ϕ	rescaled nanoparticle volume fraction
v	kinematic viscosity of the fluid
λ_1	heat generation or heat absorption parameter
η	similarity variable

τ	ratio between heat capacitances of the nanoparticles and base fluid
τ_w	wall shear stress
ψ	stream function
μ	viscosity
ρ	density of the nanofluid
ρ_{bf}	density of the base fluid
ρ_p	density of the nanoparticle
$(\rho c)_f$	heat capacitance of the base fluid
$(\rho c)_p$	heat capacitance of the nanoparticles
σ^*	Stefan-Boltzmann constan
σ	electrical conductivity
∇	gradient
ω	angular velocity
β	Casson parameter

Subscripts

∞	condition at ambient medium
w	condition at the surface

Superscripts

$\prime$	differentiation with respect to η

CHAPTER ONE

INTRODUCTION

Chapter in hand begins by introducing the general background of the problems under study in Section 1.1. In addition, some important definitions in Section 1.2 are presented that are relevant to this thesis. Moreover, scope and motivation along with problem statement and objectives of the research are presented in Sections 1.3, 1.4, and 1.5, respectively. Section 1.6 highlights the significance of the study, and Section 1.7 presents the research methodology. The Keller-box method and its implementation is explained in Section 1.8. Lastly, Section 1.9 presents the thesis outline.

1.1 Research Background

The development in the subject of fluid mechanics was initiated in 1755 when Euler offered well-known equation of liquid flow for ideal (inviscid) fluids in his celebrated paper entitled "*General principles of the motion of liquids*". Meanwhile, fluid dynamics is its subset in which we particularly discuss materials which are in motion. A fluid is a substance that deforms continuously by applying a shear (tangential) stress (Fox and McDonald, 1994), which is normally studied under two lenses in order to explain the concept at length such as the Newtonian and non-Newtonian liquid. The shear stress relates with rate of strain (velocity gradient) can mathematically be presented as (Currie, 1974):

$$\tau \propto \frac{du}{dy}, \tag{1.1}$$

and

$$\tau = \mu \frac{du}{dy}, \tag{1.2}$$

where τ is the shearing stress, μ is the constant of proportionality and $\frac{du}{dy}$ denotes rate of deformation. In Newtonian fluids, shearing strain shows direct relation with shearing stress as given in Equation (1.1). Whereas, in non-Newtonian liquids, shearing strain and shearing stress show inverse correspondence with each other. Newtonian fluids contain, kerosene oil, air, water and mercury. In addition, blood, paints, grease and coal tar are classified as non-Newtonian liquids (Kumar et al., 2017).

Here, those liquids which do not act upon Newton's law of viscosity are under consideration. The quantity of resistance among fluid to relative motion within the liquid is stated the viscosity. Non-Newtonian fluids have several applications in manufacturing and technological process such as in boring processes and ergonomics.

Casson nanofluid changes the viscosity of the fluid to deviate the classical Newton's law of viscosity such as multi grade oils, blood, lubricants, printer inks, greases, ceramics and fruit juices. Casson fluid reveals the yield stress similar as elastic solid. It means that a fluid behaves similarly to a solid when yield pressure greater than shear stress is act upon it. Whereas, it begins to move when yield pressure less than shear stress. A shear thinning liquid which exhibits high shear viscosity and yield stress is called Casson fluid. The examples of Casson fluid are tomato paste, jam, rigorous fruit juices, blood and honey (Kumar et al., 2017). Casson fluid flow also has important place in engineering. Viscosity found to decrease with the increase in shear rate, giving rise to the shear thinning behavior. Shear thinning of a non-Newtonian fluid depends on length and amount of shear stress being applied. Some complex and suspensions fluids such as paint, ketchup, blood, nail polish and whipping cream are examples of shear thinning behavior (Barnes et al., 1989).

In recent era, non-Newtonian liquid has been of interest as its uses are more versatile. Some examples are in drilling mud, paper production, plastic polymer, liquid detergents, and multi grade oils (Ajayi et al., 2017). Venkatesan et al. (2013) considered blood as type of Casson liquid to analyze the movement of blood through bell shaped stenosis. Shehzad et al. (2013) examined the influence of mass transport in Casson fluid flow and found a sequence of results for resultant non-linear flow by considering porous sheet. Further, Koriko et al. (2016) examined Casson fluid flow for exponential surface.

Micropolar fluids are non-Newtonian fluid with suspended particles. This class of fluids exhibit certain microscopic effects that arising from the local microstructure and micro-motion of the fluid elements. The theory of micropolar fluids, firstly proposed by Eringen (1966) has gained much attention because the traditional Newtonian fluids cannot precisely describe the characteristics of the fluid flow with suspended particles. Examples of the micropolar fluids are industrial colloidal fluids, polymeric suspensions and liquid crystals. Besides the man-made fluids stated above, micropolar fluids with microstructures are also capable of representing naturally occurring fluidal phenomena, for instance, the behaviour of blood flow in arteries and capillaries with stenosis (Devanathan and Parvathamma, 1983), red blood cells spin distribution, the thickness of the cell-free plasma layer and the cell concentration distribution in the tube, human body fluids flowing in brain as well as animal blood properties (Lok, 2008). Shamshuddin and Thumma (2019) discussed energy and species exchange phenomenon of microplar liquid flow numerically for slanted geometry. In addition, Characteristics of constant heat flux effect on micropolar fluid over a surface was investigated by Majid et al. (2019). Recently, Fatunmbi and Okoya (2020) examined heat transfer process in magneto-micropolar fluid by incorporating temperature dependent properties.

A nanofluid is a fluid engineered by interrupting naturally made nanoparticles with the base fluids. Due to less thermal conductivity, base liquids such as oil, water and ethylene glycol mixture are considered. These liquids have low energy exchange capacities. To advance thermal properties of these liquids, nano or micro-sized particles are added (Reddy et al., 2017). This type of fluids called nano fluids was engineered by Choi and Eastman (1995).

This fluid plays a key role for potential cooling applications in electronics, photonics, transportation, biomedical processes, genetic and chemical sensors (Das et al., 2007). These nano sized particles show a quick resolving in the base fluid and stay settled for a long time as compared to micro elements. Therefore, this property shows that nanoparticles prolong stable suspensions to increase heat transfer and other characteristics of the flow (Keblinski et al., 2005).

Nanofluid has high heat exchange ability compared to the base liquid due to its high thermal conductivity. Therefore, it is very important in industrial practical applications in cooling systems (Roy et al., 2004). Eastman et al. (1996) studied that by adding CuO nanoparticles with volume fraction 5% into the base liquid (water), its thermal conductivity improved by 60%. There are several common ways adopted for the preparation of nanofluid such as Kool-Aid method, inter-gas condensation process, chemical vapor evaporation and chemical synthesis. Moreover, to study better heat transfer characteristics which improve the diffusion rates and rapid suspension of nanoparticles, a small amount of thioglycolic acid is added in nanofluid. Nanofluid based on metal oxide nanoparticles (average diameter 35 nm) has less thermal conductivity than nanofluid containing copper nanoparticles (Das et al., 2007). Chopkar et al. (2006) produced nanofluid by adding $Al_{70}Cu_{30}$ nanoparticles in ethylene glycol which improve the thermal conductivity up to 200%. This development in thermal

conductivity is investigated by the transient hot wire method (Chon and Kihm, 2005).

The Brownian motion behaves as key parameter for the rapid enhancement in thermal conductivity of the nanofluid (Jang and Choi, 2004). Moreover, because of it this increasing behavior is also present in photographic study by showing the optical microscopy images (Chon and Kihm, 2005). This property was not predicted by Maxwell theory (1873). Buongiorno (2006) completed a comprehensive survey by using scale analysis on nanofluid by incorporating Brownian motion and thermophoretic factors.

To date, there is no common constitutive model present in the literature demonstrating the characteristics of nanofluid. These characteristics are important for researchers working in different areas of nanotechnology to explore variety of nanofluids that play vital role in many industrial processes such as metal-cutting fluids, hydraulic fluids, lubricants and coolants (Das et al., 2007).

The heat and mass transfer in nanofluids are significant because of its importance in the field of engineering and industry. The resulting governing equations with energy and mass exchange in nanofluid motion are nonlinear and more complex than the Navier-Stokes equations. Therefore, it is very important to know about flow analysis of nanofluids. Babu et al. (2013) examined different impacts of parameters including particle extent, particle volume section and element material; and several processes to improve the energy exchange abilities including Brownian motion, thermophoresis, and assembling of nanoparticles, to name just a few. Zaimi et al. (2014) investigated the energy transport of nanofluid flow for power law porous surface numerically. They found dual solution for both shrinking and stretching sheet. Sharma et al. (2016) investigated rheological property of nanofluid and found that particle

shape and volume fraction affect the rheological behavior of any nanofluid and concluded that nanofluid shows Newtonian behavior at small shear rate. Meanwhile, at high shear rate values, they behave like non-Newtonian. In the next subsection, we provide few important definitions in relation to non-Newtonian nanofluid study.

1.2 Important Definitions and Concepts

1.2.1 Micropolar Fluid

Eringen (1964) announced a new category of simple microfluids called micropolar fluids to simplify the model of microfluids. In view of Eringen philosophy, micropolar fluids can signify fluids comprising of firm arbitrarily oriented particles adjourned in a viscid medium, where the distortion of particles is unnoticed. The attraction behind this theory is that it is mutually a noteworthy overview of the classical Navier-Stokes model. Interested readers can refer to Eringen (1964) and Lukaszewicz (1999) for detailed theory of micropolar fluids.

1.2.2 Heat and Mass Transfer

Energy exchange is a thermal heat which transport from one place to another because of spatial temperature difference. Heat transport can take place due to temperature difference between the mediums (Bergman et al., 2011). Meanwhile, mass transfer occurs due to the concentration difference between mediums. Just as the rise in temperature starts the driving potential for energy exchange, the change in species

concentration in a blend offers the moving potential for mass transport. The energy as heat always transfer from higher temperature to lower temperature until both mediums have same temperature. Three are three modes of transportation conduction, convection and radiation. Whereas, in all ways, heat transfer occurs because of the temperature difference.

1.2.3 Conduction

Conduction is the transmission of energy from one particle of the body to another particle as a consequence of connections between the particles. Whereas, its rate depends on the geometry of the material, width and temperature gradient. On the other hand, in fluids, energy transfer takes place due to crashes and dispersion of particles throughout their irregular movements. In the case of solids, it depends on the free electrons and vibrations of the particles.

1.2.4 Convection

Convection refers to heat exchange between a solid surface and a fluid in motion when they have altered temperatures. Whereas, the transfer of temperature is governed by fluid motion. If the fluid molecules do not move collectively, then conduction is the only way due to which energy transport from a solid surface to the neighboring liquid. On the other hand, if the fluid molecules move in a group, the heat exchange increases between liquid and surface, but it is difficult to determination the amount of energy exchange in this problem. The flow phenomenon on a heated surface classified as free, forced and mixed convection. Force convection is the mode

of convection in which the flow is initiated by outer resources. In addition, free convection is the form of convection in which motion of the liquid is caused because of buoyancy impacts. In addition, collectively forced and free convection results in mixed convection.

1.2.5 Radiation

Heat transfer due to electromagnetic waves (or alternatively, photons) specially through infrared region is called radiation. Radiation released by a body is due to temperature difference of its molecules. As the body increasing in temperature, it quickly increase in power, and also increase in frequency. Black body can be used to express radiation heat transfer. A black body is a body that fascinates every wavelengths of thermal radiations that fall on it. Max Planck was the pioneer who developed the emission spectrum of the black body. According to Stefan-BoltzmannlLaw radiation, energy per unit time from a black body can be written mathematically as $q_r = \sigma^* T^4 A$. Meanwhile, Stefan-Boltzman law for other than ideal black bodies (as gray bodies) can be expressed as $q_r = \varepsilon^* T^4 A$, where ε is emissivity of a black body and σ^* denotes Stefan-Boltzman constant. The fluid is taken to be a gray body and the Rosseland calculation is applied to express the radiative heat flux in heat equation (Rohsenow et al., 1998).

1.2.6 Magnetohydrodynamics (MHD)

Magnetohydrodynamics is the field of study which discusses about electrically conducting fluids including salt water, ionized gases, and liquid metals (gallium, molten

iron, mercury) by the result of magnetic field. The principal significance of MHD impact in nanofluid is valuable in planetary atmosphere investigation. Electrical conductivity perform a significant role in biological processes and micro mixing technology for instance mixing of organic liquid in micro channels. Magnetic nanoparticles are very useful in medical field such as in drug delivery vehicles utilized for cancer cures (Chandrasekar and Suresh, 2009). Besides, magnetic nanoparticles can control nanoparticle delivery where nanoparticle hyperthermia is used for confined cancer tumors (Shah et al., 2020). The magnetic field impact on non-Newtonian nanofluid experienced a force induced by the electric current which results in the modification non-Newtonian nanofluid flow. Due to frequent uses of MHD boundary layer flow over a stretching surface in industry and engineering significant endeavors have been directed towards understanding the heat and mass transfer features of this fluid for stretching geometry.

1.2.7 Brownian Motion

Brownian motion was introduced by a physician Robert Brown in 1827 during the microscopic observation of suspension of tiny particles in water. He found that the small particles to be in motion. Later, he observed the other particles mixed with inorganic minerals are also busy in continuous movements, now termed Brownian motion. He analyzed that Brownian movement takes place in numerous fluids, not only in water, that exhibits the life cycle also in different fluid, that are harmful for life (e.g. acid solutions). Brown observed this irregular collisions of small particles is related to physics. Not limiting to fluid, Louis Bacheleir introduced this concept in finance in "The Theory of Speculation", where Brownian motion is translated in to the random movement of stock prices in market. In year 1905, Albert Einstein has suffi-

ciently developed the statistic prperties of Brownian motion by using a probabilistic model (Michaelides, 2015).

1.2.8 Thermophoresis

Thermophoresis is a consequence effect of Brownian motion to particles in liquids with external constant temperature. Due to temperature difference in the flow field of the suspension, small particles scattered quicker in the warmer region relative to colder region. The migration of a colloidal particle (or large molecule) in a solution in reaction to the incline of macroscopic temperature is termed thermophoresis. Tyndall (1870) initially observed this phenomenon in 1877.

1.2.9 Boundary Layer

The concept of boundary layer flow of a liquid on a surface was first studied by Prandtl (1874-1953) in his paper entitled "*on the motion of fluids with very little friction*". He introduced the idea of boundary layer, which later being reformed as the analysis of viscous flows in the twentieth century. Boundary layer is the thin section of flow nearby the surface where flow is retorted due to the effect of viscous forces between a solid surface and liquid (see Fig 1.1) (Anderson Jr, 2010). In view of Prandtl boundary layer theory, viscous forces have significant effects in the thin region adjacent to the surface because of velocity gradient. Though far from surface, the viscous forces were insignificant if one finds the flow field. The surface attached to the surface has zero velocity because of the viscous forces. This condition is referred to as no slip condition. For more explanation of this concept, see Schlichting

et al. (1960).

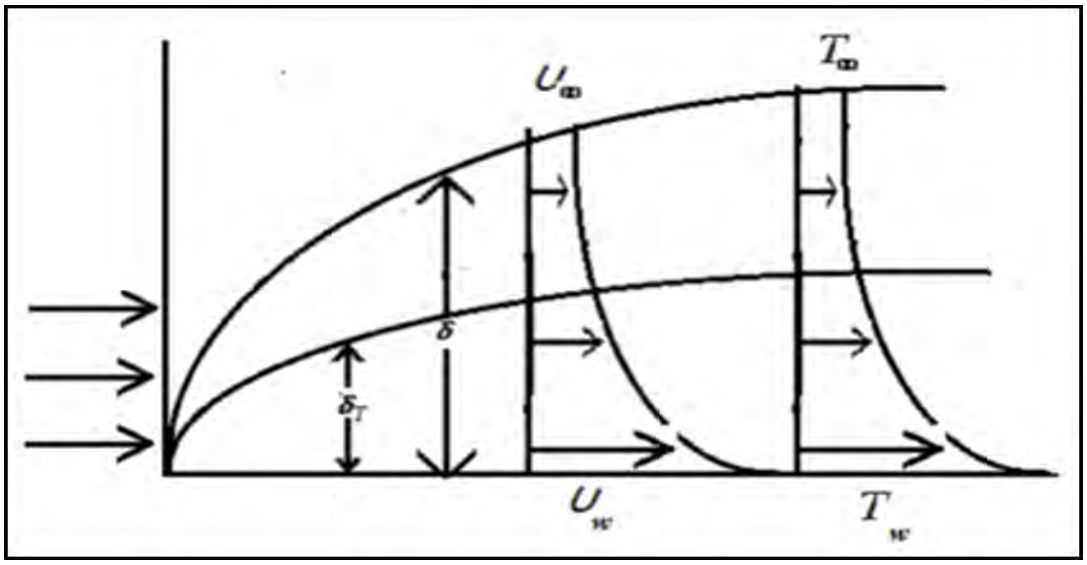

Figure 1.1. Boundary layer configuration in two dimension

1.2.10 Stretching Sheet

The flow towards a stretching sheet has established much intention because of its importance in the field of engineering and industry such as materials manufactured by extrusion, paper production, hot rolling, making of elastic and rubber extrusion, fiber construction, and extrusion of the polymer sheets (Khan and Pop, 2010). Sakiadis (1961) was initiated debates on laminar boundary layer flow of a viscous fluid initiated by constant moving rigid body. Crane (1970) extended this work by discussing the flow towards a stretching sheet. The flow behavior of nanofluid over stretching surface by introducing new parameters for instance thermophoresis and Brownian motion was first analyzed by Khan and Pop (2010).

1.3 Scope and Motivation

The stretching surface in quiescent or moving fluid has received great consideration due to its importance in the area of industry and engineering. In industrial processes, some examples of the problems related to flow due to stretching surface are metallurgical processes like drawing of constant fibers over motionless liquids, strengthening of copper wires, engineering of malleable and flexible sheets, rock emergent, fiber spinning and constant cooling to mention a few (Imtiaz et al., 2020). In addition, such flows find an applications in engineering, for instance extrusion of polymer, making foods and paper, in textile industry and glass fiber manufacture (Suriyakumar and Devi, 2015). Present day development in the area of chemical reaction investigation shows effort in providing mathematical models for a system to predict the reactor performance. In precise, the energy and mass exchange using chemical reaction has great significance in hydrometallurgical and chemical productions. Chemical reaction may be categorized by heterogeneous or homogeneous procedures.

Moreover, the influence of thermal radiations and chemical reaction on energy and mass transport on extending surface is an interesting area for research because of its extensive series of uses in physics and engineering, such as in atomic power plants, geophysics and several force devices for military hardware, jet, satellites and space automobiles (Reddy, 2016). The influence of magnetic field on free convective flows are significant in electrolytes, ionized vapors and molten metals. The conduction tool in ionized gases is not similar to that in metal substance because of the incorporation of magnetic effect.

In view of the above stated applications, the boundary layer flow over a stretching surface with energy and mass exchange that consider different aspects of physical

features of the fluid is important in this research work.

1.4 Problem Statement

Motivated by the applications quoted in the previous section, this study emphasize on energy and mass exchange of MHD boundary layer flow over an inclined stretching surface. Many researchers have been investigating this kind of flow behavior towards an inclined stretching surface. Energy and mass exchange MHD boundary layer flow of nanofluids over an inclined stretching surface has attained a great importance because of its extensive variety of appliations in the area of industry and engineering. However there is a deficiency of studies on the geometry of inclined stretching surface for micropolar nanofluids and Casson nanofluids. Therefore, this research focuses on energy and mass exchange MHD boundary layer flow of micropolar and Casson nanofluids on inclined stretching geometry, with more emphasize is given on the factors including radiations, inclination, chemical reaction, suction or injection, heat generation or absorption and magnetic field. The linear, permeable and power law inclined stretching surfaces are taken into account in viscous micropolar-nano fluids.

This research will elucidate the answers to the following questions.

1. How the available Navier-Stokes models expressing the behavior of boundary layer flow relate with nanofluid models presented in this study?

2. How does the flow of micropolar and Casson nanofluid on a slanted geometry compare by other fluid problems? How do the Brownian motion and thermophoresis

factors affect energy and mass exchange charecteristics?

3. How does the energy and mass exchange of nanofluids flow examined by the Keller-box method?

4. How does the problems discussed in this thesis match with the existing fluid problems?

Specifically, the problems consider in this research are as follow:

1. To develop the effect of micropolar nanofluid flow for linear inclined stretching surface;

2. To examine the boundary layer flow of micropolar nanofluid over permeable inclined stretching surface;

3. To investigate the boundary layer flow of micropolar nanofluid over power law inclined stretching surface;

4. To analyze the boundary layer flow of Casson nanofluid over linear inclined stretching surface;

5. To examine the boundary layer flow of Casson nanofluid over power law inclined stretching surface;

1.5 Objectives of Research

This research scrutinizes the theoretical development of heat and mass exchange MHD boundary layer flow of non-Newtonian nanofluid over an inclined stretching surface. The objectives of this study contain the formation of appropriate mathematics models by formulating boundary layer equations and their numerical simulation.

Specifically, this thesis focuses on the following objectives:

1. To develop and extend mathematical models of micropolar and Casson nanofluid flow over an inclined surface;

2. To develop an algorithm in MATLAB software program in order to get the solution of all problems ;

3. To analyze the effect of pertinent parameters on concentration, velocity and temperature distributions along with the variations of skin friction, Sherwood number and local Nusselt number;

1.6 Significance of the Study

This research describes numerical results of energy and mass exchange for flow of non-Newtonian nanofluid towards a slanted extending surface. The heat and mass transport MHD boundary layer flow for inclined geometry has generated a much consideration due to its noticeable uses in industry such as in hot rolling, metal sheets in bath, broadsheet production and exclusion of malleable pieces. In addition, such

type of flows has extensive variety of uses in chemical engineering, electrochemistry and polymer processing (Jamaludin et al., 2018).

The thermal radiation and MHD impacts over a stretching surface are very important especially in energy and mass transport, the stability of convective flows, nuclear reactors, MHD accelerators and geophysics. These effects have many engineering and physical uses for instance thermal insulation, metallurgical process, polymer technology, packed-bed catalytic reactors, and in power generators. (Peng et al., 2019).

1.7 Research Methodology

The problems discussed in current study carry out the following research methodology:

1.7.1 Mathematical modeling

The full boundary layer equations are derived and mathematical model for micropolar and Casson nanofluid flow problems are developed.

1.7.2 Mathematical Analysis

The governing equations are converted into coupled nonlinear ordinary differential equations by utilizing the compatible similarity transformations available in the published literature.

1.7.3 Numerical Simulation

The converted ordinary differential equations with boundary conditions are solved via the Keller-box scheme executed in Matlab program.

1.8 Keller Box Method and Matlab Implementaion

In the light of available literature, a variety of numerical methods exist for solving couple ordinary differential equations for instance shooting method, Labatto-3Stage formula, homotopy analysis method and Keller-box method. In this thesis, we employed the Keller box scheme for numerical simulation. It is easy to program, user friendly, much quicker, and informal to practice (Keller and Cebeci, 1972).

Nowadays, many researchers utilized Keller box scheme successfully such as Ishak et al. (2008), Deswita et al. (2010), Anwar et al. (2017), and Ullah et al. (2019). The detail of Keller-box scheme is explained in Appendix A. Readers can refers to Cebeci and Bradshaw (2012) for complete algorithm of this scheme. This method consists following steps:

1. Convert nonlinear ODE's to first order ODE's.
2. Construct transformation equations by means of central differences.
3. Apply the Newton method and expressed the results into matrices.
4. Employ the block tridiagonal method.

The coding of Keller-box scheme in Matlab for problem 1 is presented in Appendix A.

1.9 Thesis Outline

This thesis comprises eight chapters. It begins with introductory chapter which consists of research background, important definitions and concepts, scope and motivation, problem statement, objectives, significance, methodology of this research, Keller-box method and Matlab implementation. Chapter 2 presents review on relevant literature in particular problems regarding energy and mass exchange boundary layer flow of non-Newtonian nanofluid over linear, as well as nonlinear inclined stretching surface. Chapter 3 is concerned with governing equations of two dimensional energy and mass exchange nanofluid as well as micropolar and Casson fluid boundary layer flow. Further, this chapter discusses boundary layer flow of micropolar nanofluid on linear inclined stretching geometry.

For boundary layer flow of micropolar nanofluid, Keller-box scheme is utilized to obtain numerical solution for all field equations of momentum, microrotation, energy and concentration. Results for the embedded flow parameters including Brownian motion constraint (Nb), thermophoresis factor (Nt), material factor (K), Hartmann number (M), Prandtl number (Pr), local Grashof number (Gr), Lewis number (Le), local modified Grashof number (Gc), inclination factor (γ) in terms of $-\phi'(0)$, $-\theta'(0), C_{fx}(0)$, velocity profile $f'(\eta)$, microrotation profile $h(\eta)$, temperature $\theta(\eta)$ and concentration $\phi(\eta)$ profiles are exhibited in tables and graphical forms. The features of flow characteristics are analyzed and discussed for material parameter K. The case when $m_0 = 0$ is considered which represents the concentrated nanoparticles flow in which the micro-elements close to the wall surface are unable to rotate (Jena and Mathur, 1981). The complete Matlab program for first problem is presented in Appendix A.

Flow on permeable linear inclined geometry with combined effects of chemical reaction and heat generation or absorption are considered in Chapter 4. This chapter contains similar flow parameters as considered in Chapter 3 except for the effects of suction or injection, chemical reaction, heat generation or absorption factors. The core aim of this chapter is to investigate flow characteristics over permeable inclined extending surface.

In Chapter 5, the boundary layer flow of micropolar nanofluid over inclined power law stretching surface is discussed. In this problem, the surface is stretched by power law velocity. Further, in this Chapter Rosseland approximation on micropolar nanofluid flow is constructed by incorporating convective boundary conditions. This problem extends the previous study presented in this Chapter for constant wall temperature, introduces Biot number and radiations factor N. The novel aspect of this problem is to focus on the conjugate effects of energy and mass transport between three temperature differences $T_f > T_w > T_\infty$ with variable wall temperature. The current study reduces to the problem considered in Chapter 6 when $N = 0$ and $\gamma_1 \to \infty$.

Chapter 6 is concerned with the flow of Casson nanofluid for linear inclined geometry by incorporating magnetic effect. For numerical simulation of this problem, once again Keller-box scheme is applied. In this chapter, the impacts of Casson factor β on $-\theta'(0)$ and $-\phi'(0)$ is presented in tables and graphical form.

Further, Chapter 7 extends Chapter 6 problem by adding radiations effect in the original problem. Its surface is also stretched with the power law velocity. Chapter 8 concludes the thesis by providing the summary and some potential future works.

CHAPTER TWO

LITERATURE REVIEW

2.1 Introduction

This chapter reviews literature on various problems related to the thesis. Section 2.2 focuses on boundary layer flow over a linear inclined stretching surface. Section 2.3 investigates the boundary layer flow over permeable inclined stretching surface. Section 2.4 focuses on boundary layer flow over power law inclined stretching surface. Finally Section 2.6 presented literature with convective boundary conditions.

2.2 Boundary Layer Flow Over a Linear Inclined Stretching Surface

Over the past few years, scholars have set extraordinary consideration on the flows towards a linear stretching slanted geometry because of its uses. Earlier study such as Mucoglu and Chen (1979) discusses the bouncy effects on the heat transfer features of laminar forced convection flow towards a slanted surface and concluded the numerical results against Prandtl numbers 0.7 and 7. They considered the angle of inclination fluctuating from 0 to 90^0 with the perpendicular direction. Later, Chen et al. (1986) have made an analysis of natural convection boundary layer over vertical, inclined and horizontal inclined plates. Moreover, they considered surface heat flux and wall temperature in power form of axial coordinate. In their study they discussed the heat exchange effect on the flow that may have potential to be extended for mass transfer effect.

Further, new formulation for laminar flow on isothermal slanted plate based on a proper inclination factor was conducted by Yu and Lin (1988). They made this formulation in particular for liquids with Prandtle number range between 0.001 to infinity. This work can be further refined by discussing the mass transfer effect. Lee et al. (1992) studied the vertex instability properties on natural convection flow over a slanted plate which makes horizontal angle. They employed linear non-parallel flow stability theory in this investigation. The results showed that increment in the inclination factor made the flow more stable to the vertex mode of instability.

In more recent work, Chamkha and Khaled (2001) numerically studied the coupled energy and mass exchange characteristics of electrically conducting Newtonian fluid over an inclined surface. Both the wall concentration and temperature according to power law model vary with the distance along the plate were used in this research. Their investigation showed that the ratio of concentration to thermal buoyancies enhanced the heat and mass exchange rate, Such enhancement was due to the increment in the absolute wall temperature. On the other hand, Ramesh et al. (2012) carried out the investigation of momentum and heat exchange for the dusty fluid flow by incorporating magnetic field and energy source. They considered the fluid and dust particles in this research and revealed from the investigation that fluid particle interaction factor shows opposite effect in the case of dust and clean fluid velocities. From this research, it is observed that the heat source improved the heat exchange rate. This study is in particular for dusty fluid. In view of potential coupled energy and mass exchange study in the industry, this work can be extended for the non-Newtonian nanofluid flow over an inclined surface.

In addition, Suriyakumar and Devi (2015) carried out a numerical investigation using copper water along with alumina water based nanofluids. They incorporated internal

energy generation and suction effects. They observed similar effects of suction and volume fraction on heat exchange rate. While in the case of velocity field for both alumina water based nanofluid and copper water based nanofluids, opposite effect can be seen for volume fraction. We can further improve this research by adding some other relevant factors such as Brownian motion and thermophoretic impacts in concentration equation.

Meanwhile, Rawi et al. (2017) investigated the g-jitter effects on nanofluid flow inclined geometry. They performed this research for the unsteady flow of water based nanofluid containing copper. They observed that the heat exchange rate was higher for the silver-water nanofluid as compared to copper oxide and alumina-water nanofluid. They utilized the Keller-box scheme in this examination with grid size 0.02. In addition, Afridi et al. (2017) discussed the viscous fluid flow over an inclined stretching sheet. They used compatible similarity transformation and then utilized shooting technique for the numerical simulation. They also calculate the expression for Bejan number and entropy generation in nondimensional form. They discussed the entropy generation per unit volume and revealed that the Bejan number shows inverse correspondence against thermal convective factor. This work was carried out for the heat exchange analysis of viscous fluid which can be improved by discussing the mass exchange characteristics.

Anjali Devi and Suriyakumar (2017) studied the Sakiadis and classical Blasius flow towards a stretching inclined plate numerically. They considered two type of nanoparticles alumina and copper in water base liquid. They carried out the study of hydromagnetic nanofluid flow over an inclined plate for the Blasius and Sakiadis flow. They observed that the inclusion of nanoparticles in the base liquid upsurges the energy exchange rate for both cases. In addition, they concluded that for copper water

nanofluid, skin friction improves for the Blasius flow as compared to alumina-water nanofluid. But opposite trend was seen in the case of Sakiadis flow.

Recently, Saeed et al. (2019) probed the nanofluid flow over a slanted disk by incorporating Casson effect. They scrutinized Brownian motion and thermophoresis effects on energy and mass transport in this work. They observed that heat exchange rate increases on increasing the radiation factor. In addition, Tlili (2019) discussed the Jeffery fluid flow over an inclined stretching sheet. This study was carried out in a microgravity environment and the investigation showed how gravity modulation and Deborah number affected the energy transport. He found that the Deborah number shows direct correspondence versus energy exchange coefficient. This research can be explored for two dimensional steady flow of nanofluid on slanted geometry. Recently, Fatunmbi and Okoya (2020) studied energy transport of micropolar fluid flow over a stretching sheet. They considered prescribed heat flux (PHF) and prescribed surface temperature (PST). They found that heat exchange rate declines for increase in material parameter. Further, Imtiaz et al. (2020) investigated flow behavior of viscous fluid over stretching sheet. They used Homotopy analysis method for convergence series solution. In latest paper, Khan et al. (2020) considered Buongiorno model for examined the flow behavior of nanofluid. They utilized appropriate similarity transformations for non-dimensionality, and discussed the Brownian motion thermophoresis effects on physical quantities via Homotopy analysis method.

From earlier presented literature review, it is revealed that no work has investigated the energy and mass transport of micropolar as well as Casson nanofluid flow over an inclined stretching surface.

2.3 Boundary Layer Flow Over a Permeable Inclined Stretching Surface

This Section presented literature review for permeable linear inclined stretching surface by incorporating heat generation or absorption with suction or injection effect. Chen (2004) calculated the energy and mass exchange of magnetohydrodynamic (MHD) natural convective flow by considering the ohmic heating and viscous dissipation effect. He observed that energy and mass exchange rates rise as compared to impermeable surface in the presence of suction effect while the opposite impact had been seen in the case of injection since momentum transport declines near the wall. This work expressed the energy and mass transport for the electrically conducting Newtonian liquid flow. In view of growing applications of energy and mass transport in industry, this work can be extended for non-Newtonian nanofluid over an inclined surface. The investigation of two dimensional MHD mixed convection flow towards a porous inclined surface was examined by Alam et al. (2008). In this research, they considered thermal radiations factor as well as thermophoresis effect and variable suction. They focused on energy and mass transport of the viscous liquid flow by assuming that thermophysical processes experienced by relatively small number of particles do not affect the main stream velocity and temperature field since the mass flux of the particles is sufficiently small and the fluid is taken to be gray.

From the investigation of this work, it is observed that the inclination put restrictions on the energy and exchange rates. Another reason behind this behavior is the buoyancy effect. In addition, Rahman et al. (2010) discussed convective flow of micropolar fluid over an inclined porous plate by incorporating the uniform heat flux. They studied heat transport of viscous micropolar fluid numerically and observed that when thermal conductivity and viscosity depend on temperature for realistic result, Prandtl number must be treated as a variable. However, in this work, analysis was

conducted for energy transfer. This research can be explored for both energy and mass transportation for micropolar nanofluid flow.

Later, Uddin (2011) examined flow of micropolar fluid by incorporating heat generation or absorption. He applied shooting method for numerical analysis and revealed that energy exchange amount is developed in highly concentrated micropolar fluid as compared to weakly concentrated micropolar fluid. His results showed that the increment in vertex viscosity declines skin friction coefficient and improves the plat couple stress.

Das et al. (2015) investigated MHD mixed convection flow through porous inclined sheet. They follow the work of Chen (2004) and considered both aiding and opposing buoyancy conditions. In this study, they observed how the buoyancy effect have made an impact on the ratio of energy and mass exchange. They utilized the shooting method for numerical results in this study. Sandeep and Kumar (2016) examined the MHD nanofluid flow over a porous inclined extending surface by taking radiation, non-uniform heat source or sink and chemical reaction into account. In this research, they incorporated the mixture of Cu-water nanfluid with dust particles. They observed that the interaction of Cu-water nanofluid with dust particle had showed higher heat transfer rate. In addition, the chemical reaction plays a key role in the enhancement of mass transfer rate of dusty nanofluid.

Usman et al. (2018) examined the Casson nanofluid flow over a porous inclined cylindrical geometry. In this study, they mostly emphasized on velocity and thermal slip effects on heat and mass exchange rates. They observed that thermophoretic impacts shows direct relation with the mass exchange rate. This study was in cylindrical geometry, and have potential for extension to the inclined surface setting. Cur-

rently, Kebede et al. (2020) discussed energy and mass exchange phenomenon of Williamson nanofluid towards permeable stretching geometry. They utilized Buongiorno model for unsteady case. They found Williamson parameter declined velocity field. Further, energy species transfer of nanofluid by incorporating Buongiorno model was examined by Sudarsana Reddy and Sreedevi (2020). They considered both steady and unsteady cases with the effect of double stratification.

In view of the literature, there is no study on flow of micropolar nanofluid towards permeable linear slanted stretching surface. Therefore, there is a potential to study micropolar nanofluid flow through permeable linear slanted stretching surface that is among the intention in this thesis.

2.4 Boundary Layer Flow Over a Power Law Inclined Stretching Surface

Sections 2.2 and 2.3 all discussion limited in linear inclined stretching surface. Moving forward, this section is prepared in particular for the flow over a power law inclined stretching surface.The flow over nonlinearly stretchable geometry was initially conducted by Chiam (1995). He performed this study for Newtonian fluid, but only consider momentum equation along with continuity equation. He utilized the Crocco's transformation for skin friction factor.

Later, Vajravelu (2001) examined the flow behavior and energy transport characteristics of a viscous liquid over a power law extending sheet. He observed that energy each time move from an extending surface towards the liquid by applying shooting scheme along with fourth order Runge-Kutta technique in numerical investigation. Cortell (2007) premeditated the viscous flow and heat transfer over a nonlin-

early stretching sheet. He provided numerical outcomes using shooting method with Runge-Kutta algorithm. He illustrated that both vertical and horizontal components of dimensionless velocity decreases with the increase in value of nonlinear stretching parameter.

Meanwhile, Shit and Majee (2014) initially carried out the investigation of viscous liquid flow by taking inclined geometry into account. In this analysis, they assumed that the viscosity depends on temperature. They observed that problem reduced to the hydrodynamic boundary layer flow towards stretching surface for a special case whose results found by Crane (1970). Further, observed that heat exchange rate had shown dual characteristic because of critical value of heat generation or absorption. This numerical analysis was done via finite difference scheme.

Further, Bohra and Jain (2017) probed three dimensional boundary layer flow of incompressible fluid over an inclined nonlinear enlarging sheet. The effects of convective boundaries and chemical reaction are incorporated in this problem. They employed suitable similarity transformation to recover the coupled nonlinear ordinary differential equations and shared numerical outcomes via shooting method. Results showed that nonlinear stretching parameter showed inverse relation with velocity profile. However this work failed to consider two dimensional fluid flow, where we can extend this study for inclined geometry. According to Khan et al. (2018), the goal of their research was to probe the influence of viscosity ratio factor on the heat exchange of Carreau fluid flow. In this work, momentum and energy equations are taken in to account. In this research, non-Newtonian fluid was used because of its practical applications. They found multiple and dual solution by using the shooting technique. They observed that the viscosity ratio parameter showed different impact on the wall shear stress for the first and second solution. This research was conducted over a

shrinking inclined sheet which can be extended for the stretching inclined surface for heat and transport mechanism for non-Newtonian nanofluid.

Recently, Ghadikolaei et al. (2018) investigated energy and mass exchange of non-fluid flow for the inclined geometry numerically. Results showed that the energy transport rate had been increased more significantly on the nonlinear stretching surface as compared to the linear in manifestation of chemical reaction. They also observed that thermophoresis was helpful to increases the heat exchange rate. However, this work does not explain the micro-rotation effects on the flow field of the nanofluid, therefore it can be extended for the micropolar type nanofluid flow. Latest paper on heat and species exchange phenomenon of micropolar fluid flow over nonlinear stretching surface discussed by Reddy and Ferdows (2020). They found numerical simulation via Runge-Kutta integration technique. Recently, Mondal and Pal (2020) examined nanofluid flow over nonlinear stretching sheet by incorporating variable viscosity. There is a potential to extend foe inclined geometry. From above cited work, very limited literature is available on the boundary layer flow over power law slanted stretching surface. Thus, we take it as a new problem in this thesis. Now, we are going to draw a light on the literature review of boundary layer flow by incorporating convective boundary conditions in the next section.

2.5 Boundary Layer Flow with Convective Boundary condition

This section contains literature review on convective boundary conditions. Singh and Makinde (2012) examined the boundary layer flow over an inclined plate with exponentially decaying heat source. They followed the work of Chamkha and Khaled (2001) and perceived that normally, skin friction and magnetic effect behave inversely

although in the case of Newtonian heating, its behavior is opposite. They convert the partial differential equations into ordinary differential equations by using appropriate similarity transformations, then utilized shooting technique for numerical investigation. They carried out this study for incompressible viscous fluid by considering momentum and energy equation, thus it can be extended for heat and species transport of naofluid flow for inclined geometry.

Jain and Chaudhary (2013) succeeded in investigating the exact solution of unsteady free convection boundary layer flow over an inclined plate. In this study, they considered the inclined plate that is oscillating and studied the heat and mass exchange rates. They applied Laplace transformation for analytical solution of the problem, however, the lack of numerical investigation of this study exist. Their results revealed, that Newtonian heat effects help out the heat exchange rate, while opposite impact can be seen against time. This study can be extended for the mass transfer analysis of nanofluid fluid flow on a non-oscillating slanted plate.

Meanwhile, Ashraf et al. (2015) examined flow of Maxwell fluid for slanted sheet incorporating convective boundary conditions. They carried out three dimensional Maxwell fluid in this study which lack of non-Newtonian nanofluid flow with convective boundary conditions. The authors applied compatible similarity transformation on boundary layer flow equations and recovered nonlinear ordinary differential equations together with its similarity solution. Thermophoresis factor also taken into account. It was observed that the stretching ratio and inclination show similar impact on the rate of heat exchange i.e. stretching ratio and inclination are favorable for the heat exchange rate.

Further, Seth et al. (2016) studied convective boundaries effect on inclined stretch-

ing sheet. They analyzed the heat exchange behavior of non-Newtonian nanofluid (viscoelastic nanofluid) due to the boundary convection condition. They used finite element technique for numerical solution and concluded that velocity profile declines with the increase in inclination. Ramesh et al. (2016) investigated boundary layer flow on an inclined plate with convective boundaries. They explored the work of Ishak et al. (2011) by incorporating the influence of inclination. The heat exchange analysis was conducted for both cases when the inclined plate is stationary and also moving. They observed that when velocity ratio factor is equal to zero, the problem went into stationary plate (Blasius flow) while when velocity ratio equal to one, it converts to moving plate (Sakiadis flow). However, they only considered cold incompressible fluid over an inclined plate, in which this work can be extended to mass transport analysis with nanofluid towards stretching inclined surface.

Moreover, unsteady nanofluid flow over an inclined streching sheet has been done by Rashad (2017). He extended the work of Chamkha (2000) by considering nanofluid with the effect of convective boundaries. He employed the finite scheme in this work for numerical investigation. He observed that convective boundary helps to enhance the heat exchange rate. This work demonstrated three dimensional flow of nanofluid flow over inclined surface. We can further extend this work for steady non-Newtonian nanofluid two dimensional flow over an inclined surface. Khan et al. (2017) scrutinized the Carreau fluid flow on a slanted stretchable cylinder. They examined the effects of convective boundaries and Joule heating numerically. They studied Carreau nanofluid flow for cylindrical geometry while it can be examined for the non-Newtonian nanfluid fluid for inclined geometry. Ibrahim and Gamachu (2020) discussed convective boundary condition effects on dusty nanofluid flow. They applied bvp5c Matlab program for numerical outcomes and analyzed energy transport behavior.

By the above mentioned literature review, To date, no study conducted on flow of micropolar type nanofluid for slanted surface by incorporating the effects of convective boundary conditions. Therefore, in this thesis, we aim to develop mathematical equations for energy and mass transport against inclined surface with convective boundary conditions.

This chapter highlighted available literature on Newtonian and non-Newtonian fluids flow for inclined geometry. In the following chapters, the boundary layer equations will be derived supported by numerical simulation of boundary layer flow for inclined geometry.

CHAPTER THREE

MICROPOLAR NANOFLUID BOUNDARY LAYER FLOW OVER A LINEAR INCLINED STRETCHING SURFACE

3.1 Introduction

In present chapter, the MHD effect on flow of micropolar nanofluid on linear slanted stretching geometry is discussed. A parametric study by incorporating γ^* (spin gradient viscosity) is carried out by considering the effects of angular microrotations N^*. The novel aspect of current study is the investigation of micropolar nanofluid for slanted geometry. The numerical outcomes of current results show a good agreement with Khan and Pop (2010) in the absence of Hartmann number M, material parameter K local Grashof number Gr, local modified Grashof number Gc and inclination factor γ. This chapter divided in the following Sections. Section 3.2 prepared for formulation of MHD flow over an inclined surface. Section 3.3 contains the governing equations of first problem. Section 3.4, expressed the numerical procedure. Section 3.5 presented the results and discussion.

3.2 Mathematical Formulation

This section focuses on governing equations utilized in this thesis. The current model contains Brownian motion and thermophoresis effects as proposed by Buongiorno (2006). The concept of Pfautsch (2008) uses in the modeling of governing equations for control volume of the nanofluid. The layout of the formulation of governing equations consists on the following Sub-sections: Sub-section 3.2.1 is prepared for

mass equation. Sub-section 3.2.2 manages equation of momentum. Sub-section 3.2.3 contains conservation of energy. Sub-section 3.2.4 is expressed the non-dimensional analysis. Momentum equations for micropolar liquid are exhibited in Sub-section 3.2.5. Momentum equation for Casson fluid is presented in Sub-section 3.2.6.

3.2.1 Conservation of Mass

The mass conservation principle states that the mass cannot be destroyed nor created it should remain unchanged in a closed system with respect to time. The mass of product and reactant during a chemical reaction in an isolated system conserved. In view of (Pfautsch, 2008), consider a control volume (V) displayed in Figure 3.1 where S_1, ρ, dS_1 and $\mathbf{V}$ denote the surface, nanofluid density, differential surface area and velocity as well as $\mathbf{n}$ (outward normal).

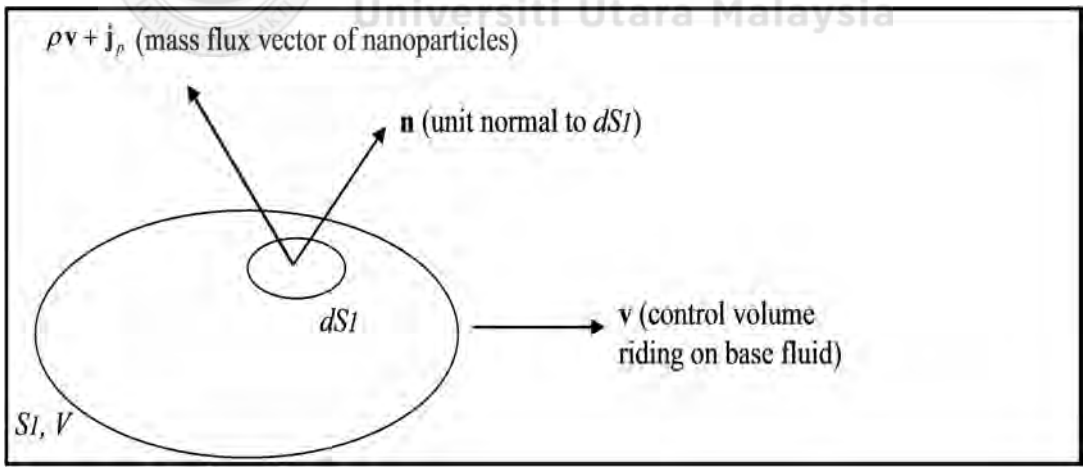

Figure 3.1. Geometry of control volume.

By addition of chemical reaction total mass of the control volume is given by

$$\mathbf{M}(t) = \int_{V_m(t)} \rho \; dV - R^*(C - C_\infty), \tag{3.1}$$

here $\mathbf{M}(t)$, ρ, and $V_m(t)$ signify the total mass, local density, control volume and R^* means chemical reaction ratio and C_∞ denotes ambient nanoparticle fraction respectively. In view of Anwar (2013), $\mathbf{j}_p$ demarcated as

$$\mathbf{j}_p = \mathbf{j}_{P,T} + \mathbf{j}_{P,B}. \tag{3.2}$$

Here, the mass flux due to thermophoresis diffusions is denoted by $\mathbf{j}_{P,T}$ and mass flux due to Brownian motion signifies by $\mathbf{j}_p$. By applying Reynolds theorem, change in total mass will be

$$\frac{D}{Dt}\int\limits_{V_m(t)} \rho dV = \int\limits_{V_a(t)} \frac{\partial p}{\partial t} dV + \int\limits_{S_a(t)} (\rho \mathbf{V})\cdot \mathbf{n} dS_1 - R^*(C - C_\infty), \tag{3.3}$$

By replacing $\rho\mathbf{V} + \mathbf{j}_p$ with $\rho\mathbf{V}$ and employing divergence theorem we have

$$\frac{D}{Dt}\int\limits_{V_m(t)} \rho dV = -\int\limits_{V_a(t)} \nabla\cdot(\rho\mathbf{V} + \mathbf{j}_p) dV - R^*(C - C_\infty). \tag{3.4}$$

As $\rho = C\rho_p + (1-C)\rho_{bf}$ denotes the nanofluid density where ρ_p stands for nano particle density and ρ_{bf} denotes base fluid density (Buongiorno, 2006). Therefore, in terms of base fluid and nanoparticles Equation (3.4) converted into

$$\frac{D}{Dt}\int\limits_{V_m(t)} (1-C)\rho_{bf} dV = -\int\limits_{V_a(t)} \nabla\cdot\rho\mathbf{V} dV, \tag{3.5}$$

and

$$\frac{D}{Dt}\int\limits_{V_m(t)} C\rho_p dV = -\int\limits_{V_a(t)} \nabla\cdot\mathbf{j}_p dV - R^*(C - C_\infty). \tag{3.6}$$

In view of Anwar (2013) $(1-C)\rho_{bf} \to \rho$ and for incompressible flow Equation (3.5) becomes

$$\nabla\cdot\rho\mathbf{V} + \rho\cdot\nabla\mathbf{V} = 0, \tag{3.7}$$

finally it will be converted to,

$$\nabla\cdot\mathbf{V} = 0, \tag{3.8}$$

which represents equation of continuity i.e.

$$\frac{\partial \bar{u}}{\partial \bar{x}} + \frac{\partial \bar{v}}{\partial \bar{y}} + \frac{\partial \bar{w}}{\partial \bar{z}} = 0, \tag{3.9}$$

Moreover, by using Reynolds transport and divergence theorem Equation (3.6) becomes

$$\int\limits_{V_a(t)} \frac{\partial (C\rho_P)}{\partial t} dV + \int\limits_{V_a(t)} \nabla \cdot C\rho_p \mathbf{V} dV_1 = - \int\limits_{V_a(t)} \nabla \cdot \mathbf{j}_p dV - R^*(C - C_\infty). \tag{3.10}$$

By following same assumption as for Equation (3.5), and using $\mathbf{j}_p$ value above equation (3.10) can be converted into

$$\frac{\partial C}{\partial t} + \mathbf{V} \cdot \nabla C = \nabla \cdot \left[D_{B^*} \cdot \nabla C + D_{T^*} \frac{\nabla T}{T_\infty} \right] - R^*(C - C_\infty), \tag{3.11}$$

which is called principle of mass. It can also expressed by

$$\begin{aligned} \frac{\partial \bar{C}}{\partial \bar{t}} + \bar{u}\frac{\partial \bar{C}}{\partial \bar{x}} + \bar{v}\frac{\partial \bar{C}}{\partial \bar{y}} + \bar{w}\frac{\partial \bar{C}}{\partial \bar{z}} &= D_{B^*} \left[\frac{\partial^2 \bar{C}}{\partial \bar{x}^2} + \frac{\partial^2 \bar{C}}{\partial \bar{y}^2} + \frac{\partial^2 \bar{C}}{\partial \bar{z}^2} \right] \\ &+ \left(\frac{D_{T^*}}{T_\infty} \right) \left[\frac{\partial^2 \bar{T}}{\partial \bar{x}^2} + \frac{\partial^2 \bar{T}}{\partial \bar{y}^2} + \frac{\partial^2 \bar{T}}{\partial \bar{z}^2} \right] - R^*(\bar{C} - C_\infty). \end{aligned} \tag{3.12}$$

3.2.2 Conservation of Momentum

Total momentum in an isolated system is remain same with respect to time termed principle for conservation of momentum. By Newton's second law of motion $\mathbf{F}_{total} = m^{'}\mathbf{a}$, here $\mathbf{F}_{total}$ means sum of body forces and surface forces $\mathbf{T}$. Moreover, body force for this research is $\mathbf{F} = -\rho g_x + \mathbf{F_1}$. Here, the buoyancy force which would act on the inclined geometry as mentioned by Jaluria (1980) is given as $g_x = gcos\gamma$, where γ denotes inclination, $\mathbf{a} = \frac{d\mathbf{V}}{dt}$ means acceleration and $m^{'}$ signify object mass.

Then for momentum equation we have

$$\frac{d}{dt} \int\limits_{V_m(t)} \rho \mathbf{V} dV = \int\limits_{S_a(t)} \mathbf{T} dS_1 + \int\limits_{V_a(t)} [-\rho g cos\gamma + \mathbf{F_1}] dV. \tag{3.13}$$

Since flow is driven due to the buoyancy effects arising from the density difference caused by temperature and concentration difference, the density difference can be expressed by the following equation (Palani, 2001):

$$d\rho = \frac{\partial \rho}{\partial T'} dT' + \frac{\partial \rho}{\partial C'} dC'. \tag{3.14}$$

Here, the effect of buoyancy forces will be expressed in the form of coefficient of thermal expansion β_t and coefficient of concentration expansion β_c. As referred to the explanation by Leal (1992) and Demuren and Grotjans (2009), this approximation can be formulized as follows

$$\rho - \rho_\infty = -\rho[\beta_t(T - T_\infty) + \beta_c(C - C_\infty)]. \tag{3.15}$$

After using Equation (3.14) and Equation (3.15) in Equation (3.13), we get

$$\frac{d}{dt} \int\limits_{V_m(t)} \rho \mathbf{V} dV = \int\limits_{S_a(t)} \mathbf{T} dS_1 + \int\limits_{V_a(t)} [\rho g[\beta_t(T - T_\infty) + \beta_c(C - C_\infty)] cos\gamma + \mathbf{F_1}] \, dV. \tag{3.16}$$

Following Anwar (2013) $\int\limits_{S_a(t)} \mathbf{T} dS_1$ takes the form

$$\int\limits_{S_a(t)} \mathbf{T} dS_1 = \int\limits_{S_a(t)} \mathbf{T} \cdot \mathbf{n} dS_1. \tag{3.17}$$

Utilizing above expression and Reynolds theorem Equation (3.16) will be

$$\int\limits_{V_a(t)} \frac{\partial(\rho \mathbf{V})}{\partial t} dV + \int\limits_{S_a(t)} \rho \mathbf{V}(\mathbf{V} \cdot \mathbf{n}) dS_1 = \tag{3.18}$$

$$\int\limits_{S_a(t)} \mathbf{T} \cdot \mathbf{n} dS_1 + \int\limits_{V_a(t)} [\rho g[\beta_t(T - T_\infty) + \beta_c(C - C_\infty)] cos\gamma + \mathbf{F_1}] \, dV.$$

via divergence theorem, above expression can also written as

$$\int\limits_{V_a(t)} \frac{\partial \rho \mathbf{V}}{\partial t} dV + \int\limits_{V_a(t)} \nabla \cdot (\rho \mathbf{V} \mathbf{V}) dV = \int\limits_{V_a(t)} \nabla \cdot \mathbf{T} dV + \tag{3.19}$$

$$\int\limits_{V_a(t)} [\rho g[\beta_t(T - T_\infty) + \beta_c(C - C_\infty)] cos\gamma + \mathbf{F_1}] \, dV,$$

and can be written as

$$\frac{(\partial \rho \mathbf{V})}{\partial t} + \nabla \cdot (\rho \mathbf{V} \mathbf{V}) = div \mathbf{T} + [\rho g[\beta_t(T - T_\infty) + \beta_c(C - C_\infty)] cos\gamma + \mathbf{F_1}]. \tag{3.20}$$

Further, above equation takes the form

$$\rho\frac{\partial \mathbf{V}}{\partial t}+\mathbf{V}\left[\frac{\partial \rho}{\partial t}+\nabla\cdot(\rho\mathbf{V})\right]+\rho\mathbf{V}\cdot\nabla\mathbf{V}=div\mathbf{T}+\rho g\beta_t(T-T_\infty)cos\gamma \qquad (3.21)$$
$$+\rho g\beta_c(C-C_\infty)cos\gamma+\mathbf{F_1}.$$

As local density takes constant, thus

$$\rho\left[\frac{\partial \mathbf{V}}{\partial t}+\mathbf{V}\cdot\nabla\mathbf{V}\right]=div\mathbf{T}+[\rho g[\beta_t(T-T_\infty)+\beta_c(C-C_\infty)]cos\gamma+\mathbf{F_1}]. \qquad (3.22)$$

Here, $\mathbf{T}$ (Cauchy stress tensor) in view of (Abbas, 2009) can be expressed as

$$\mathbf{T}=-p\mathbf{I}+\mu\mathbf{A}_1, \qquad (3.23)$$

where, P denotes pressure, $\mathbf{I}$ represent identity tensor, μ means viscosity and $\mathbf{A}_1$ means first Rivlin-Ericksen tensor.

Following (Anwar, 2013) by using value of $div\mathbf{T}$ Equation (1.22) becomes

$$\rho\left[\frac{\partial \mathbf{V}}{\partial t}+\mathbf{V}\cdot\nabla\mathbf{V}\right]=-\nabla p+\nabla\cdot\mu\left[(\nabla\mathbf{V})^T+\nabla\mathbf{V}\right]+\rho g[\beta_t(T-T_\infty)]cos\gamma \qquad (3.24)$$
$$+\rho g[\beta_c(C-C_\infty)]cos\gamma+\mathbf{J}\times\mathbf{B}$$

where $\mathbf{J}\times\mathbf{B}$ denotes the Lorentz force where $\mathbf{B}$ means total magnetic field i.e. sum of applied magnetic field ($\mathbf{B_0}$) and the induced magnetic field ($\mathbf{b}$). While ∇p is the pressure gradient. $\mathbf{B}$ expressed as

$$\mathbf{B}=\mathbf{B_0}+\mathbf{b}, \qquad (3.25)$$

and $\mathbf{J}$ (current density) in terms of Ohm's law

$$\mathbf{J}=\sigma(E+\mathbf{V}\times\mathbf{B}), \qquad (3.26)$$

where σ denotes electrical conductivity of the nanofluid and E signifies polarization due to electric charges. In this study, polarization effects are ignored i.e. $E=0$ (Chen, 2008) therefore

$$\mathbf{J}=\sigma(\mathbf{V}\times\mathbf{B}). \qquad (3.27)$$

Taking cross product with **B** on both sides, we get

$$\mathbf{J}\times\mathbf{B}=\sigma(\mathbf{V}\times\mathbf{B})\times\mathbf{B}, \tag{3.28}$$

and with the help of vector identity, we obtain

$$\mathbf{J}\times\mathbf{B}=\sigma(\mathbf{V}\cdot\mathbf{B})\mathbf{B}-(\mathbf{B}\cdot\mathbf{B})\mathbf{V}. \tag{3.29}$$

Following Afify (2009), it is assumed that the induced magnetic field **b** is negligible and the magnetic field **B** taken normal to flow and hence we get

$$\mathbf{J}\times\mathbf{B}=-\sigma {B_0}^2 x^{m-1}\mathbf{V}. \tag{3.30}$$

Here, $\mathbf{B_0}$ means uniform magnetic field strength. Thus Equation (3.24) becomes

$$\rho\left[\frac{\partial\mathbf{V}}{\partial t}+\mathbf{V}\cdot\nabla\mathbf{V}\right]=-\nabla p+\nabla\cdot\mu\left[(\nabla\mathbf{V})^T+\nabla\mathbf{V}\right]+\rho g\beta_t(T-T_\infty)\cos\gamma \tag{3.31}$$

$$+\rho g\beta_c(C-C_\infty)\cos\gamma-\sigma B_0^2 x^{m-1}\mathbf{V}.$$

Putting $\nu=\frac{\mu}{\rho}$, we have (Anwar, 2013):

$$\frac{\partial\bar{u}}{\partial\bar{t}}+\bar{u}\frac{\partial\bar{u}}{\partial\bar{x}}+\bar{v}\frac{\partial\bar{u}}{\partial\bar{y}}+\bar{w}\frac{\partial\bar{u}}{\partial\bar{z}}=-\frac{\partial\bar{p}}{\partial\bar{x}}\frac{1}{\rho}+\nu\left[\frac{\partial^2\bar{u}}{\partial\bar{x}^2}+\frac{\partial^2\bar{u}}{\partial\bar{y}^2}+\frac{\partial^2\bar{u}}{\partial\bar{z}^2}\right]+$$

$$g\left[\beta_t(\bar{T}-T_\infty)+\beta_c(\bar{C}-C_\infty)\right]\cos\gamma-\frac{\sigma}{\rho}B_0^2 x^{m-1}\bar{u}, \tag{3.32}$$

$$\frac{\partial\bar{v}}{\partial\bar{t}}+\bar{u}\frac{\partial\bar{v}}{\partial\bar{x}}+\bar{v}\frac{\partial\bar{v}}{\partial\bar{y}}+\bar{w}\frac{\partial\bar{v}}{\partial\bar{z}}=-\frac{\partial\bar{p}}{\partial\bar{y}}\frac{1}{\rho}+\nu\left[\frac{\partial^2\bar{v}}{\partial\bar{x}^2}+\frac{\partial^2\bar{v}}{\partial\bar{y}^2}+\frac{\partial^2\bar{v}}{\partial\bar{z}^2}\right], \tag{3.33}$$

$$\frac{\partial\bar{w}}{\partial\bar{t}}+\bar{u}\frac{\partial\bar{w}}{\partial\bar{x}}+\bar{v}\frac{\partial\bar{w}}{\partial\bar{y}}+\bar{w}\frac{\partial\bar{w}}{\partial\bar{z}}=-\frac{\partial\bar{p}}{\partial\bar{z}}\frac{1}{\rho}+\nu\left[\frac{\partial^2\bar{w}}{\partial\bar{x}^2}+\frac{\partial^2\bar{w}}{\partial\bar{y}^2}+\frac{\partial^2\bar{w}}{\partial\bar{z}^2}\right]. \tag{3.34}$$

3.2.3 Conservation of Energy

If energy of an isolated system remain unchanged, i.e. energy can neither be destroyed nor be created, termed principle of energy conservation. According to Pfautsch (2008), Figure 3.2 is utilized for the equation of energy. The equation of energy by

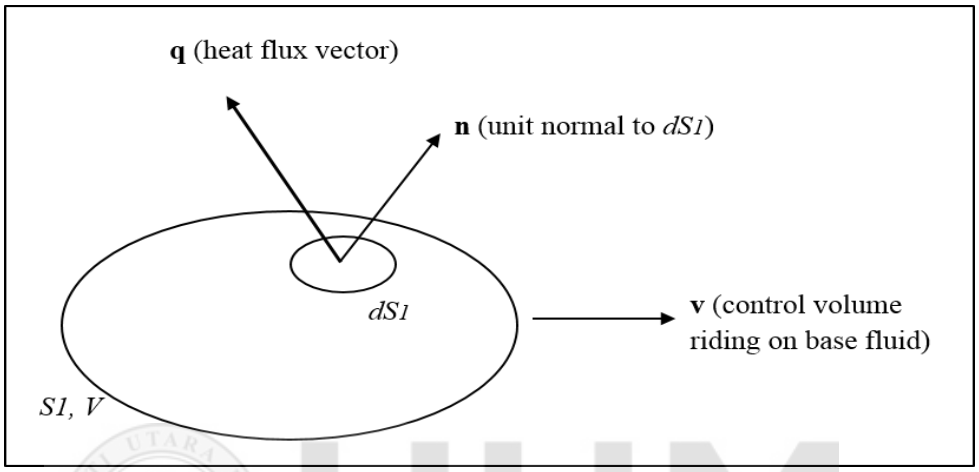

Figure 3.2. Geometry of control volume.

incorporating radiations and heat generation or absorption effects is given by:

$$(\rho c)_f \left[\frac{\partial T}{\partial t} + V \cdot \nabla T\right] = -\nabla \cdot q + h_p \nabla \cdot j_p - \frac{1}{(\rho c)_f} \nabla \cdot q_r + \frac{Q_0}{(\rho c)_p}(T - T_\infty), \quad (3.35)$$

where c_p presents the nanoparticle specific heat, Q_0 denotes heat generation or absorption factor, enthalpy of nanoparticle means h_p and $(\rho c)_f$ denotes heat capacitance of regular liquid, q signify heat flux corresponds to velocity of nanofluid (Buongiorno, 2006) and q_r denotes Rosseland approximation given as Anwar (2013);

$$q_r = -\frac{4\sigma^*}{3k_*}\left[\frac{\partial T^4}{\partial x}, \frac{\partial T^4}{\partial y}, \frac{\partial T^4}{\partial z}\right]. \quad (3.36)$$

Here, k^* is the mean absorption coefficient and σ^* is the Stefan-Boltzmann constant. By expanding T^4 in a Taylor series about T_∞ and ignoring higher order terms, thus

$$T^4 \cong 4T_\infty^3 T - 3T_\infty^4. \quad (3.37)$$

By utilizing values of T^4 and q_r Equation (3.35) converted in to

$$(\rho c)_f \left[V \cdot \nabla T + \frac{\partial T}{\partial t} \right] = -\nabla \cdot h_p j_p + h_p \nabla \cdot j_p + \nabla \cdot k \nabla T$$

$$+ \frac{16\sigma^* T_\infty^3}{3k^*(\rho c)_f} \nabla^2 T + \frac{Q_0}{(\rho c)_p}(T - T_\infty). \tag{3.38}$$

By applying divergence property, term $\nabla \cdot h_p j_p$ becomes

$$\nabla \cdot h_p j_p = h_p \nabla \cdot j_p + j_p \cdot \nabla h_p. \tag{3.39}$$

inserting above expression into Equation (3.38), becomes

$$(\rho c)_f \left[V \cdot \nabla T + \frac{\partial T}{\partial t} \right] = \nabla \cdot K^* \nabla T - h_p \nabla \cdot j_p - j_p \cdot \nabla h_p + h_p \nabla \cdot j_p$$

$$+ \frac{16\sigma^* T_\infty^3}{3k^*(\rho c)_f} \nabla^2 T + \frac{Q_0}{(\rho c)_p}(T - T_\infty). \tag{3.40}$$

By replacing j_p value Equation (3.40) converted into

$$\left[V \cdot \nabla T + \frac{\partial T}{\partial t} \right] = \left(\alpha^* + \frac{16\sigma^* T_\infty^3}{3k^*(\rho c)_f} \right) \nabla^2 T + \frac{Q_0}{(\rho c)_p}(T - T_\infty)$$

$$+ \tau \left[D_{T^*} \frac{\nabla^2 T}{T_\infty} + D_{B^*} \nabla C \cdot \nabla T \right]. \tag{3.41}$$

Above expression can also expressed by

$$\frac{\partial \bar{T}}{\partial \bar{t}} + \bar{u}\frac{\partial \bar{T}}{\partial \bar{x}} + \bar{v}\frac{\partial \bar{T}}{\partial \bar{y}} + \bar{w}\frac{\partial \bar{T}}{\partial \bar{z}} = \left(\alpha^* + \frac{16\sigma^* T_\infty^3}{3k^*(\rho c)_f} \right) \left[\frac{\partial^2 \bar{T}}{\partial \bar{x}^2} + \frac{\partial^2 \bar{T}}{\partial \bar{y}^2} + \frac{\partial^2 \bar{T}}{\partial \bar{z}^2} \right] \tag{3.42}$$

$$+ \frac{Q_0}{(\rho c)_p}(\bar{T} - T_\infty) + \tau \left[\begin{array}{r} D_{B^*} \left(\frac{\partial \bar{C}}{\partial \bar{x}} \frac{\partial \bar{T}}{\partial \bar{x}} + \frac{\partial \bar{C}}{\partial \bar{y}} \frac{\partial \bar{T}}{\partial \bar{y}} + \frac{\partial \bar{C}}{\partial \bar{z}} \frac{\partial \bar{T}}{\partial \bar{z}} \right) \\ + \left(\frac{D_{T^*}}{T_\infty} \right) \left\{ \left(\frac{\partial \bar{T}}{\partial \bar{x}} \right)^2 + \left(\frac{\partial \bar{T}}{\partial \bar{y}} \right)^2 + \left(\frac{\partial \bar{T}}{\partial \bar{z}} \right)^2 \right\} \end{array} \right]$$

3.2.4 Non-dimensional Form

According to Bejan (2013), the aim behind scale analysis is to produce order of magnitudes estimates for the quantities of concern represented by "$*$" in the non-dimensional variables which are In view of Anwar (2013) defined as

$$x=\frac{\bar{x}}{L}, u=\frac{\bar{u}}{U_\infty}, T=\frac{\bar{T}-T_\infty}{\triangle T}, C=\frac{\bar{C}-C_\infty}{\triangle C}, y=\frac{\bar{y}}{Y^*}, v=\frac{\bar{v}}{V^*}, p=\frac{\bar{p}}{P^*}, M=\frac{\sigma {B_0}^2 L}{\rho U_\infty},$$

where L denotes characteristic length, U_∞ represents reference velocity, T_∞ (ambient temperature), $\triangle T$ signifies temperature difference between the wall and the free stream, C means volume fraction of the nanoparticles, $\triangle C$ denotes concentration difference and M denotes Hartmann number. The chain rule for the above transformations are

$$\frac{\partial}{\partial \bar{x}}=\frac{\partial}{\partial x}\frac{\partial x}{\partial \bar{x}}=\frac{1}{L}\frac{\partial}{\partial x}, \frac{\partial}{\partial \bar{y}}=\frac{\partial}{\partial y}\frac{\partial y}{\partial \bar{y}}=\frac{1}{Y^*}\frac{\partial}{\partial y}\frac{\partial p}{\partial \bar{p}}=\frac{1}{P^*},$$

$$\frac{\partial^2}{\partial \bar{x}^2}=\frac{1}{L^2}\frac{\partial^2}{\partial x^2}, \frac{\partial^2}{\partial \bar{y}^2}=\frac{1}{Y^{*2}}\frac{\partial^2}{\partial y^2}.$$

Applying the above mentioned chain rule Equation (3.8) i.e. equation of continuity, Equation (3.32) and (3.33) i.e. momentum equation, Equation (3.42) i.e. energy equation and mass Equation (3.12) for steady two dimensional coordinates derived in earlier section are converted to non-dimension Equation after simplifications as follows (Anwar, 2013):

$$\frac{\partial u}{\partial x}\frac{U_\infty}{L}+\frac{\partial v}{\partial y}\frac{V^*}{Y^*}=0 \tag{3.43}$$

$$\frac{U_\infty^2}{L}u\frac{\partial u}{\partial x}+\frac{U_\infty V^*}{Y^*}v\frac{\partial u}{\partial y}=-\frac{1}{\rho}\frac{P^*}{L}\frac{\partial p}{\partial x}+\nu\frac{U_\infty}{L^2}\frac{\partial^2 u}{\partial x^2}+\nu\frac{{U_\infty}^2}{Y^{*2}}\frac{\partial^2 u}{\partial y^2}$$

$$+g\beta_t(\triangle T)T\cos\gamma+g\beta_c(\triangle C)C\cos\gamma-M\frac{U_\infty^2}{L}x^{m-1}u, \tag{3.44}$$

$$\frac{U_\infty V^*}{L}u\frac{\partial v}{\partial x}+v\frac{\partial v}{\partial y}\frac{V^{*2}}{Y^*}=-\frac{1}{\rho}\frac{\partial p}{\partial y}\frac{P^*}{Y^*}+\nu\frac{V^*}{L^2}\frac{\partial^2 v}{\partial x^2}+\nu\frac{V^*}{Y^{*2}}\frac{\partial^2 v}{\partial y^2}, \tag{3.45}$$

$$u\frac{\partial T}{\partial x}\frac{U_\infty}{L}+v\frac{\partial T}{\partial y}\frac{V^*}{Y^*}=\left(\alpha^*+\frac{16\sigma^* T_\infty^3}{3k^*(\rho c)_f}\right)\left[\frac{1}{L^2}\frac{\partial^2 T}{\partial x^2}+\frac{1}{Y^{*2}}\frac{\partial^2 T}{\partial y^2}\right]$$

$$+\frac{\triangle T Q_0}{(\rho c)_p}T+\tau\left[\begin{array}{r} D_{B^*}\left(\frac{\triangle C}{L^2}\frac{\partial T}{\partial x}\frac{\partial C}{\partial x}+\frac{\triangle C}{Y^{*2}}\frac{\partial T}{\partial y}\frac{\partial C}{\partial y}\right) \\ +\left(\frac{D_{T^*}}{T_\infty}\right)\left\{\left(\frac{\partial T}{\partial x}\right)^2\frac{\triangle T}{L^2}+\left(\frac{\partial T}{\partial y}\right)^2\frac{\triangle T}{Y^{*2}}\right\}\end{array}\right] \tag{3.46}$$

$$u\frac{\partial C}{\partial x}\frac{U_\infty}{L}+v\frac{\partial C}{\partial y}\frac{V^*}{Y^*}=D_{B^*}\frac{\triangle C}{L^2}\frac{\partial^2 C}{\partial x^2}+D_{B^*}\frac{\triangle C}{Y^{*2}}\frac{\partial^2 C}{\partial y^2}$$

$$+\frac{\triangle T}{L^2}\left(\frac{D_{T^*}}{T_\infty}\right)\frac{\partial^2 T}{\partial x^2}+\frac{\triangle T}{Y^{*2}}\left(\frac{D_{T^*}}{T_\infty}\right)\frac{\partial^2 T}{\partial y^2}-\triangle C R^* C. \tag{3.47}$$

The objective of boundary layer scale analysis is to simplify the equations of conservation laws. These equations can be simplified to get an approximate set of equations, termed boundary layer equations. From Equations (3.43) to (3.47), since all involved variables and derivatives are non-dimensional, the coefficients of all the terms must be of the same order of magnitude $(\sim)$. With reference of Anwar (2013), by doing a scale analysis on the boundary layer and by ignoring few terms without significantly affecting the accuracy of solution. Hence, we apply the scaling

$$V^* \sim U_\infty, P^* \sim \rho U_\infty^2, Y^* \sim L. \tag{3.48}$$

On using Equation (3.48) into Equations (3.43) to (3.47), we get

$$\frac{\partial u}{\partial x}+\frac{\partial v}{\partial y}=0, \tag{3.49}$$

$$u\frac{\partial u}{\partial x}+v\frac{\partial u}{\partial y}=-\frac{\partial p}{\partial x}+\frac{1}{Re}\frac{\partial^2 u}{\partial x^2}+\frac{1}{Re}\frac{\partial^2 u}{\partial y^2} \tag{3.50}$$

$$+g\beta_t(\triangle T)T\cos\gamma+g\beta_c(\triangle C)C\cos\gamma-Mx^{m-1}u,$$

$$u\frac{\partial v}{\partial x}+v\frac{\partial v}{\partial y}=-\frac{\partial p}{\partial y}+\frac{1}{Re}\frac{\partial^2 v}{\partial x^2}+\frac{1}{Re}\frac{\partial^2 v}{\partial y^2}, \tag{3.51}$$

$$u\frac{\partial T}{\partial x}+v\frac{\partial T}{\partial y}=\left(\alpha^*+\frac{16\sigma^* T_\infty^3}{3k^*(\rho c)_f}\right)\frac{1}{\nu Re}\left[\frac{\partial^2 T}{\partial x^2}+\frac{\partial^2 T}{\partial y^2}\right] \tag{3.52}$$

$$+\triangle T\frac{Q_0}{(\rho c)_p}T+\tau\left[\begin{array}{c} D_{B^*}\dfrac{\triangle C}{\nu Re}\cdot\left(\dfrac{\partial C}{\partial x}\dfrac{\partial T}{\partial x}+\dfrac{\partial C}{\partial y}\dfrac{\partial T}{\partial y}\right) \\ +\left(\dfrac{D_{T^*}\triangle T}{T_\infty\nu Re}\right)\left\{\left(\dfrac{\partial T}{\partial x}\right)^2+\left(\dfrac{\partial T}{\partial y}\right)^2\right\}\end{array}\right]$$

$$u\frac{\partial C}{\partial x}+v\frac{\partial C}{\partial y}=\frac{D_{B^*}\triangle C}{\nu Re}\left[\frac{\partial^2 C}{\partial x^2}+\frac{\partial^2 C}{\partial y^2}\right] \tag{3.53}$$

$$+\left(\frac{D_{T^*}\triangle T}{T_\infty\nu Re}\right)\left[\frac{\partial^2 T}{\partial x^2}+\frac{\partial^2 T}{\partial y^2}\right]-\triangle CR^*C,$$

where $Re=\frac{U_\infty L}{\nu}$ is the Reynolds number. By considering $V=\nu Re^{\frac{1}{2}}$ and $Y=yRe^{\frac{1}{2}}$ following Lok (2008), equations (3.49) to (3.53) are converted to the form

$$\frac{\partial u}{\partial x}+\frac{\partial V}{\partial Y}=0, \tag{3.54}$$

$$u\frac{\partial u}{\partial x}+V\frac{\partial u}{\partial Y}=-\frac{\partial p}{\partial x}+\frac{1}{Re}\frac{\partial^2 u}{\partial x^2}+\frac{\partial^2 u}{\partial Y^2} \tag{3.55}$$

$$+g\beta_t(\triangle T)T\cos\gamma+g\beta_c(\triangle C)C\cos\gamma-Mx^{m-1}u,$$

$$\frac{1}{Re^{\frac{1}{2}}}\left[u\frac{\partial V}{\partial x}+V\frac{\partial V}{\partial Y}\right]=-\frac{\partial p}{\partial y}+\frac{1}{Re^{\frac{3}{2}}}\frac{\partial^2 V}{\partial x^2}+\frac{1}{Re^{\frac{1}{2}}}\frac{\partial^2 V}{\partial Y^2}, \tag{3.56}$$

$$u\frac{\partial T}{\partial x}+V\frac{\partial T}{\partial Y}=\left(\alpha^*+\frac{16\sigma^* T_\infty^3}{3k^*(\rho c)_f}\right)\frac{1}{\nu Re}\frac{\partial^2 T}{\partial x^2}+\frac{1}{\nu}\frac{\partial^2 T}{\partial Y^2} \tag{3.57}$$

$$+\triangle T\frac{Q_0}{(\rho c)_p}T+\tau\left[\begin{array}{c}\dfrac{\partial C}{\partial x}\dfrac{\partial T}{\partial x}\dfrac{D_{B^*}\triangle C}{\nu Re}+\dfrac{\partial C}{\partial Y}\dfrac{\partial T}{\partial Y}\dfrac{D_{B^*}\triangle C}{\nu}\\ +\left(\dfrac{\partial T}{\partial x}\right)^2\left(\dfrac{D_{T^*}\triangle T}{T_\infty \nu Re}\right)+\left(\dfrac{\partial T}{\partial y}\right)^2\left(\dfrac{D_{T^*}\triangle T}{T_\infty \nu}\right)\end{array}\right]$$

$$u\frac{\partial C}{\partial x}+V\frac{\partial C}{\partial Y}=\frac{D_{B^*}\triangle C}{\nu Re}\frac{\partial^2 C}{\partial x^2}+\frac{D_{B^*}\triangle C}{\nu}\frac{\partial^2 C}{\partial Y^2} \tag{3.58}$$

$$+\left(\frac{D_{T^*}\triangle T}{T_\infty \nu Re}\right)\frac{\partial^2 T}{\partial x^2}+\left(\frac{D_{T^*}\triangle T}{T_\infty \nu}\right)\frac{\partial^2 T}{\partial Y^2}-\triangle C R^* C.$$

Sharma and Deka (2012) studied that Reynolds number (Re) measures the ratio of inertial forces to viscous forces and consequently quantifies the relative significance of these two kinds of forces for given flow conditions. On account of high Reynolds number, the viscous forces are small enough relative to the inertial forces but we cannot ignore viscous impacts completely. Moreover, in such a condition, the Reynolds number becomes asymptotically large and all terms in the above Equations involving Reynolds number in the denominator tend to zero. Therefore, Equations (3.54) to (3.58) convert to the following equations by using original notation:

$$\frac{\partial u}{\partial x}+\frac{\partial v}{\partial y}=0, \tag{3.59}$$

$$u\frac{\partial u}{\partial x}+v\frac{\partial u}{\partial y}=-\frac{\partial p}{\partial x}+\frac{\partial^2 u}{\partial y^2}+g\beta_t(\triangle T)T\cos\gamma+g\beta_c(\triangle C)C\cos\gamma-Mx^{m-1}u, \tag{3.60}$$

$$\frac{\partial P}{\partial y}=0, \tag{3.61}$$

$$u\frac{\partial T}{\partial x}+v\frac{\partial T}{\partial y}=\left(\alpha+\frac{16\sigma^* T_\infty^3}{3k^*(\rho c)_f}\right)\frac{\partial^2 T}{\partial y^2} \tag{3.62}$$

$$+\triangle T\frac{Q_0}{(\rho c)_p}T+\tau\left[D_B\frac{\partial T}{\partial y}\frac{\partial C}{\partial y}+\left(\frac{\partial T}{\partial y}\right)^2\frac{D_T}{T_\infty}\right],$$

$$u\frac{\partial C}{\partial x}+v\frac{\partial C}{\partial y}=\frac{\partial^2 C}{\partial y^2}D_B+\frac{\partial^2 T}{\partial y^2}\frac{D_T}{T_\infty}-\triangle CR^*C, \tag{3.63}$$

where $\alpha=\frac{\alpha^*}{\nu}, D_B=\frac{D_B^*}{\nu}$ and $D_T=\frac{D_T^*\triangle T}{\nu}$.

Note that the pressure $p=p(x)$ is only a function of x, therefore it can be expressed as $\frac{\partial p}{\partial x}=\frac{dp}{dx}$. In boundary layer region, the pressure outside the boundary layer region is equal to the pressure inside the boundary layer region, hence

$$\frac{dp}{dx}=\frac{dp_\infty}{dx}. \tag{3.64}$$

In view of Rawi (2018), $\frac{dp}{dx}=0$, hence $\frac{\partial p}{\partial x}=0$ in Equation (3.60), we get

$$u\frac{\partial u}{\partial x}+v\frac{\partial u}{\partial y}=\frac{\partial^2 u}{\partial y^2}+g\beta_t(\triangle T)T\cos\gamma+g\beta_c(\triangle C)C\cos\gamma-Mx^{m-1}u. \tag{3.65}$$

For linear stretching, in Equation (3.30), we can take $\mathbf{J}\times\mathbf{B}=-\sigma {B_0}^2\mathbf{V}$ while for the case of power stretching $\mathbf{J}\times\mathbf{B}=-\sigma {B_0}^2x^{m-1}\mathbf{V}$.

3.2.5 Momentum Equations for Micropolar Fluid

In view of Anwar (2013) total angular momentum demarcated as

$$\frac{d}{dt}\int\limits_{V_m(t)}\rho\big(\mathbf{X}\times\mathbf{V}+\mathbf{I}\big)dV=\int\limits_{v_a(t)}\big(\mathbf{T}_x+\mathbf{X}\times(\nabla\cdot\mathbf{T})+(\nabla\cdot\mathbf{C})\big)dV+\int\limits_{V_a(t)}\big(\mathbf{X}\times\mathbf{F}\big)dV. \tag{3.66}$$

when $\mathbf{V}=\mathbf{I}+\mathbf{X}\times\mathbf{V}$, following equations (3.22) to (3.25), above equation takes the form

$$\rho\frac{D\mathbf{I}}{Dt}+\rho\frac{D}{Dt}\big(\mathbf{X}\times\mathbf{V}\big)=\nabla\cdot\mathbf{C}+\mathbf{X}\times(\nabla\cdot\mathbf{T})+\mathbf{T}_x+\mathbf{X}\times\mathbf{F}. \tag{3.67}$$

Further it is converted in to

$$\rho\frac{D}{Dt}\big(\mathbf{V}\times\mathbf{X}\big)=\mathbf{X}\times(\nabla\cdot\mathbf{T})+\mathbf{X}\times\mathbf{F}. \tag{3.68}$$

applying vector property, above equation converted in to

$$\frac{D\mathbf{V}}{Dt}\rho = \mathbf{F} + \nabla \cdot \mathbf{T}. \tag{3.69}$$

In tensor form it becomes

$$t_{kl,k} + f_k - \rho v_{\cdot k} = 0, \tag{3.70}$$

According to Eringen (1966), the stress tensor for micropolar fluid can be demarcated as

$$t_{kl} = \big(-\pi + v_{r,r}\lambda_v\big)\delta_{kl} + \big(v_{l,k} + v_{k,l}\big)\mu_v + \big(v_{l,k} - \upsilon_r \varepsilon_{klr}\big)k_v \tag{3.71}$$

$$t_{kl,k} = \big(-\pi_{,k} + v_{r,rk}\lambda_v\big)\delta_k l + \big(v_{l,kk} + v_{k,lk}\big)\mu_v + \big(v_{l,kk} - \varepsilon_{klr}\upsilon_{r,k}\big)k_v \tag{3.72}$$

After using the values of t_{kl} and $t_{kl,k}$, Equation (3.70) becomes

$$-\pi_{,k} + \big(\mu_v + \lambda_v\big)v_{l,kl} + \big(k_v + \mu_v\big)v_{k,ll} + k_v\varepsilon_{klm}\upsilon_{m,l} + f_k - \rho v_{\cdot k} = 0, \tag{3.73}$$

Further it can be converted in to

$$\big(\mu_v + \lambda_v + k_v\big)\nabla\big(\nabla \cdot \mathbf{V}\big) - \big(k_v\mu_v\big)\nabla \times \nabla \times \mathbf{V} + k_v\nabla \times \mathbf{N}^* - \nabla\pi + \mathbf{F} = \rho\frac{D\mathbf{V}}{Dt}, \tag{3.74}$$

here $v = \mathbf{V}$, and by the reference Guohua (1999) $\lambda_v = 0$ and Equation (3.74) becomes

$$\rho\frac{D\mathbf{V}}{Dt} = -\nabla p + \big({k_1}^* + \mu\big)\nabla^2\mathbf{V} + \big(\nabla \times N^*\big){k_1}^* + \big[(-\rho g cos\gamma + \mathbf{J} \times \mathbf{B})\big], \tag{3.75}$$

where $\mathbf{F} = -\rho g cos\gamma + \mathbf{J} \times \mathbf{B}$, $k_v = {k_1}^*$, $\pi = p$ and $\mu_v = \mu$.

Further by using Equation (3.15), above equation takes the form

$$\rho\frac{D\mathbf{V}}{Dt} = -\nabla p + \big(\mu + {k_1}^*\big)\nabla^2\mathbf{V} + {k_1}^*\big(\nabla \times N^*\big) + \rho g(\beta_t(T - T_\infty))\cos\gamma \tag{3.76}$$

$$+\rho g(\beta_c(C-C_\infty))\cos\gamma+\mathbf{J}\times\mathbf{B}.$$

Now from Equation (3.67) and from Equation (3.68), we have

$$\rho\left(\frac{D\mathbf{I}}{Dt}\right)=\nabla\cdot\mathbf{C}+\mathbf{T}_x. \tag{3.77}$$

In view of Anwar (2013), for $\mathbf{I}\frac{j^*}{2}\omega$, Equation (3.67) is converted into

$$\frac{D\omega}{Dt}\frac{\rho j^*}{2}=\mathbf{T}_x+\nabla\cdot\mathbf{C}. \tag{3.78}$$

In tensor form it takes the form

$$m_{rk,r}+\varepsilon_{klr}t_{lr}-\rho j^*\upsilon_k=o, \tag{3.79}$$

where $2\upsilon_k=\frac{D\omega}{Dt}$, $m_{rk,r}=\nabla\cdot\mathbf{C}$, $\varepsilon_{klr}t_{lr}=\mathbf{T_x}$. The couple stress tensor in the case of micropolar fluid can de defined as Eringen (1966)

$$\begin{aligned}
&m_{rk}=\alpha_\nu\upsilon_{r,k}\delta_{kl}+\beta_\nu\upsilon_{r,k}+\gamma_n u\upsilon_{k,r}\\
&m_{r,kr}=\upsilon_{r,kr}\Big(\beta_\nu+\alpha_\nu\Big)+\gamma_\nu\upsilon_{k,rr},\\
&\varepsilon_{klr}t_{lr}=k_\nu\varepsilon_{klm}\nu_{m,l}-2k_\nu\upsilon_k,
\end{aligned} \tag{3.80}$$

where γ_ν, β_ν, α_ν denotes the coefficients of viscosity. By following (Anwar, 2013) Equation (3.69) converted in to

$$\Big(\alpha_\nu+\beta_\nu\Big)\upsilon_{r,kr}+\gamma_\nu\upsilon_{k,rr}+k_\nu\varepsilon_{klm}\nu_{m,l}-2k_\nu\upsilon_k-\rho j^*\upsilon_k=0. \tag{3.81}$$

Further Equation(3.70) takes the form

$$\Big(\alpha_\nu+\gamma_\nu+\beta_\nu\Big)\nabla\Big(\nabla\cdot N^*\Big)-\gamma_\nu\nabla\times\nabla\times N^*+k_\nu\nabla\times\mathbf{V}-2k_\nu\mathbf{N}^*=\frac{D\mathbf{N}^*}{Dt}\rho j^*, \tag{3.82}$$

here $\upsilon=N^*$. In view of Guohua (1999) in the case of two dimensional, compressible

fluid $(\alpha_v + \beta_v)$ will be vanish. Finally, above equation becomes

$$\gamma_v \nabla^2 \mathbf{N}^* + k_v \nabla \times \mathbf{V} - 2k_v \mathbf{N}^* = \rho j^* \frac{D\mathbf{N}^*}{Dt}, \tag{3.83}$$

when $\gamma_v = \gamma^*$, above equation takes the form

$$\rho j^* \frac{D\mathbf{N}^*}{Dt} = \gamma^* \nabla^2 \mathbf{N}^* + {k_1}^* \bigg(-2\mathbf{N}^* + \nabla \times \mathbf{V} \bigg), \tag{3.84}$$

where $\frac{D}{Dt} = \frac{\partial}{\partial t} + V \cdot \nabla$, the gradient $\nabla = \frac{\partial}{\partial x} i + \frac{\partial}{\partial} j + \frac{\partial}{\partial z} k$ and $N^*, k_1^*, j^*, \gamma^*$ are the microrotation or angular velocity, vertex viscosity, the gyration factor of the liquid and spin gradient, respectively. The terms $\bigg(\nabla \times \mathbf{N}^* \bigg)$ in Equation (3.76) and $\bigg(\nabla \times \mathbf{V} \bigg)$ in Equation (3.84) are defined as

$$\nabla \times \mathbf{N}^* = \begin{vmatrix} i & j & k \\ \frac{\partial}{\partial x} & \frac{\partial}{\partial y} & \frac{\partial}{\partial z} \\ 0 & 0 & N^* \end{vmatrix} = \frac{\partial N^*}{\partial y} i + \frac{\partial N^*}{\partial x} j, \tag{3.85}$$

$$\nabla \times \mathbf{V} = \begin{vmatrix} i & j & k \\ \frac{\partial}{\partial x} & \frac{\partial}{\partial y} & \frac{\partial}{\partial z} \\ u & v & w \end{vmatrix} = \left(\frac{\partial v}{\partial x} + \frac{\partial u}{\partial y} \right) k.$$

For the steady flow, the dimensional form of Equations (3.76) and (3.84) in two dimensional Cartesian coordinates is

$$\bar{u} \frac{\partial \bar{u}}{\partial \bar{x}} + \bar{v} \frac{\partial \bar{u}}{\partial \bar{y}} = -\frac{1}{\rho} \frac{\partial \bar{p}}{\partial \bar{x}} + \left(\frac{\mu + k_1^*}{\rho} \right) \left(\frac{\partial^2 \bar{u}}{\partial \bar{x}^2} + \frac{\partial^2 \bar{u}}{\partial \bar{y}^2} \right) + \frac{k_1^*}{\rho} \frac{\partial \bar{N}^*}{\partial \bar{y}} \tag{3.86}$$

$$+ g\beta_T (\bar{T} - T_\infty) \cos\gamma + g\beta_C (\bar{C} - C_\infty) \cos\gamma - M x^{m-1} \bar{u},$$

$$\bar{u} \frac{\partial \bar{v}}{\partial \bar{x}} + \bar{v} \frac{\partial \bar{v}}{\partial \bar{y}} = -\frac{1}{\rho} \frac{\partial \bar{p}}{\partial \bar{y}} + \left(\frac{\mu + k_1^*}{\rho} \right) \left(\frac{\partial^2 \bar{v}}{\partial \bar{x}^2} + \frac{\partial^2 \bar{v}}{\partial \bar{y}^2} \right) + \frac{k_1^*}{\rho} \frac{\partial \bar{N}^*}{\partial \bar{y}}, \tag{3.87}$$

$$\bar{u} \frac{\partial \bar{N}^*}{\partial \bar{x}} + \bar{v} \frac{\partial \bar{N}^*}{\partial \bar{y}} = \left(\frac{\gamma^*}{j^* \rho} \right) \left(\frac{\partial^2 \bar{N}^*}{\partial \bar{x}^2} + \frac{\partial^2 \bar{N}^*}{\partial \bar{y}^2} \right) - \left(\frac{k_1^*}{j^* \rho} \right) \left(2\bar{N}^* + \frac{\partial \bar{u}}{\partial \bar{y}} - \frac{\partial \bar{v}}{\partial \bar{x}} \right). \tag{3.88}$$

Adopting similar process as shown in Sub-Section 3.2.4, Equations (3.86) to (3.88) in non-dimensional becomes

$$u\frac{\partial u}{\partial x}+v\frac{\partial u}{\partial y}=\left(\frac{\mu+k_1^*}{\rho}\right)\frac{\partial^2 u}{\partial y^2}+\left(\frac{k_1^*}{\rho}\right)\frac{\partial N^*}{\partial y}$$

$$+g\left[\beta_t(T-T_\infty)+\beta_c(C-C_\infty)\right]\cos\gamma-Mx^{m-1}u, \tag{3.89}$$

$$u\frac{\partial N^*}{\partial x}+v\frac{\partial N^*}{\partial y}=\left(\frac{\gamma^*}{j^*\rho}\right)\left(\frac{\partial^2 N^*}{\partial y^2}\right)-\left(\frac{k_1^*}{j^*\rho}\right)\left(2N^*+\frac{\partial u}{\partial y}\right). \tag{3.90}$$

For linear stretching in Equation (3.75), we can take $\mathbf{J}\times\mathbf{B}=-\sigma {B_0}^2\mathbf{V}$ whereas versus power stretching $\mathbf{J}\times\mathbf{B}=-\sigma {B_0}^2 x^{m-1}\mathbf{V}$.

3.2.6 Momentum Equation for Casson Fluid

As referenced from Nakamura and Sawada (1988) and Animasaun (2015), the rheological equation for Casson fluid is demarcated as

$$\tau_{ij}=\begin{cases}2\left(\mu_B+\dfrac{P_y}{\sqrt{2\Pi}}\right)e_{ij}, \Pi>\Pi_c\\ 2\left(\mu_B+\dfrac{P_y}{\sqrt{2\Pi_c}}\right)e_{ij} \Pi<\Pi_c\end{cases} \tag{3.91}$$

Here, $\Pi=e_{ij}e_{ij}$ and e_{ij} are deformation rate of (i,j)th component and is defined as

$$e_{ij}=\frac{1}{2}\left(\frac{\partial u_i}{\partial x_j}+\frac{\partial u_j}{\partial x_i}\right),$$

also, τ_{ij} is the component of stress tensor, $\beta=\frac{\mu_B\sqrt{2\Pi_c}}{P_y}$ is parameter of the Casson fluid, Π_c is the critical value of the product of the rate of strain tensor with itself.

In case of Casson fluid flow (Animasaun et al., 2016) where $\Pi>\Pi_c$, it is possible

that

$$\mu = \mu_B + \frac{P_y}{\sqrt{2\Pi}}. \tag{3.92}$$

here $P_y$denotes yield stress of Casson fluid and presented by

$$P_y = \frac{\mu_B \sqrt{2\Pi}}{\beta}. \tag{3.93}$$

Here, dynamic viscosity of Casson fluid is denoted by μ_B. See Animasaun et al. (2016), Using (3.93) into (3.92)

$$\mu = \mu_B \left(1 + \frac{1}{\beta}\right). \tag{3.94}$$

Therefore, Equation (3.24) in terms of Equation (3.94) for the Casson liquid takes the form

$$\rho \left[\mathbf{V}\cdot\nabla\mathbf{V} + \frac{\partial \mathbf{V}}{\partial t}\right] = -\nabla p + \nabla \cdot \mu_B \left(1 + \frac{1}{\beta}\right)\left[(\nabla \mathbf{V})^T + \nabla \mathbf{V}\right] + \rho g \beta_t (T - T_\infty) cos\gamma \tag{3.95}$$

$$+\rho g \beta_c (C - C_\infty) cos\gamma + \mathbf{J} \times \mathbf{B}$$

By following the Equations (3.24) to (3.31) the above equation converted in to the form

$$\rho \left[\mathbf{V}\cdot\nabla\mathbf{V} + \frac{\partial \mathbf{V}}{\partial t}\right] = -\nabla p + \nabla \cdot \mu_B \left(1 + \frac{1}{\beta}\right)\left[(\nabla \mathbf{V})^T + \nabla \mathbf{V}\right] + \rho g \beta_T (T - T_\infty)\cos\gamma \tag{3.96}$$

$$+\rho g \beta_C (C - C_\infty)\cos\gamma - \sigma B_0^2 x^{m-1}\mathbf{V}.$$

Considering $\nu = \frac{\mu}{\rho}$, Equation (3.96) is converted to

$$\frac{\partial \bar{u}}{\partial \bar{t}} + \bar{u}\frac{\partial \bar{u}}{\partial \bar{x}} + \bar{v}\frac{\partial \bar{u}}{\partial \bar{y}} + \bar{w}\frac{\partial \bar{u}}{\partial \bar{z}} = -\frac{1}{\rho}\frac{\partial \bar{p}}{\partial \bar{x}} + \left[\frac{\partial^2 \bar{u}}{\partial \bar{x}^2} + \frac{\partial^2 \bar{u}}{\partial \bar{y}^2} + \frac{\partial^2 \bar{u}}{\partial \bar{z}^2}\right]\nu\left(1 + \frac{1}{\beta}\right) +$$

$$g\beta_T(\bar{T} - T_\infty)\cos\gamma + g\beta_C(\bar{C} - C_\infty)\cos\gamma - \frac{\sigma}{\rho}B_0^2 x^{m-1}\bar{u}, \tag{3.97}$$

$$\frac{\partial \bar{v}}{\partial \bar{t}} + \bar{u}\frac{\partial \bar{v}}{\partial \bar{x}} + \bar{v}\frac{\partial \bar{v}}{\partial \bar{y}} + \bar{w}\frac{\partial \bar{v}}{\partial \bar{z}} = -\frac{1}{\rho}\frac{\partial \bar{p}}{\partial \bar{y}} + \nu\left(1+\frac{1}{\beta}\right)\left[\frac{\partial^2 \bar{v}}{\partial \bar{x}^2} + \frac{\partial^2 \bar{v}}{\partial \bar{y}^2} + \frac{\partial^2 \bar{v}}{\partial \bar{z}^2}\right], \quad (3.98)$$

$$\frac{\partial \bar{w}}{\partial \bar{t}} + \bar{u}\frac{\partial \bar{w}}{\partial \bar{x}} + \bar{v}\frac{\partial \bar{w}}{\partial \bar{y}} + \bar{w}\frac{\partial \bar{w}}{\partial \bar{z}} = -\frac{1}{\rho}\frac{\partial \bar{p}}{\partial \bar{z}} + \nu\left(1+\frac{1}{\beta}\right)\left[\frac{\partial^2 \bar{w}}{\partial \bar{x}^2} + \frac{\partial^2 \bar{w}}{\partial \bar{y}^2} + \frac{\partial^2 \bar{w}}{\partial \bar{z}^2}\right]. \quad (3.99)$$

The procedure as discussed in Sub-Section 3.2.4 is also applicable for the momentum equation of Casson fluid can be written as

$$u\frac{\partial u}{\partial x} + v\frac{\partial u}{\partial y} = \nu\left(1+\frac{1}{\beta}\right)\frac{\partial^2 u}{\partial y^2} + g\left[\beta_T(T-T_\infty) + \beta_C(C-C_\infty)\right]\cos\gamma - Mx^{m-1}u \quad (3.100)$$

For linear stretching, in Equation (3.30), we can take $\mathbf{J}\times\mathbf{B} = -\sigma {B_0}^2\mathbf{V}$. While for the case of power stretching, $\mathbf{J}\times\mathbf{B} = -\sigma {B_0}^2 x^{m-1}\mathbf{V}$.

3.3 Governing Equations of the Micropolar Nanofluid Flow over a Linear inclined Stretching Surface

An incompressible steady micropolar nanofluid flow generated by linearly stretching inclined surface is studied. The inclination of stretching surface is γ with vertical direction. Further, an applied transverse magnetic field acts perpendicular to the surface. Due to small Reynolds number, electric as well as magnetic field impacts are negligible (Mishra et al., 2016). The micropolar and nanoparticles are uniformly dispersed in the base liquid. In addition, particles gyrate in liquid field and results for spinning impacts in micropolar nanofluid. Moreover, Brownian motion and thermophoretic influences are incorporated. In addition, the constant values of temperature and concentration at wall are T_w and C_w, while at $y \to \infty$, the temperature and mass fractions are T_∞ and C_∞, see in Figure 3.3.

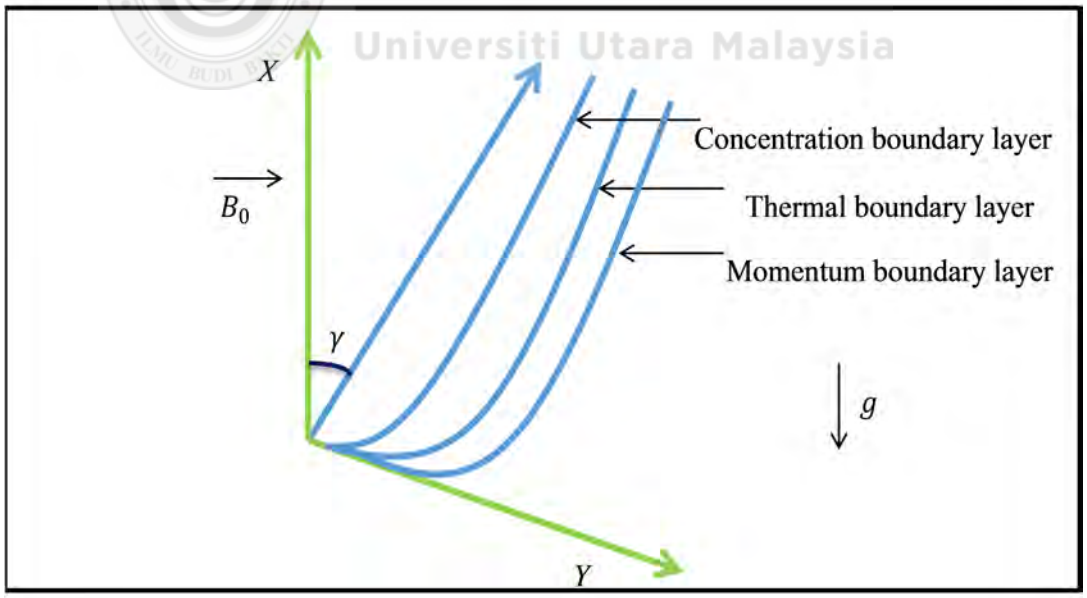

Figure 3.3. Physical geometry of the study.

From Section 3.2, the governing boundary layer equations which are based on the balance laws of momentum, angular microrotation, energy and mass for the present analysis are expressed as (see Equations 3.59, 3.62 (when $Q_0 = \sigma^* = 0$), 3.63 (when $R^* = 0$), 3.89 and 3.90):

$$\frac{\partial u}{\partial x} + \frac{\partial v}{\partial y} = 0,$$

$$u\frac{\partial u}{\partial x} + v\frac{\partial u}{\partial y} = \left(\frac{\mu + k_1^*}{\rho}\right)\frac{\partial^2 u}{\partial y^2} + \left(\frac{k_1^*}{\rho}\right)\frac{\partial N^*}{\partial y} + g\beta_t(T - T_\infty)\cos\gamma$$

$$+ g\beta_c(C - C_\infty)\cos\gamma - \left(\frac{\sigma {B_0}^2}{\rho}\right)u,$$

$$u\frac{\partial N^*}{\partial x} + v\frac{\partial N^*}{\partial y} = \left(\frac{\gamma^*}{j^*\rho}\right)\left(\frac{\partial^2 N^*}{\partial y^2}\right) - \left(\frac{k_1^*}{j^*\rho}\right)\left(2N^* + \frac{\partial u}{\partial y}\right), \tag{3.101}$$

$$u\frac{\partial T}{\partial x} + v\frac{\partial T}{\partial y} = \alpha\frac{\partial^2 T}{\partial y^2} + \tau\left[D_B\frac{\partial C}{\partial y}\frac{\partial T}{\partial y} + \frac{D_T}{T_\infty}\left(\frac{\partial T}{\partial y}\right)^2\right],$$

$$u\frac{\partial C}{\partial x} + v\frac{\partial C}{\partial y} = D_B\frac{\partial^2 C}{\partial y^2} + \frac{D_T}{T_\infty}\frac{\partial^2 T}{\partial y^2},$$

where v, u stands for velocity factors against y and x directions, g means gravitational acceleration, B_0 stands for magnetic field strength, electrical conductivity presented by σ, μ stands for viscosity, ${k_1}^*$ signifies vortex viscosity, β_t means thermal expansion, concentration expansion presented by β_c, γ^* represents gyration viscosity, j^* means micro inertia factor, N^* stands for microrotation, D_B is Brownian motion dispersion constraint, D_T means thermophoresis dispersion amount, k stands for thermal conductivity, and heat capacity for nanoparticles represented as $(\rho c)_p$, $(\rho c)_f$. Moreover, $\alpha = \frac{k}{(\rho c)_f}$ and $\tau = \frac{(\rho c)_p}{(\rho c)_f}$.

The subjected boundary settings are given by

$$u = u_w = ax\ , v = 0\ , T = T_w\ , N^* = -m_0 \frac{\partial u}{\partial y}\ , C = C_w \qquad at \qquad y = 0,$$

$$u \to u_\infty = 0\ , v \to 0\ , T \to T_\infty\ , N^* \to 0\ , C \to C_\infty \qquad as \qquad y \to \infty. \qquad (3.102)$$

In view of Anwar (2013), when $m_0 = 0$ means microelements, adjacent the wall surface are unable to revolve. where m_0 is a constant and $0 \leq m_0 \leq 1$.

3.3.1 Similarity Transformations

In this section, governing equations are reduced into nonlinear ordinary differential equations. The stream function for this problem is defined by

$$u = \frac{\partial \psi}{\partial y}\ , \quad v = -\frac{\partial \psi}{\partial x}, \qquad (3.103)$$

where Equation (3.101) i.e. continuity equation is satisfied identically. The similarity transformations are characterized as

$$u = axf'(\eta)\,, \eta = y\sqrt{\frac{a}{v}}, v = -\sqrt{av} f(\eta)\,,$$

$$\theta = \frac{T - T_\infty}{T_w - T_\infty}, N^* = ax\sqrt{\frac{a}{v}} h(\eta)\,, \phi = \frac{C - C_\infty}{C_w - C_\infty}. \qquad (3.104)$$

By using above equation, Equations (3.101) converted to the following nonlinear ordinary differential equations:

$$(1+K) f''' + ff'' - f'^2 + Kh' + (Gr_x \theta + Gc_x \phi)\, cos\gamma - (M) f' = 0,$$

$$\left(1 + \frac{K}{2}\right) h'' + fh' - hf'^2 - K\left(2h + f''\right) = 0,$$

$$\left(\frac{1}{\Pr}\right)\theta'' + f\theta' + Nb\theta'\phi' + Nt\theta'^2 = 0, \tag{3.105}$$

$$\phi'' + Lef\phi' + Nt_b\theta'' = 0,$$

where,

$$\Pr = \frac{v}{\alpha}, Le = \frac{v}{D_B}, Nb = \frac{\tau D_B\left(C_W - C_\infty\right)}{v}, Nt = \frac{\tau D_T\left(T_W - T_\infty\right)}{vT_\infty},$$

$$M = \frac{\sigma {B_0}^2}{a\rho}, Gr_x = \frac{g\beta_t\left(T_W - T_\infty\right)x^{-1}}{a^2}, Nt_b = \frac{Nt}{Nb}, Re_x = \frac{u_w(x)x}{\nu},$$

$$Gc_x = \frac{g\beta_c\left(C_W - C_\infty\right)x^{-1}}{a^2}. \tag{3.106}$$

Here, primes means the differentiation concerning η, Gr_x denotes the local Grashof number, the local modified Grashof number is expressed by Gc_x, M stands for magnetic factor, Pr means Prandtl number, Le stands for Lewis number, K signifies dimensionless vertex thickness, where Nb is the Brownian motion parameter and Nt is the thermophoresis parameter. It is worth mentioning here that to achieve true similarity solution, Gr_x and Gc_x must be constant and free from x. This condition can be achieved if thermal and concentration expansion coefficients β_t and β_c are proportional to x^1. Thus, from Makinde and Olanrewaju (2010), Olanrewaju and Hayat (2014), Ilias et al. (2016), we assume that

$$\beta_t = nx^1, \beta_c = n_1x^1, \tag{3.107}$$

where n and n_1 are constants. By substituting Equation (3.135) into the parameters Gr_x and Gc_x, we get

$$Gr = \frac{gn\left(T_W - T_\infty\right)}{a^2}, Gc = \frac{gn_1\left(C_W - C_\infty\right)}{a^2}. \tag{3.108}$$

The corresponding boundary conditions are transformed to

$$f(\eta)=0, f'(\eta)=1,\ h(\eta)=0, \phi(\eta)=1, \theta(\eta)=1 \ at\ \eta=0,$$

$$f'(\eta)\to 0,\ h(\eta)\to 0, \phi(\eta)\to 0, \theta(\eta)\to 0 \ \ at\ \ \eta\to\infty. \tag{3.109}$$

It is observed that for $K=0$, the model consideration is reduced to nanofluid model. The physical quantities including C_f (skin friction), Sherwood number i.e. Sh and Nusselt number i.e. Nu are expressed as

$$C_f=\frac{\tau_w}{\rho\ u_w^2},\ Sh=\frac{x\ q_m}{D_B(C_w-C_\infty)},\ Nu=\frac{x\ q_w}{k(T_w-T_\infty)}, \tag{3.110}$$

where $\tau_w=(\mu+k_1^*)\frac{\partial u}{\partial y}+\ k_1^*\ N^*,\ \ q_m=-\ D_B\frac{\partial C}{\partial y},\ \ q_w=-\ k\frac{\partial T}{\partial y}$, at $y=0$ are the shearstress, mass and energy rates. The final forms for (Skin friction coefficient) $C_{fx}(0)=(1+K)\ f''(0)$, $-\phi'(0)$ (local Sherwood number) and $-\theta'(0)$ (local Nusselt number) are defined as

$$C_{fx}(0)=\ C_f\sqrt{Re_x}, -\phi'(0)=\frac{Sh}{\sqrt{Re_x}}, -\theta'(0)=\frac{Nu}{\sqrt{Re_x}}, \tag{3.111}$$

where, $Re_x=\frac{u_w(x)x}{\nu}$ denotes local Reynold's number.

3.4 Numerical Procedure

The Keller-box scheme used for the numerical results of this problem. This scheme is considered as it is very friendly and highly accurate in performing numerical analysis for different flow problems (Keller and Cebeci, 1972). Besides, this method allows easy programming for the coupled highly nonlinear PDE's (Cebeci and Bradshaw, 2012). The complete numerical scheme for this problem is given in Appendix A.

3.5 Results and Discussion

The numerical results of ordinary differential equations (3.105) against boundary conditions (3.109) are obtained via Keller-box scheme. The Matlab program along with initial guess for this study is presented in Appendix A. Numerical outcomes versus physical factors including (local Grashof number) Gr, Nb (Brownian motion constraint), thermophoresis constraint Nt, local modified Grashof number Gc, M (magnetic factor), γ i.e. factor for inclination, Prandtl number i.e. Pr, material parameter K, and Lewis number Le are presented through accompanied tables and graphs. In Table 3.1, current results are reduced to published literature of Khan and Pop (2010) which authenticate the employed numerical scheme.

The effects of skin friction coefficient i.e. $C_{fx}(0)$, $-\theta'(0)$ (reduced Nusselt number) and reduced Sherwood number i.e. $-\phi'(0)$ versus physical factors incorporated under study are shown in Table 3.2. The consequences showed $-\theta'(0)$ diminishes against factors Le, γ, Nb, M, Nt and increases versus growth of K, Gr, Gc, and Pr. Moreover, $-\phi'(0)$ enhances on improving the factors $Gc, Nb, Gr, Nt, K, Le, Pr$ numerically, while shows contrary behavior against M and γ. Further, $C_{fx}(0)$ exhibits direct relation with parameters Le, Nb, K, M, γ and inverse relation with factors Nt, Gr, Gc and Pr.

Table 3.1
Comparison of the local Nusselt number $-\theta'(0)$ *and the local Sherwood number* $-\phi'(0)$ *when* $M, K, Gr, Gc = 0$ *,* $Pr = Le = 10$ *and* $\gamma = 90^0$.

Nb	Nt	Khan and Pop (2010)		Present Results	
		$-\theta'(0)$	$-\phi'(0)$	$-\theta'(0)$	$-\phi'(0)$
0.1	0.1	0.9524	2.1294	0.9524	2.1294
0.2	0.2	0.3654	2.5152	0.3654	2.5152
0.3	0.3	0.1355	2.6088	0.1355	2.6088
0.4	0.4	0.0495	2.6038	0.0495	2.6038
0.5	0.5	0.0179	2.5731	0.0179	2.5731

Table 3.2
Variations of the local Nusselt number $-\theta'(0)$, the local Sherwood number $-\phi'(0)$ and Skin-friction coefficient $C_{fx}(0)$.

Nb	*Nt*	Pr	*Le*	*M*	*K*	*Gr*	*Gc*	γ	$-\theta'(0)$	$-\phi'(0)$	$C_{fx}(0)$
0.1	0.1	6.5	5.0	0.1	1.0	0.1	0.9	45^0	1.1292	1.2066	1.1424
0.5	0.1	6.5	5.0	0.1	1.0	0.1	0.9	45^0	0.2322	1.6888	1.1988
0.1	**0.5**	6.5	5.0	0.1	1.0	0.1	0.9	45^0	0.5300	1.6542	0.9534
0.1	0.1	**10.0**	5.0	0.1	1.0	0.1	0.9	45^0	1.1754	1.2142	1.1390
0.1	0.1	6.5	**10.0**	0.1	1.0	0.1	0.9	45^0	1.0035	2.1626	1.2239
0.1	0.1	6.5	5.0	**0.5**	1.0	0.1	0.9	45^0	1.1166	1.1695	1.3872
0.1	0.1	6.5	5.0	0.1	**3.0**	0.1	0.9	45^0	1.1469	1.2606	1.6077
0.1	0.1	6.5	5.0	0.1	1.0	**0.5**	0.9	45^0	1.1329	1.2138	1.0510
0.1	0.1	6.5	5.0	0.1	1.0	0.1	**2.0**	45^0	1.1431	1.2376	0.8272
0.1	0.1	6.5	5.0	0.1	1.0	0.1	0.9	$\mathbf{60}^0$	1.1254	1.1980	1.2268
0.1	0.1	6.5	5.0	0.1	1.0	0.1	0.9	$\mathbf{90}^0$	1.1158	1.1758	1.4349

Figure 3.4 reveals effect of M on $f'(\eta)$, i.e. velocity profile. $f'(\eta)$ falls by improving M numerically. It is true due to the fact that magnetic field yields Lorentz force, which causes resistance in liquid speed. The similar outcome has been seen for $h(\eta)$ (angular velocity) versus M in Figure 3.5. In the same vein, contrary impacts of M on $\theta(\eta)$ (temperature distribution) is displayed in Figure 3.6 and on $\phi(\eta)$ (concentration profile) in Figure 3.7. In addition, Figure 3.8 exhibits $f'(\eta)$ upturns by enhancing factor K because thickness of boundary enhances. Physically, this increment in thickness shows that drag force declines in the boundary layer separation with the effect of micropolar factor. In addition, similar behavior for angular velocity profile can be seen for growth of K indicates in Figure 3.9. The reason behind higher magnitudes of K shorten the boundary layer thickness. On the other hand Figures 3.10 and 3.11 show contrary results for various values of K. $f'(\eta)$ upsurges in Figure 3.12 by strengthening local Grashof number Gr.

Physically, enhancement in Gr declines the viscous effect which helps to liquid flow, in result faster motion. While, similar result is seen for (local modified Grashof number) Gc on velocity distribution shown in Figure 3.13, because kinematic viscosity,

concentration difference, and length affected factor Gc. In addition, viscosity and velocity of the liquid are inversely connected with each other. Viscosity of the liquid declines on improving factor Gc whereas concentration enhance in result velocity profile upturns. Finally, Gc shows direct relation with $f'(\eta)$. Figure 3.14 portrays consequence of inclination factor γ on $f'(\eta)$. Which shows that $f'(\eta)$ diminishes with the increment in factor γ. The fact behind circumstance is that when $\gamma = 0$, the gravitational force will be very high. While, against $\gamma = 90^0$ the velocity contour decreases because of the weaker buoyancy forces. On the other side, opposite result discovered in Figures 3.15 and 3.16 on increasing inclination factor γ in the instance of $\theta(\eta)$ and $\phi(\eta)$ sketches.

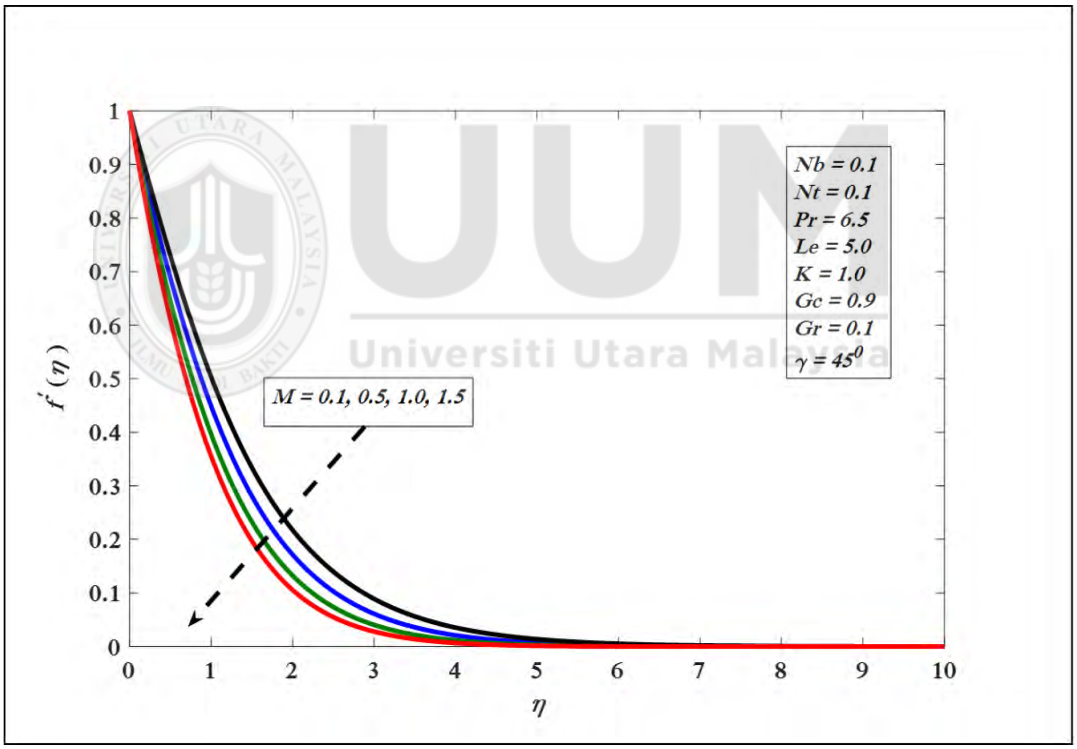

Figure 3.4. Variations in velocity profile for several values of M.

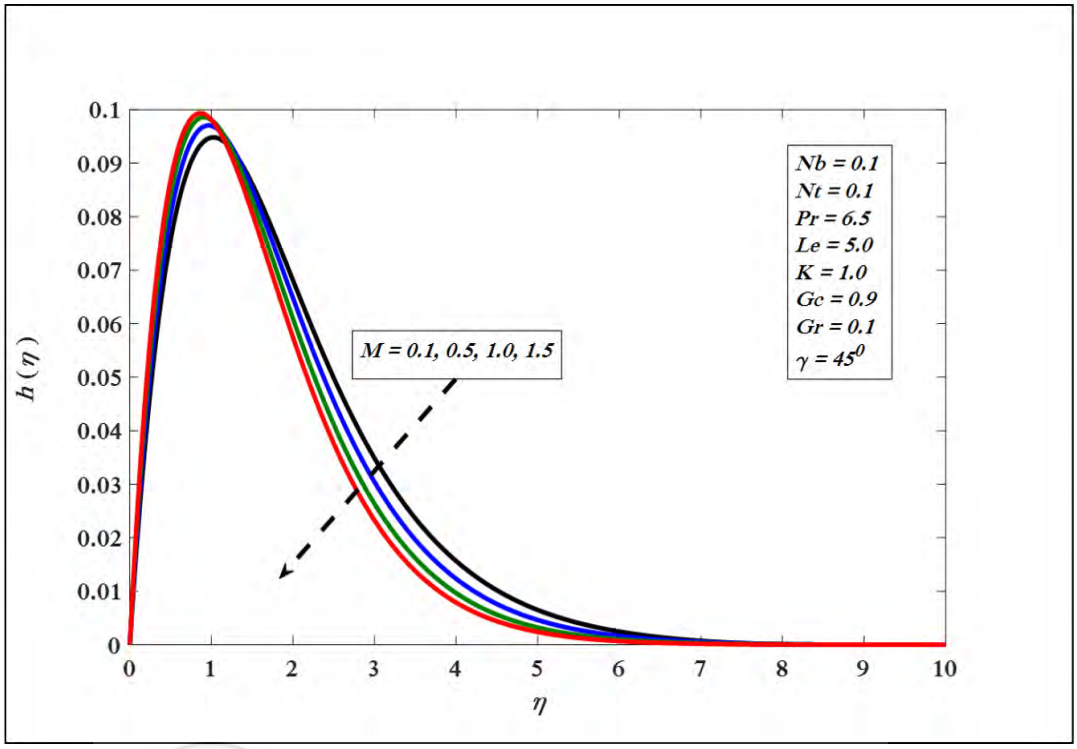

Figure 3.5. Variations in angular velocity for several values of M.

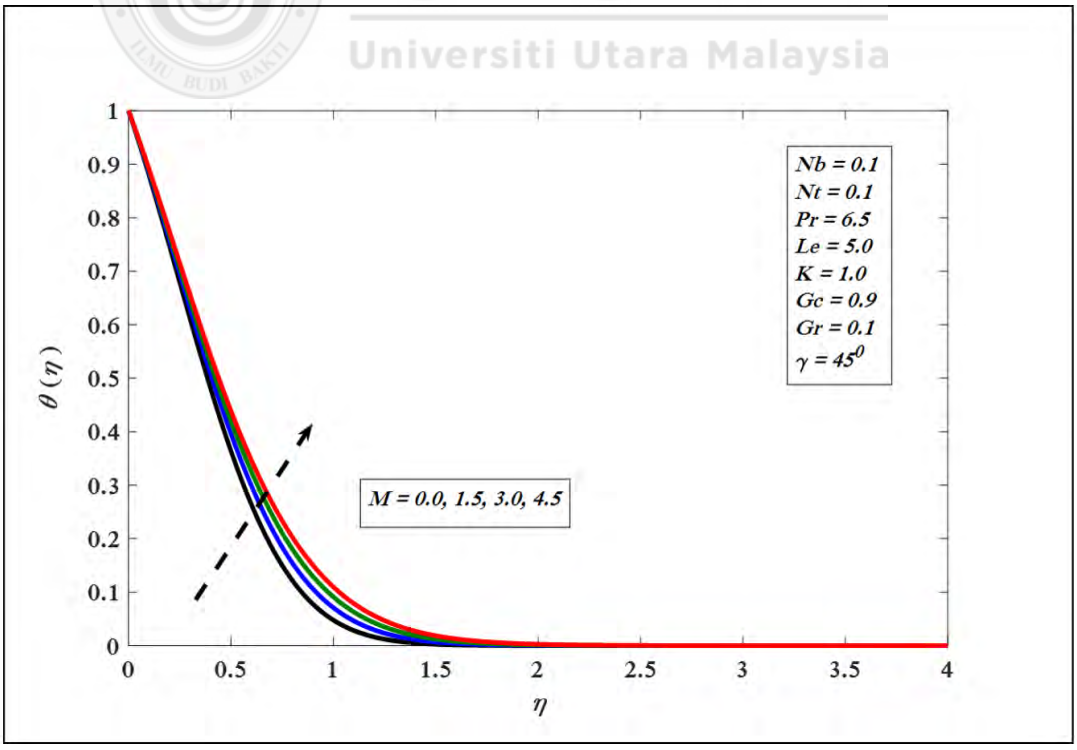

Figure 3.6. Variations in temperature profile for several values of M.

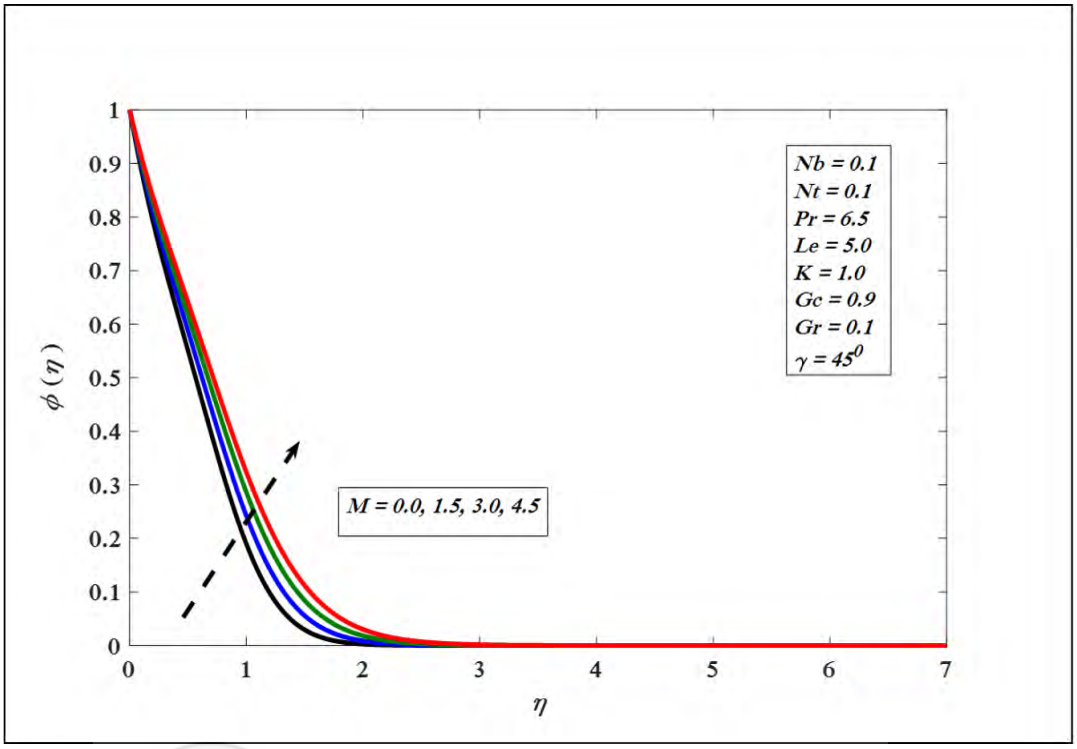

Figure 3.7. Variations in concentration profile for several values of M.

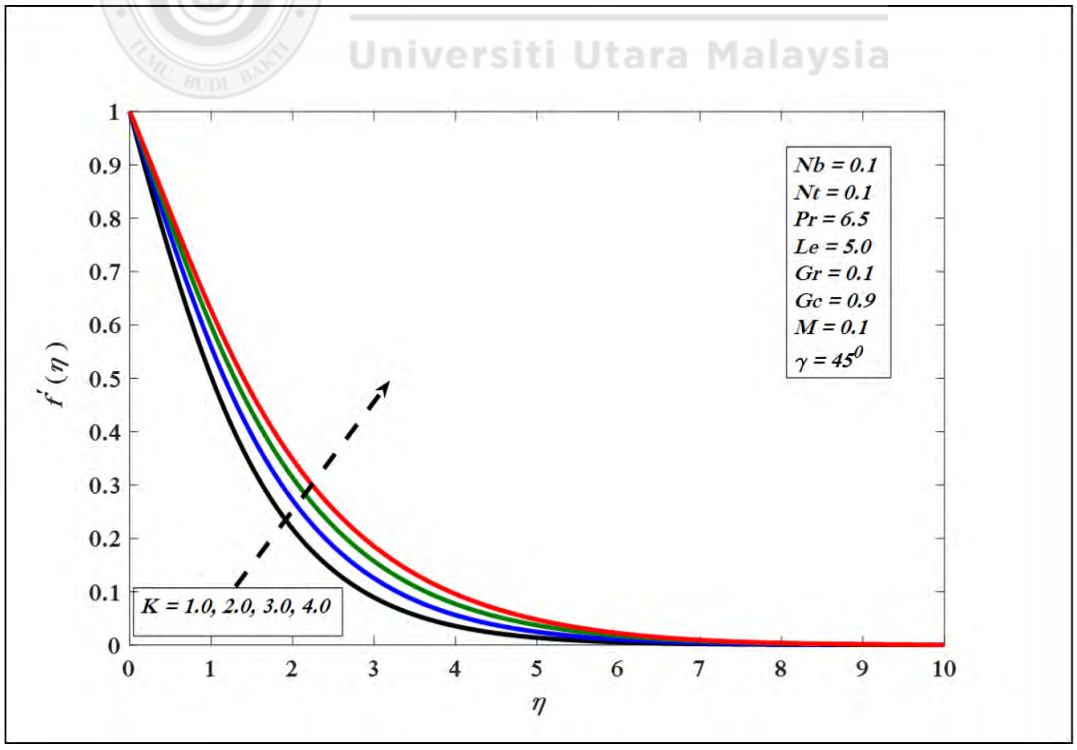

Figure 3.8. Variations in velocity profile for several values of K.

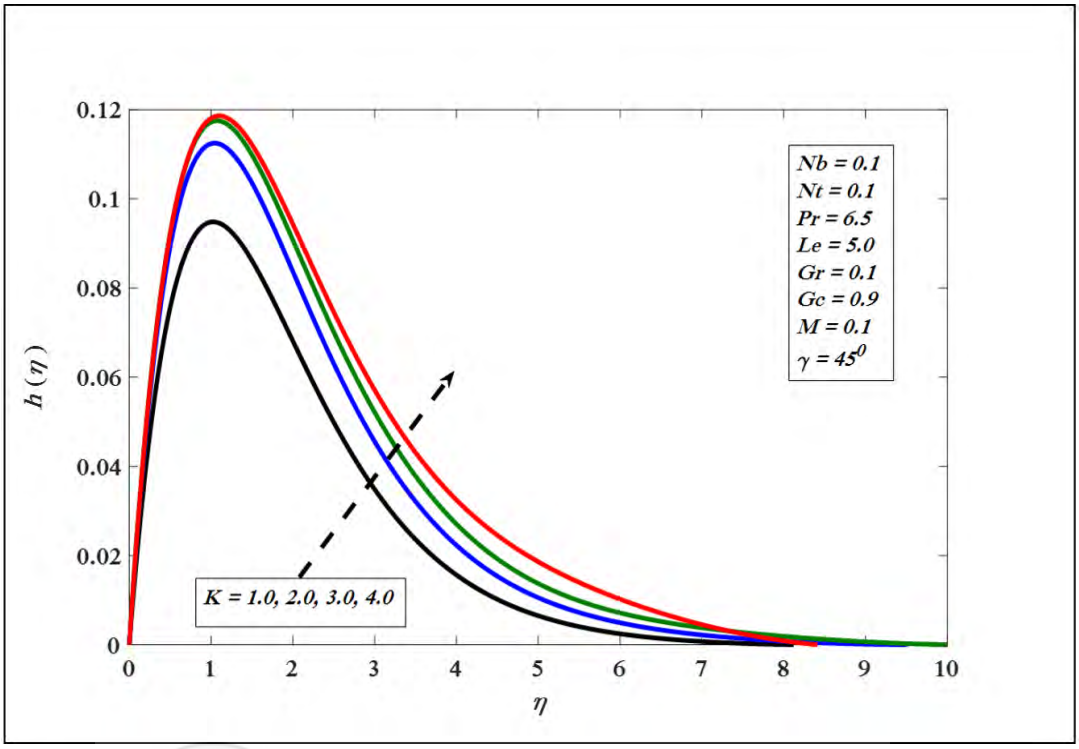

Figure 3.9. Variations in angular velocity for several values of K.

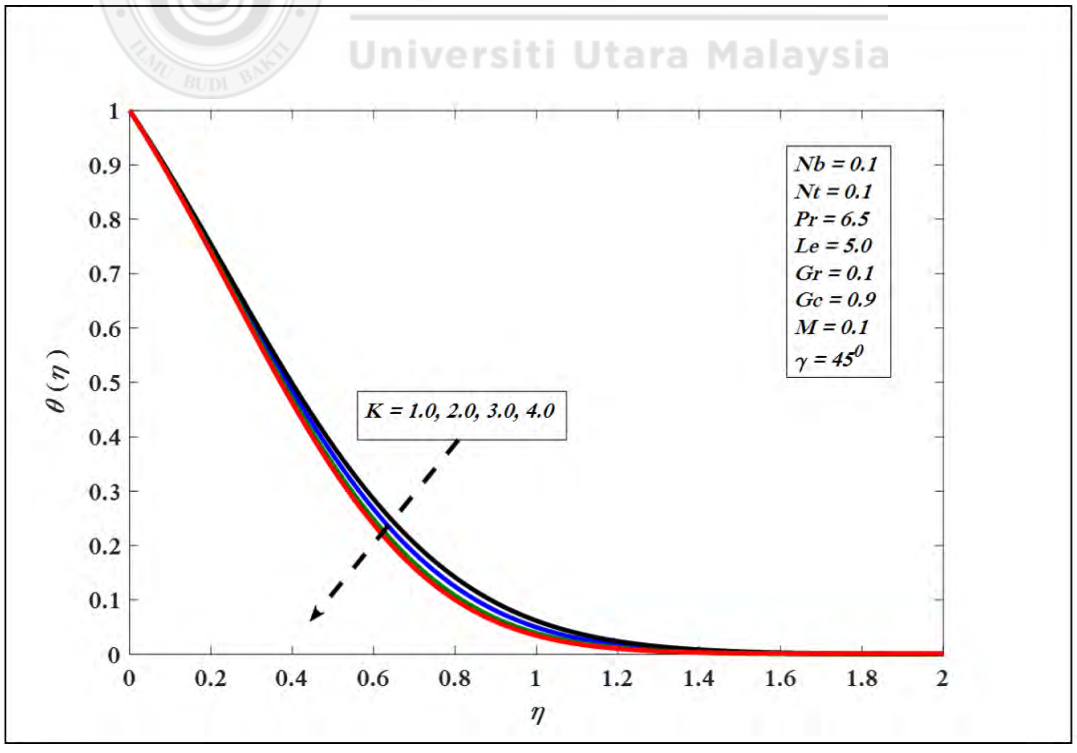

Figure 3.10. Variations in temperature profile for several values of K.

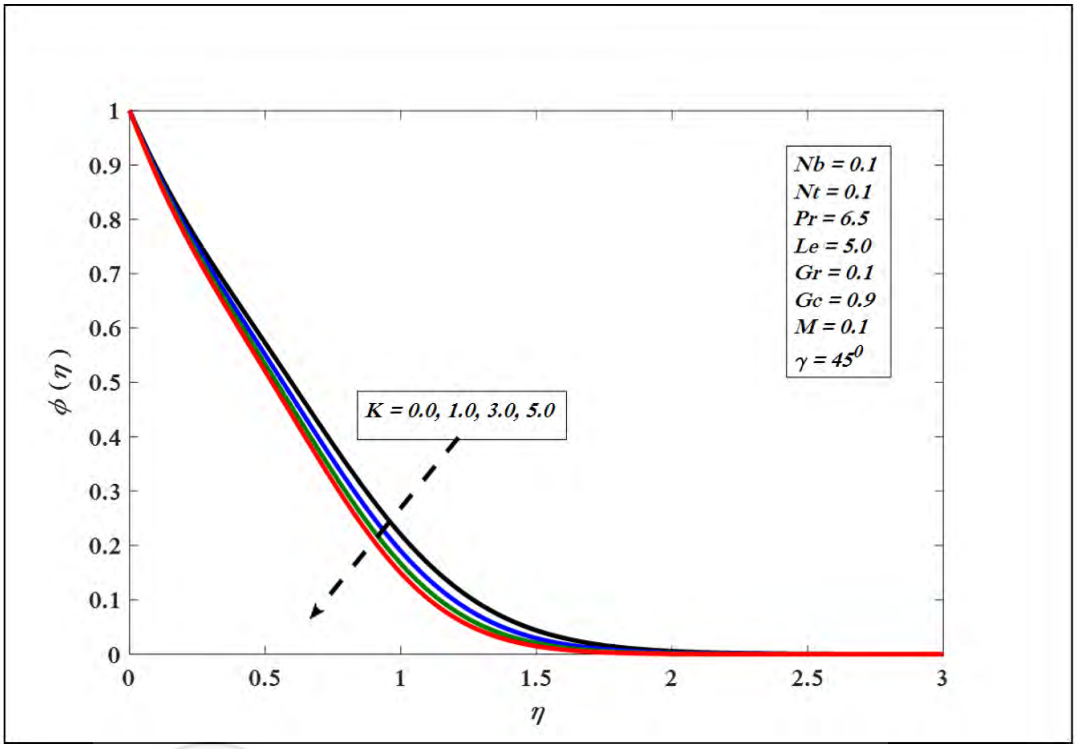

Figure 3.11. Variations in concentration profile for several values of K.

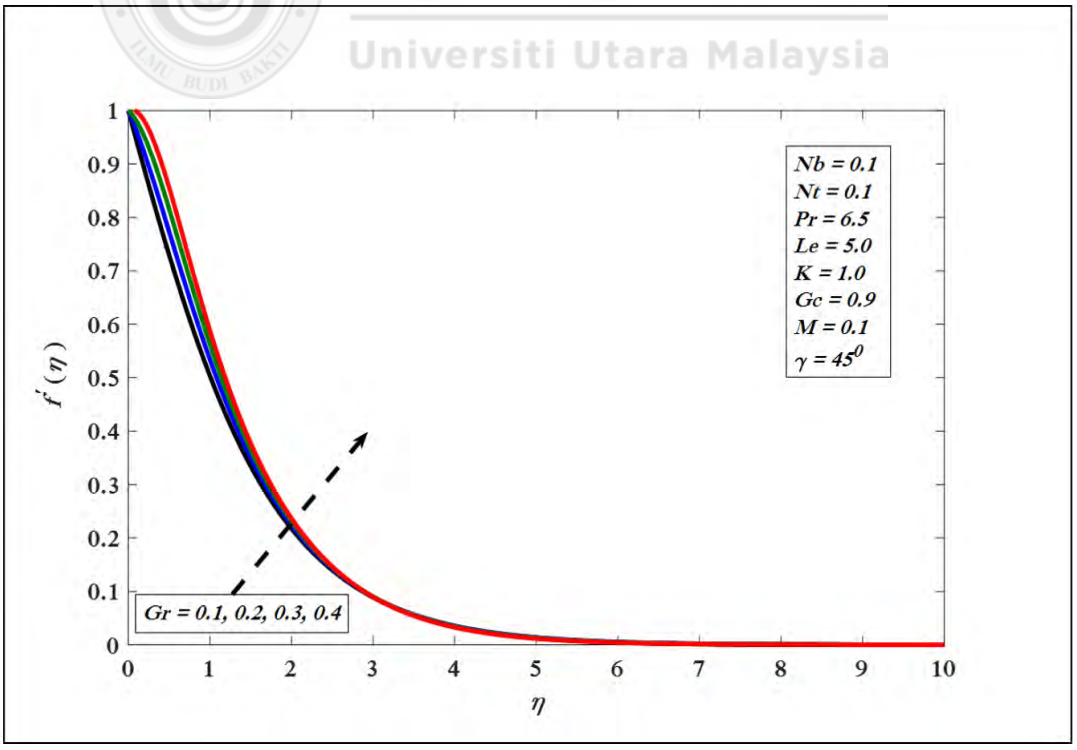

Figure 3.12. Variations in velocity profile for several values of Gr.

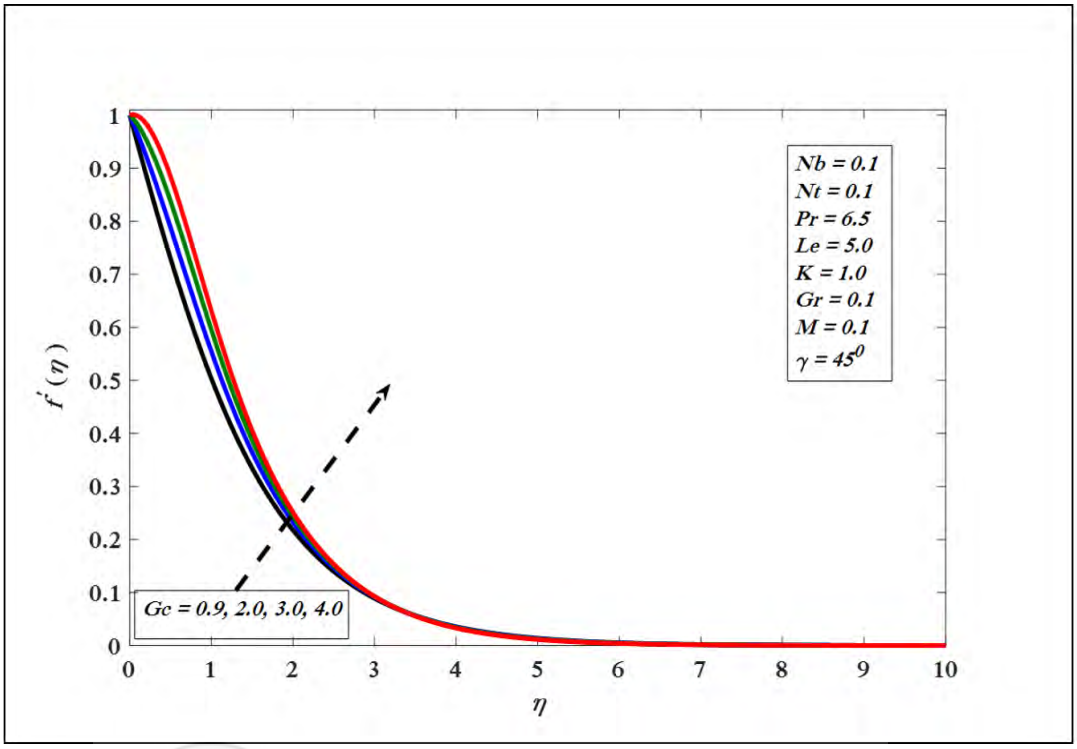

Figure 3.13. Variations in velocity profile for several values of *Gc*.

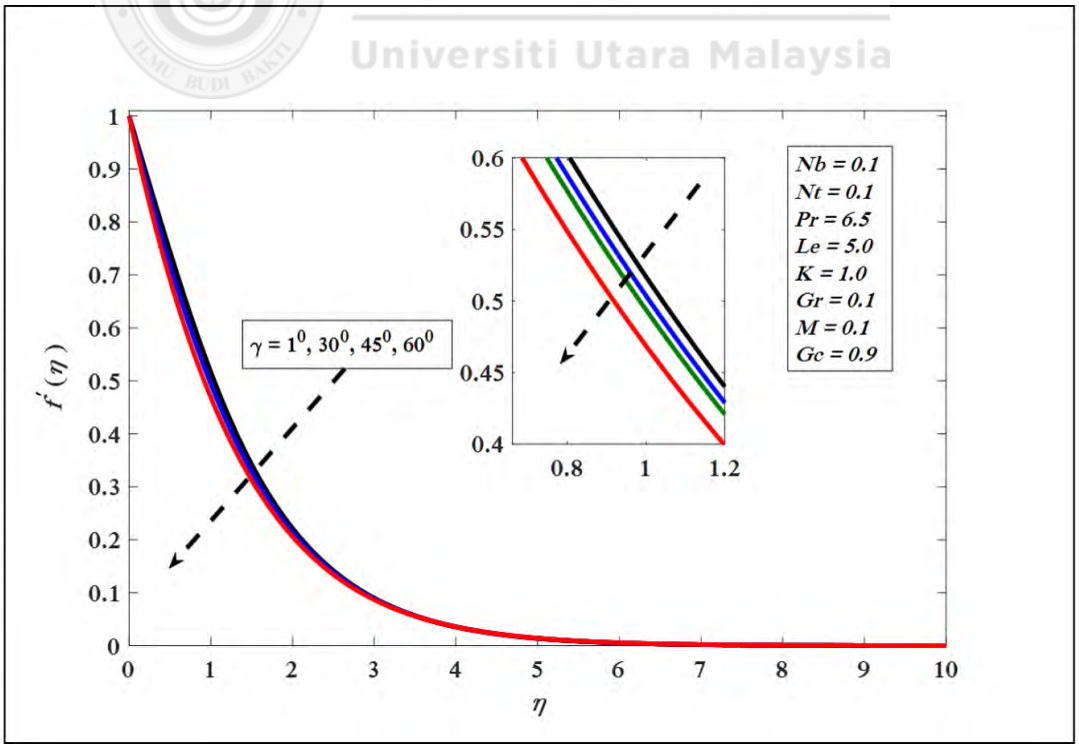

Figure 3.14. Variations in velocity profile for several values of γ.

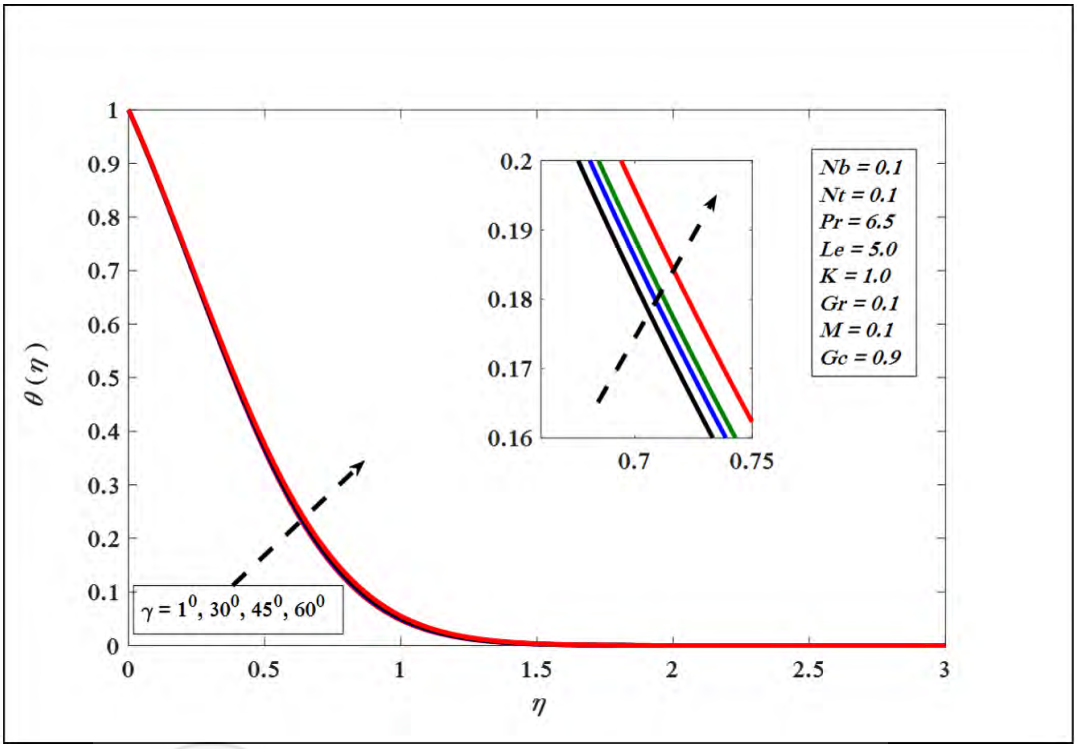

Figure 3.15. Variations in temperature profile for several values of γ.

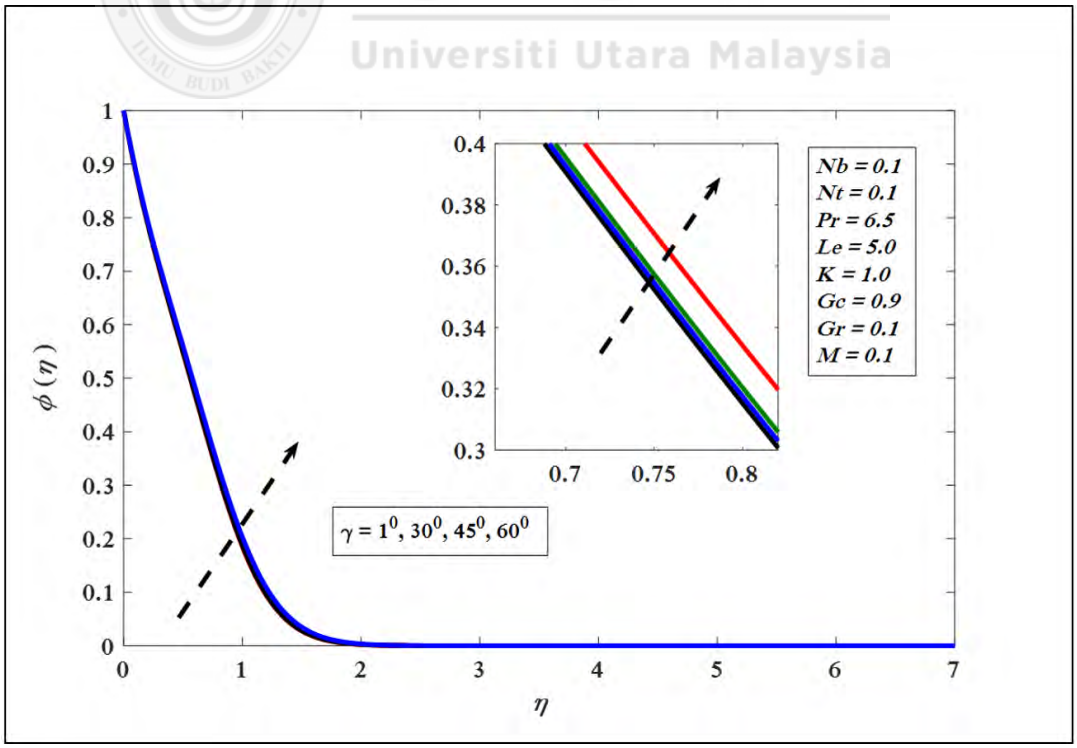

Figure 3.16. Variations in concentration profile for several values of γ.

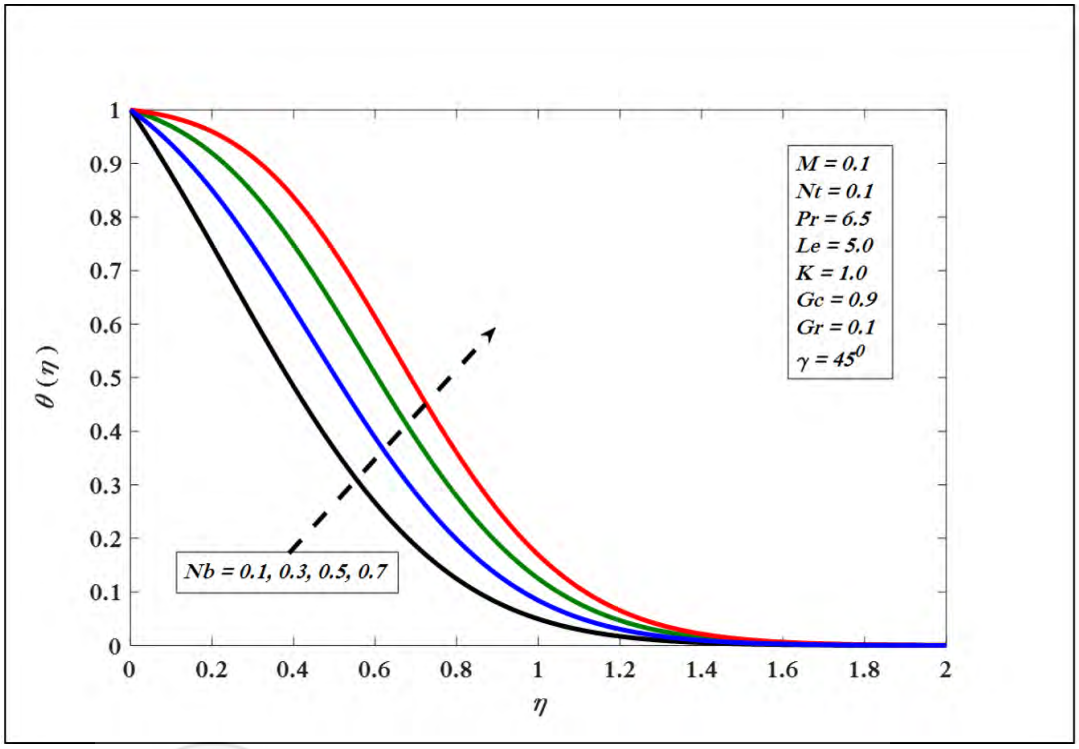

Figure 3.17. Variations in temperature profile for several values of *Nb*.

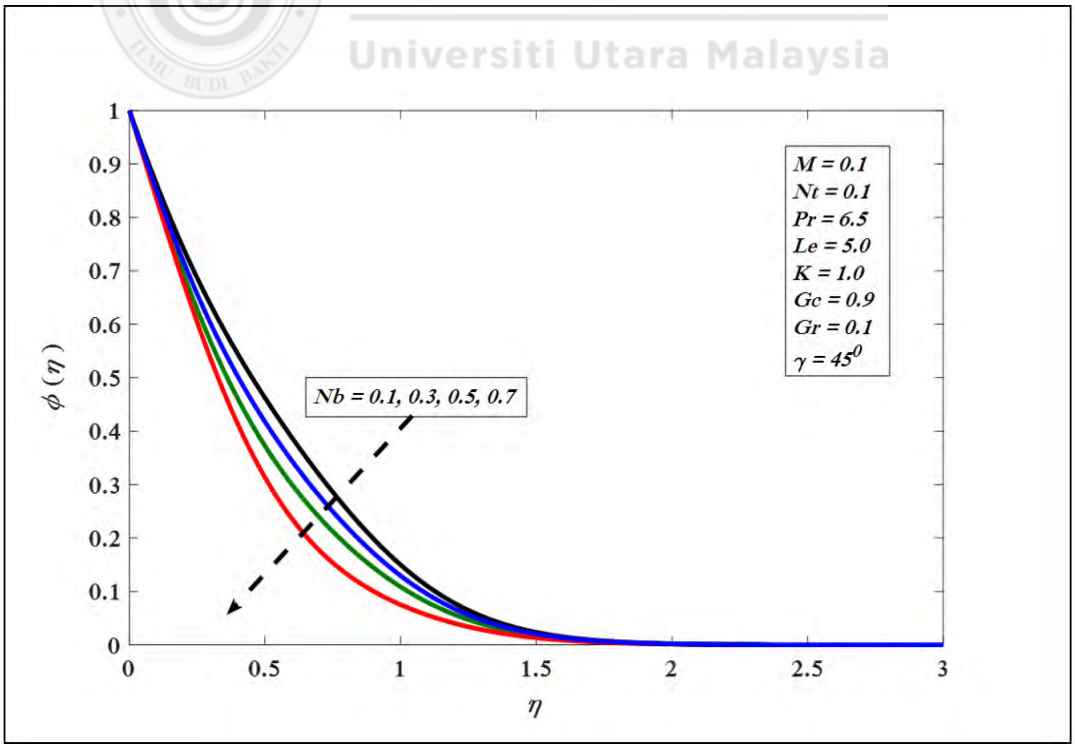

Figure 3.18. Variations in concentration profile for several values of *Nb*.

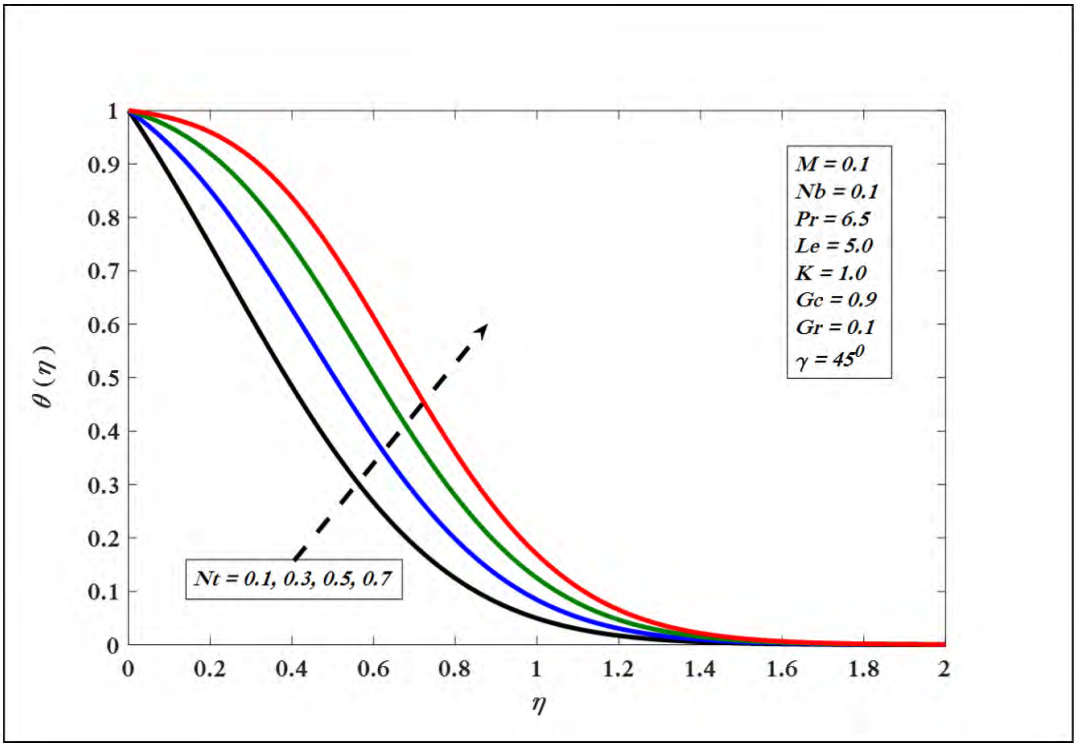

Figure 3.19. Variations in temperature profile for several values of Nt.

Figures 3.17 and 3.18 display the effect of Brownian movement on $\theta(\eta)$ and $\phi(\eta)$ respectively. $\theta(\eta)$ enhances on improving Nb, while, $\phi(\eta)$ exhibits inverse behavior. Physically, Brownian motion warms the boundary layer thus nanoparticles shift from the stretching surface towards motionless liquid, thus the concentration of nanoparticles decline. Figures 3.19 and 3.20 display $\theta(\eta)$ and $\phi(\eta)$ versus various values of thermophoresis parameters Nt. It is exhibited that $\theta(\eta)$ and $\phi(\eta)$ enhance by increasing Nt. Thermophoresis support to warm boundary layer for different numeric of Prandtl number and Lewis number. Moreover, the amount of energy and species exchange reduce with increase of (thermophoresis constraint) Nt. Figure 3.21 presents that on increasing Prandtl number factor Pr numerically $\theta(\eta)$ diminishes, because thermal boundary layer viscosity decreases by growing Pr. Physically, an increment in Pr portrays slow the amount of thermal distribution.

Figure 3.22 shows influence of Le on $\phi(\eta)$. The boundary layer viscosity lessening

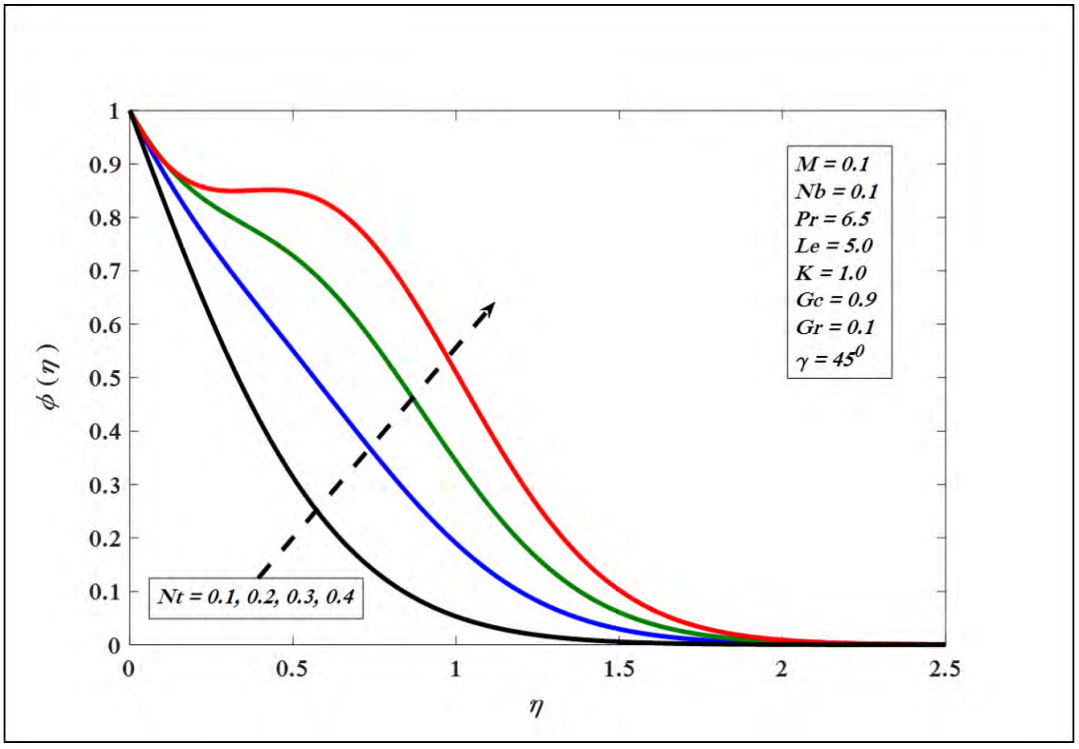

Figure 3.20. Variations in concentration profile for several values of Nt.

on increasing numerical values of Le. Equation (3.105) indicates that the factors Nb, Nt, γ, and K influences $-\theta'(\eta)$ and $-\phi'(\eta)$. Therefore, the behavior of heat and mass exchange rates are presented in Figures 3.23 to 3.30 for altered values of Nb, Nt, γ, and K. Figures 3.23 and 3.24 establish that the energy and mass transport rates diminish versus γ and Nb. Physically, the buoyancy force effect decreases with the increase in inclination by the factor $cos\gamma$ because the surface will be vertical at $\gamma = 0$. Further, $-\theta'(\eta)$ and $-\phi'(\eta)$ versus Nt show an inverse behavior with the improving magnitudes of γ and recovered the result of Chen (2004) (see Figures 3.25 and 3.26). In the same vein, Figures 3.27 and 3.28 present the energy and mass transport rates versus Nb by increasing K. It is perceived that energy and mass fluxes enhances with increment in Nb and K which show similar behavior as Uddin (2011). Moreover, the same result recovered from the Figures 3.29 and 3.30 against Nt for higher values of K.

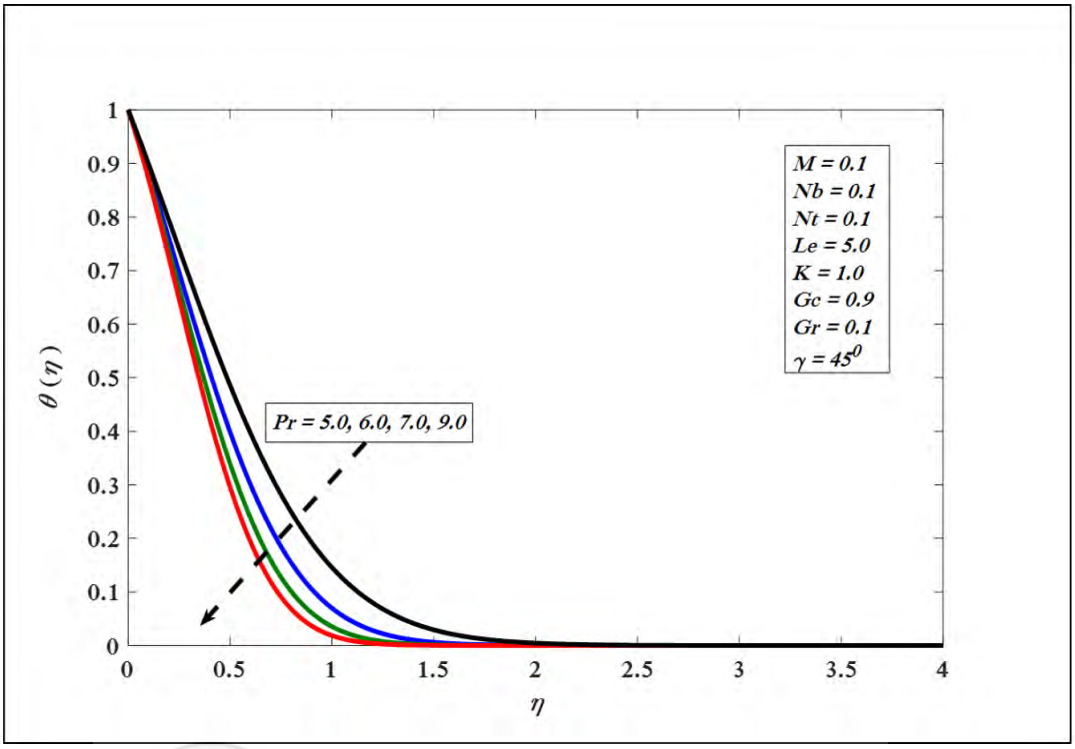

Figure 3.21. Variations in temperature profile for several values of *Pr*.

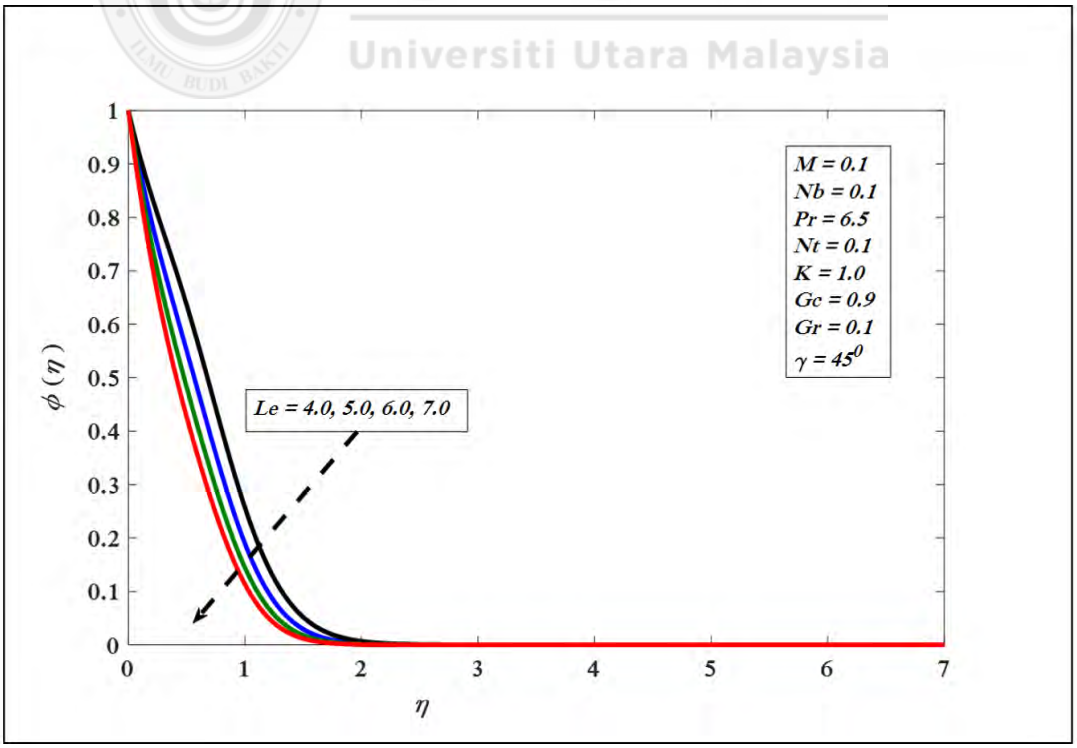

Figure 3.22. Variations in concentration profile for several values of *Le*.

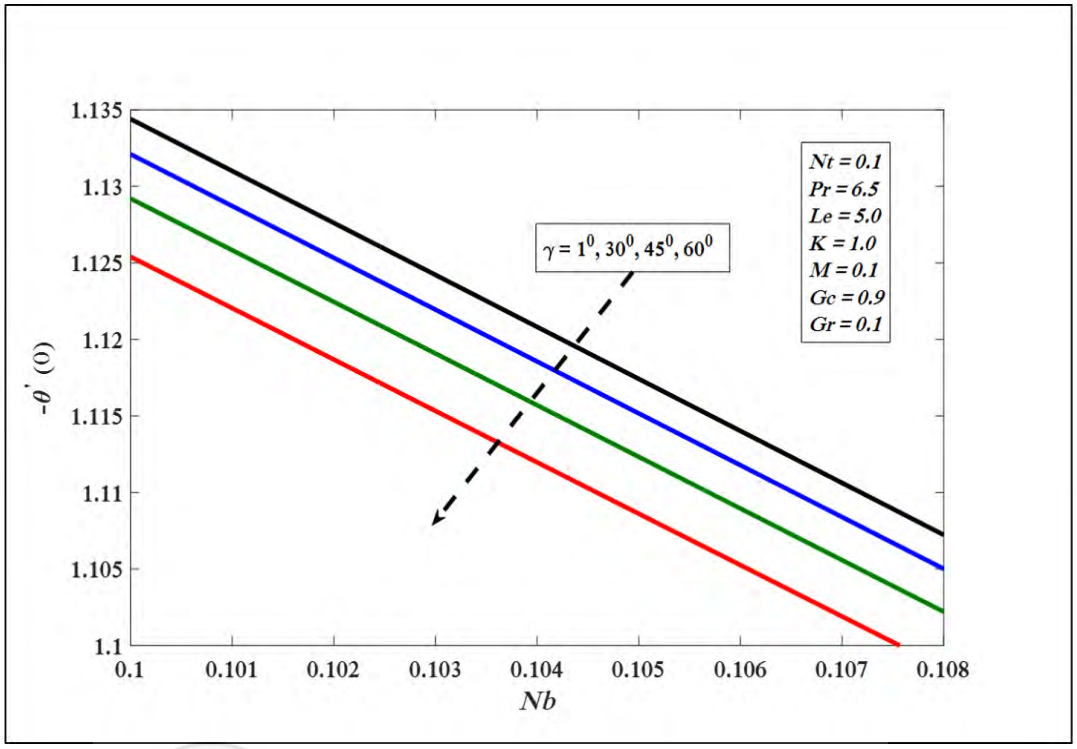

Figure 3.23. $-\theta'(0)$ against *Nb* for several values of γ.

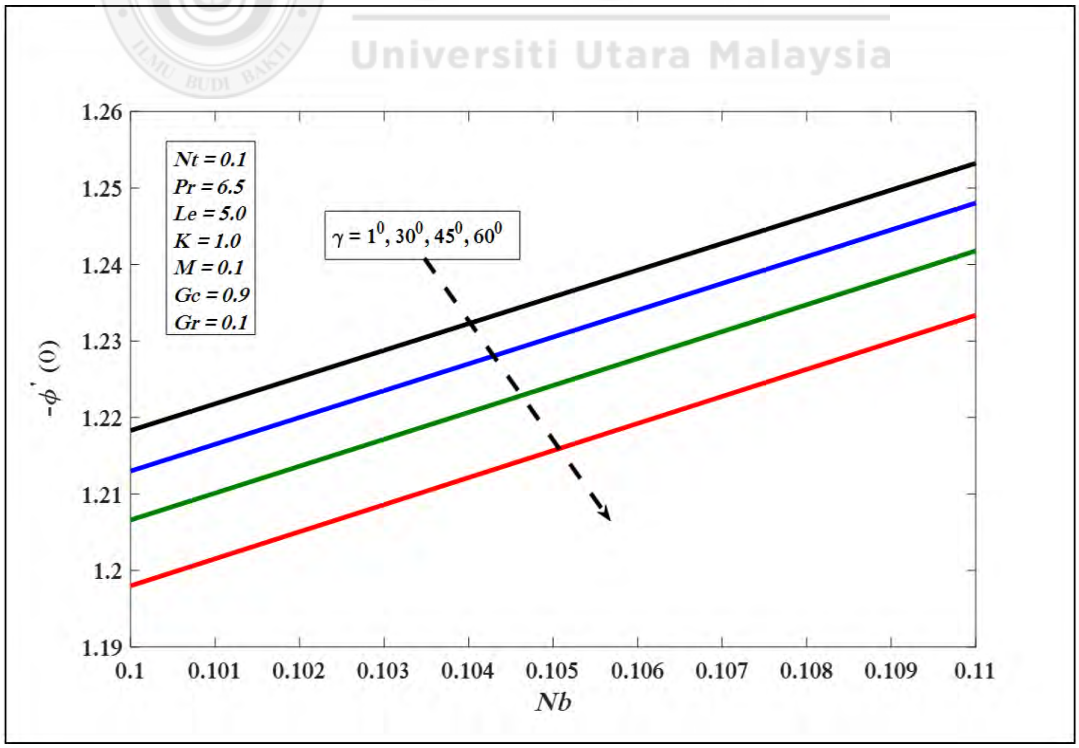

Figure 3.24. $-\phi'(0)$ against *Nb* for several values of γ.

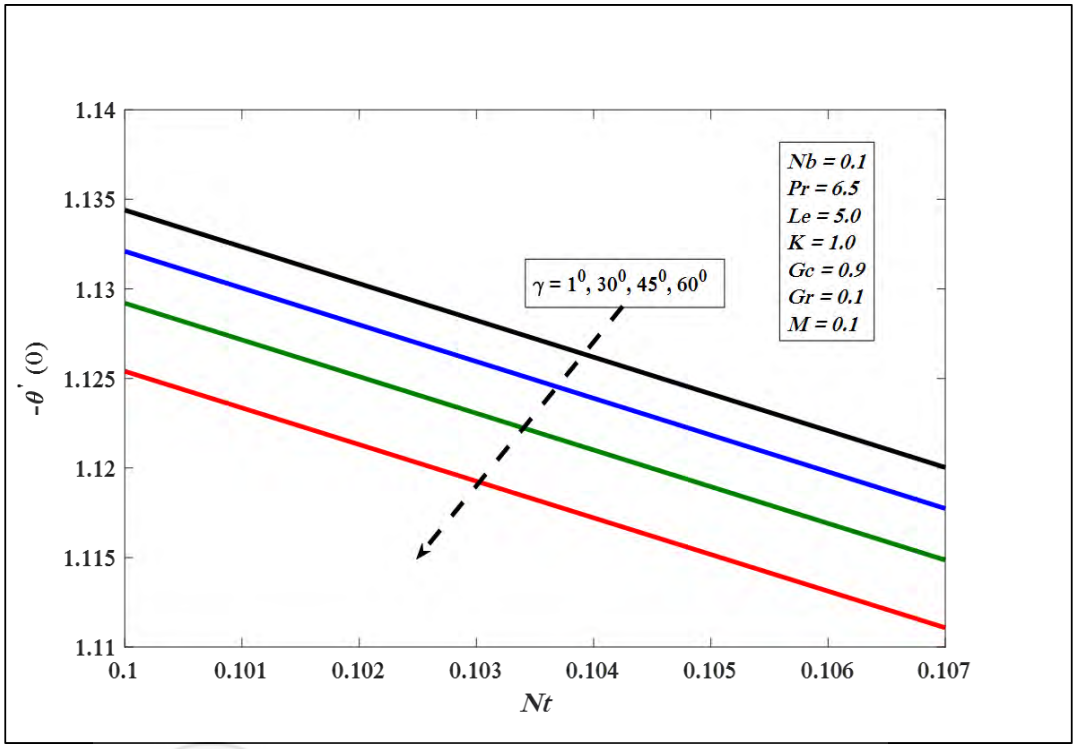

Figure 3.25. $-\theta'(0)$ against Nt for several values of γ.

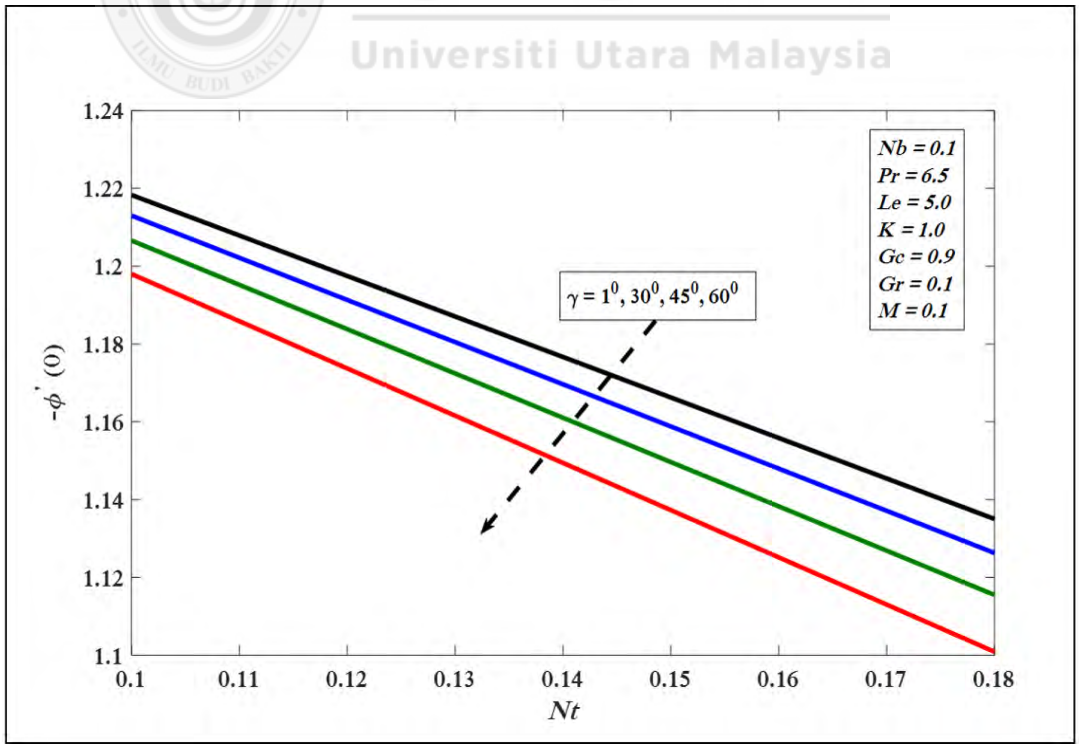

Figure 3.26. $-\phi'(0)$ against Nt for several values of γ.

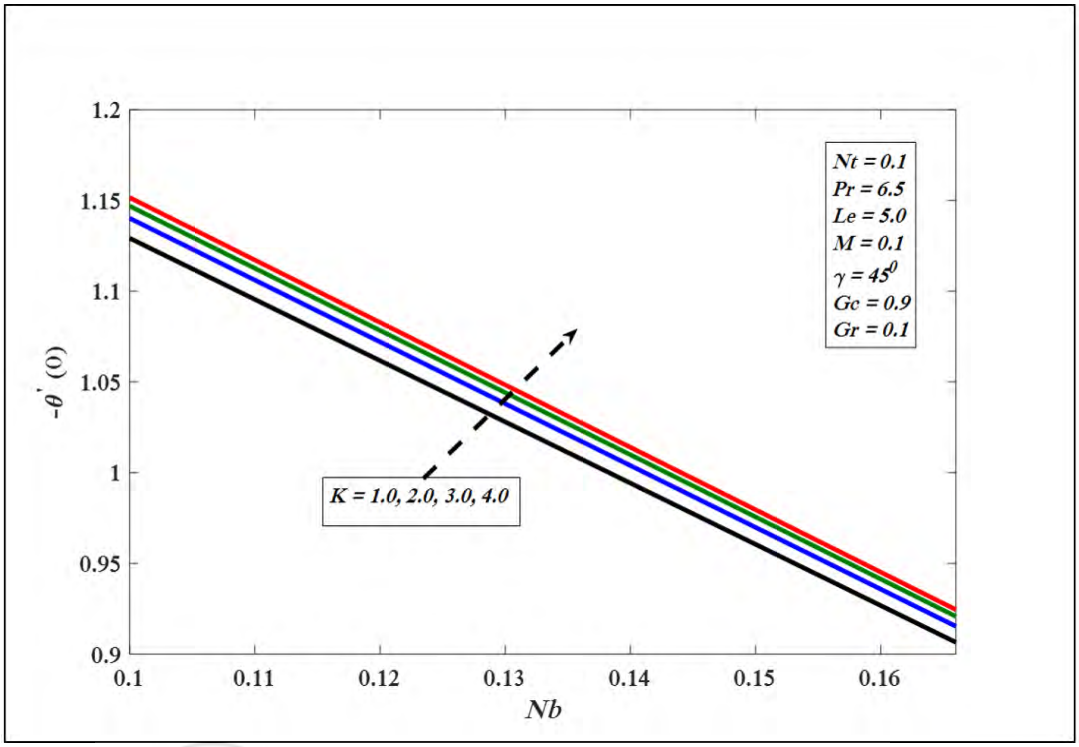

Figure 3.27. $-\theta'(\eta)$ against Nb for several values of K.

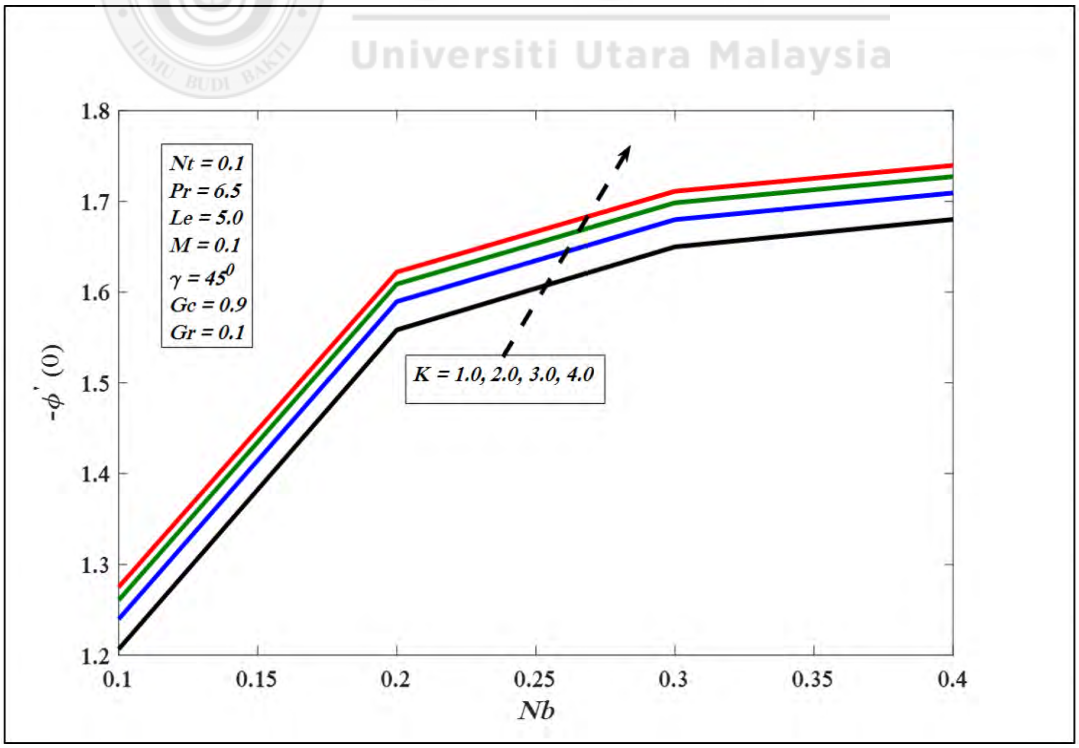

Figure 3.28. $-\phi'(\eta)$ against Nb for several values of K.

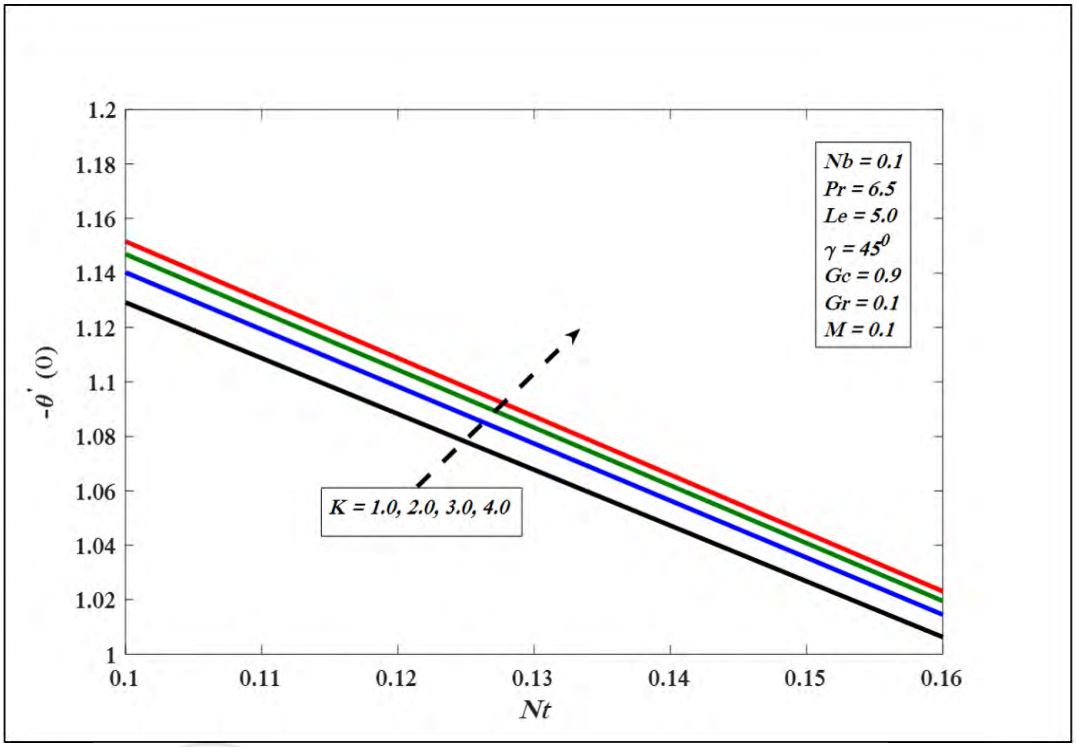

Figure 3.29. $-\theta'(\eta)$ against Nt for several values of K.

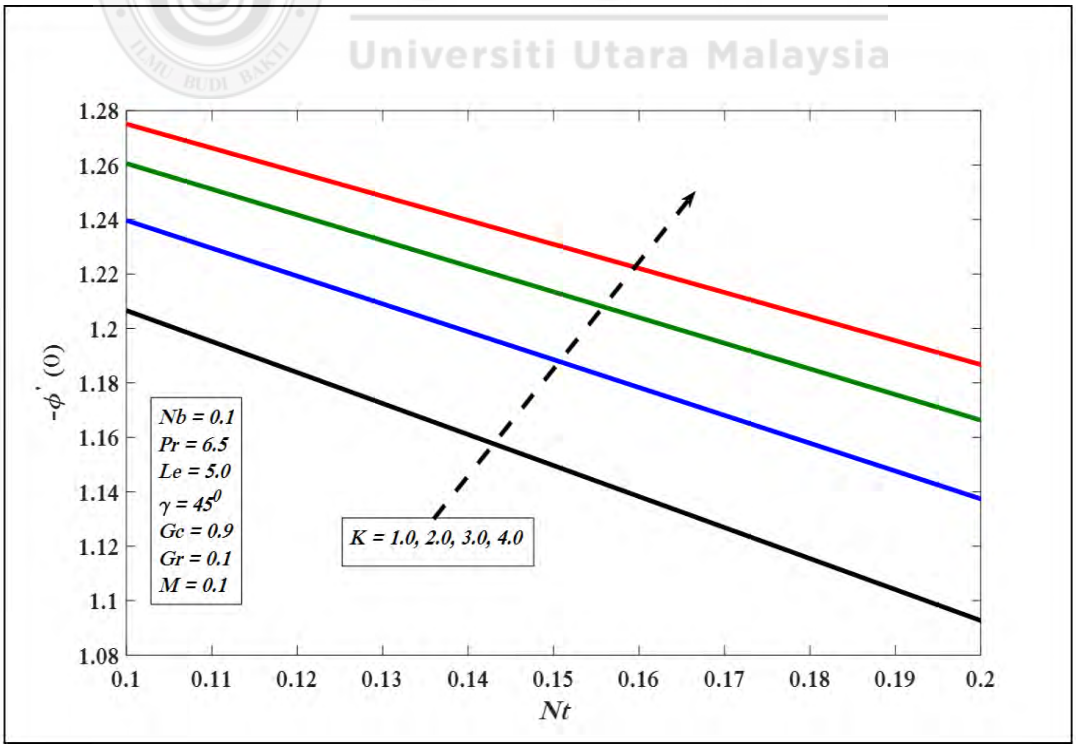

Figure 3.30. $-\phi'(\eta)$ against Nt for several values of K.

3.6 Conclusions

In this chapter, mathematical model for micropolar nanofluid and Casson nanofluid flow over an inclined surface has been developed. In addition, first problem of thesis for linear inclined geometry has been considered. The flow equations are converted in to a system of coupled differential equations. These converted equations are then by well known numerical method i.e. Keller-box method. The recovered outcomes are confirmed with already published work and established to be a good settlement. Our conclusions from this investigation are presented as:

1. $-\theta'(0)$ and $-\phi'(0)$ decrease but $C_f x(0)$ increases with increment in inclination factor.

2. $-\theta'(0)$ decreases with increase of Nb and Nt whereas $-\phi'(0)$ increases with increase of Nb and Nt.

3. $-\theta'(0)$ and $-\phi'(0)$ decrease but $C_f x(0)$ increases with by increasing magnetic parameter.

4. $-\theta'(0)$ and $-\phi'(0)$ increase by improving material parameter (K).

After presenting the derivation of governing equations and the boundary layer flow for linear inclined geometry in this chapter, we are moving to the next chapter which encloses numerical solution of boundary layer flow for permeable inclined geometry.

CHAPTER FOUR

MICROPOLAR NANOFLUID BOUNDARY LAYER FLOW OVER A LINEAR PERMEABLE INCLINED STRETCHING SURFACE

4.1 Introduction

In the continuation of non-Newtonian nanofluid studies, the chemical reaction and heat generation or absorption effects on boundary layer flow of a micropolar nanofluid over a permeable inclined geometry are considered in this chapter. In this problem, the incorporated flow factors are chemical reaction, heat generation (or absorption) and suction (or injection). Note that this study focus particularly on investigation of flow characteristics over a linear permeable inclined stretching surface. The impacts of involved parameters including suction or injection S, chemical reaction (R) and heat generation or absorption (λ_1) are investigated. The numerical outcomes of current study are verified with Khan and Pop (2010).

4.2 Governing Equations

Two dimensional steady incompressible flow of micropolar type nanofluid on a permeable slanted linear stretching surface by incorporating chemical reaction effect is considered. The influence of heat generation or absorption over micropolar nanofluid flow is taken into account. While transverse magnetic field is applied normal to the inclined surface as shown in Figure 3.3.

The governing equations for this study are as follows (see Equations 3.59, 3.62 (when $\sigma^* = 0$), 3.63, 3.89 and 3.90):

$$\frac{\partial u}{\partial x} + \frac{\partial v}{\partial y} = 0,$$

$$u\frac{\partial u}{\partial x} + v\frac{\partial u}{\partial y} = \left(\frac{\mu + k_1^*}{\rho}\right)\frac{\partial^2 u}{\partial y^2} + \left(\frac{k_1^*}{\rho}\right)\frac{\partial N^*}{\partial y} + g\beta_t(T - T_\infty)\cos\gamma$$

$$+ g\beta_c(C - C_\infty)\cos\gamma - \left(\frac{\sigma {B_0}^2}{\rho}\right)u,$$

$$u\frac{\partial N^*}{\partial x} + v\frac{\partial N^*}{\partial y} = \left(\frac{\gamma^*}{j^*\rho}\right)\left(\frac{\partial^2 N^*}{\partial y^2}\right) - \left(\frac{k_1^*}{j^*\rho}\right)\left(2N^* + \frac{\partial u}{\partial y}\right), \tag{4.1}$$

$$u\frac{\partial T}{\partial x} + v\frac{\partial T}{\partial y} = \alpha\frac{\partial^2 T}{\partial y^2} + \tau\left[D_B\frac{\partial C}{\partial y}\frac{\partial T}{\partial y} + \frac{D_T}{T_\infty}\left(\frac{\partial T}{\partial y}\right)^2\right] + \triangle T\frac{Q_0}{(\rho c)_p}T,$$

$$u\frac{\partial C}{\partial x} + v\frac{\partial C}{\partial y} = D_B\frac{\partial^2 C}{\partial y^2} + \frac{D_T}{T_\infty}\frac{\partial^2 T}{\partial y^2} - \triangle C R^* C.$$

The boundary settings are

$$u = u_w(x) = ax\ , v = v_w\ , T = T_w\ , N^* = -m_0\frac{\partial u}{\partial y}\ , C = C_w \qquad at \qquad y = 0,$$

$$u \to u_\infty(x) = 0\ , v \to 0\ , T \to T_\infty\ N^* \to 0\ , C \to C_\infty \qquad as \qquad y \to \infty, \tag{4.2}$$

in which $v_w < 0$ shows the injection or blowing velocities whereas $v_w > 0$, corresponds to a suction velocity (Arifin et al., 2011).

4.2.1 Similarity Transformations

By applying similarity transformations as expressed in Equation (3.104), Equation (4.1) reduces to

$$(1+K)\,f''' + ff'' - f'^2 + Kh' + (Gr_x\theta + Gc_x\phi)\,cos\gamma - (M)\,f' = 0,$$

$$\left(1+\frac{K}{2}\right)h'' + fh' - hf'^2 - K\left(2h+f''\right) = 0,$$

$$\left(\frac{1}{\mathrm{Pr}}\right)\theta'' + f\theta' + \lambda_1\theta + Nb\theta'\phi' + Nt\theta'^2 = 0, \tag{4.3}$$

$$\phi'' + Lef\phi' + Nt_b\theta'' - Le_R\phi = 0,$$

here $\lambda_1 = \frac{\triangle TQ_0}{a\rho c_p}$ is the heat generation $(\lambda_1 > 0)$ or heat absorption $(\lambda_1 < 0)$ parameter, $Le_R = LeR$ where $R = \frac{\triangle CR^*}{a}$ is the chemical reaction rate parameter and the other involved flow parameters are the same as defined in Chapter 3. The respective boundary conditions in (4.2) are transformed into

$$f(\eta) = S,\ f'(\eta) = 1,\ h(\eta) = 0, \theta(\eta) = 1, \phi(\eta) = 1\ at\ \eta = 0,$$

$$f'(\eta) \to 0,\ h(\eta) \to 0, \theta(\eta) \to 0, \phi(\eta) \to 0\ \ at\ \ \eta \to \infty, \tag{4.4}$$

where $S = \frac{-v_w}{\sqrt{av}}$ is the suction $(S > 0)$ or injection $(S < 0)$ parameter (Rosca et al., 2012). The associated expressions of the concern physical quantities such as Skin-friction coefficient $C_{fx}(0) = (1+K)\,f''(0)$, the local Nusselt number $-\theta'(0)$ and the local Sherwood number $-\phi'(0)$ are defined similar as expressed in the previous problem.

4.3 Results and Discussion

This part presented numerical outcomes of Equation (4.3) recovered by utilizing Equation (4.4) and there influences on physical quantities. For numerical simulation, similar steps are followed as explained for the previous problem in Appendix A. Further, for numerical result of physical factors of our concern including thermophoresis constraint Nt, magnetic factor M, local Grashof number Gr, local modified Grashof number Gc, Brownian motion constraint Nb, inclination factor γ, Prandtl number Pr, Lewis number Le, heat generation or absorption parameter λ_1, chemical reaction parameter R, suction or injection parameter i.e S, and material constraint i.e. K, several figures and table 4.1 are presented. The contrast of present results (when $M, K, Gr, Gc, \lambda_1, S, R = 0,\ Pr = \ Le = 10$ and $\gamma = 90^0$), for local Nusselt number i.e. $-\theta'(0)$ and local Sherwood number i.e. $-\phi'(0)$ through outcomes recovered by Khan and Pop (2010) (see Table 3.1) established a good agreement.

Table 4.1
Variations of $-\theta'(0)$, $-\phi'(0)$ *and* $C_{fx}(0)$.

Nb	Nt	Pr	Le	M	K	Gr	Gc	λ_1	S	R	γ	$-\theta'(0)$	$-\phi'(0)$	$C_{fx}(0)$
0.1	0.1	7.0	5.0	0.5	1.0	0.1	0.9	0.1	0.1	1.0	45^0	1.1123	2.9146	1.5227
0.5	0.1	7.0	5.0	0.5	1.0	0.1	0.9	0.1	0.1	1.0	45^0	0.0978	3.1368	1.5550
0.1	**0.5**	7.0	5.0	0.5	1.0	0.1	0.9	0.1	0.1	1.0	45^0	0.3667	4.5619	1.4355
0.1	0.1	**10**	5.0	0.5	1.0	0.1	0.9	0.1	0.1	1.0	45^0	1.1212	2.9771	1.5206
0.1	0.1	7.0	**10**	0.5	1.0	0.1	0.9	0.1	0.1	1.0	45^0	0.9984	4.5817	1.5818
0.1	0.1	7.0	5.0	**1.5**	1.0	0.1	0.9	0.1	0.1	1.0	45^0	1.0760	2.9014	2.0284
0.1	0.1	7.0	5.0	0.5	**3.0**	0.1	0.9	0.1	0.1	1.0	45^0	1.1457	2.9288	2.0779
0.1	0.1	7.0	5.0	0.5	1.0	**1.0**	0.9	0.1	0.1	1.0	45^0	1.1218	2.9175	1.3303
0.1	0.1	7.0	5.0	0.5	1.0	0.1	**2.0**	0.1	0.1	1.0	45^0	1.1237	2.9185	1.2989
0.1	0.1	7.0	5.0	0.5	1.0	0.1	0.9	**0.5**	0.1	1.0	45^0	0.3832	3.4477	1.5301
0.1	0.1	7.0	5.0	0.5	1.0	0.1	0.9	0.1	**0.5**	1.0	45^0	2.4776	3.0066	1.7661
0.1	0.1	7.0	5.0	0.5	1.0	0.1	0.9	0.1	**0.0**	1.0	45^0	0.8317	2.8251	1.4666
0.1	0.1	7.0	5.0	0.5	1.0	0.1	0.9	0.1	**-0.5**	1.0	45^0	0.0228	1.8648	1.2083
0.1	0.1	7.0	5.0	0.5	1.0	0.1	0.9	0.1	0.5	**2.0**	45^0	1.0466	3.8926	1.5556
0.1	0.1	7.0	5.0	0.1	1.0	0.1	0.9	0.1	0.5	1.0	$\mathbf{60}^0$	1.1092	2.9136	1.5830

The effects of reduced Nusselt number $-\theta'(0)$, reduced Sherwood number $-\phi'(0)$

and skin friction coefficient $C_{fx}(0)$ against changed values of incorporated physical constraints $M, S, R, \lambda_1, K, Gr, Gc, Pr, \gamma, Le, Nt$ and Nb are shown in Table 4.1. It is noted that $-\theta'(0)$ diminishes for increasing λ_1, Nt, Le, R, Nb, γ, M as well as on decreasing of S and increased by enhancing the numerical values of K, Gr, Gc, Pr and S. Moreover, it is perceived that $-\phi'(0)$ enhanced with the larger values of Nb, Le, K, $Pr, R, Nt, Gr, \lambda_1, Gc$ and S decreases versus increment in γ and M and decreasing values of S. On the other hand, $C_{fx}(0)$ rises with the growth of $Le, \lambda_1, Nb, M, K, R, S$, γ and diminishes with the increment in Nt, Gr, Gc, Pr and on descending of S.

Figure 4.1 shows that $f'(\eta)$ inversely related with S. It is observed that as the mass exchange process goes from injection to suction, the velocity profile falls. Physically, by increasing factor S peak velocity transfers nearby the sheet surface and thickness of the boundary layer reduces. Similarly, $\theta(\eta)$ shows an inverse relation with parameter S on improving from injection to suction in Figure 4.2. From Figures 4.1 and 4.2, it is meaningful to say that the wall transpiration (suction or injection) offers an effective means of controlling the flow and energy transport characteristics.

Figure 4.3 expressed heat generation impact on $\theta(\eta)$. It is noted that $\theta(\eta)$ increases by growing λ_1. The reason behind in fluid flow regime, the rate of heat exchange reduces with sink ($\lambda_1 < 0$) as a medium of heat absorption. On the other hand, the heat exchange rate enhances in the existence of energy source ($\lambda_1 > 0$) in nanofluid flow process. The velocity of fluid enhances with the improvement in heat generation, due to which heat generates in the flow region and the temperature increases in thermal boundary layer. Practically, these processes are possible in the chemical reactions, for instance in endothermic or exothermic reactions. Physically, in an endothermic reaction, more heat is required in a chemical reaction. Whereas, in exothermic reactions, there is a heat generation, which results in an increment in heat exchange.

Figure 4.4 indicates that $\phi(\eta)$ declines by increasing the factor S. Moreover, $\phi(\eta)$ falls with the improvement in chemical reaction parameter R because R depends upon nanofluid concentration. This decline in $\phi(\eta)$ versus increment in R is owing to higher conversion of reactants to resultant products. On the other hand, it shows the efficiency of heat exchange and more conversion of the reactants in nanofluids. To get more products, to reduce process cost, and to enhance the over all reaction rate such types of processes play a key role in chemical reactions.

Figures 4.6 to 4.11 present the influences of involved factors on $-\theta'(0)$ and $-\phi'(0)$. In Figure 4.6, $-\theta'(0)$ enhances with increase in the factors M and S. As compared to impermeable surface, $-\theta'(0)$ falls in the case of injection i.e. for negative values of S and enhances for suction when $S > 0$. This is due to momentum transport that is declined adjacent the wall as the injection is applied at the wall. Further, Figure 4.7 presents $-\phi'(0)$ increases versus different values of factors M and S. This behavior may be meaningful by the fact that the concentration distribution broaden due to blowing. In return, the wall concentration gradient diminishes and finally $-\phi'(0)$ results. In addition, Figure 4.8 reveals that $-\theta'(0)$ improves with the increment in λ_1 and in Pr. Physically, the wall temperature gradient enhances for the growing magnitudes of Pr due to which the thermal boundary layer thickness reduces. While, $-\phi'(0)$ shows direct correspondence with factors λ_1, Pr (see Figure 4.9). Moreover, in Figure 4.10, $-\theta'(0)$ shows an inverse correspondence with R, Nt, and Nb. Whereas, $-\phi'(0)$ presents direct relation with R, Nt, and Nb in Figure 4.11.

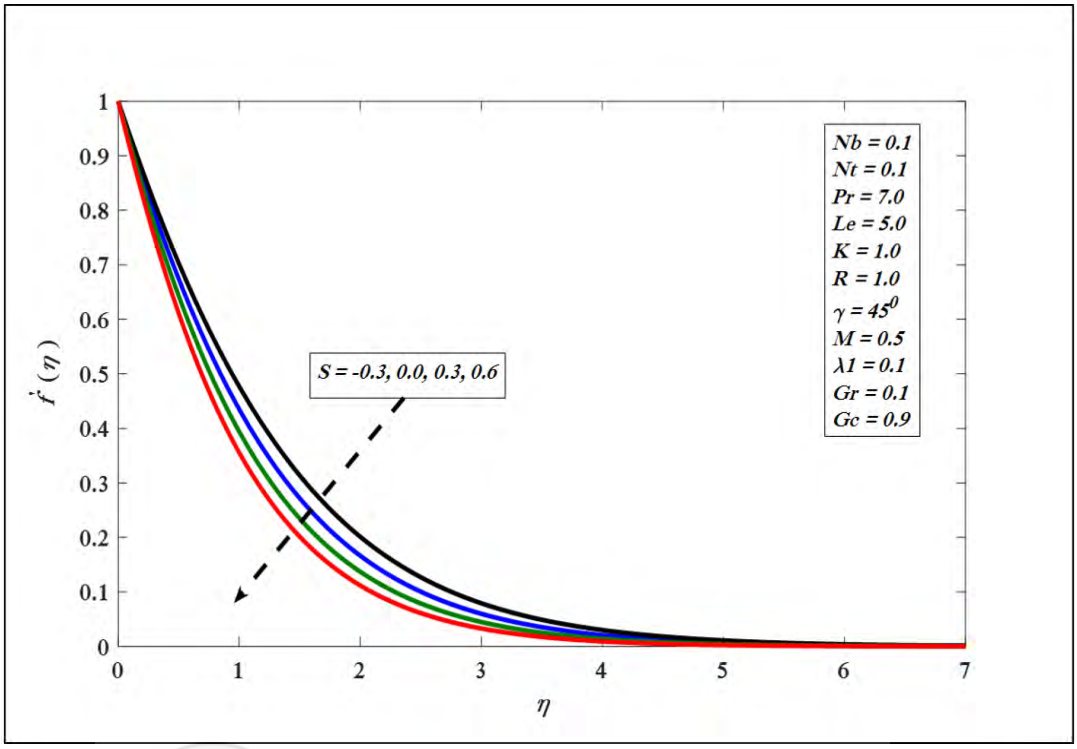

Figure 4.1. Variations in velocity profile for several values of S

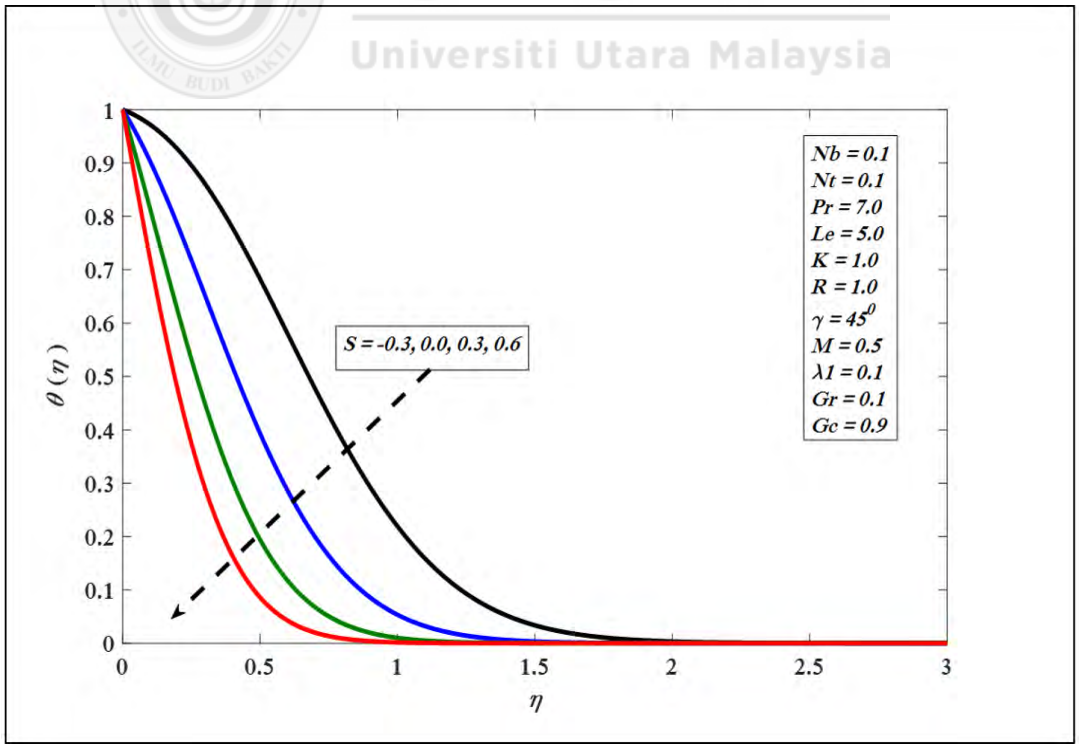

Figure 4.2. Variations in temperature profile for several values of S.

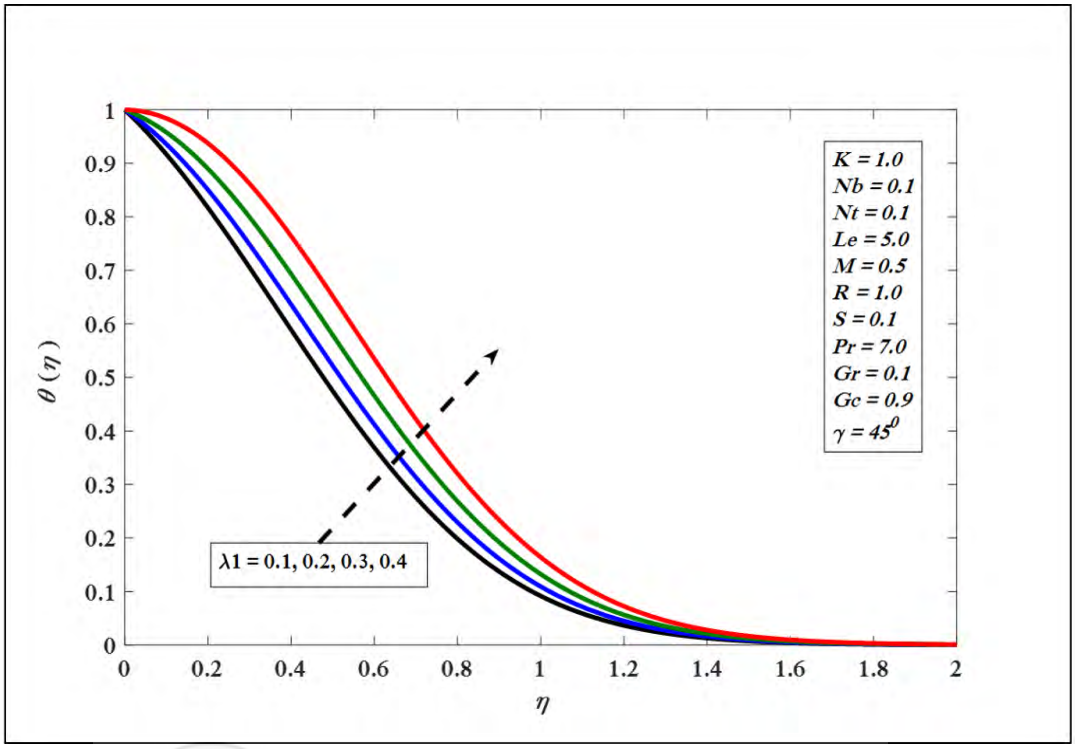

Figure 4.3. Variations in temperature profile for several values of λ_1.

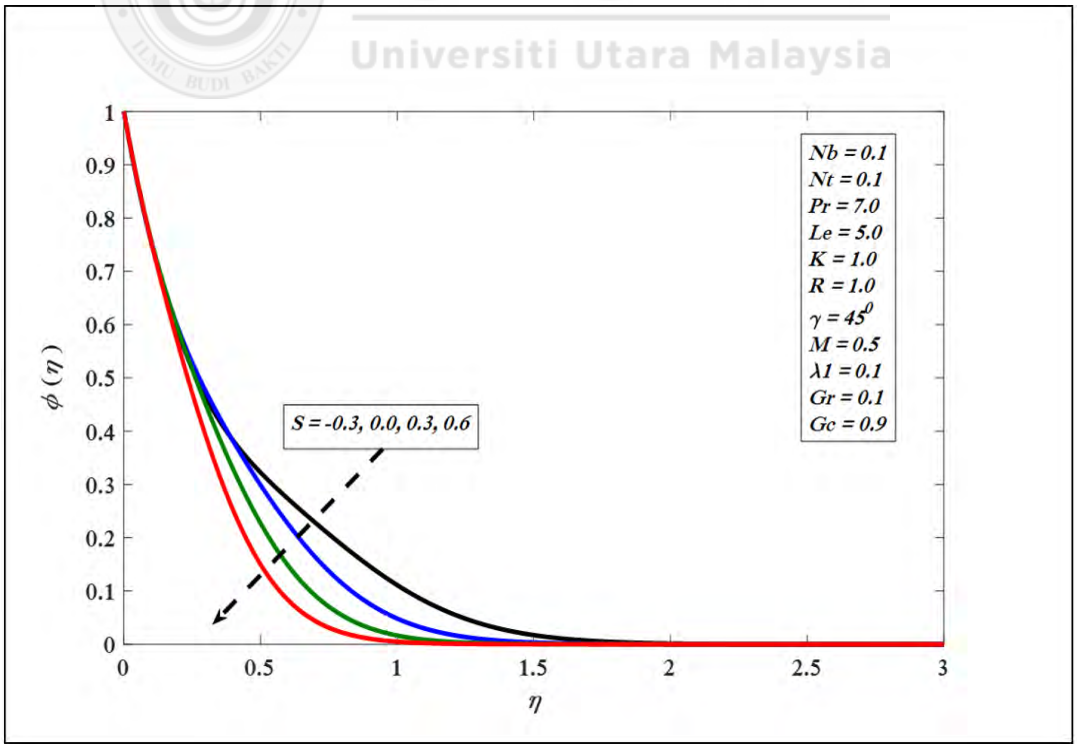

Figure 4.4. Variations in concentration profile for several values of S.

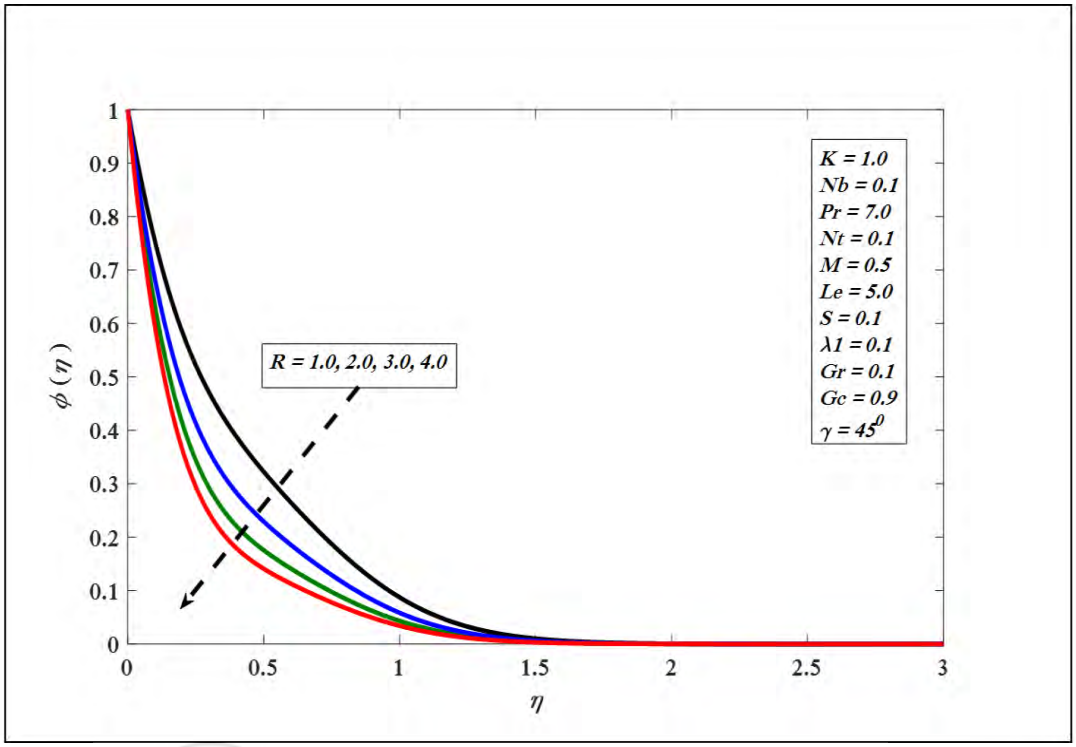

Figure 4.5. Variations in concentration profile for several values R.

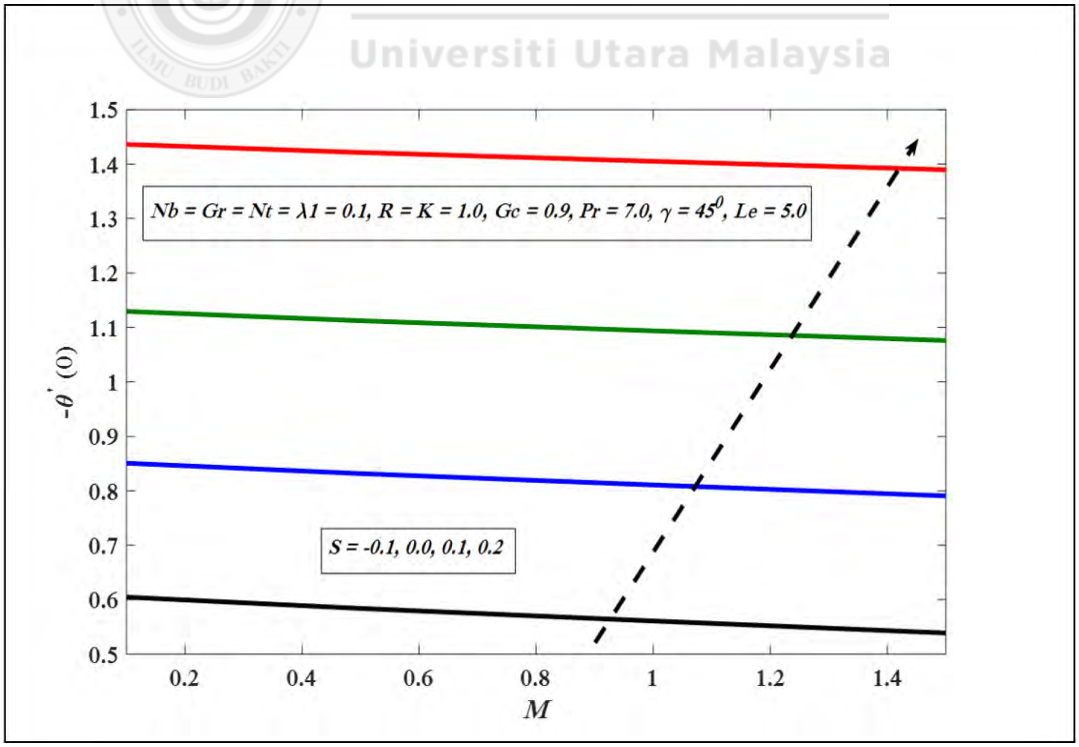

Figure 4.6. $-\theta'(0)$ against M for several values of S.

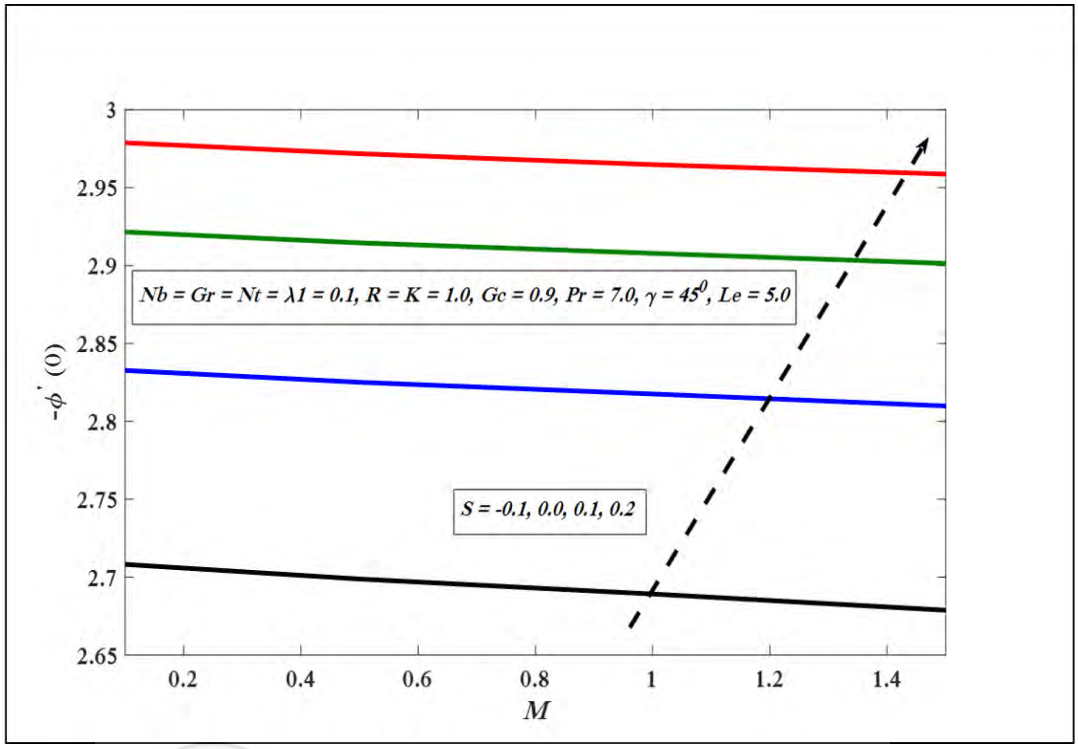

Figure 4.7. $-\phi'(0)$ against M for several values of S.

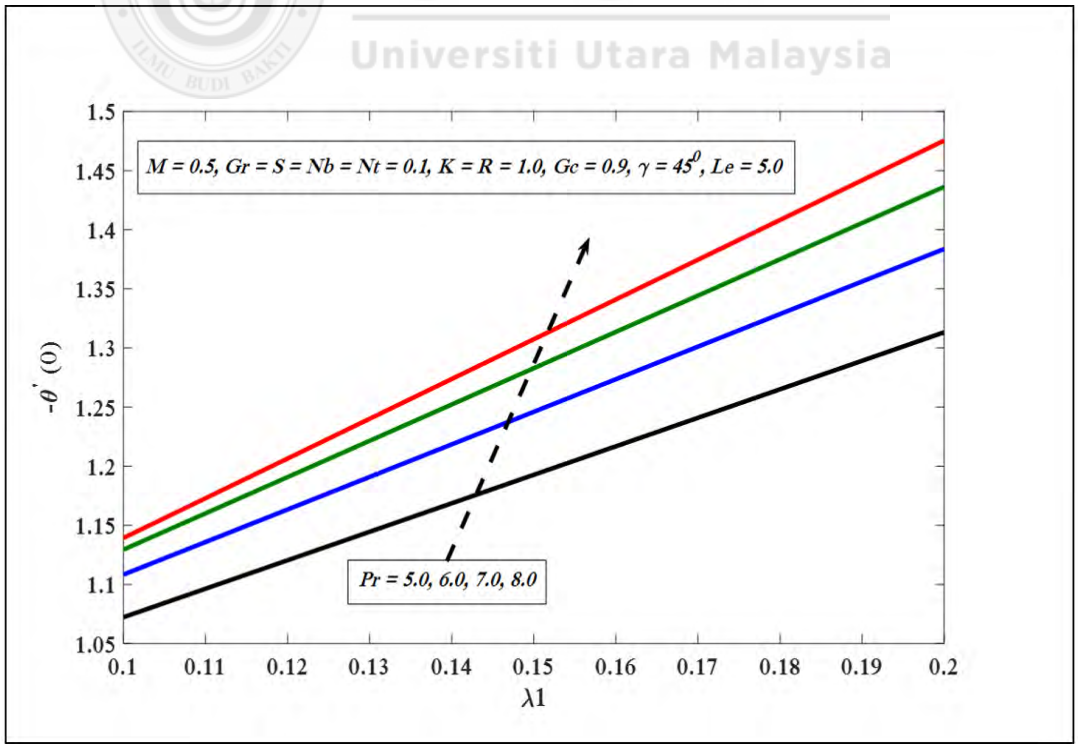

Figure 4.8. $-\theta'(0)$ λ_1 for several values of Pr.

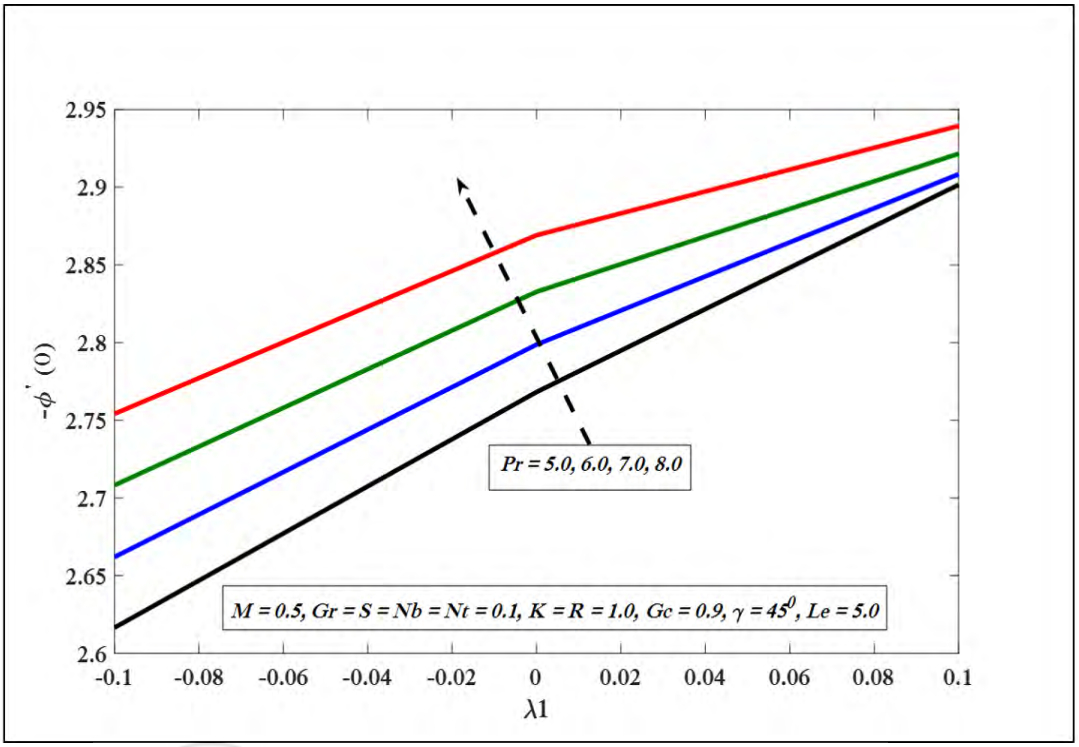

Figure 4.9. $-\phi'(0)$ against λ_1 for several values of Pr.

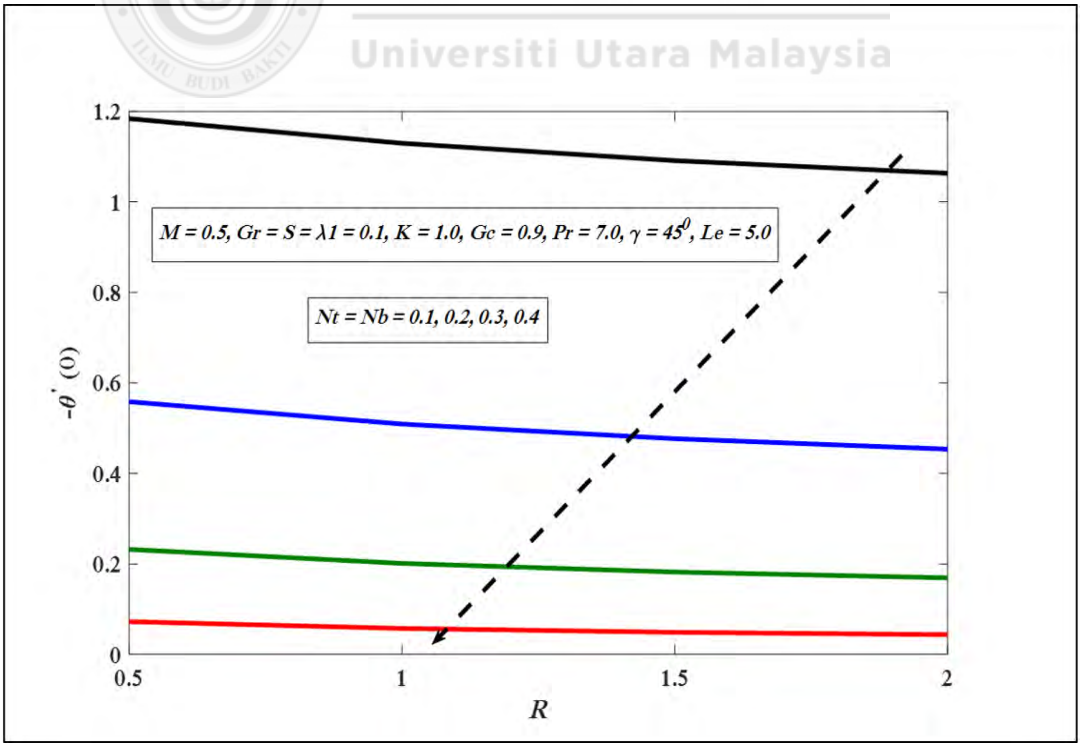

Figure 4.10. $-\theta'(0)$ against R for several values of $Nt = Nb$.

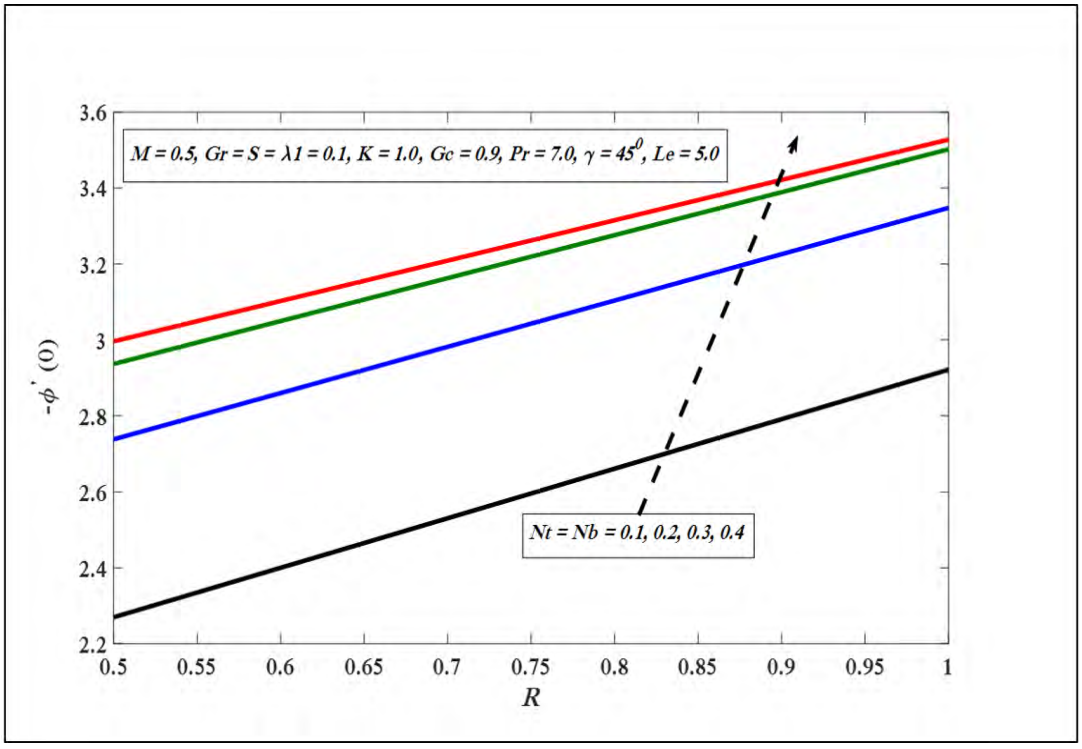

Figure 4.11. $-\phi'(0)$ against R for several values of $Nt = Nb$.

4.4 Conclusions

The problem of steady incompressible flow of a micropolar nanofluid on permeable inclined stretching surface along with influence of chemical reaction and suction or injection is investigated numerically. The governing equations are converted in to ordinary differential equations by applying similar similarity transformation and solved by utilizing Keller box scheme. The effects of suction or injection, heat generation or absorption on physical quantities of our interest are presented in the form of table and graphs. The notable conclusions of the problem under concern are:

1. $-\theta'(0)$ decreases and $-\phi'(0)$ increases with enhancement in chemical reaction.

2. Suction parameter increase $-\theta'(0)$ and $-\phi'(0)$ whereas injection show contrary impact.

3. $-\theta'(0)$ decreases and $-\phi'(0)$ increases due to heat generation.

CHAPTER FIVE

MICROPOLAR NANOFLUID BOUNDARY LAYER FLOW OVER A POWER LAW INCLINED STRETCHING SURFACE

5.1 Introduction

The problem of flow of micropolar nanofluid towards a power law inclined stretching surface is investigated in first part of this chapter. While the second part consists on micropolar nanofluid flow generated due to nonlinear inclined stretching surface by incorporating convective boundary conditions and thermal radiations. The slanted surface is stretched nonlinearly in the existence of non-uniform magnetic field $B(x) = B_0 x^{\frac{m-1}{2}}$ acting normal to flow direction. By using appropriate similarity transformations, the governing nonlinear PDE's are transformed into ODE's. The impacts of different factors such as velocity exponent factor m, as well as Hartmann number M, Prandtl number Pr and Lewis number Le, respectively are discussed via tabulated and graphical form. A comparative study is also being made with those of Khan and Pop (2010).

5.2 Governing Equations

A steady, two dimensional boundary layer flow of micropolar nano fluid over an inclined nonlinear stretching with an angle γ is taken into account. Note that, $u_w(x) = ax^m$ signifies velocity due to stretching surface while $u_\infty(x) = 0$ represents free stream velocity. The transverse magnetic field $B(x) = B_0 x^{\frac{m-1}{2}}$ is considered at right angle to flow. The Brownian motion and thermophoresis effects are taken into

account. The temperature T and nano particle fraction C take the constant values T_w and C_w at the wall, while the encompassing structures for nanofluid temperature and mass divisions T_∞ and C_∞ are achieved as y tends to infinity as shown in Figure 3.3. The governing equations for this problem are as follows (see Equations 3.59, 3.62 when $Q_0 = \sigma^* = 0$), Equation 3.63 when $R^* = 0$, Equation 3.89 and 3.90)

$$\frac{\partial u}{\partial x} + \frac{\partial v}{\partial y} = 0,$$

$$u\frac{\partial u}{\partial x} + v\frac{\partial u}{\partial y} = \left(\frac{\mu + k_1^*}{\rho}\right)\frac{\partial^2 u}{\partial y^2} + \left(\frac{k_1^*}{\rho}\right)\frac{\partial N^*}{\partial y} + g\beta_t(T - T_\infty)\cos\gamma$$

$$+ g\beta_c(C - C_\infty)\cos\gamma - \left(\frac{\sigma B^2(x)}{\rho}\right)u,$$

$$u\frac{\partial N^*}{\partial x} + v\frac{\partial N^*}{\partial y} = \left(\frac{\gamma^*}{j^*\rho}\right)\left(\frac{\partial^2 N^*}{\partial y^2}\right) - \left(\frac{k_1^*}{j^*\rho}\right)\left(2N^* + \frac{\partial u}{\partial y}\right), \tag{5.1}$$

$$u\frac{\partial T}{\partial x} + v\frac{\partial T}{\partial y} = \alpha\frac{\partial^2 T}{\partial y^2} + \tau\left[D_B\frac{\partial C}{\partial y}\frac{\partial T}{\partial y} + \frac{D_T}{T_\infty}\left(\frac{\partial T}{\partial y}\right)^2\right],$$

$$u\frac{\partial C}{\partial x} + v\frac{\partial C}{\partial y} = D_B\frac{\partial^2 C}{\partial y^2} + \frac{D_T}{T_\infty}\frac{\partial^2 T}{\partial y^2}.$$

The subject boundary conditions are

$$u = u_w(x) = ax^m\ , v = 0\ , T = T_w\ , N^* = -m_0\frac{\partial u}{\partial y}\ , C = C_w \qquad at \qquad y = 0,$$

$$u \to u_\infty(x) = 0\ , v \to 0\ , T \to T_\infty\ , N^* \to 0\ , C \to C_\infty \qquad as \qquad y \to \infty. \tag{5.2}$$

5.2.1 Similarity Transformations

The stream function use for this procedure is given as

$$u = \frac{\partial \psi}{\partial y}, \quad v = -\frac{\partial \psi}{\partial x}, \tag{5.3}$$

where continuity equation in Equation (5.1) is satisfied identically. Similarity transformations are characterized as

$$\psi = \sqrt{\frac{2\nu a x^{m+1}}{m+1}} f(\eta), \eta = y\sqrt{\frac{(m+1)a x^{m-1}}{2\nu}},$$

$$N^* = a x^m \sqrt{\frac{a(m+1)x^{m-1}}{2\nu}} h(\eta), \theta(\eta) = \frac{T - T_\infty}{T_w - T_\infty}, \phi(\eta) = \frac{C - C_\infty}{C_w - C_\infty}. \tag{5.4}$$

On substituting Equation (5.4), system of equations (5.1) converted to the following nonlinear ordinary differential equations:

$$(1+K) f''' + f f'' - \left(\frac{2m}{m+1}\right) f'^2 + K h' + \frac{2}{m+1}(Gr_x \theta + Gc_x \phi) cos\gamma - \frac{2}{m+1}(M) f' = 0,$$

$$\left(1 + \frac{K}{2}\right) h'' + f h' - \frac{3m-1}{m+1} h f'^2 - \frac{2k}{m+1}\left(2h + f''\right) = 0,$$

$$\left(\frac{1}{\mathrm{Pr}}\right) \theta'' + f\theta' + Nb\theta'\phi' + Nt\theta'^2 = 0, \tag{5.5}$$

$$\phi'' + Lef\phi' + Nt_b\theta'' = 0,$$

where,

$$Gc_x = \frac{g\beta_c (C_W - C_\infty) x^{-2m+1}}{a^2}, Gr_x = \frac{g\beta_T (T_W - T_\infty) x^{-2m+1}}{a^2}. \tag{5.6}$$

Here, Gr_x denotes the local Grashof number and local modified Grashof number is given by Gc_x, It is worth mentioning here that to achieve true similarity solution, Gr_x

and Gc_x must be constant and free from x. This condition can be achieved if thermal and concentration expansion coefficients β_t and β_c are proportional to x^{2m-1}.

Thus, following Makinde and Olanrewaju (2010), Olanrewaju and Hayat (2014) and Ilias et al. (2016), we assume that

$$\beta_t = nx^{2m-1}, \beta_c = n_1 x^{2m-1}, \tag{5.7}$$

By using Equation (5.7), Gr_x and Gc_x takes the form

$$Gr = \frac{gn\,(T_W - T_\infty)}{a^2}, Gc = \frac{gn_1\,(C_W - C_\infty)}{a^2}. \tag{5.8}$$

Equation (5.2) converted in to the form

$$f(\eta) = 0,\ f'(\eta) = 1,\ h(\eta) = 0, \theta(\eta) = 1, \phi(\eta) = 1 \ at\ \eta = 0,$$

$$f'(\eta) \to 0,\ h(\eta) \to 0, \theta(\eta) \to 0, \phi(\eta) \to 0 \ \ at \ \ \eta \to \infty. \tag{5.9}$$

The concern quantities including (skin friction) C_f, (Nusselt number) Nu and (Sherwood number) Sh are defined as

$$C_f = \frac{2\tau_w}{\rho\ u_w^2}, Nu = \frac{x\ q_w}{k\,(T_w - T_\infty)}, Sh = \frac{x\ q_m}{D_B\,(C_w - C_\infty)}. \tag{5.10}$$

The expressions for $C_{fx}(0) = (1+K)\ f''(0)$ (Skin-friction), $-\theta'(0)$ (local Nusselt number) and $-\phi'(0)$ (local Sherwood number) are demarcated as

$$C_{fx}(0) = \frac{C_f}{2}\sqrt{\frac{2Re_x}{m+1}}, -\theta'(0) = \frac{Nu}{\sqrt{\frac{m+1}{2}}Re_x}, -\phi'(0) = \frac{Sh}{\sqrt{\frac{m+1}{2}}Re_x}, \tag{5.11}$$

where, $Re_x = \frac{u_w(x)\ x}{\nu}$ represents Reynold's number.

5.3 Results and Discussion

Numerical results of the nonlinear ordinary differential equations (5.5) subjected to the boundary settings (5.9) are obtained via Keller-box scheme. Results of physical parameters of our concern such as Prandtl number Pr, local modified Grashof number Gc, thermophoresis parameter Nt, Brownian motion parameter Nb, magnetic factor M, local Grashof number Gr, inclination factor γ, (Lewis number) Le and (material factor) K, are exhibited by various figures and tables. In the deficiency of Gr, Gc, M and K with $\gamma = 90^0$, the outcomes of (reduced Nusselt number) $-\theta'(0)$, (reduced Sherwood number) $-\phi'(0)$ are compared with Khan and Pop (2010) (see Table 3.1) and showed good agreement. The effects of $-\phi'(0)$, $-\theta'(0)$ and $C_{fx}(0)$ versus involved physical constraints Nb, Nt, M, K, Gr, Gc, γ, m, Le and Pr are shown in Table 5.1. From Table 5.1, it is clear that $-\theta'(0)$ declines with the increase in M, Le, Nb, Nt, m, γ and increases by enhancing the numerical values of K, Gr, Gc, and Pr. In addition, $-\phi'(0)$ enhances versus larger values of $Le, Nb, Gr, Gc, Nt, Pr, K$ and decreases with the increase in M, m and γ. While, $C_{fx}(0)$ increases against increase in K, Le, M, γ, m, Pr and decreases with the increment in Nt, Gr, Gc, and Nb.

Table 5.1
Variations of local Nusselt number $-\theta'(0)$, local Sherwood number $-\phi'(0)$ and skin friction coefficient $C_{fx}(0)$.

Nb	Nt	Pr	Le	M	K	Gr	Gc	m	γ	$-\theta'(0)$	$-\phi'(0)$	$C_{fx}(0)$
0.1	0.1	7.0	5.0	0.1	1.0	1.0	0.9	0.5	45^0	1.1618	1.2482	0.6326
0.5	0.1	7.0	5.0	0.1	1.0	1.0	0.9	0.5	45^0	0.2147	1.7428	0.6065
0.1	**0.5**	7.0	5.0	0.1	1.0	1.0	0.9	0.5	45^0	0.5199	1.9167	0.3007
0.1	0.1	**10.0**	5.0	0.1	1.0	1.0	0.9	0.5	45^0	1.1902	1.2594	0.6514
0.1	0.1	7.0	**10.0**	0.1	1.0	1.0	0.9	0.5	45^0	1.0231	2.2201	0.7370
0.1	0.1	7.00	5.0	**0.5**	1.0	1.0	0.9	0.5	45^0	1.1458	1.1979	0.9755
0.1	0.1	7.0	5.0	0.1	**5.0**	1.0	0.9	0.5	45^0	1.1744	1.3052	1.3112
0.1	0.1	7.0	5.0	0.1	1.0	**3.0**	0.9	0.5	45^0	1.1823	1.2887	0.0514
0.1	0.1	7.0	5.0	0.1	1.0	1.0	**2.0**	0.5	45^0	1.1783	1.2864	0.2174
0.1	0.1	7.0	5.0	0.1	1.0	1.0	0.9	**5.0**	45^0	1.1251	1.1644	1.5270
0.1	0.1	7.0	5.0	0.1	1.0	1.0	0.9	0.5	$\mathbf{90}^0$	1.1345	1.1862	1.3003

Figure 5.1 gives a picture of the upshot of factor M on velocity profile. The velocity outline slows down as we upsurge the magnetic field constraint M. It is since the use of magnetic field yields Lorentz force, by means retard speed of the fluid. Moreover, similar behavior of the magnetic field on $h(\eta)$ is shown in Figure 5.2. Whereas, different impacts of M on $\theta(\eta)$ and $\phi(\eta)$ shown in Figures 5.3 and 5.4. $\theta(\eta)$ and $\phi(\eta)$ increase with the increase in factor M. In addition, Figure 5.5 presents γ variation on $f'(\eta)$. It can be justified from the situation that highest gravitational force act on the flow for $\gamma = 0^0$, since in this condition the sheet will be vertical. While, as $\gamma = 90^0$, the buoyancy forces reduces in this situation because the sheet will be horizontal due to which $f'(\eta)$ falls. Whereas, $\theta(\eta)$ and $\phi(\eta)$ show direct relation with inclination factor in Figures 5.6 and 5.7.

Figure 5.8 presents $f'(\eta)$ decreases with the increment in non-linear stretching factor m. Besides, $\theta(\eta)$ and $\phi(\eta)$ increases versus m is presented in Figures 5.9 and 5.10, respectively. Figures 5.11 and 5.12 display the effect of Nb on the $\theta(\eta)$ and $\phi(\eta)$ sketches separately. The temperature sketch enlarges on improving Nb, whereas, $\phi(\eta)$ enlighten dissimilar style. Physically, boundary layer heat up due to the development in Brownian motion which inclines to travel nanoparticles from the extending sheet to the motionless liquid. Therefore, the absorption nanoparticle lessens. Figures 5.13 and 5.14 present $\theta(\eta)$ and $\phi(\eta)$ versus Nt behavior. Both $\theta(\eta)$ and $\phi(\eta)$ upsurge by growing Nt. Thermophoresis favor to warm boundary layer for altered values of Le and Pr. Whereas, the extent of energy and mass transport reduce with increase in Nt. Figure 5.15 exhibits an increment in Pr, $\theta(\eta)$ drops, because thermal boundary layer viscosity declining by growing Pr. In short, an upturn in Pr express slow extent of thermal distribution. Figure 5.16 represents the outcome of Le on $\phi(\eta)$. The boundary layer viscosity lessening with the increment in Le.

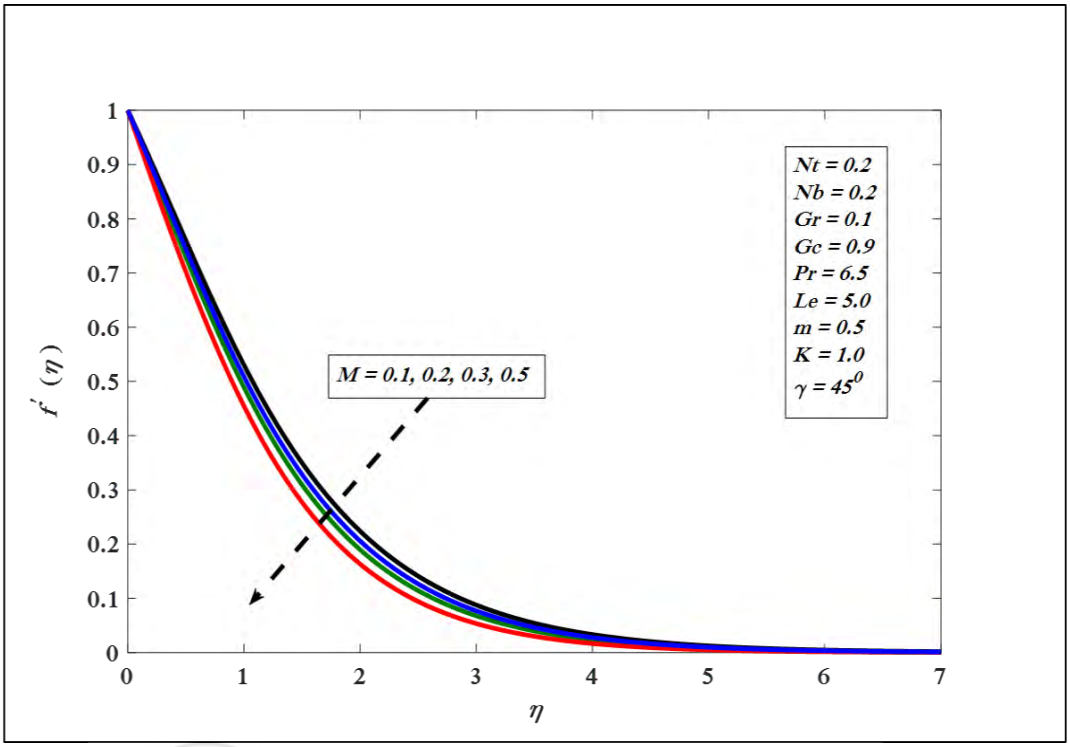

Figure 5.1. Variations in velocity profile for several values of M.

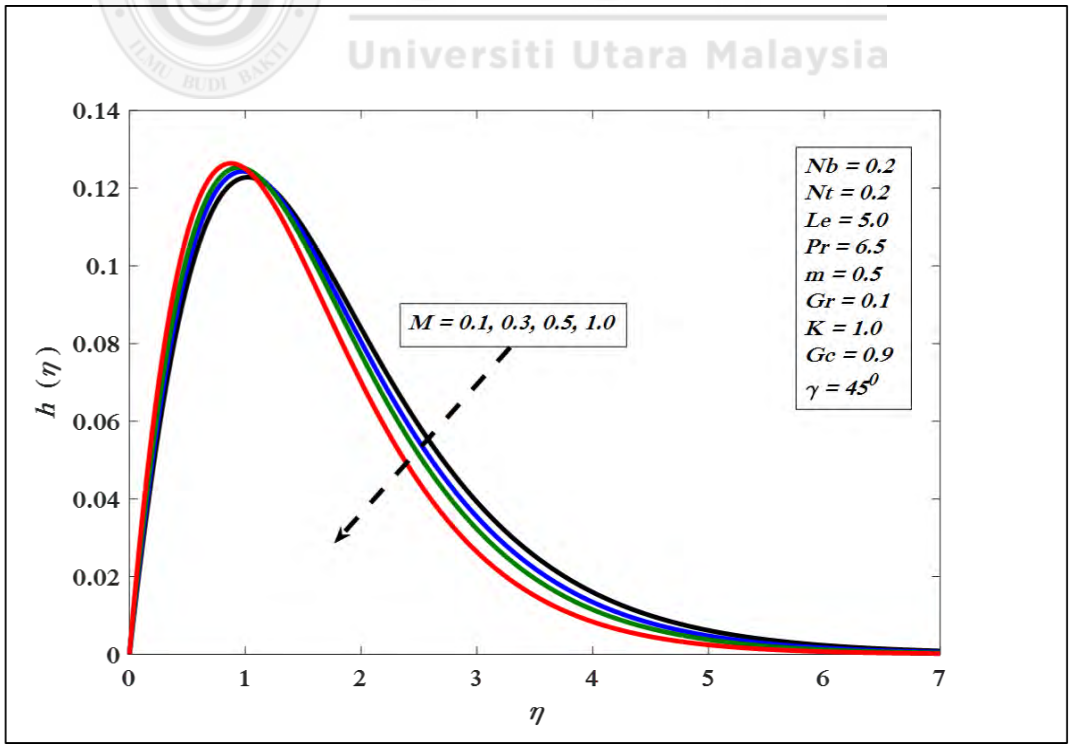

Figure 5.2. Variations in angular velocity for several values of M.

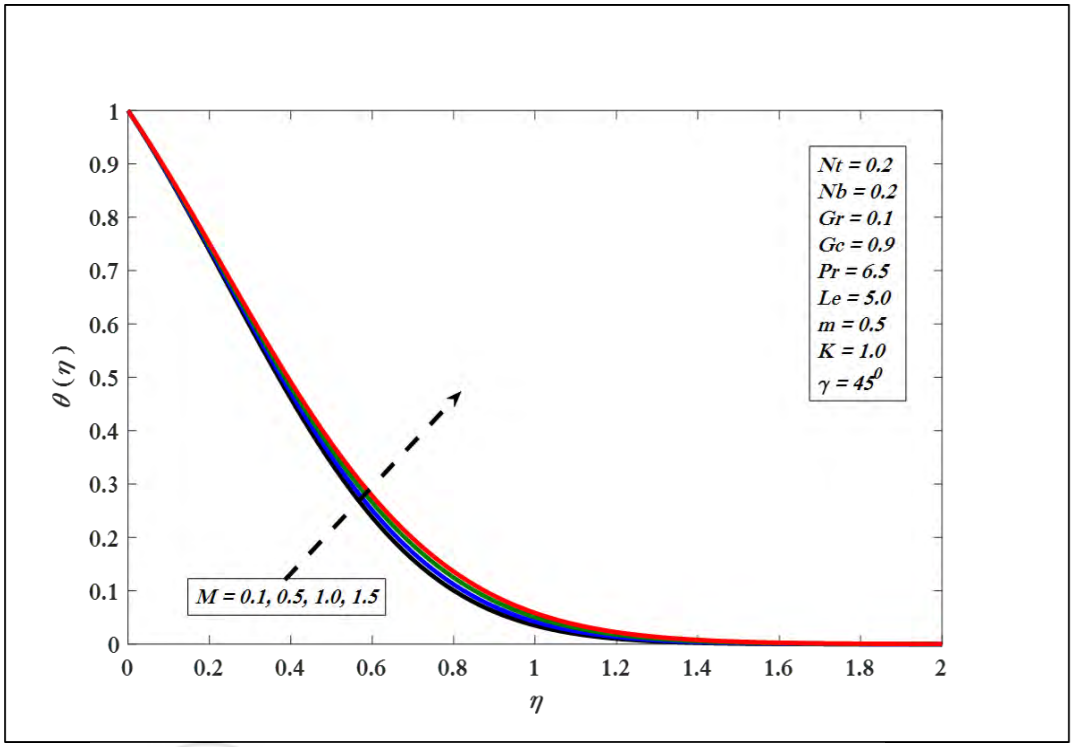

Figure 5.3. Variations in temperature profile for several values of M.

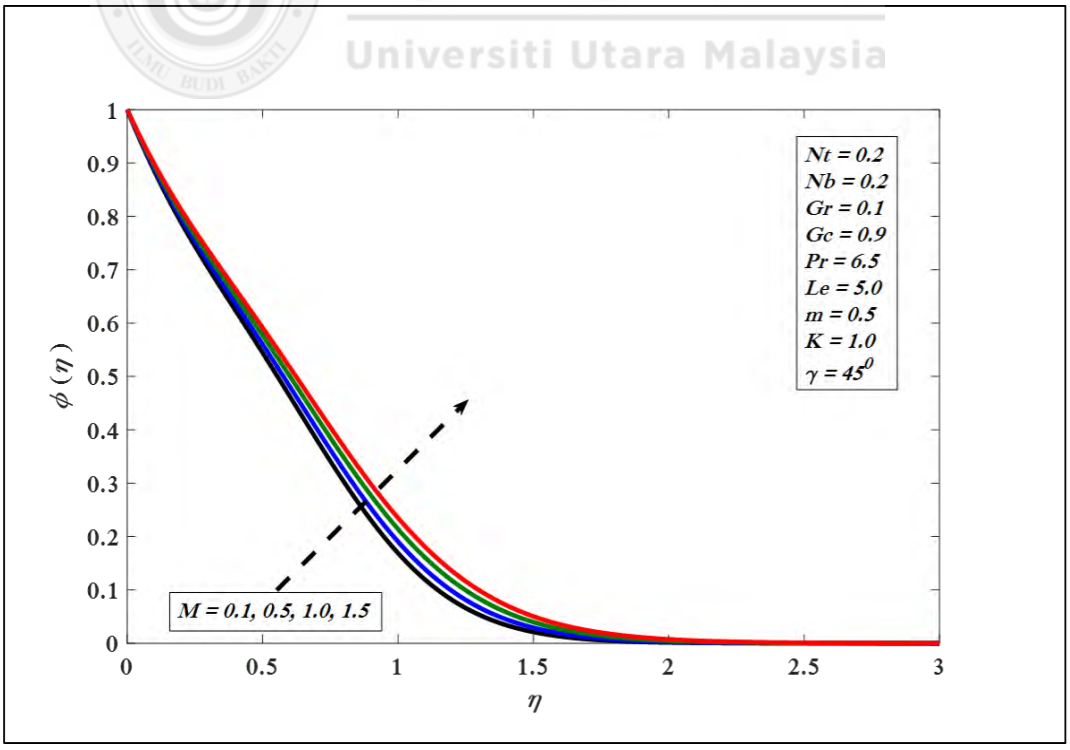

Figure 5.4. Variations in concentration profile for several values of M.

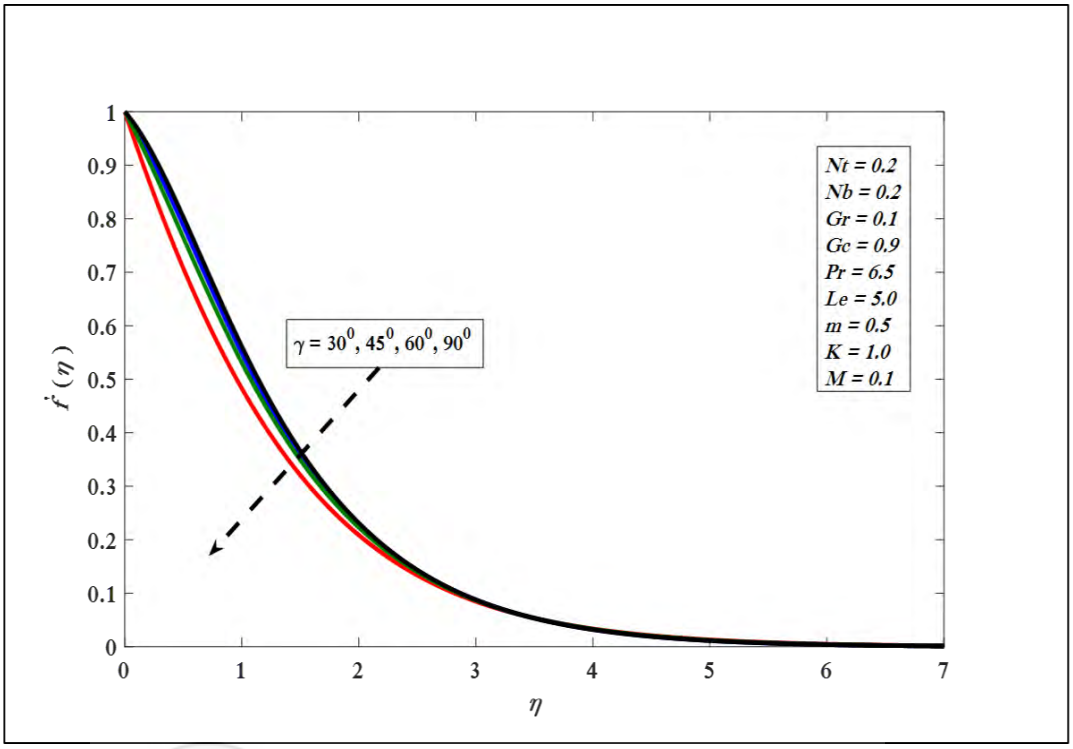

Figure 5.5. Variations in velocity profile for several values of γ.

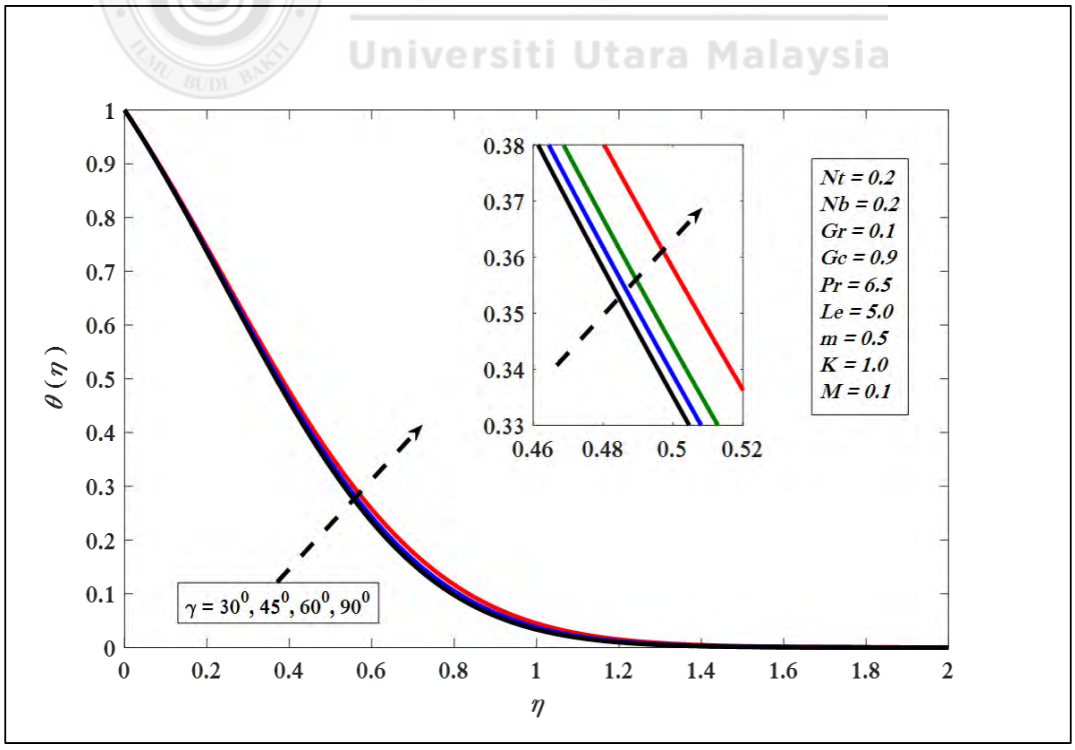

Figure 5.6. Variations in temperature profile for several values of γ.

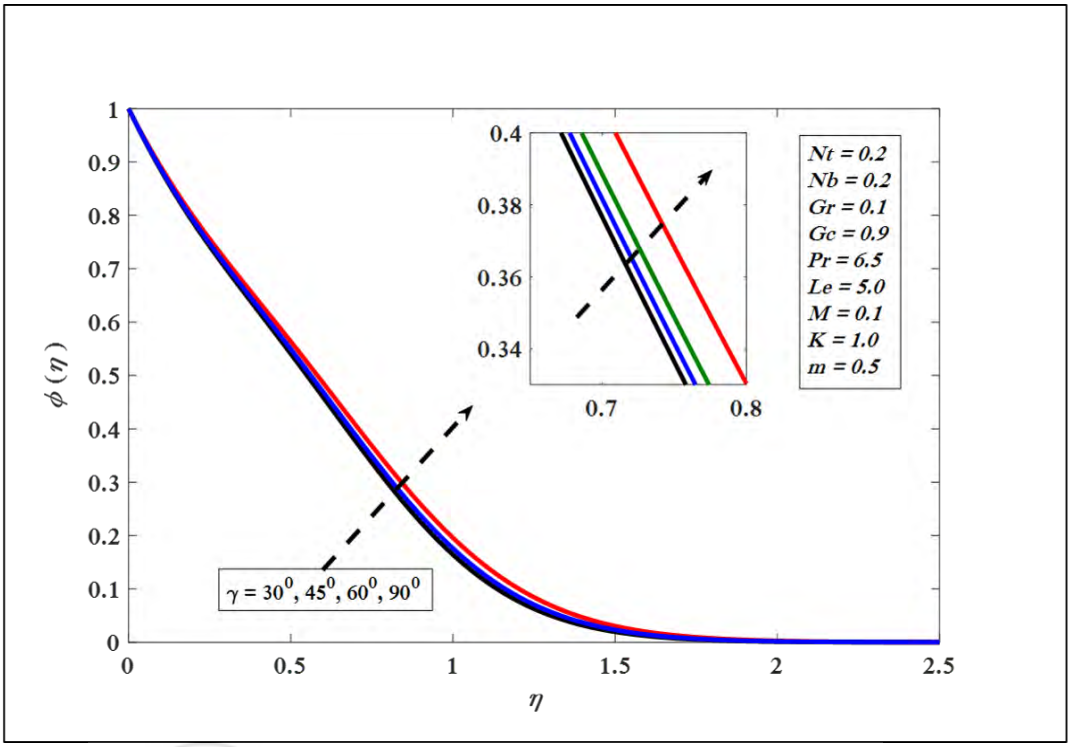

Figure 5.7. Variations in concentration profile for several values of γ.

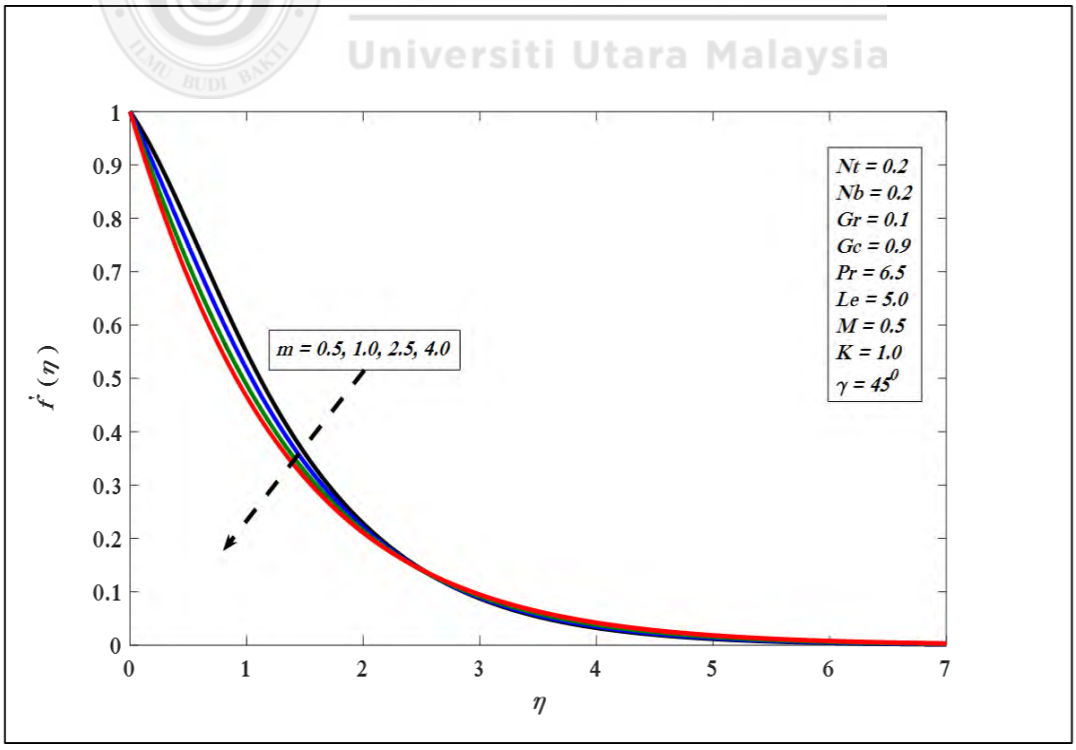

Figure 5.8. Variations in velocity profile for several values of m.

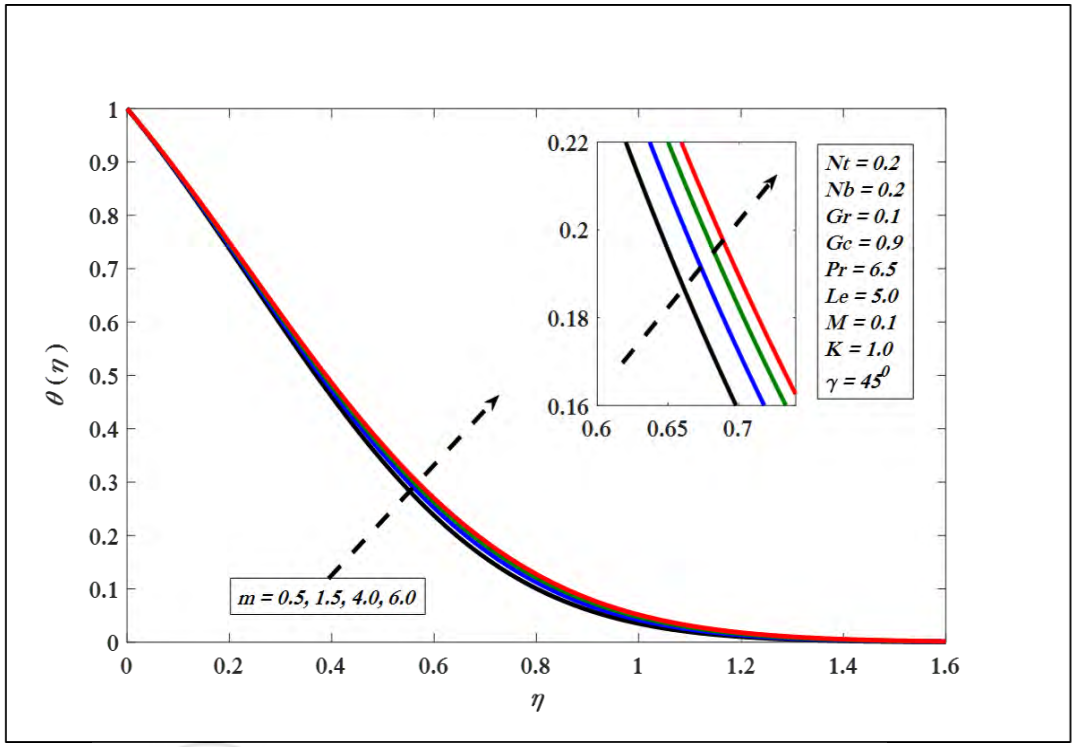

Figure 5.9. Variations in temperature profile for several values of *m*.

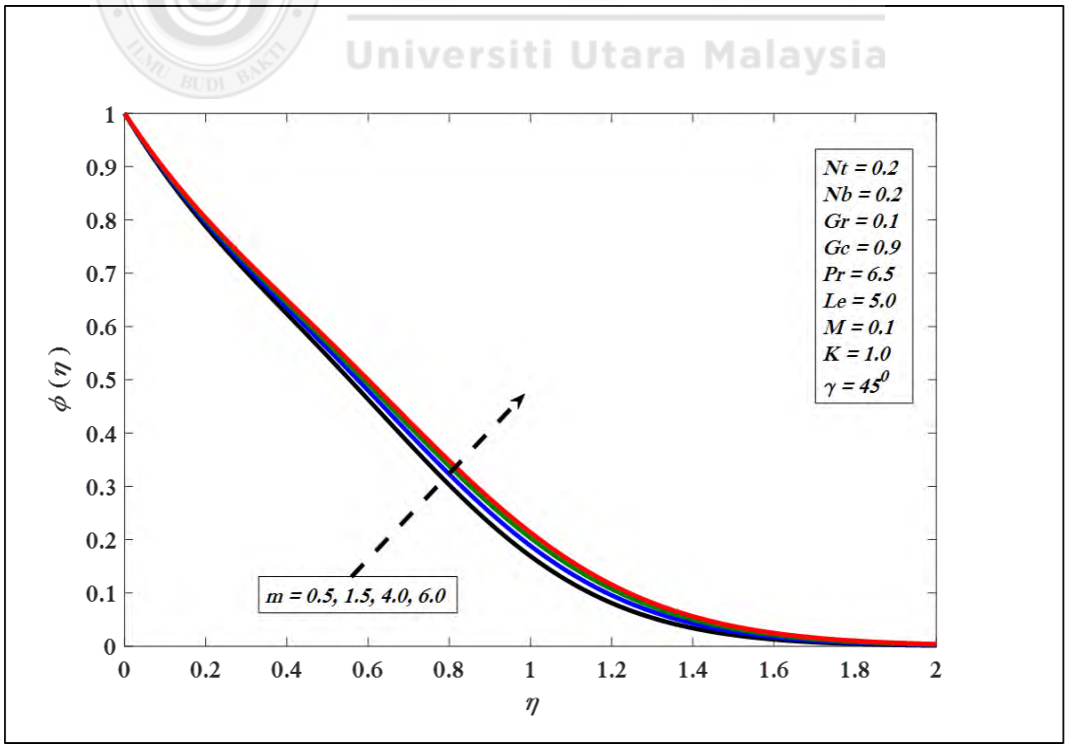

Figure 5.10. Variations in concentration profile for several values of *m*.

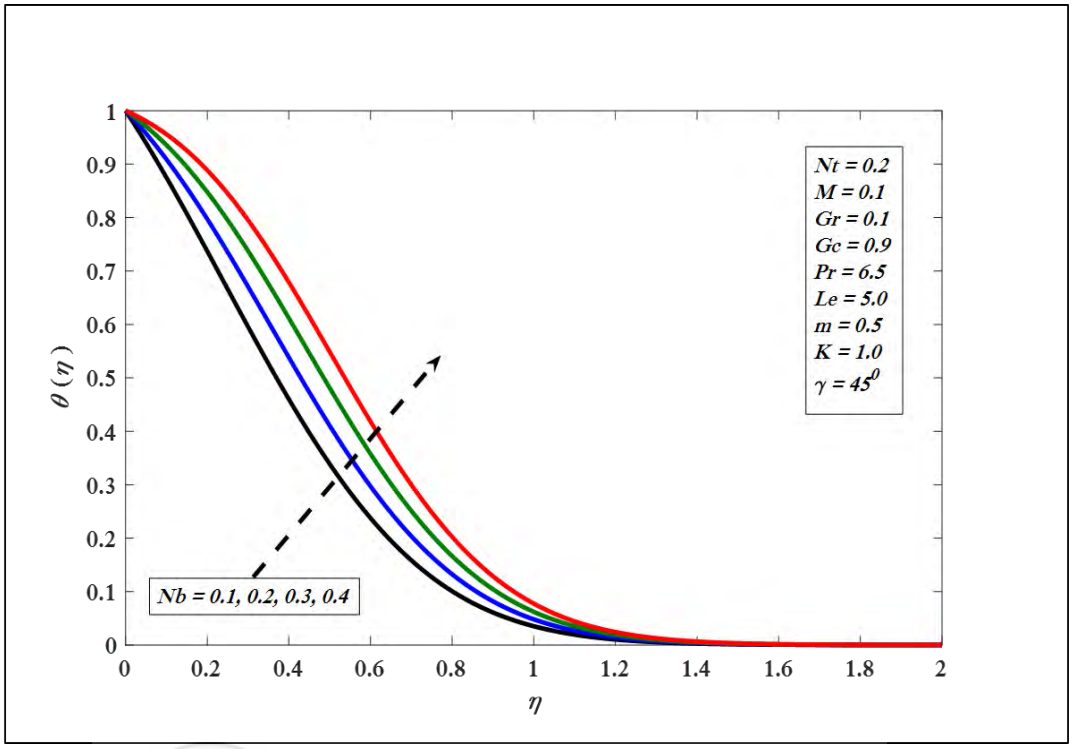

Figure 5.11. Variations in temperature profile for several values of *Nb*.

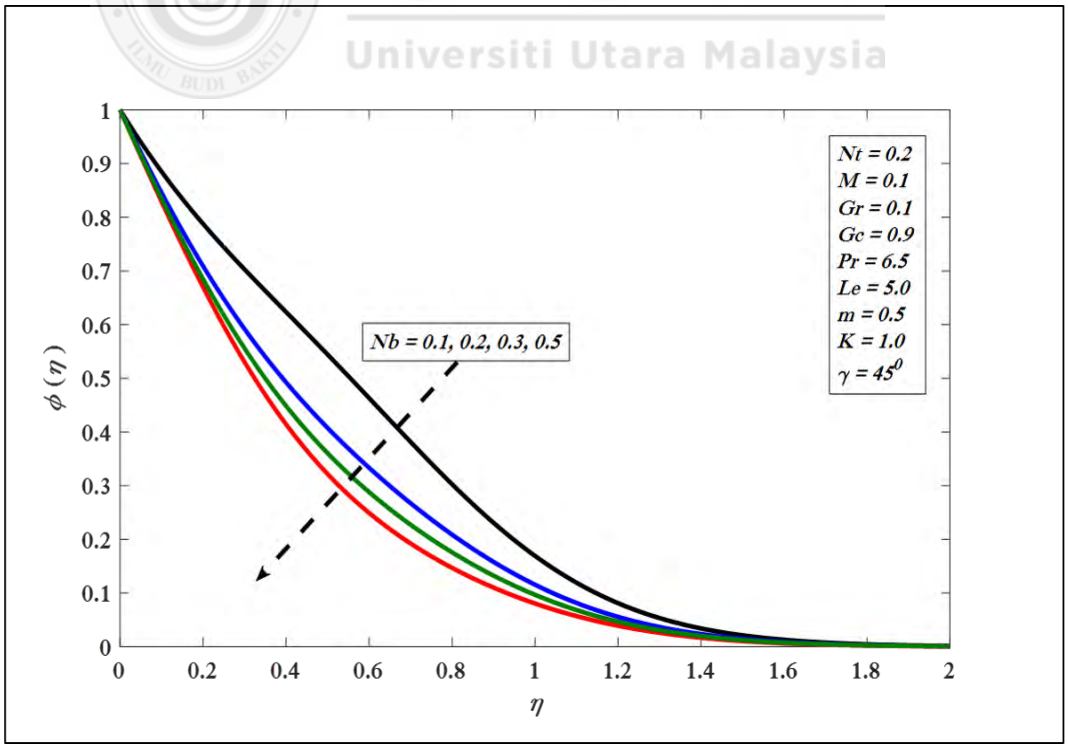

Figure 5.12. Variations in concentration profile for several values of *Nb*.

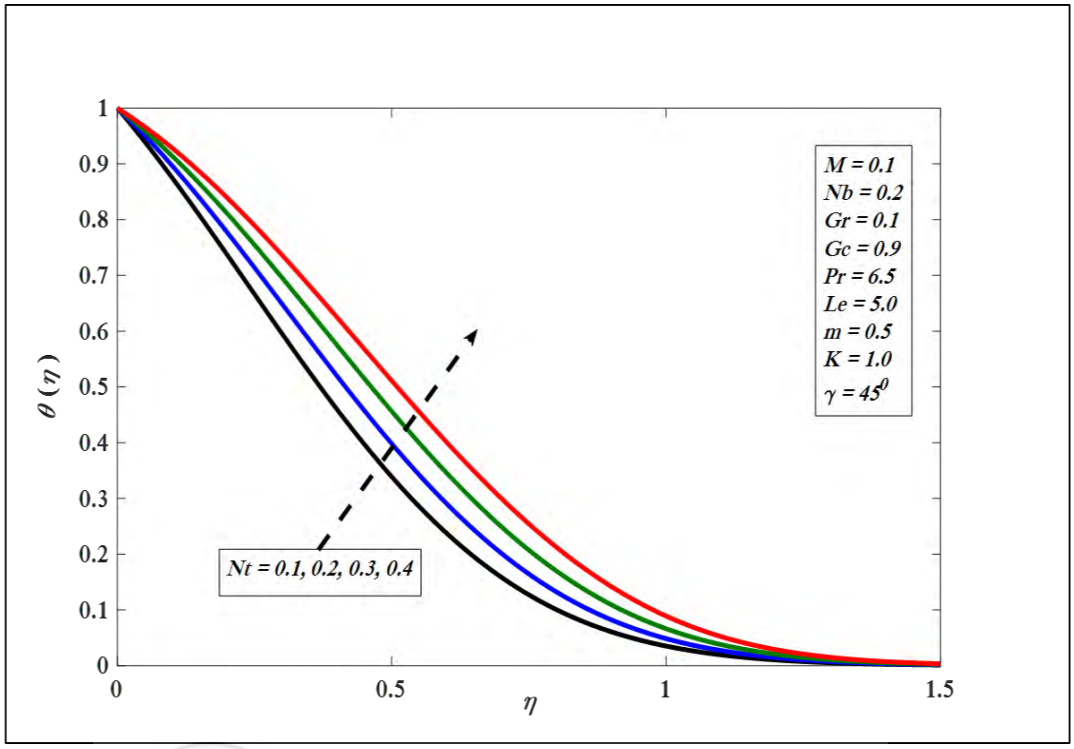

Figure 5.13. Variations in temperature profile for several values of Nt.

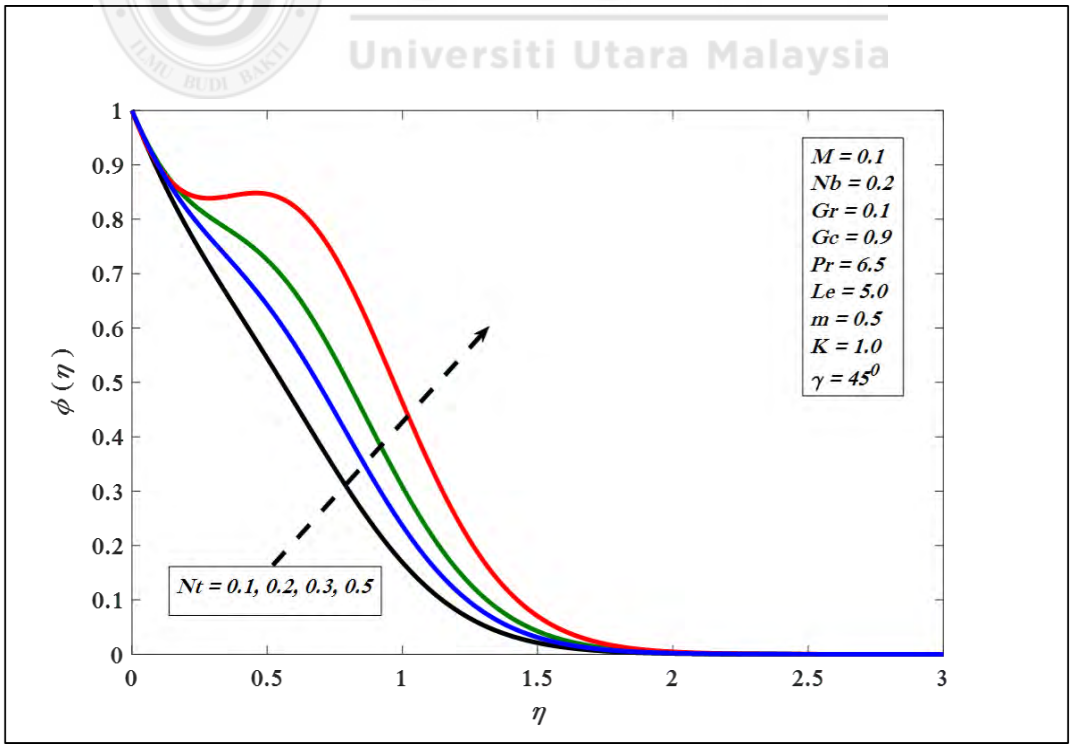

Figure 5.14. Variations in concentration profile for several values of Nt.

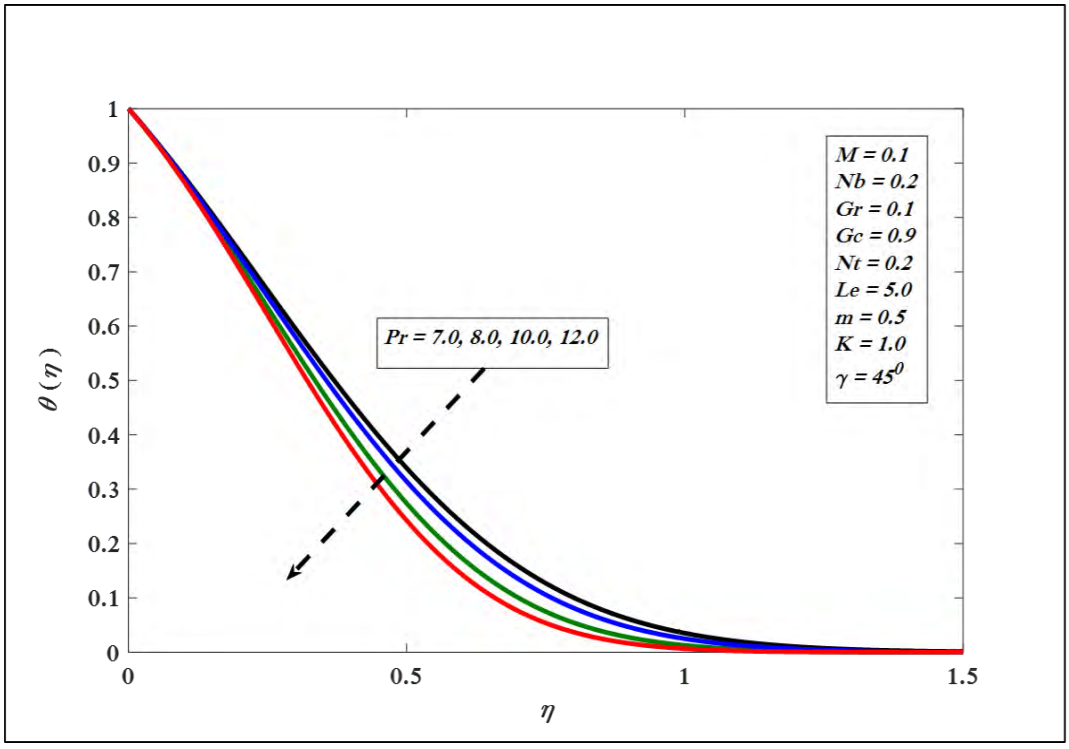

Figure 5.15. Variations in temperature profile for several values of *Pr*.

Figures 5.17 to 5.24 present impacts of $-\theta'(0)$ and $-\phi'(0)$ versus various involved factors. It is observed that $-\theta'(0)$ and $-\phi'(0)$ diminish with the increase of factors *Nb* and γ, see Figures 5.17 and 5.18. Similar behavior of $-\theta'(0)$ and $-\phi'(0)$ versus γ and *Nt* are presented in Figures 5.19 and 5.20. On the other hand, Figures 5.21 and 5.22 show that $-\theta'(0)$ declines on improving the factors *Nb*, *Nt* and *Pr*. Whereas, $-\phi'(0)$ enhances for growth of *Nb* and *Pr*, and declines on enhancing the factors *Nt* and *Pr*, see Figures 5.23 and 5.24.

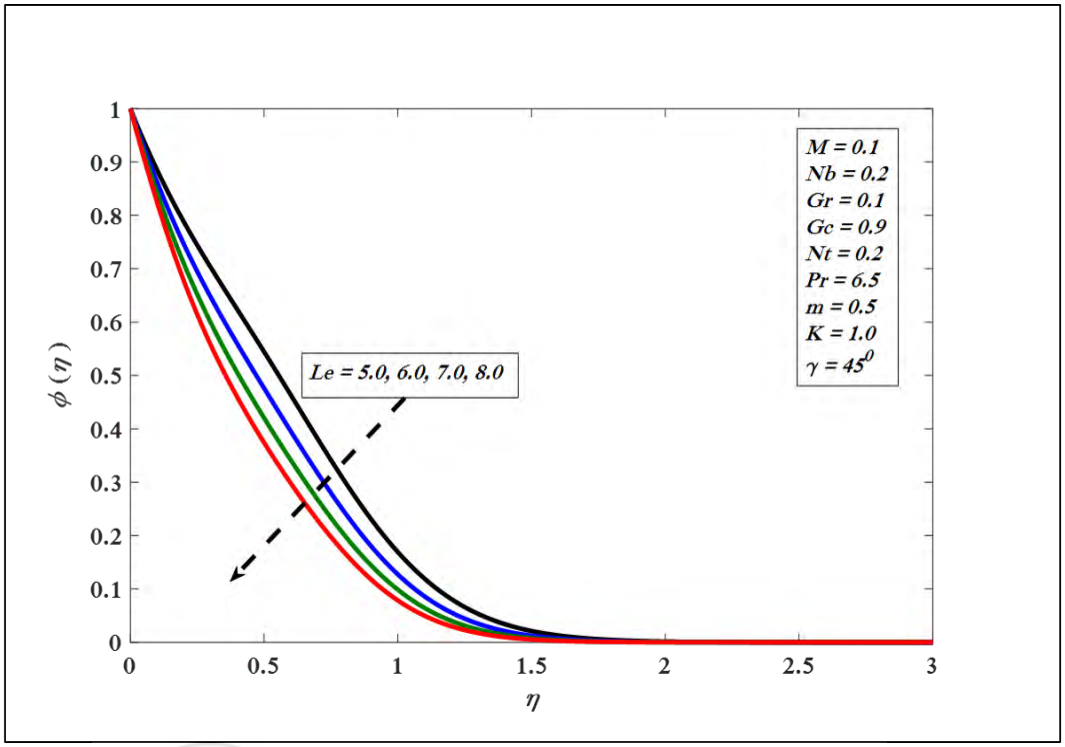

Figure 5.16. Variations in concentration profile for several values of *Le*.

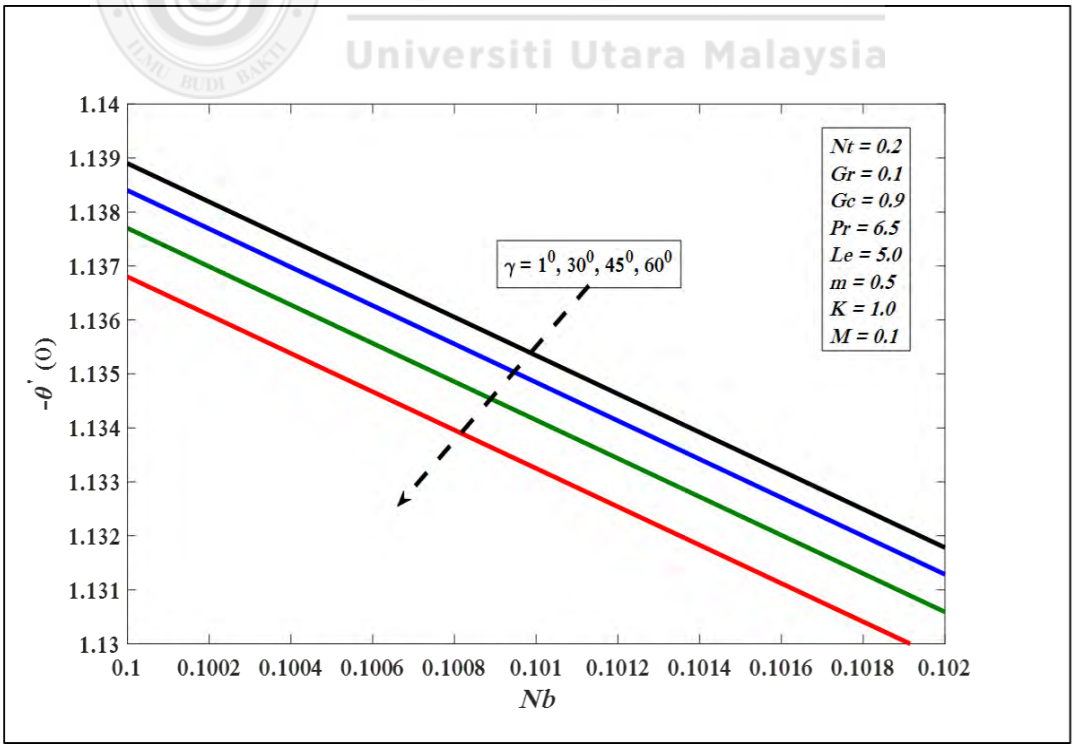

Figure 5.17. $-\theta'(0)$ against *Nb* for several values of γ

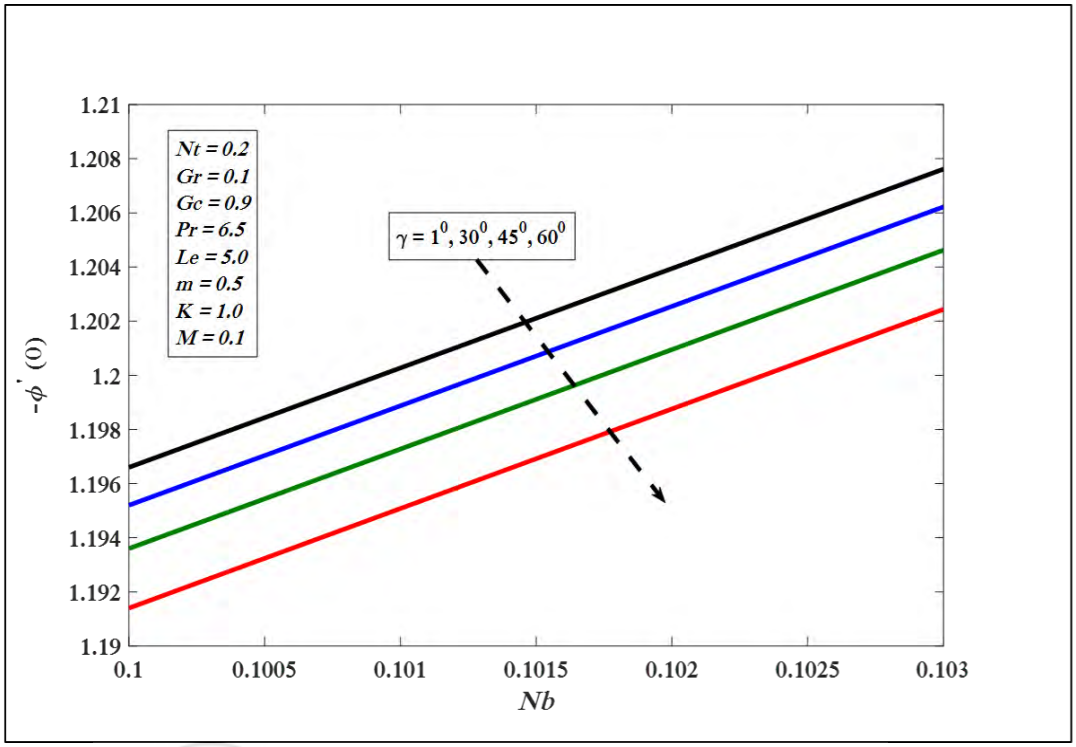

Figure 5.18. $-\phi'(0)$ against Nb for several values of γ

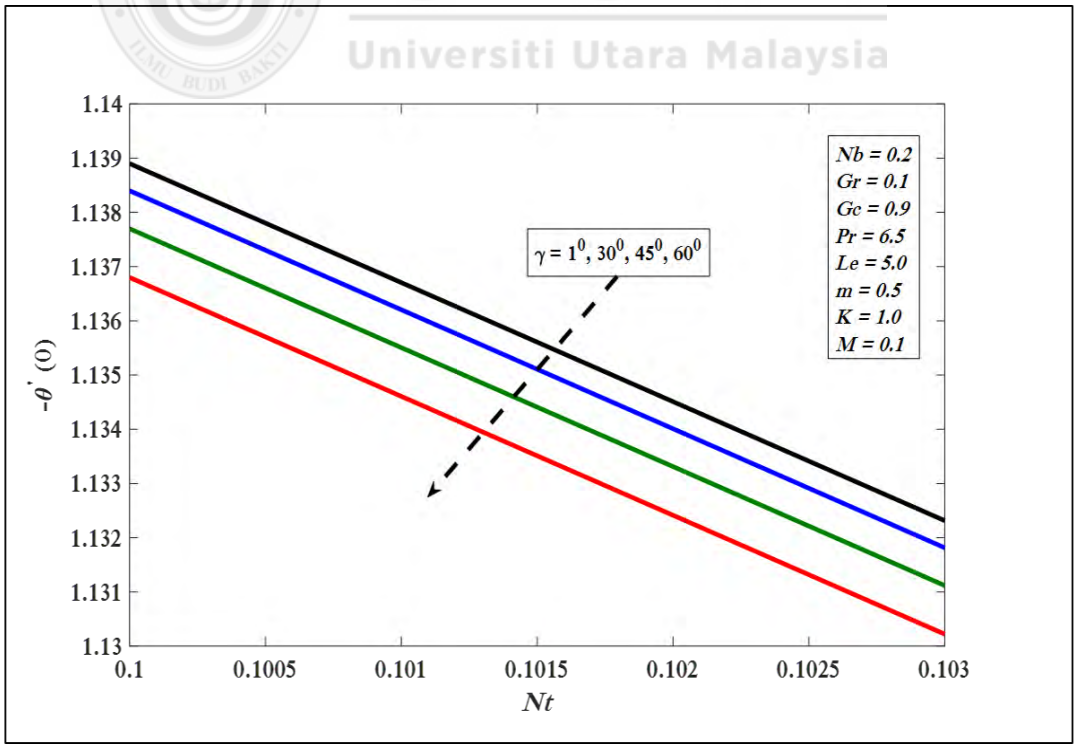

Figure 5.19. $-\theta'(0)$ against Nt for several values of γ

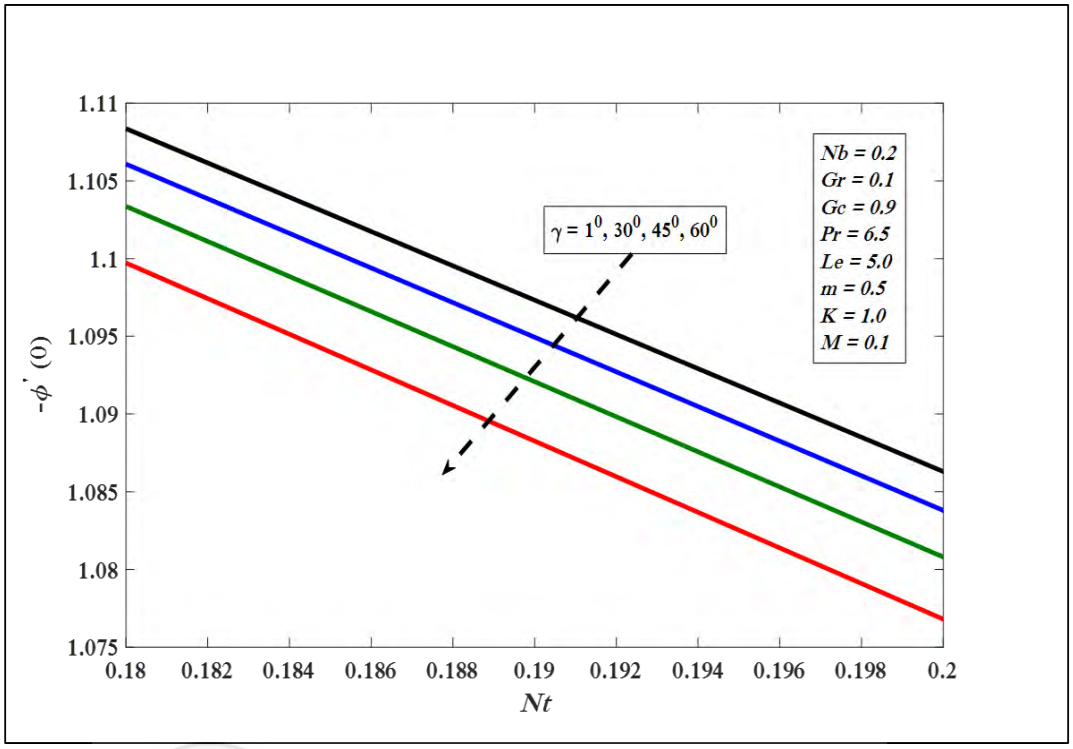

Figure 5.20. $-\phi'(0)$ against *Nt* for several values of γ

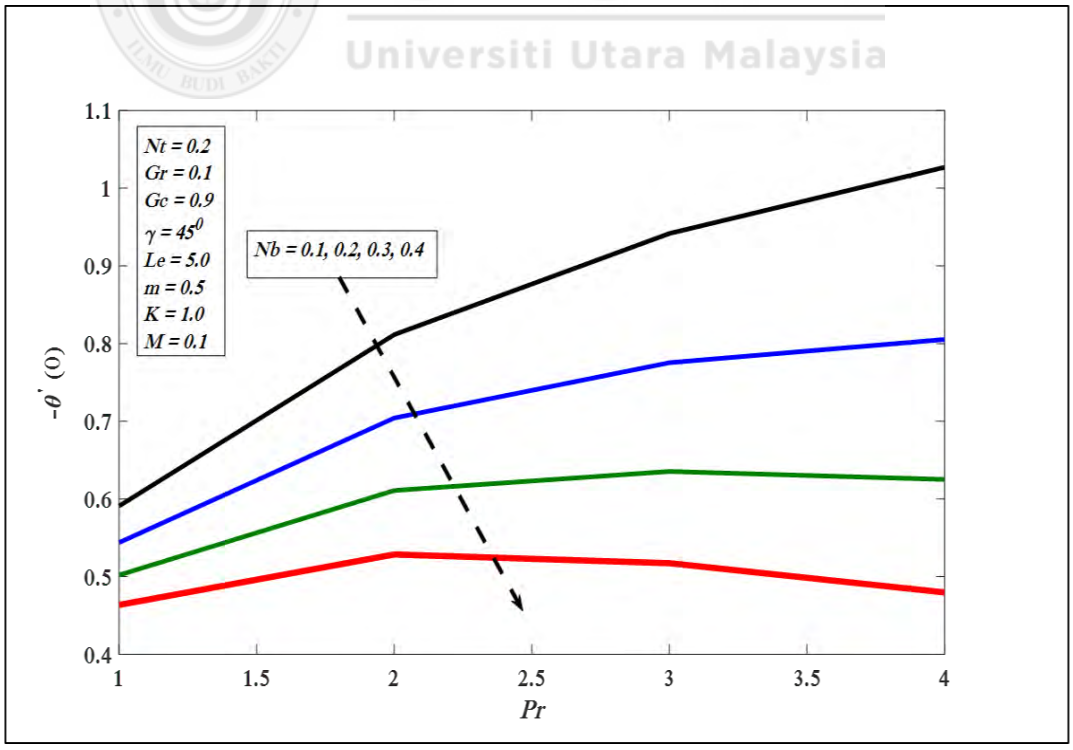

Figure 5.21. $-\theta'(0)$ against *Pr* for several values of *Nb*

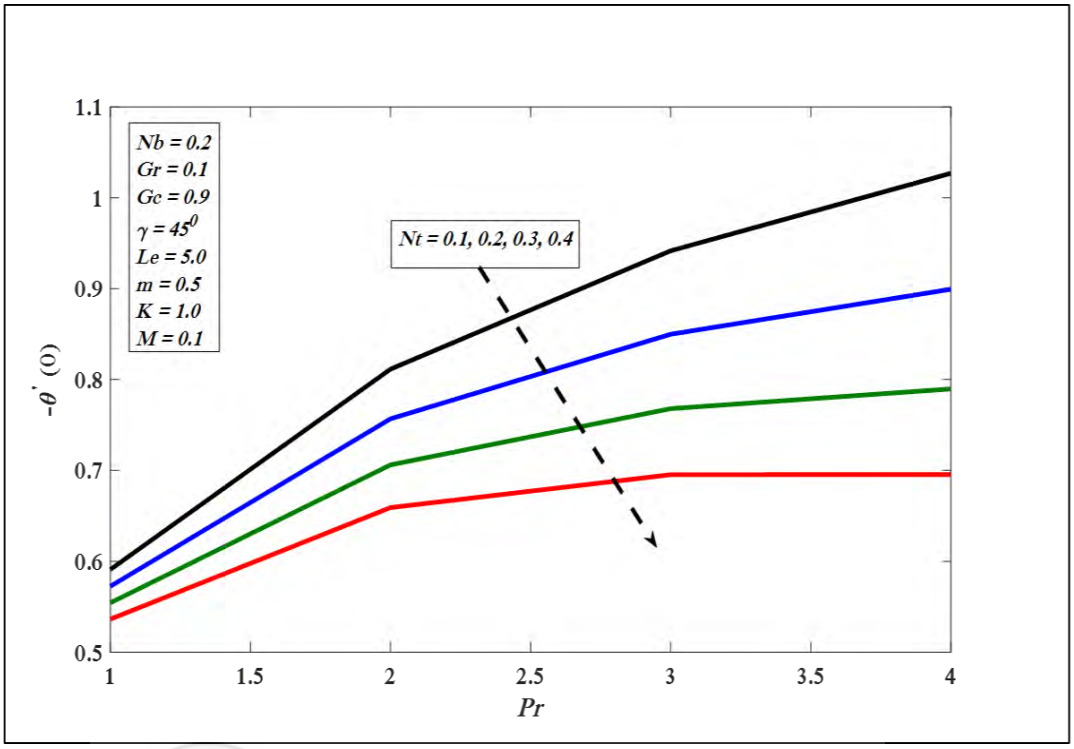

Figure 5.22. $-\theta'(0)$ against *Pr* for several values of *Nt*

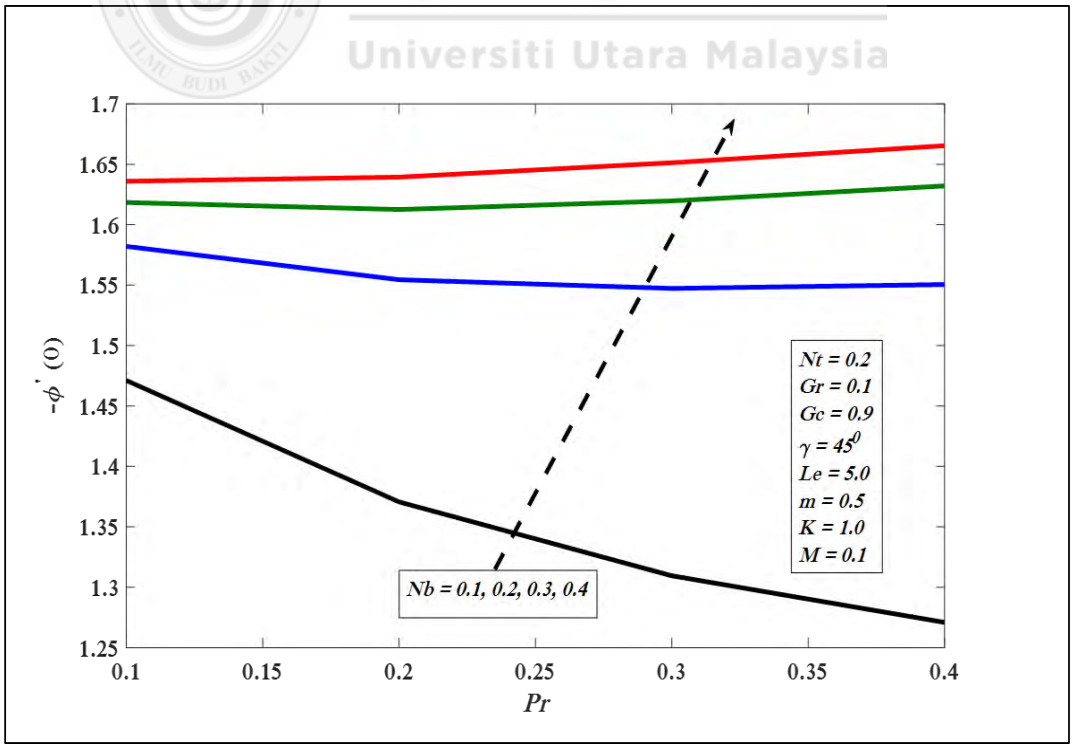

Figure 5.23. $-\phi'(0)$ against *Pr* for several values of *Nb*

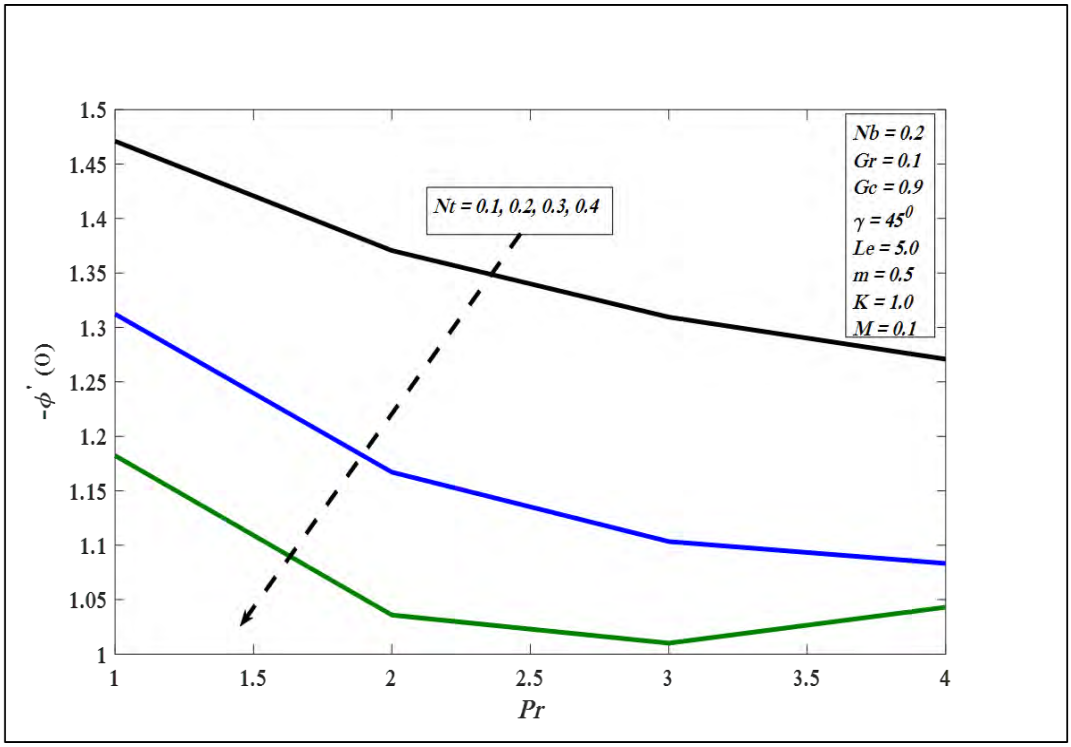

Figure 5.24. $-\phi'(0)$ against *Pr* for several values of *Nt*

5.4 Conclusions

In this problem heat and species transfer of micropolar nanofluid flow generated via nonlinear slanted stretching surface is numerically studied. The magnetic effect is taken in to account. Using appropriate similarity transformations flow equations are transformed in to ordinary differential equations and solved numerically via Keller box scheme. The influence of nonlinear stretching parameter on variation of heat and mass transfer rates along with Skin friction examined in tabulated and graphical forms. From this study we draw the following conclusions:

1. $f'(\eta)$ decreases with the influence of m.

2. Heat and mass fluxes reduces with increase in nonlinear stretching parameter.

3. Skin friction increases with increment in nonlinear stretching parameter.

4. $-\theta'(0)$ and $-\phi'(0)$ reduce by increasing magnetic parameter.

5.5 Governing Equations of Micropolar Nanofluid Boundary Layer Flow With Convective Boundary Conditions

An incompressible flow of micropolar nanofluid for power law inclined surface by incorporating the radiation effect and convective boundary conditions is examined in current problem. This is the extension of the problem investigated in Chapter 6, the radiation effect is taken in account along with existence of convective heating procedure characterized by the heat transfer coefficient h_f which is proportional to x^{-1} and temperature T_f Makinde and Olanrewaju (2010). where $T_f > T_w > T_\infty$.
The governing equations for the this problem are as follows (see Equations 3.59, 3.62 (when $Q_0 = 0$), 3.63 (when $R^* = 0$), 3.89 and 3.90).

$$\frac{\partial u}{\partial x}+\frac{\partial v}{\partial y}=0,$$

$$u\frac{\partial u}{\partial x}+v\frac{\partial u}{\partial y}=\left(\frac{\mu+k_1^*}{\rho}\right)\frac{\partial^2 u}{\partial y^2}+\left(\frac{k_1^*}{\rho}\right)\frac{\partial N^*}{\partial y}+g\beta_t(T-T_\infty)\cos\gamma$$

$$+g\beta_c(C-C_\infty)\cos\gamma-\left(\frac{\sigma B^2(x)}{\rho}\right)u,$$

$$u\frac{\partial N^*}{\partial x}+v\frac{\partial N^*}{\partial y}=\left(\frac{\gamma^*}{j^*\rho}\right)\left(\frac{\partial^2 N^*}{\partial y^2}\right)-\left(\frac{k_1^*}{j^*\rho}\right)\left(2N^*+\frac{\partial u}{\partial y}\right), \tag{5.12}$$

$$u\frac{\partial T}{\partial x}+v\frac{\partial T}{\partial y}=\left(\alpha^*+\frac{16\sigma^* T_\infty^3}{3k^*(\rho c)_f}\right)\frac{\partial^2 T}{\partial y^2}+\tau\left[D_B\frac{\partial C}{\partial y}\frac{\partial T}{\partial y}+\frac{D_T}{T_\infty}\left(\frac{\partial T}{\partial y}\right)^2\right],$$

$$u\frac{\partial C}{\partial x}+v\frac{\partial C}{\partial y}=D_B\frac{\partial^2 C}{\partial y^2}+\frac{D_T}{T_\infty}\frac{\partial^2 T}{\partial y^2}.$$

The subject boundary conditions are

$$u=u_w(x)=ax^m\,,v=0\,,-k\frac{\partial T}{\partial y}=h_f\left(T_f-T\right),N^*=-m_0\frac{\partial u}{\partial y}\,,C=C_w \qquad at \qquad y=0,$$

$$u \to u_\infty(x) = 0\,, v \to 0\,, T \to T_\infty\,, N^* \to 0\,, C \to C_\infty \qquad as \qquad y \to \infty. \quad (5.13)$$

5.5.1 Similarity Transformations

By using the same similarity transformations as defined in Equation (5.4), the non-linear partial differential equations (5.12) are reduce to

$$(1+K)\,f''' + ff'' - \left(\frac{2m}{m+1}\right) f'^2 + Kh' + \frac{2}{m+1}\,(Gr_x\theta + Gc_x\phi)\,cos\gamma - \frac{2}{m+1}\,(M)\,f' = 0,$$

$$\left(1+\frac{K}{2}\right) h'' + fh' - \frac{3m-1}{m+1} hf'^2 - \frac{2k}{m+1}\left(2h + f''\right) = 0,$$

$$(Pr_N)\,\theta'' + f\theta' + Nb\theta'\phi' + Nt\theta'^2 = 0, \qquad (5.14)$$

$$\phi'' + Lef\phi' + Nt_b\theta'' = 0,$$

where

$Pr_N = \frac{1}{Pr}\left(1+\frac{4}{3}N\right)$. Here, $N = \frac{4\sigma^* T_\infty^3}{\alpha k^*}$ denotes radiation parameter (Anwar, 2013), other involved flow parameters are same as defined in previous chapter.

The boundary settings are transformed to

$$f(\eta) = 0,\ f'(\eta) = 1,\ h(\eta) = 0, \theta'(\eta) = -\gamma_1\sqrt{\frac{2}{m+1}}\left(1-\theta(0)\right), \phi(\eta) = 1\ at\ \eta = 0,$$

$$f'(\eta) \to 0,\ h(\eta) \to 0, \theta(\eta) \to 0, \phi(\eta) \to 0\ \ at\ \ \eta \to \infty, \qquad (5.15)$$

where $\gamma = \frac{n'}{kRe_x{}^{\frac{1}{2}}}$ is called Biot number i.e the convective factor. This problem reduces to the constant wall temperature problem of the micropolar nanofluid as discussed in previous problem in Section 5.2. On the other hand, Equations (5.14) and (5.15)

reduces to Equations (5.5) and (5.9) by taking $N = 0$ and $\gamma_1 \to \infty$. In the present study, the quantities including the local Nusselt number $-\theta'(0)$ and the local Sherwood number $-\phi'(0)$ demarcated in similar way as given in Equation (5.10), except the term $q_w = -\left[k + \frac{4\sigma^* T_\infty^3}{3k^*}\right](\frac{\partial T}{\partial y})_{y=0}$ in $-\theta'(0)$ which can be written as

$$-\theta'(0) = \frac{Nu}{\left(1 + \frac{4}{3}N\right)\sqrt{Re_x \frac{m+1}{2}}}. \tag{5.16}$$

5.6 Results and Discussion

This portion of problem is presented numerical consequences of Equations (5.14) by using boundary settings (5.15) found by employing Keller-box technique. The complete numerical procedure used for such problem is explained in Appendix A. For numerical result of physical parameters of our concern including Brownian motion parameter Nb, thermophoresis parameter Nt, magnetic factor M, local Grashof number Gr, local modified Grashof number Gc, inclination factor γ, Prandtl number Pr, Lewis number Le, radiation effect N, Biot number γ_1 and material factor K, Figures 5.25 to 5.38 are organized. In the deficiency of radiation effect N, local Grashof number Gr, local modified Grashof number Gc, magnetic factor M, and material factor K with $\gamma = 90^0$ and $\gamma_1 \to \infty$ outcomes of reduced Nusselt number $-\theta'(0)$, reduced Sherwood number $-\phi'(0)$ matched with outcomes of Khan and Pop (2010). The consequences established good settlement.

The effects of $-\theta'(0)$, $-\phi'(0)$ and $C_{fx}(0)$ by changing values of involved parameters $Nb, Nt, M, K, Gr, Gc, \gamma, m, Le, \gamma_1, N$, and Pr are shown in Table 5.2. Table 5.2 clearly showed that $-\theta'(0)$ declines for growing the values of Nb, Nt, M, Le, N, γ, and increased by enhancing numerical values of Gr, Pr, γ_1, m, Gc, and K. Moreover, it is

perceived that $-\phi'(0)$ enhanced with larger values of Nb, Gr, Gc, Le, K, N, and drops for bigger values of M, Nt, Pr, γ_1, m, and γ. Meanwhile, $C_{fx}(0)$ rises with the increase in $Nb, N, Nt, Le, M, K, \gamma, m, \gamma_1$, and diminishes for higher values of Gr, Pr and Gc.

Table 5.2
Variations of local Nusselt number $-\theta'(0)$, local Sherwood number $-\phi'(0)$ and skin friction coefficient $C_{fx}(0)$.

Nb	Nt	Pr	Le	M	K	Gr	Gc	N	γ_1	m	γ	$-\theta'(0)$	$-\phi'(0)$	$C_{fx}(0)$
0.1	0.1	7.0	5.0	0.1	1.0	0.1	0.9	1.0	0.1	0.5	45^0	0.0979	1.6151	1.0246
0.5	0.1	7.0	5.0	0.1	1.0	0.1	0.9	1.0	0.1	0.5	45^0	0.0440	1.6555	1.0312
0.1	**0.5**	7.0	5.0	0.1	1.0	0.1	0.9	1.0	0.1	0.5	45^0	0.0916	1.4976	1.1218
0.1	0.1	**10**	5.0	0.1	1.0	0.1	0.9	1.0	0.1	0.5	45^0	0.1128	1.6066	1.0241
0.1	0.1	7.0	**10**	0.1	1.0	0.1	0.9	1.0	0.1	0.5	45^0	0.0942	2.3636	1.0981
0.1	0.1	7.0	5.0	**0.5**	1.0	0.1	0.9	1.0	0.1	0.5	45^0	0.0952	1.5788	1.3632
0.1	0.1	7.0	5.0	0.1	**2.0**	0.1	0.9	1.0	0.1	0.5	45^0	0.0998	1.6375	1.2500
0.1	0.1	7.0	5.0	0.1	1.0	**1.0**	0.9	1.0	0.1	0.5	45^0	0.0982	1.6177	0.9920
0.1	0.1	7.0	5.0	0.1	1.0	0.1	**2.0**	1.0	0.1	0.5	45^0	0.0996	1.6371	0.7016
0.1	0.1	7.0	5.0	0.1	1.0	0.1	0.9	**2.0**	0.1	0.5	45^0	0.0800	1.6248	1.0250
0.1	0.1	7.0	5.0	0.1	1.0	0.1	0.9	1.0	**0.5**	0.5	45^0	0.3054	1.6096	1.1120
0.1	0.1	7.0	5.0	0.1	1.0	0.1	0.9	1.0	0.1	**5.0**	45^0	0.0946	1.5695	1.6222
0.1	0.1	7.0	5.0	0.1	1.0	0.1	0.9	0.1	0.1	0.5	$\mathbf{60}^0$	0.0966	1.5953	1.3005

Figure 5.25 portrayed the effect of nonlinear stretching factor m on velocity profile. The velocity profile falls by improving m. Physically, the boundary layer thickness reduces by improving factor m (Abbas and Hayat, 2011). Moreover, Figure 5.26 pointed out that $\theta(\eta)$ upsurged with the growth of factor M. Similarly, $\theta(\eta)$ in Figure 5.27 presents a direct relation with nonlinear stretching factor m and matched with the result of Vajravelu (2001). In addition, Figure 5.28 presents an increment in γ_1 that increases $\theta(\eta)$. Further, $\theta(\eta)$ enhances with the increase in N as can be seen in Figure 5.29.

Physically, the thermal diffusivity declines by improving factor N and it make heat diffusion far from the heat surface more deliberately and as a result enhance the temperature gradient at the wall. Whereas, $\theta(\eta)$ diminishes with the enhancement of

Pr as presented in Figure 5.30. The growth of *Pr* results for higher surface temperature to penetrate into quiescent fluid. In addition, the viscosity of the fluid play a significant role in this penetration since enhancement in *Pr* diminishes the thermal boundary layer thickness and heat exchange.

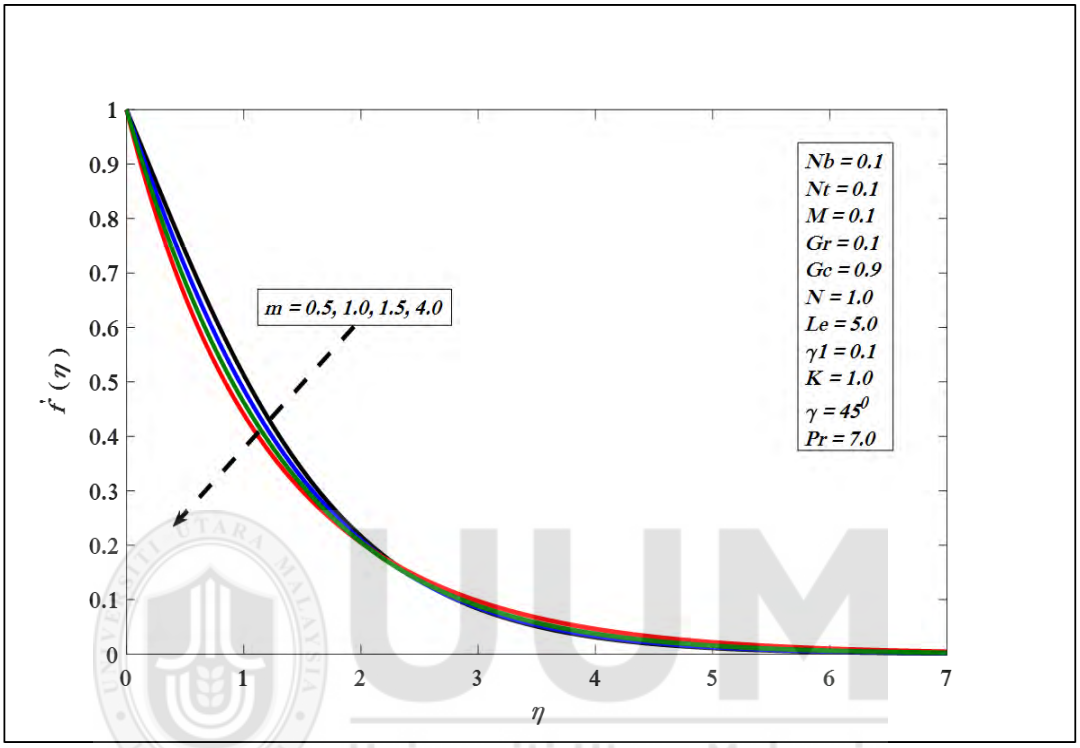

Figure 5.25. Variations in velocity profile for several values of *m*.

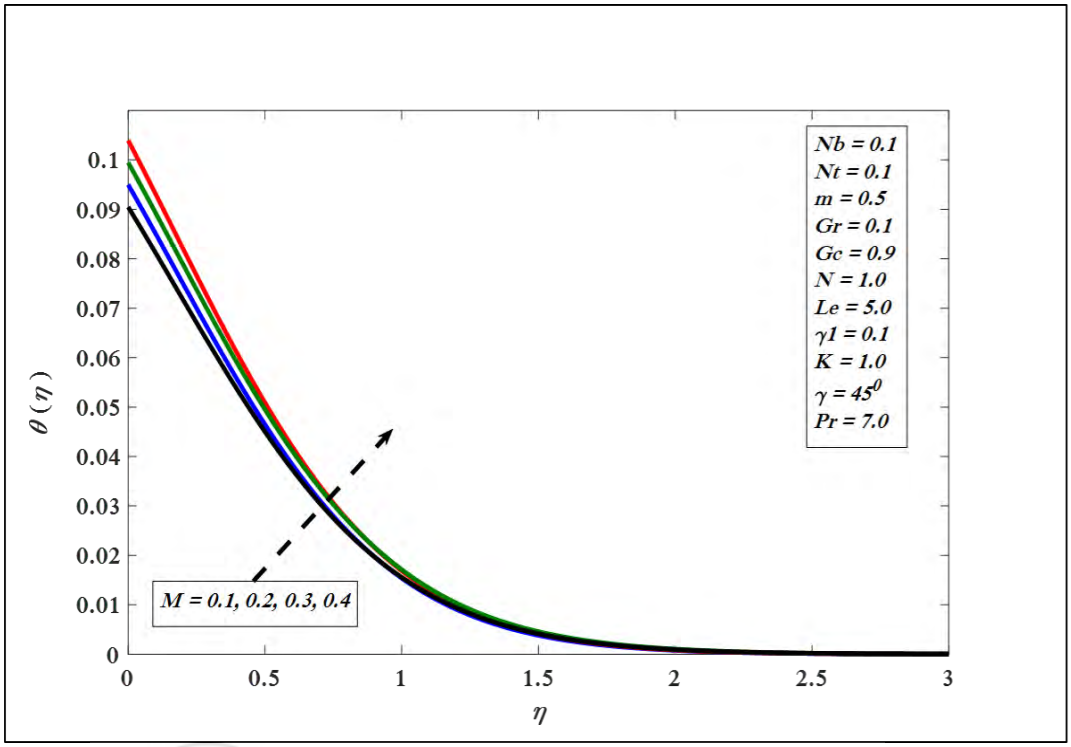

Figure 5.26. Variations in temperature profile for several values of M.

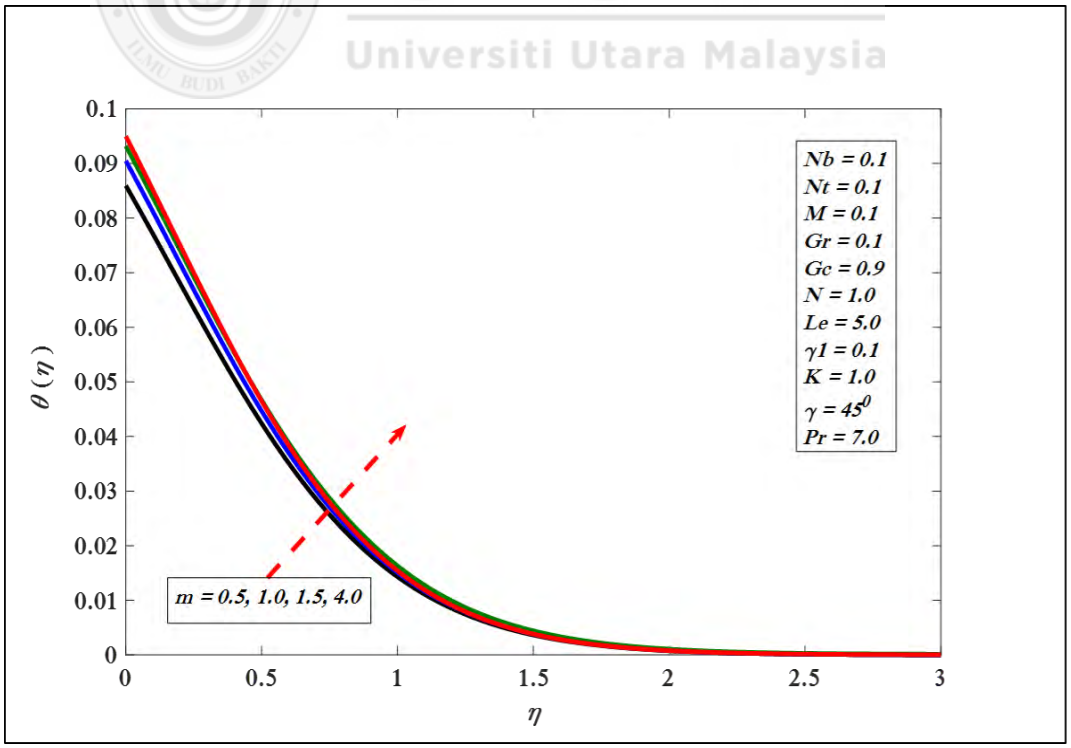

Figure 5.27. Variations in temperature profile for several values of m.

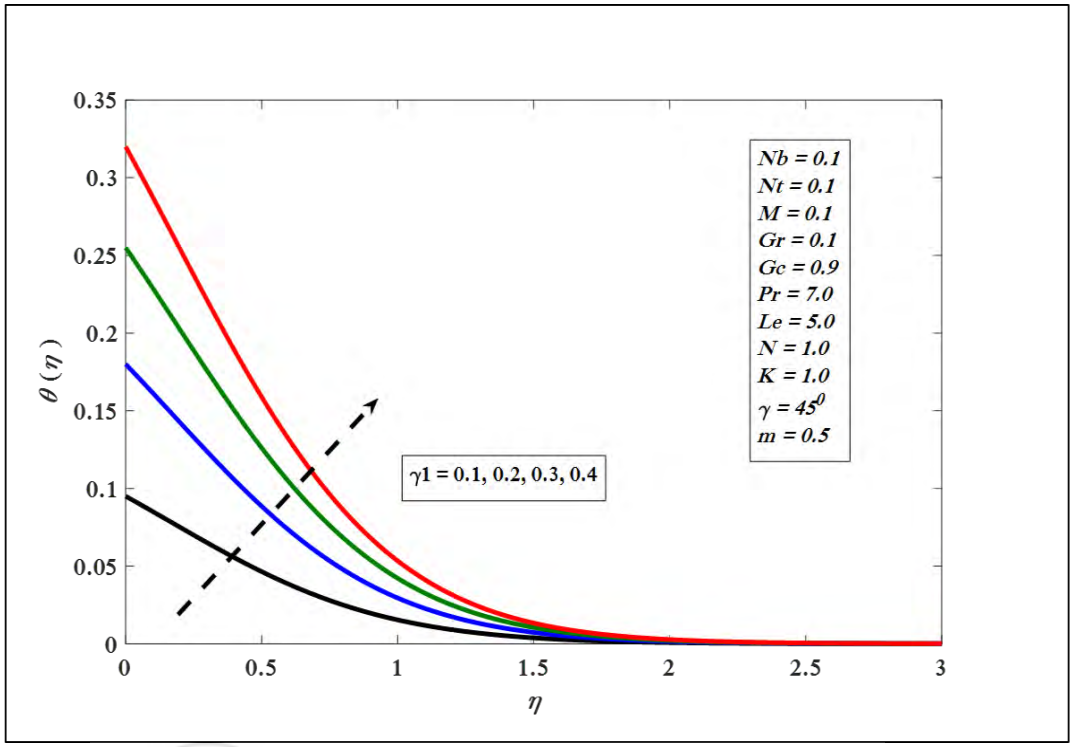

Figure 5.28. Variations in temperature profile for several values of γ_1.

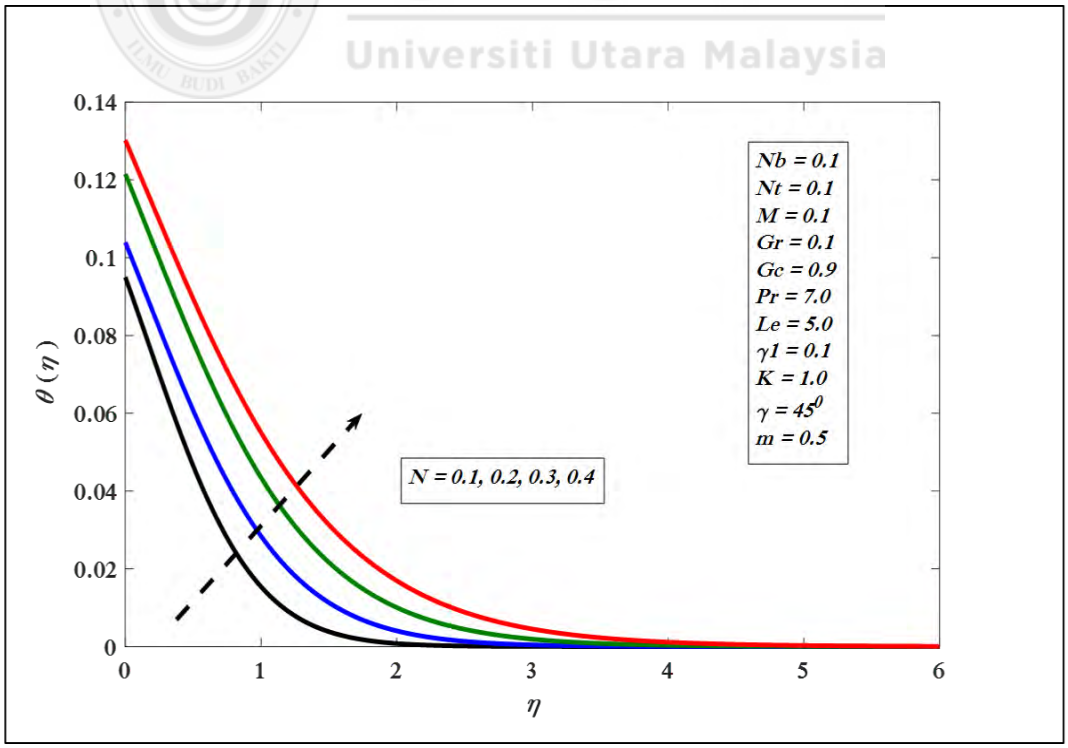

Figure 5.29. Variations in temperature profile for several values of N.

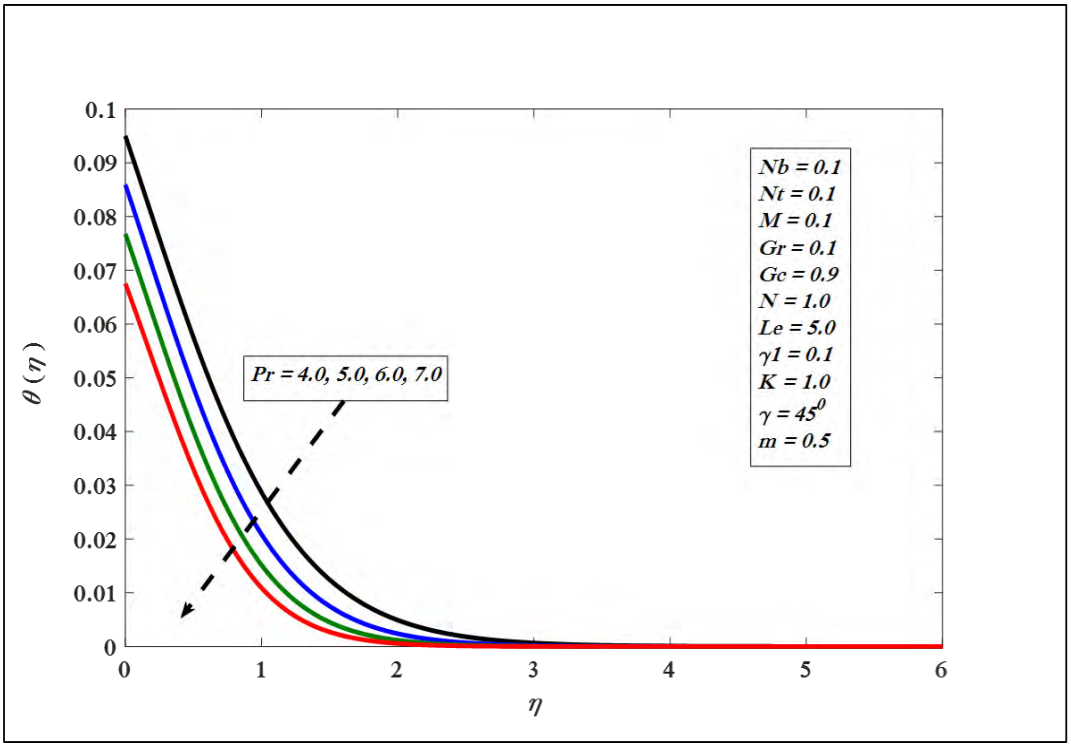

Figure 5.30. Variations in temperature profile for several values of *Pr*.

Figures 5.31 and 5.32 exhibit the influences of factors N, and γ_1 on $\phi(\eta)$, respectively. Figure 5.31 shows that N reveals an inverse relation with $\phi(\eta)$. Whereas, γ_1 presents a direct relation with $\phi(\eta)$ (see Figure 5.32). The impact of $-\theta'(0)$ and $-\phi'(0)$ against involved factors such as N, γ_1, Nb and Nt exhibited in Figures 5.33 to 5.38. Figure 5.33 shows that $-\theta'(0)$ versus N enhances with the increase of Biot number γ_1. On the other hand, an opposite impact reflects in Figure 5.34 in the case of $-\phi'(0)$ against N with the increment in factor γ_1. Moreover, $-\theta'(0)$ versus γ_1 diminishes for higher magnitudes of Nb shown in Figure 5.35. Besides, in Figure 5.36, the growth of Nb and γ_1 enhances $-\phi'(0)$. Whereas, from Figures 5.37 and 5.38, it is clearly observed that $-\theta'(0)$ and $-\phi'(0)$ decreases against enhancement in Nt and γ_1.

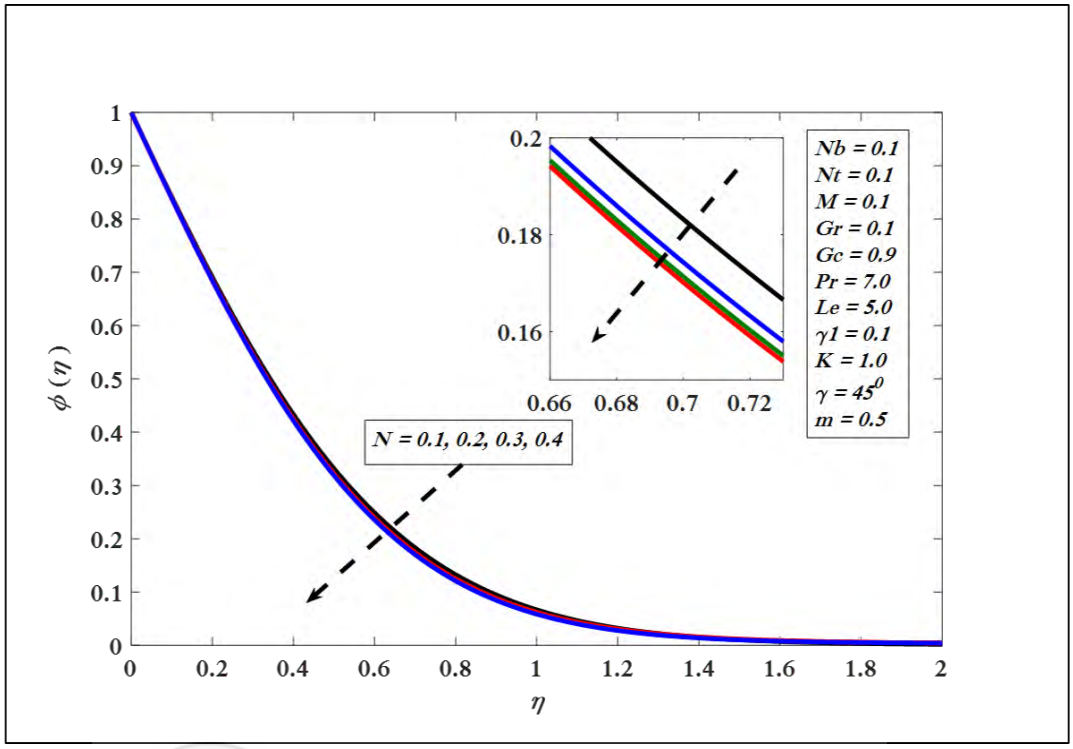

Figure 5.31. Variations in concentration profile for several values of N.

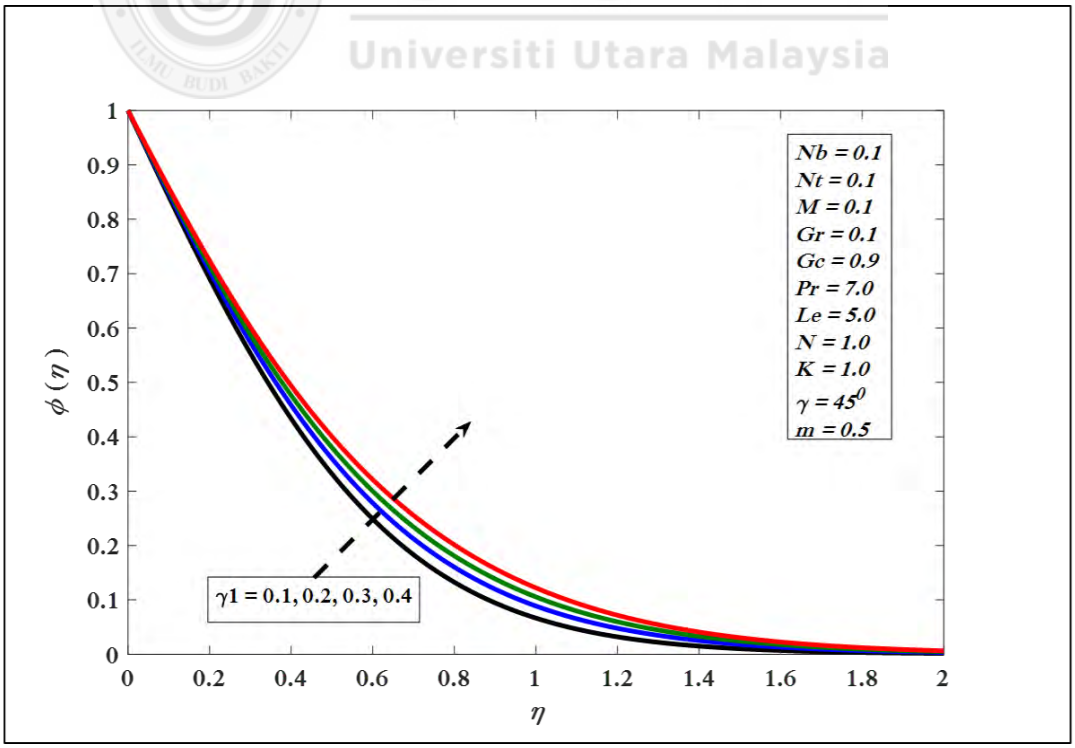

Figure 5.32. Variations in concentration profile for several values of γ_1.

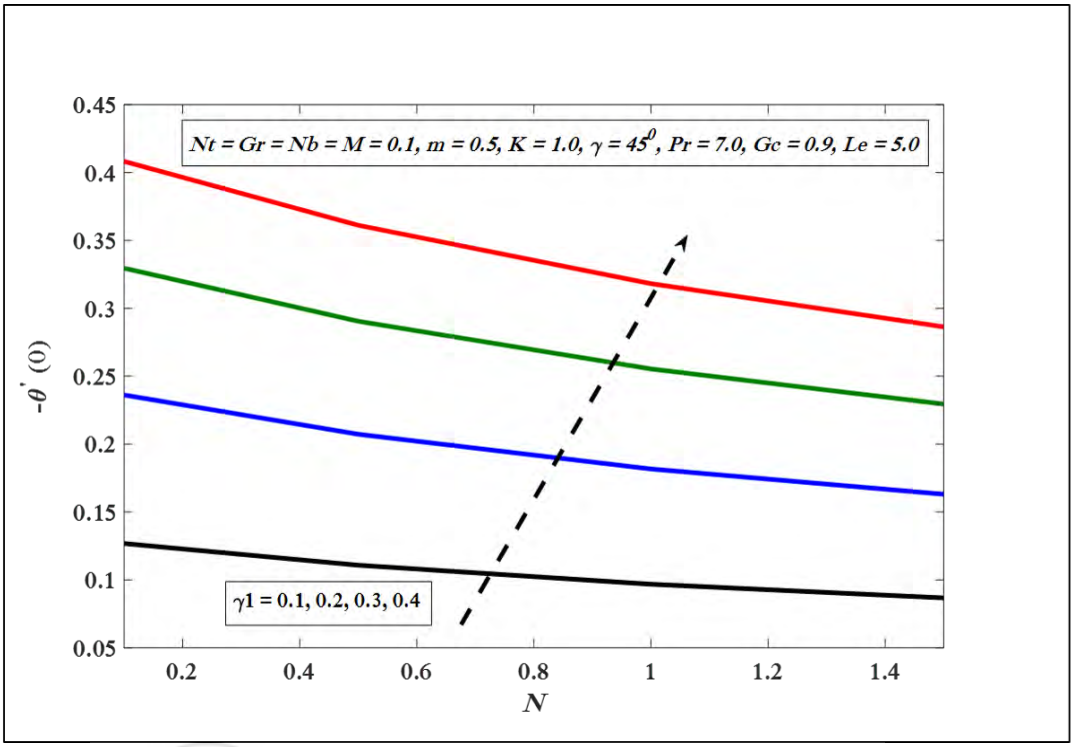

Figure 5.33. $-\theta'(0)$ against N for several values of γ_1.

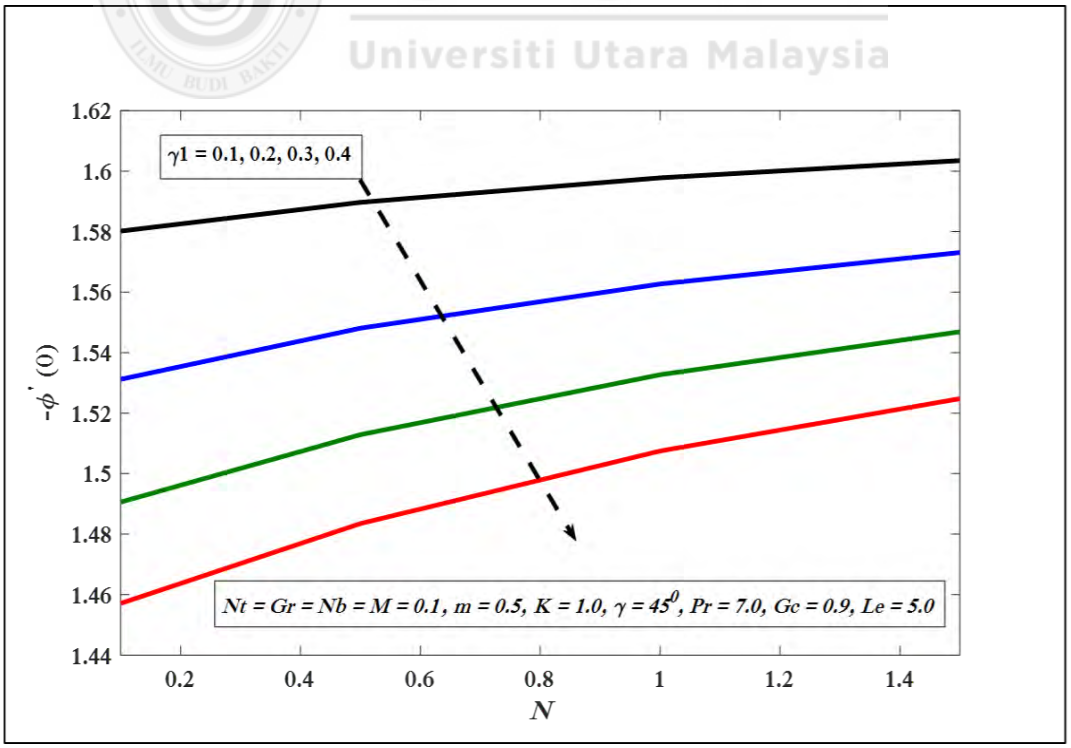

Figure 5.34. $-\phi'(0)$ against N for several values of γ_1.

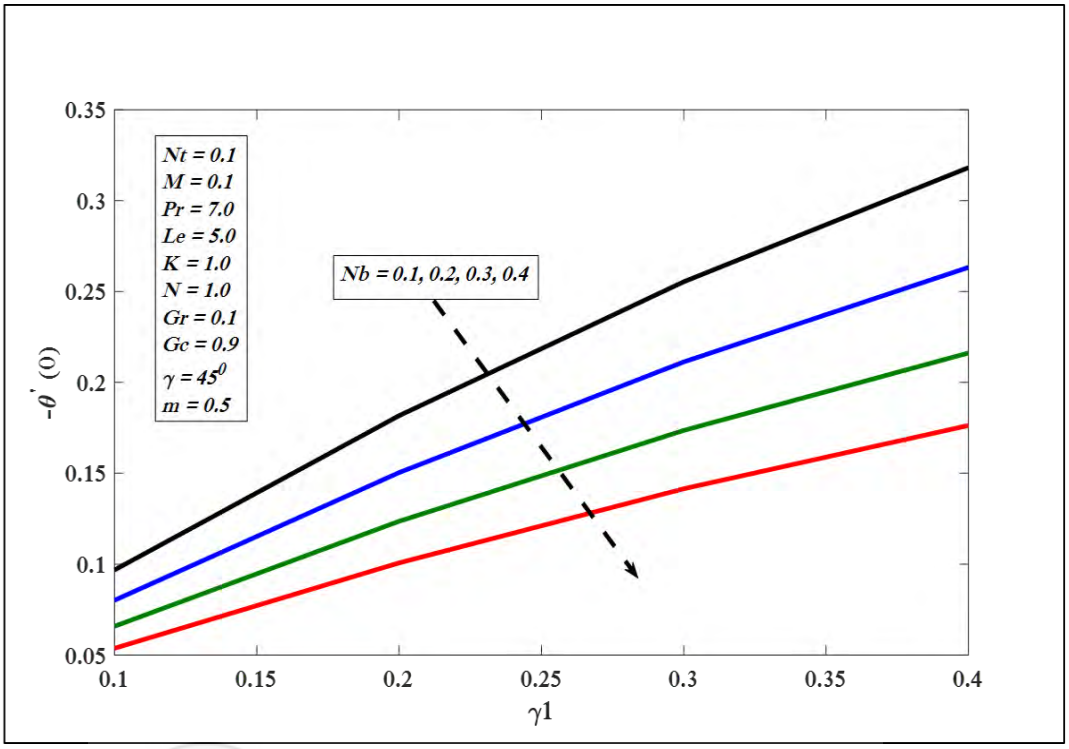

Figure 5.35. $-\theta'(0)$ against γ_1 for several values of Nb.

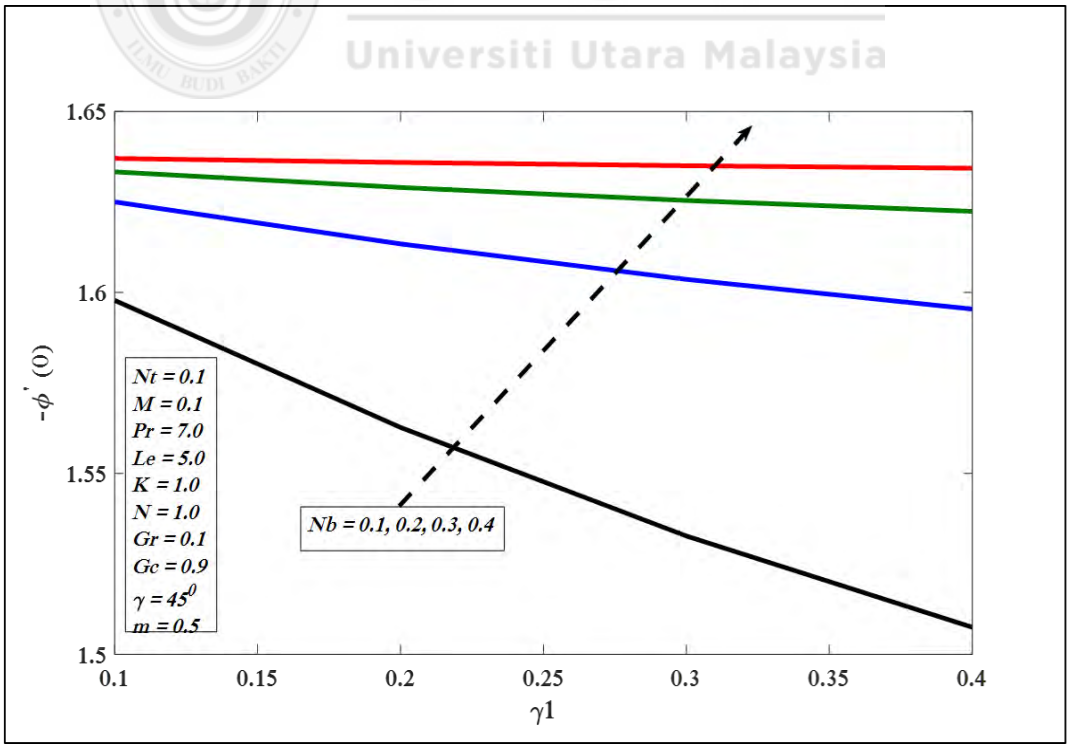

Figure 5.36. $-\phi'(0)$ against γ_1 for several values of Nb.

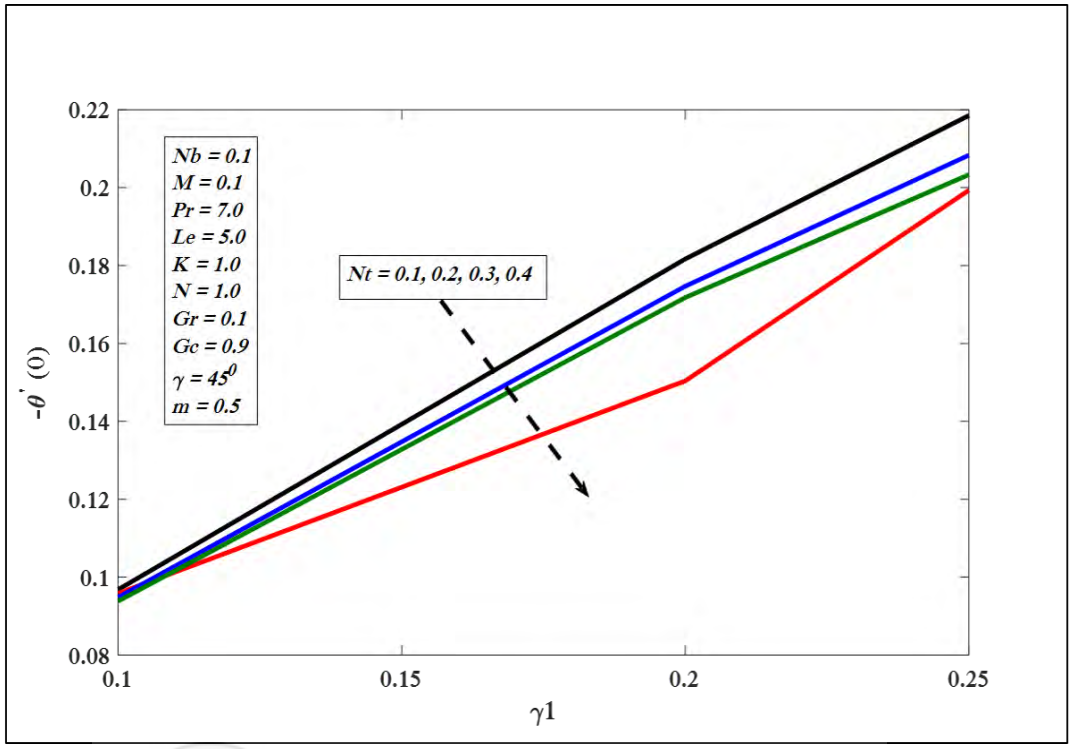

Figure 5.37. $-\theta'(0)$ against γ_1 for several values of Nt.

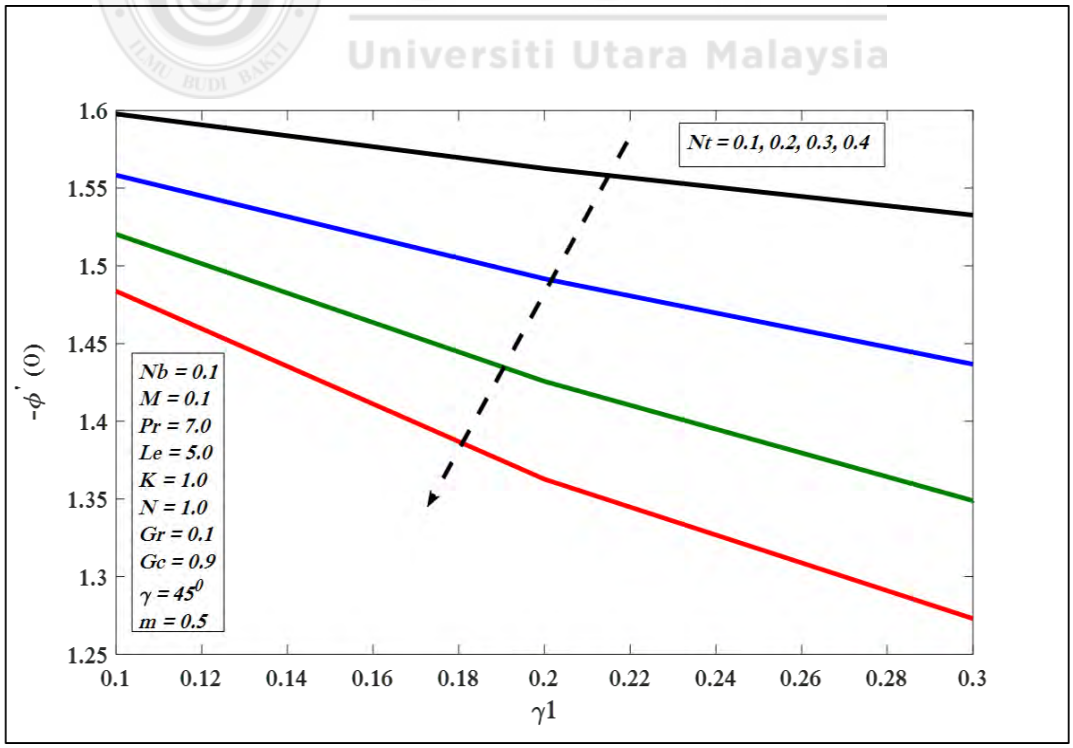

Figure 5.38. $-\phi'(0)$ against γ_1 for several values of Nt.

5.7 Conclusions

In present problem the flow of micropolar type nanofluid by considering power law slanted geometry is studied numerically via Keller box method. In this study convective boundary conditions as well as thermal radiations are considered. Brownian motion and thermophoretic impacts on heat and mass transfer rates are examined numerically and exhibited via graphs. The variations in $-\phi'(0)$ and $-\theta'(0)$ against radiation and convective parameters are presented. The core finding of the problem are given by:

1. Temperature and concentartion profiles increase by enhancing Biot number.
2. $-\theta'(0)$ against radiation and convective parameters show direct relation.
3. $-\phi'(0)$ reduces with increase in N and convective parameters.

CHAPTER SIX

CASSON NANOFLUID BOUNDARY LAYER FLOW OVER A LINEAR INCLINED STRETCHING SURFACE

6.1 Introduction

In this problem, the magnetic field impact is taken into account. The primary interest of this part is to study Casson nanofluid for linear inclined geometry. The magnetic and thermophoretic effects are considered. For numerical simulation we will convert the governing equation with y employing appropriate similarity transformations in to coupled nonlinear ODE's (ordinary differential equations). Then these equation solved by employing Keller-box scheme. For the authentication of our outcomes we are matched our numerical outcome with already published article of Khan and Pop (2010) and found to be a good agreement.

6.2 Governing Equations

In this study, steady two dimensional boundary layer flow of Casson nano fluid over a slanted surface at angle γ is considered. The stretching and free stream velocities are supposed to be of the forms $u_w(x) = ax$ and $u_\infty(x) = 0$ respectively. An external transverse magnetic field is acted at right angle of the slanted surface. Thermophoretic impacts are considered. For flow geometry see Figure 3.3.

The governing boundary layer equations for the present problem are as follows (see Equations 3.59, 3.62 (when $Q_0 = \sigma^* = 0$), 3.63 and (when $R^* = 0$) 3.100).

$$\frac{\partial u}{\partial x} + \frac{\partial v}{\partial y} = 0,$$

$$u\frac{\partial u}{\partial x} + v\frac{\partial u}{\partial y} = \left(1 + \frac{1}{\beta}\right)\nu\frac{\partial^2 u}{\partial y^2} + g\beta_t(T - T_\infty)\cos\gamma$$

$$+g\beta_c(C - C_\infty)\cos\gamma - \left(\frac{\sigma {B_0}^2}{\rho}\right)u,$$

$$u\frac{\partial T}{\partial x} + v\frac{\partial T}{\partial y} = \alpha\frac{\partial^2 T}{\partial y^2} + \tau\left[D_B\ \frac{\partial C}{\partial y}\frac{\partial T}{\partial y} + \frac{D_T}{T_\infty}\left(\frac{\partial T}{\partial y}\right)^2\right], \tag{6.1}$$

$$u\frac{\partial C}{\partial x} + v\frac{\partial C}{\partial y} = D_B\frac{\partial^2 C}{\partial y^2} + \frac{D_T}{T_\infty}\frac{\partial^2 T}{\partial y^2},$$

subjected to the boundary conditions

$$u = u_w(x) = ax\ , v = 0\ , T = T_w\ , C = C_w \qquad at \qquad y = 0,$$

$$u \to u_\infty(x) = 0\ , v \to 0\ , T \to T_\infty\ , C \to C_\infty \qquad as \qquad y \to \infty. \tag{6.2}$$

6.2.1 Similarity Transformations

In this section, nonlinear partial differential equations (6.1) are reduced into nonlinear ordinary differential equations.

The stream function use for this procedure is demarcated by

$$u = \frac{\partial \psi}{\partial y}\ , \quad v = -\frac{\partial \psi}{\partial x}, \tag{6.3}$$

The similarity transformations are characterized as

$$u = axf'(\eta), v = -\sqrt{av}f(\eta), \eta = y\sqrt{\frac{a}{v}},$$

$$\theta(\eta) = \frac{T - T_\infty}{T_w - T_\infty}, \ \phi(\eta) = \frac{C \ - C_\infty}{C_w \ - C_\infty}. \tag{6.4}$$

By using Equation (6.4), system of equations (6.1) is transformed in to following equations

$$\left(1 + \frac{1}{\beta}\right) f''' + ff'' - f'^2 + (Gr_x\theta + Gc_x\phi)\cos\gamma - (M) f' = 0,$$

$$\left(\frac{1}{\Pr}\right) \theta'' + f\theta' + Nb\theta'\phi' + Nt\theta'^2 = 0, \tag{6.5}$$

$$\phi'' + Lef\phi' + Nt_b\theta'' = 0.$$

Here, involved flow parameters are defined same as in Chapter 3.

The corresponding boundary conditions are transformed to

$$f(\eta) = 0, \ f'(\eta) = 1, \ \theta(\eta) = 1, \phi(\eta) = 1 \ at \ \eta = 0,$$

$$f'(\eta) \to 0, \theta(\eta) \to 0, \phi(\eta) \to 0 \ \ at \ \ \eta \to \infty. \tag{6.6}$$

The physical quantities of interest i.e. skin friction C_f, Nusselt number Nu and Sherwood number Sh are defined as

$$C_f = \frac{\tau_w}{\rho \ u_w^2}, \ Nu = \frac{x \ q_w}{k(T_w - T_\infty)}, \ Sh = \frac{x \ q_m}{D_B(C_w - C_\infty)}, \tag{6.7}$$

where $\tau_w = \mu(1 + \frac{1}{\beta})\frac{\partial u}{\partial y}$, $q_w = -k\frac{\partial T}{\partial y}$, $q_m = -D_B\frac{\partial C}{\partial y}$ at $y = 0$ represent shear stress, energy and mass rates respectively. The mathematical representation of the coefficient of skin friction $C_{fx}(0) = (1 + \frac{1}{\beta})f''(0)$, local Nusselt number $-\theta'(0)$ and local

Sherwood number $-\phi'(0)$ demarcated as

$$C_{fx}(0) = C_f\sqrt{Re_x}, -\theta'(0) = \frac{Nu}{\sqrt{Re_x}}, -\phi'(0) = \frac{Sh}{\sqrt{Re_x}}, \tag{6.8}$$

where, $Re_x = \frac{u_w(x)\ x}{\nu}$ means local Reynold's number.

6.3 Results and Discussion

This unit enclosed the discussions and elucidations of our results in graphical and tabular form. The Keller-box method is applied to solve the converted nonlinear ordinary differential equation (6.5) with boundary conditions (6.6). The numerical result of our concern physical factors including Brownian motion constraint Nb, thermophoresis factor Nt, Casson factor β, magnetic factor M, local Grashof number Gr, local modified Grashof number Gc, inclination parameter γ, Prandtl number Pr and Lewis number Le are exhibited by tables and figures. In the lack of Gr, Gc, M, and $Le = Pr = 10$ with $\gamma = 90^0$ against Casson parameter $\beta \to \infty$, the results for $-\theta'(0)$ and $-\phi'(0)$ are matched with the existing outcomes (see Table 3.1). The outcomes established a good settlement. The effects of reduced Nusselt number$-\theta'(0)$, reduced Sherwood number $-\phi'(0)$ and skin friction coefficient $C_{fx}(0)$ versus $Nb, Nt, \beta, M, K, Gr, Gc, \gamma, Pr$ and Le are mentioned in Table 6.1.

It is observed that $-\theta'(0)$ declines on enhancing $Nb, Gr, Le, M, Nt, \gamma$ and increases with the growing of Pr, β, and Gc. Besides, $-\phi'(0)$ upturns by growing $Pr, Nt, Nb, Le, \beta, Gc$ and decreases on the increase of M, Gr, and γ. While $C_{fx}(0)$ rises with the growth of Nb, Le, M, Gr, and γ. Further, $C_{fx}(0)$ decreases by enhancing Gc, β, Nt and Pr.

Table 6.1
Variations of local Nusselt number $-\theta'(0)$*, local Sherwood number* $-\phi'(0)$ *and skin friction coefficient* $C_{fx}(0)$.

Nb	*Nt*	*Pr*	*Le*	*M*	*Gr*	*Gc*	β	γ	$-\theta'(0)$	$-\phi'(0)$	$C_{fx}(0)$
0.1	0.1	6.5	5.0	0.1	0.1	0.9	2.0	45^0	1.1198	1.1807	0.6673
0.5	0.1	6.5	5.0	0.1	0.1	0.9	2.0	45^0	0.2304	1.6654	0.7030
0.1	**0.5**	6.5	5.0	0.1	0.1	0.9	2.0	45^0	0.5288	1.6034	0.5512
0.1	0.1	**10.0**	5.0	0.1	0.1	0.9	2.0	45^0	1.1696	1.1847	0.6651
0.1	0.1	6.5	**10.0**	0.1	0.1	0.9	2.0	45^0	0.9926	2.1325	0.7189
0.1	0.1	6.5	5.0	**0.5**	0.1	0.9	2.0	45^0	1.1050	1.1381	0.8121
0.1	0.1	6.5	5.0	0.1	**1.0**	1.0	5.0	45^0	1.1163	1.1691	0.6982
0.1	0.1	6.5	5.0	0.1	0.1	**2.0**	2.0	45^0	1.1244	1.1898	0.6082
0.1	0.1	6.5	5.0	0.1	1.0	1.0	**3.0**	45^0	1.1374	1.2197	0.4659
0.1	0.1	6.5	5.0	0.1	1.0	1.0	2.0	$\mathbf{60}^0$	1.1148	1.1696	0.7216

From Figure 6.1, we infer that velocity profile decreases by increasing inclination. This can be ascribed to the circumstance that the angle of inclination drops the result of the buoyancy force because of thermal diffusion by an influence of $Cos\gamma$. Accordingly, the driving force to the fluid declines due to the drop of fluid's velocity. On the other hand, an opposite impact of γ can be observed in the case of $\theta(\eta)$ and $\phi(\eta)$ in Figures 6.2 and 6.3. The effect of Casson parameter on velocity parameter is presented in Figure 6.4. It is observed that for different values of Casson parameter, velocity profile decreases. The reason behind this behavior is that by increasing the values of Casson parameter β increases the fluid viscosity, i.e reducing the yield stress. Therefore, the momentum boundary layer thickness reduces. Figures 6.5 and 6.6 indicate that $\theta(\eta)$ and $\phi(\eta)$ increases by enhancing the factor β.

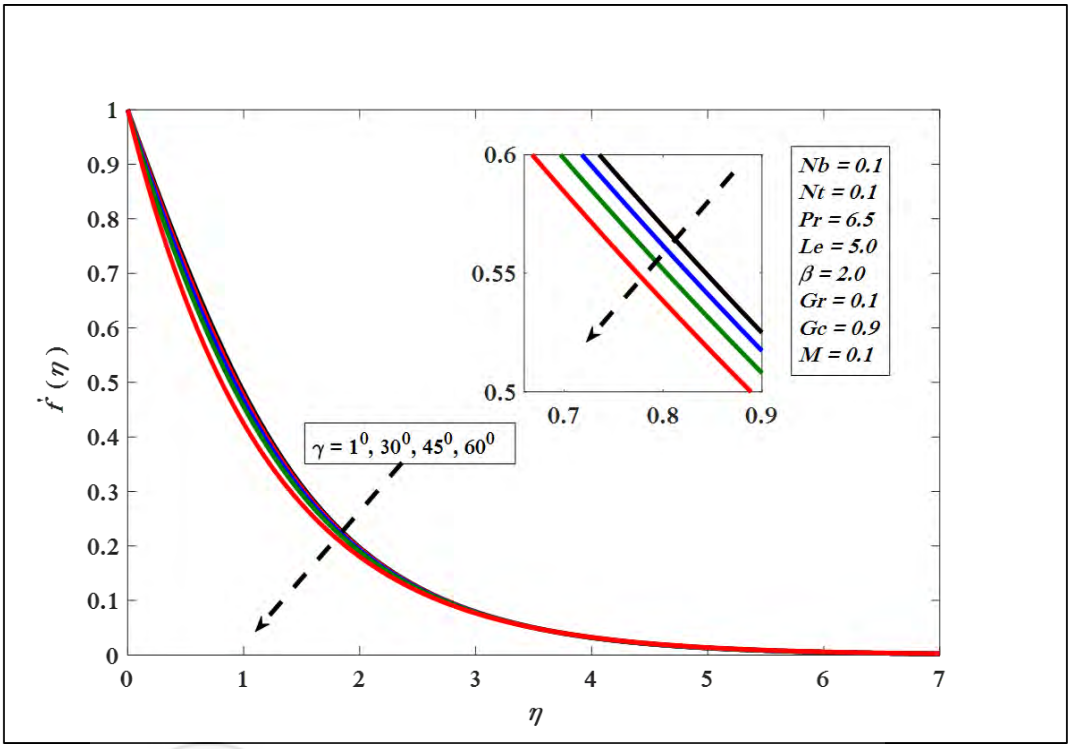

Figure 6.1. Variations in velocity profile for several values of γ.

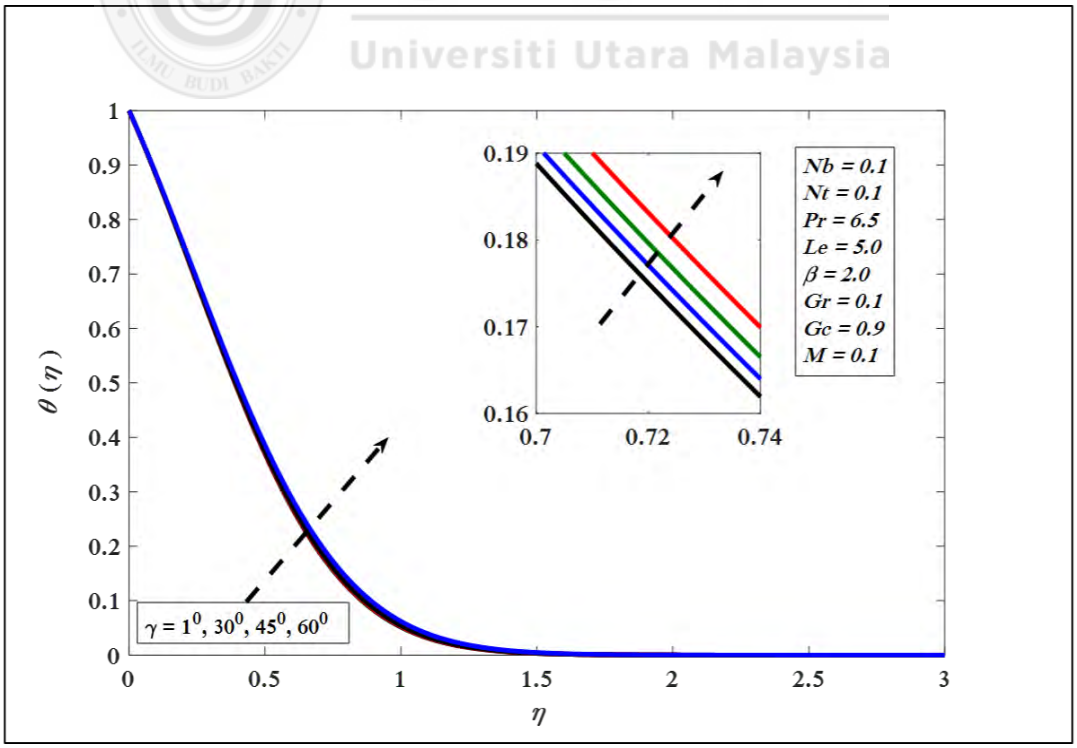

Figure 6.2. Variations in temperature profile for several values of γ

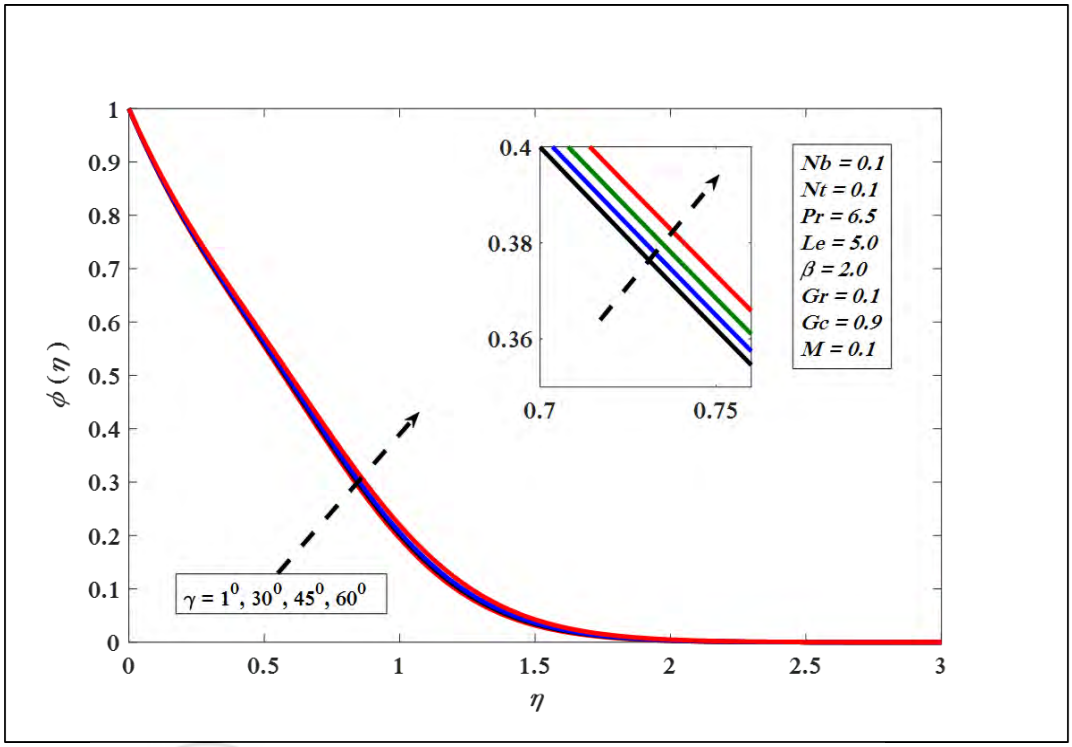

Figure 6.3. Variations in concentration profile for several values of γ.

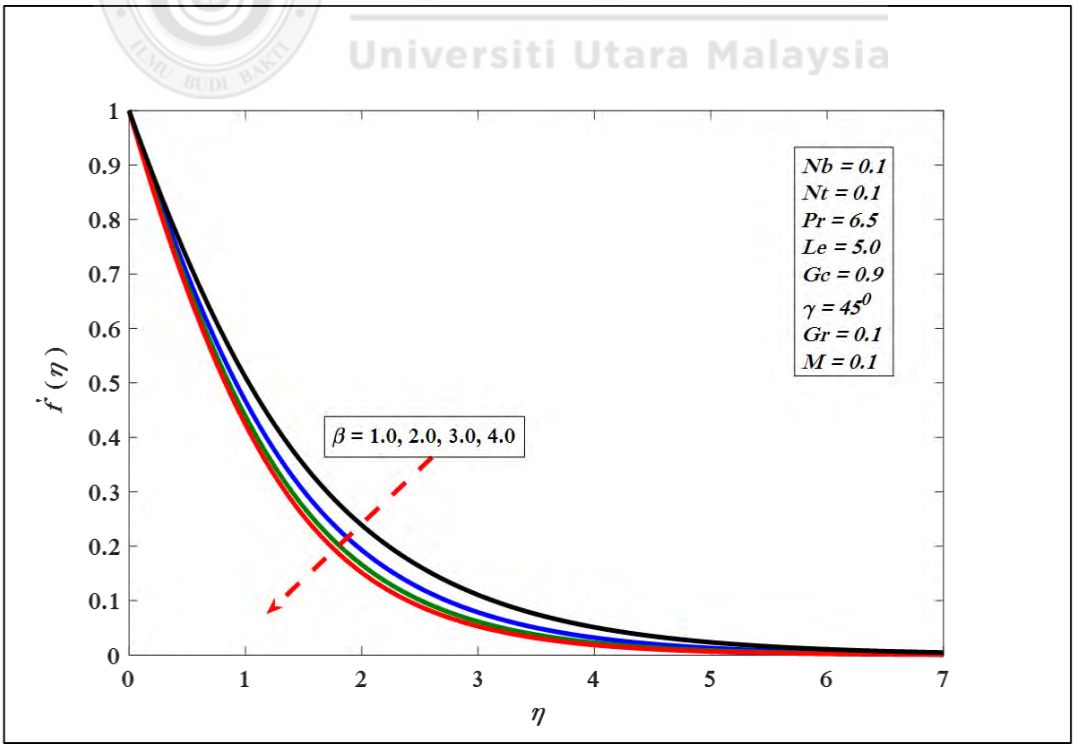

Figure 6.4. Variations in velocity profile for several values of β.

The impact of local modified Grashof number is shown in Figure 6.7. It is observed that the velocity profile rises by improving *Gc*. Physically, velocity and viscosity of a liquid are inversely proportional. Thus, enhancement in *Gc* decline viscous force as a result concentration and $f'(\eta)$ rises. Whereas, Figures 6.8 and 6.9 show an inverse relation for $\theta(\eta)$ and $\phi(\eta)$ versus *Gc*. Moreover, the relation between *Gr* and $f'(\eta)$ is presented in Figure 6.10. Here, *Gr* exhibits features of buoyancy force, which offers a direct correspondence with $f'(\eta)$. Physically, the growing magnitudes of *Gr* declines the viscous force which causes faster motion to fluid flow. Further, $\theta(\eta)$ and $\phi(\eta)$ diminishes with an increase in *Gr* presented in Figures 6.11 and 6.12.

The impressions of magnetic field are presented in Figure 6.13. It is noted that the velocity shape falls by increasing the magnetic field element *M*. Growth of *M* indicates an increment in Lorentz force, which causes decline in velocity of the liquid. Furthermore, Figures 6.14 and 6.15 depict $\theta(\eta)$ and $\phi(\eta)$ increase by strengthen parameter *M*. Figures 6.16 and 8.17 indicate the effect of *Nb* on $\theta(\eta)$ and $\phi(\eta)$. It is seen that $\theta(\eta)$ enlarges with an enhancement in *Nb*. On the other hand, contrary style is seen against $\phi(\eta)$. Physically, the enlargement in *Nb* supports in heat up the boundary layer which inclines to travel nanoparticles from the stretching sheet to the motionless liquid. Therefore, the concentration nanoparticle moderates.

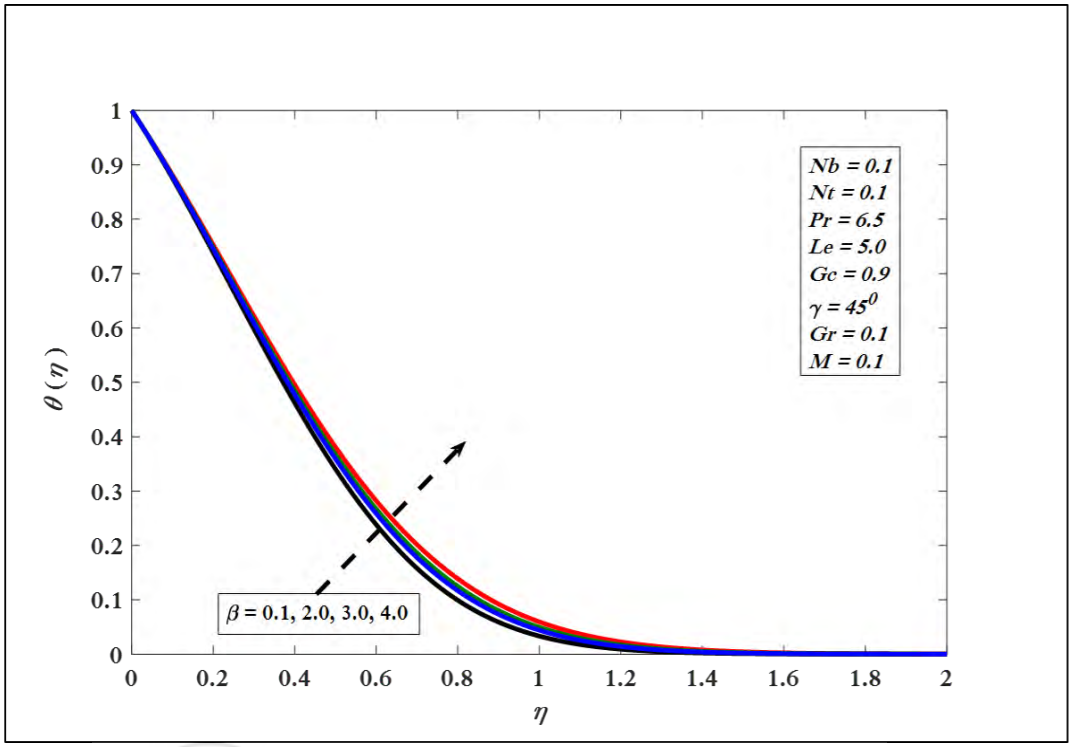

Figure 6.5. Variations in temperature profile for several values of β.

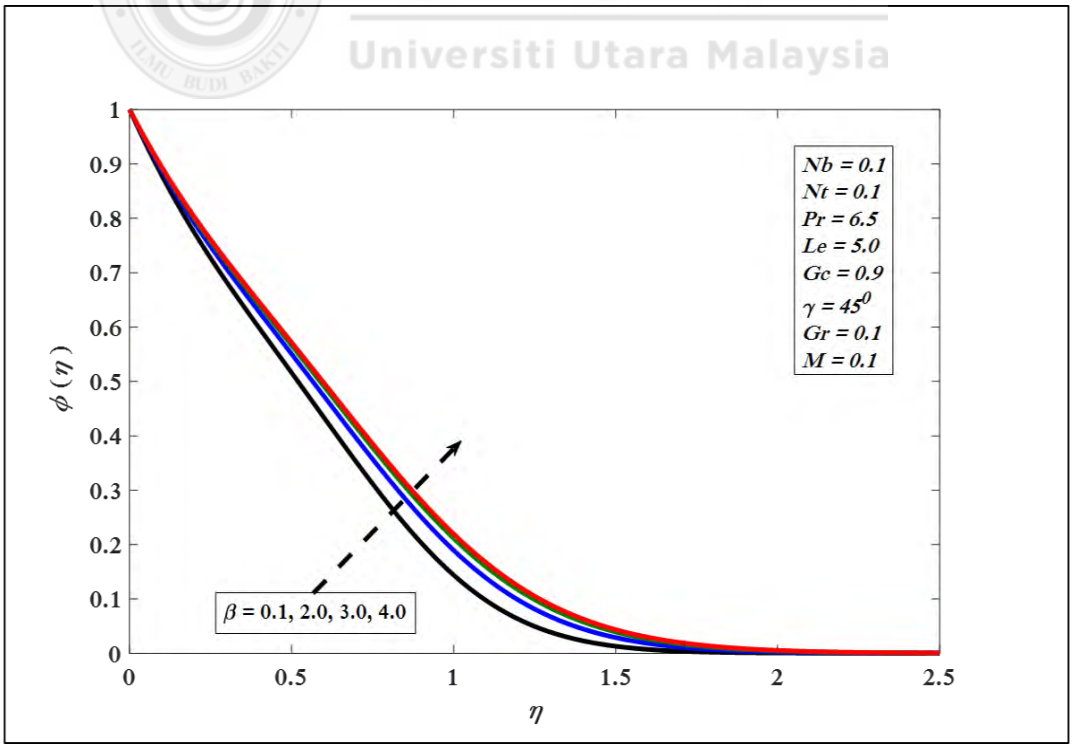

Figure 6.6. Variations in concentration profile for several values of β.

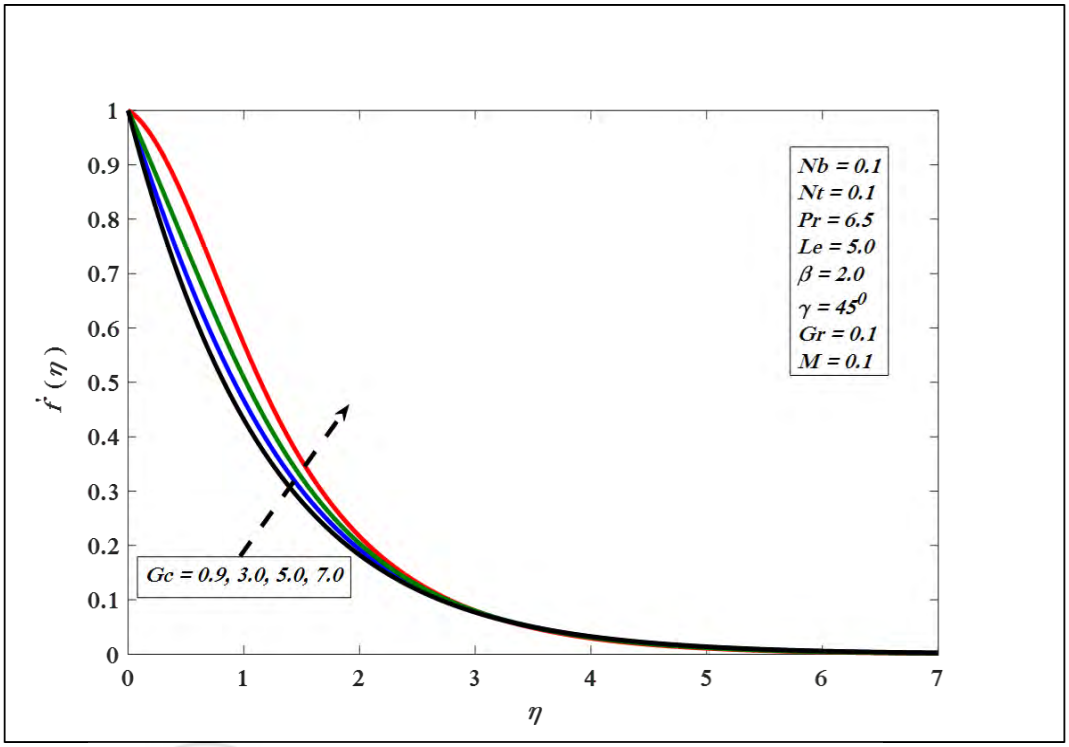

Figure 6.7. Variations in velocity profile for several values of *Gc*.

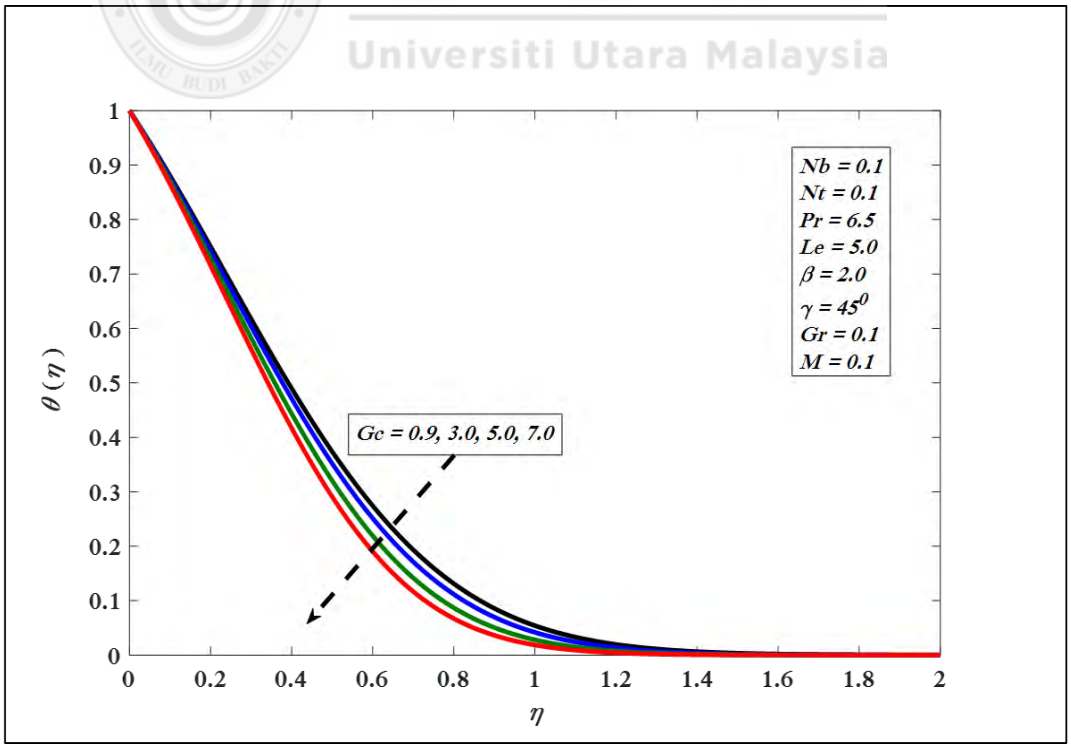

Figure 6.8. Variations in temperature profile for several values of *Gc*.

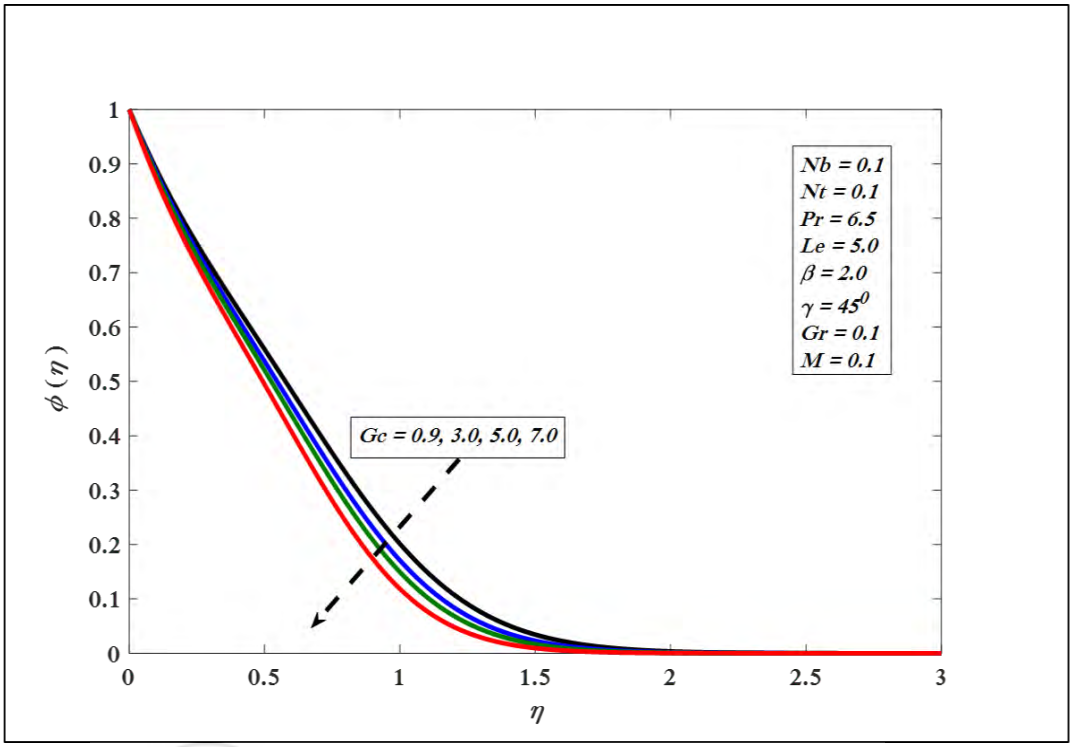

Figure 6.9. Variations in concentration profile for several values of *Gc*

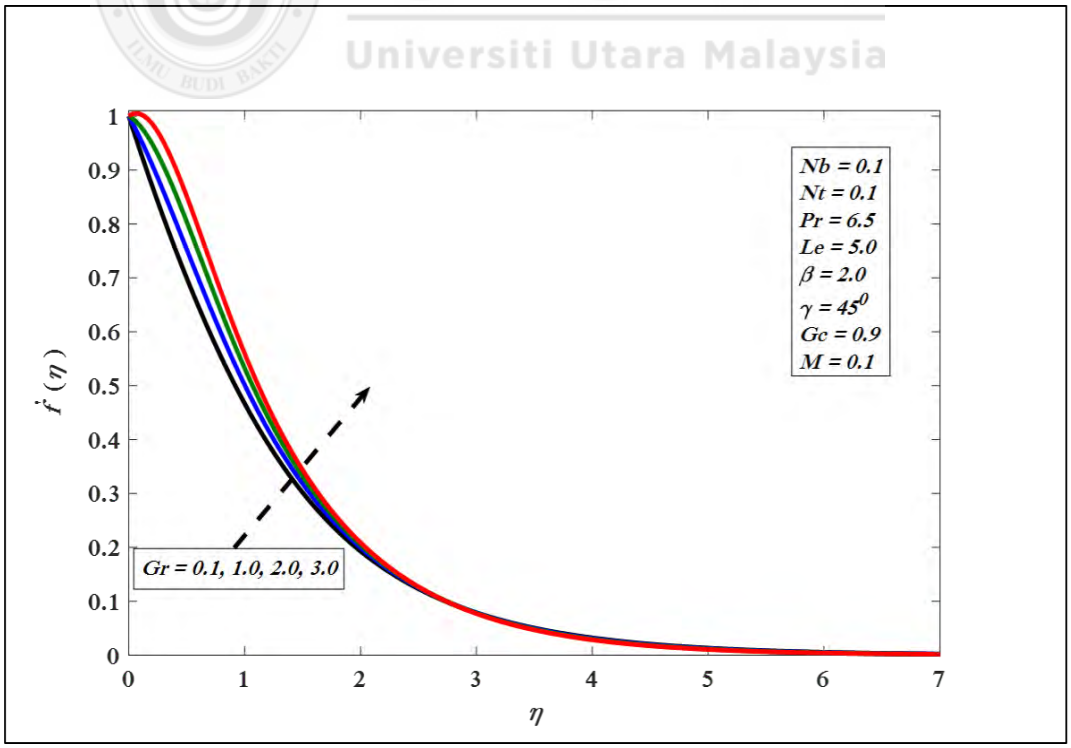

Figure 6.10. Variations in velocity profile for several values of *Gr*

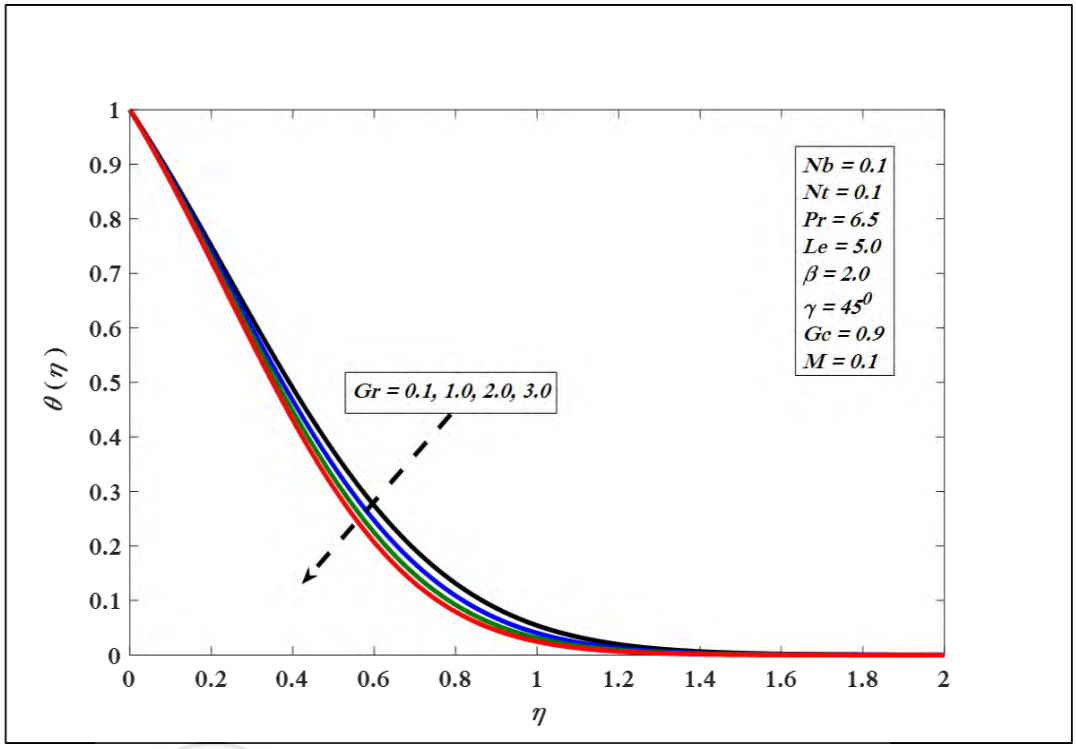

Figure 6.11. Variations in temperature profile for several values of *Gr*.

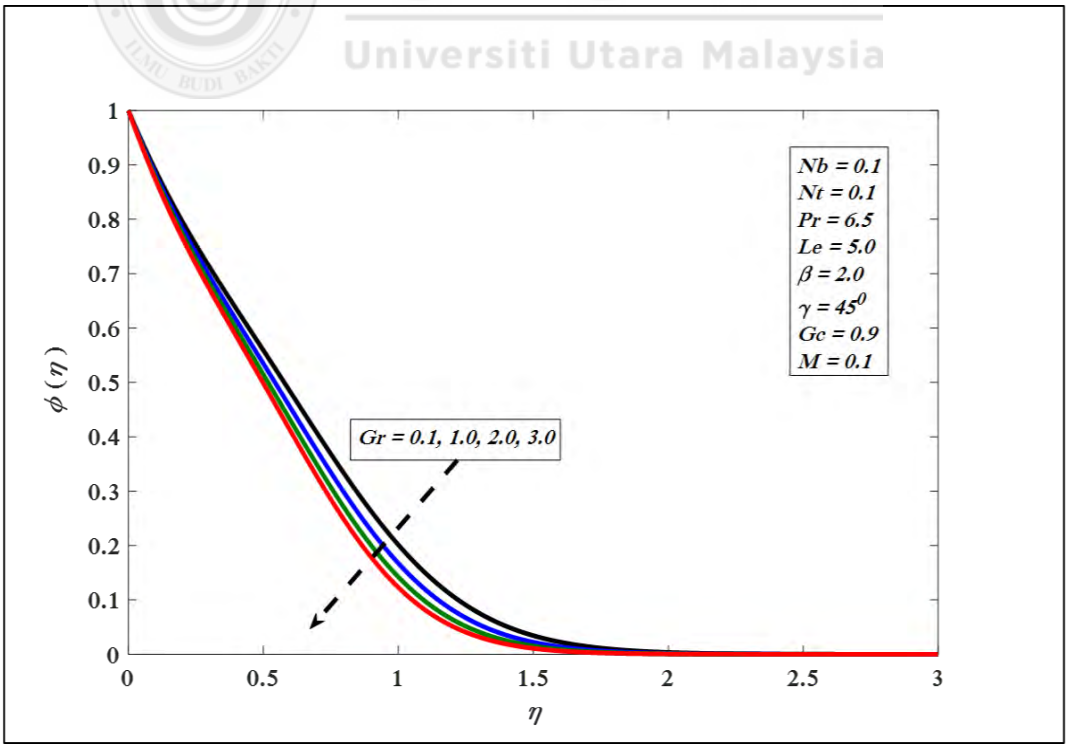

Figure 6.12. Variations in concentration profile for several values of *Gr*.

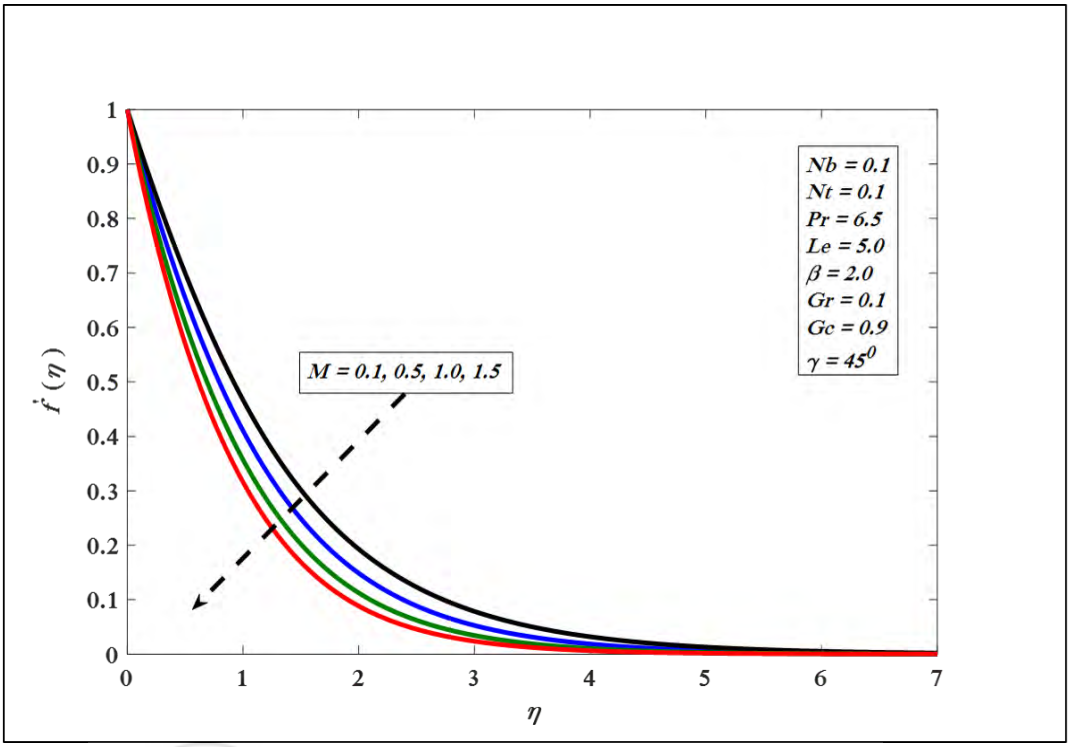

Figure 6.13. Variations in velocity profile for several values of M.

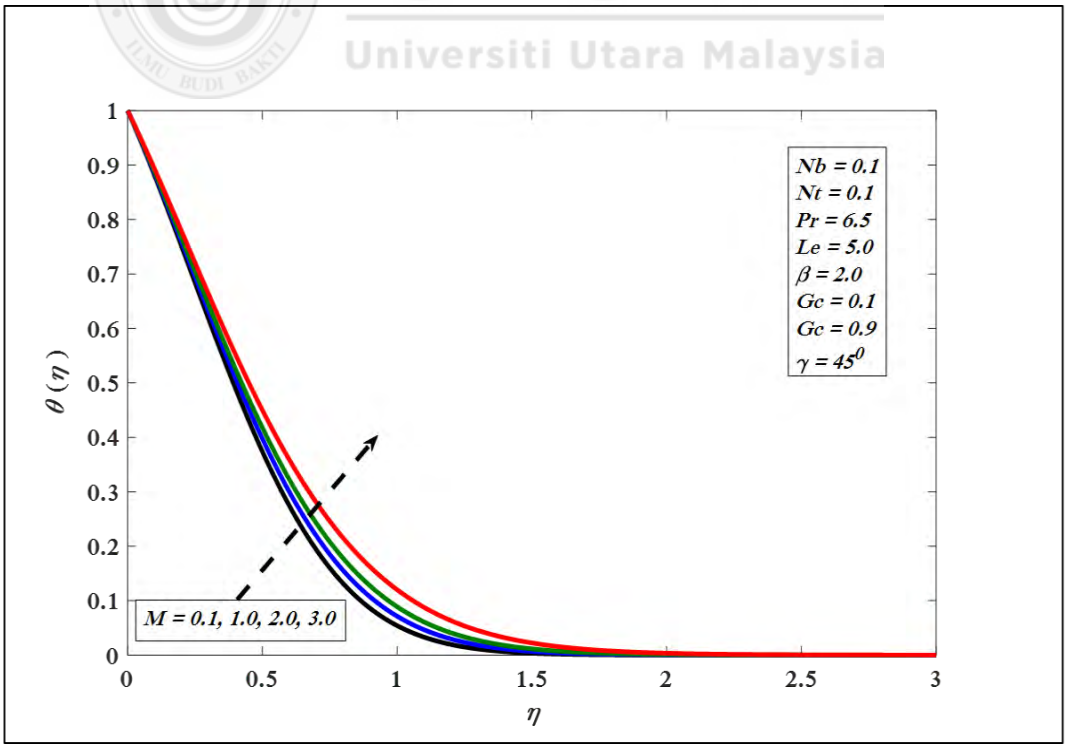

Figure 6.14. Variations in temperature profile for several values of M.

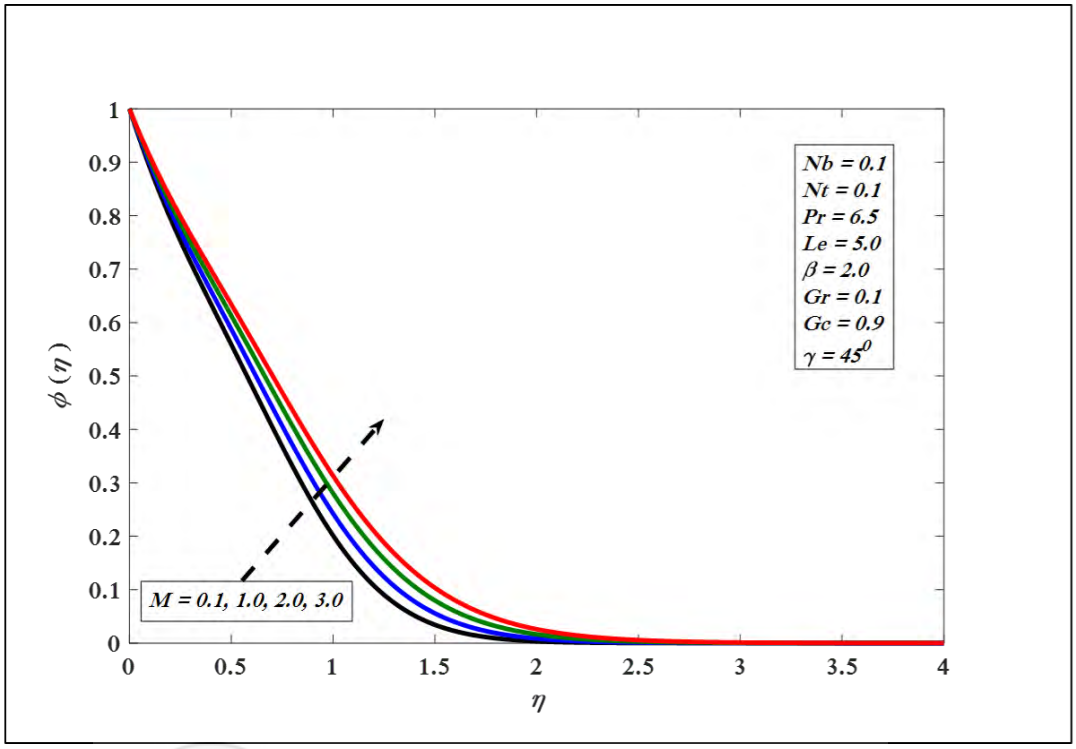

Figure 6.15. Variations in concentration profile for several values of M.

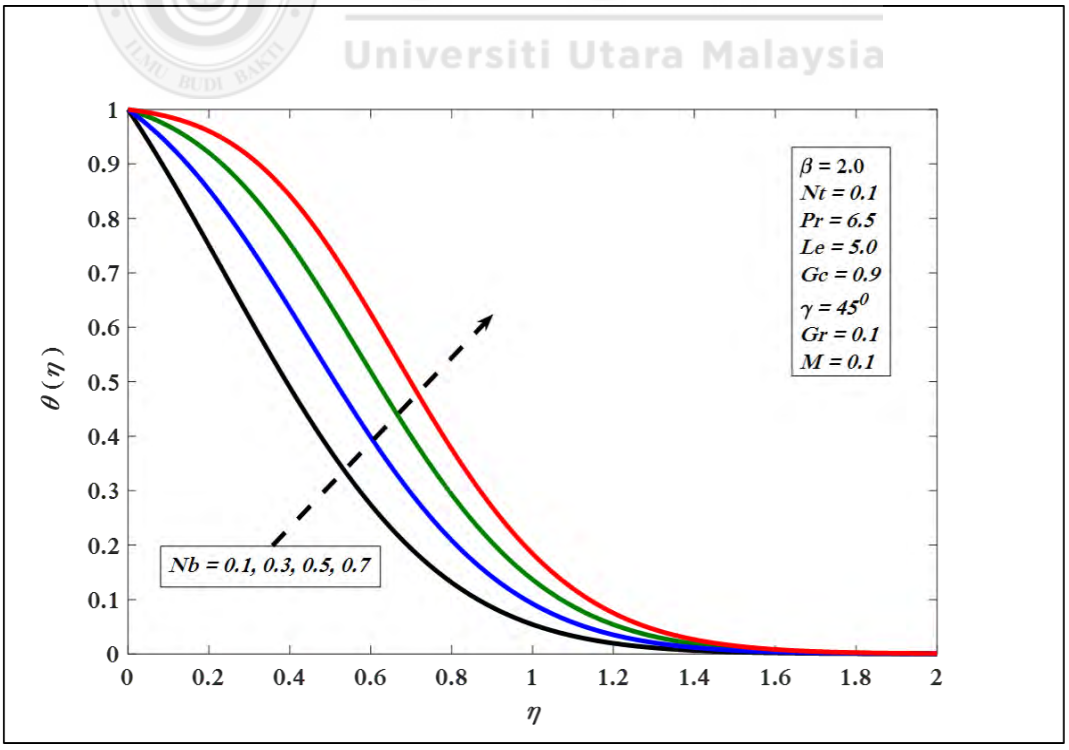

Figure 6.16. Variations in temperature profile for several values of Nb.

Figures 6.18 and 6.19 portray $\theta(\eta)$ and $\phi(\eta)$ upturn by increasing Nt. For decreasing Le and Pr boundary layer heat up due to Thermophoresis. Thus, we can infer that the flux of energy and mass exchange diminish with the growth of Nt. Figure 6.20 reveals that by growing Pr, $\theta(\eta)$ decreases because of lessening viscosity of thermal boundary layer. Finally, an increase in Pr shows slow extent of thermal diffusion. Figure 6.21 shows correspondence among Le and $\phi(\eta)$. The boundary layer thickness decreases by enhancing Le. Figures 6.22 to 6.25 show that $-\theta'(0)$ and $-\phi'(0)$ versus Nb decrease by increasing the inclination. In addition, $-\theta'(0)$ and $-\phi'(0)$ diminish by improving magnitudes of Nt and γ.

This chapter presents Casson effects on boundary layer flow over linear inclined geometry. It is natural to extends the next chapter by considering flow behavior of Casson nanofluid flow with thermal radiation effect for inclined geometry that is nonlinear.

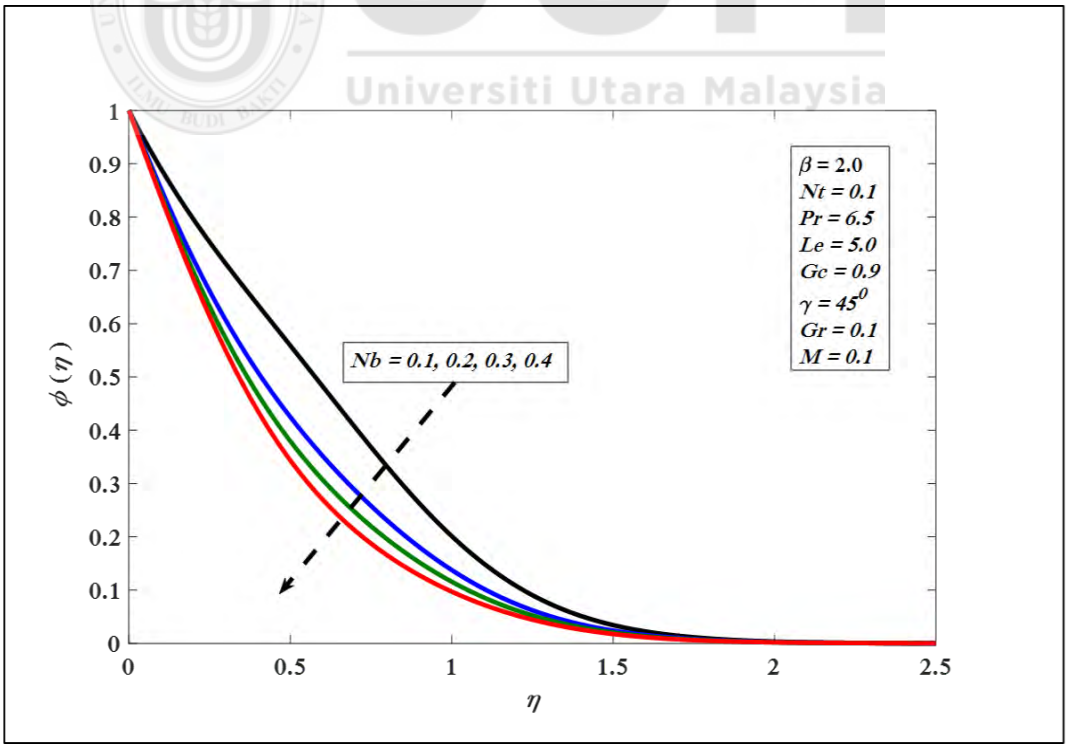

Figure 6.17. Variations in concentration profile for several values of Nb.

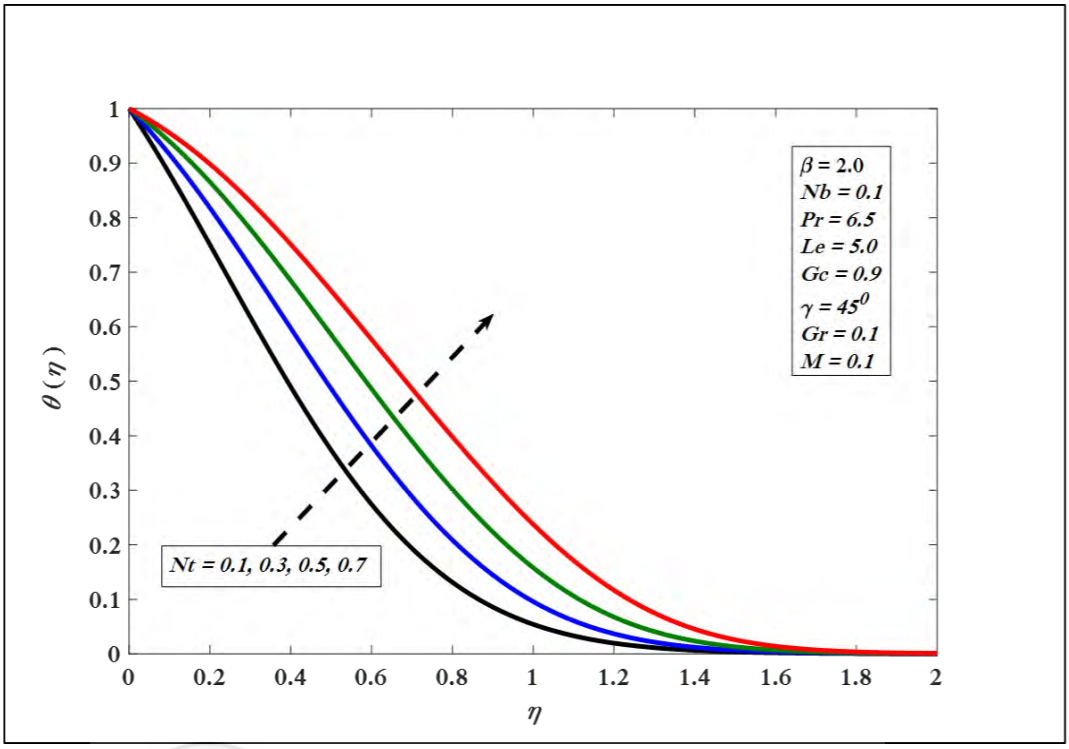

Figure 6.18. Variations in temperature profile for several values of Nt.

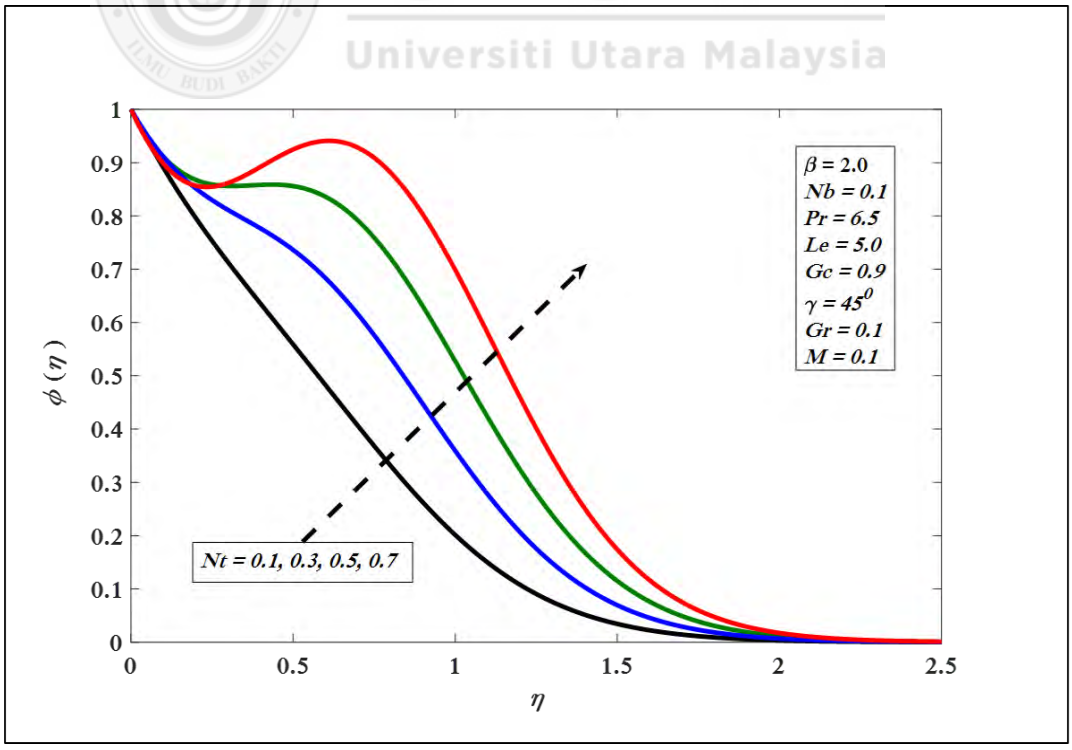

Figure 6.19. Variations in concentration profile for several values of Nt.

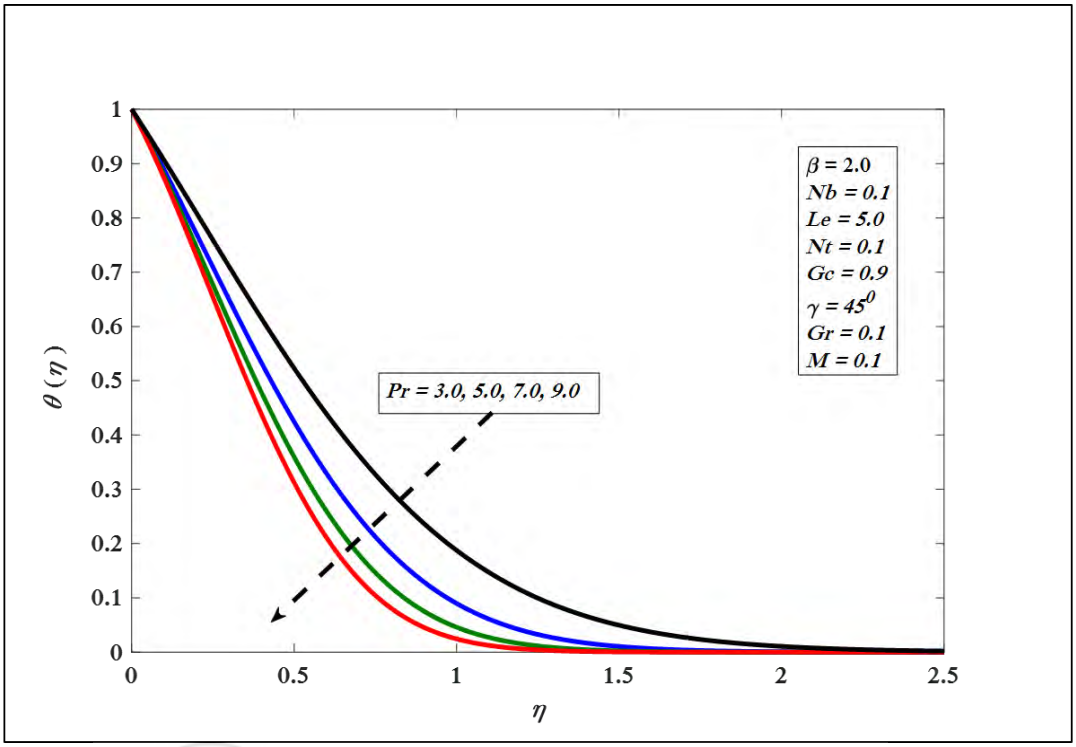

Figure 6.20. Variations in temperature profile for several values of *Pr*.

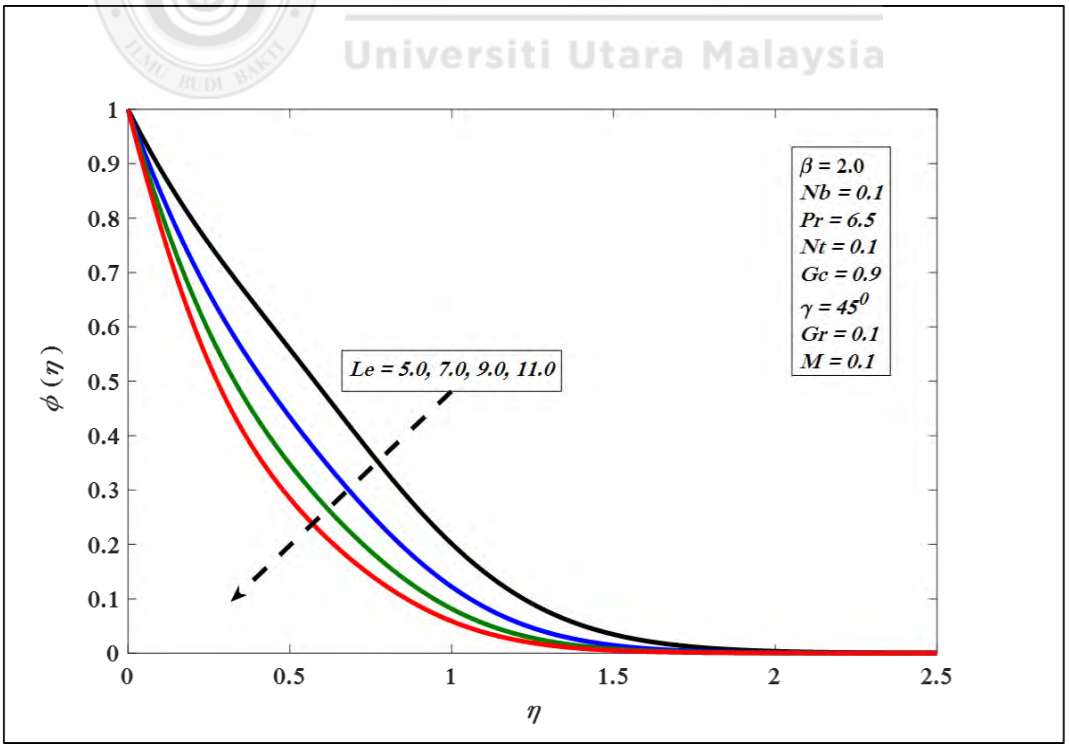

Figure 6.21. Variations in concentration profile for several values of *Le*.

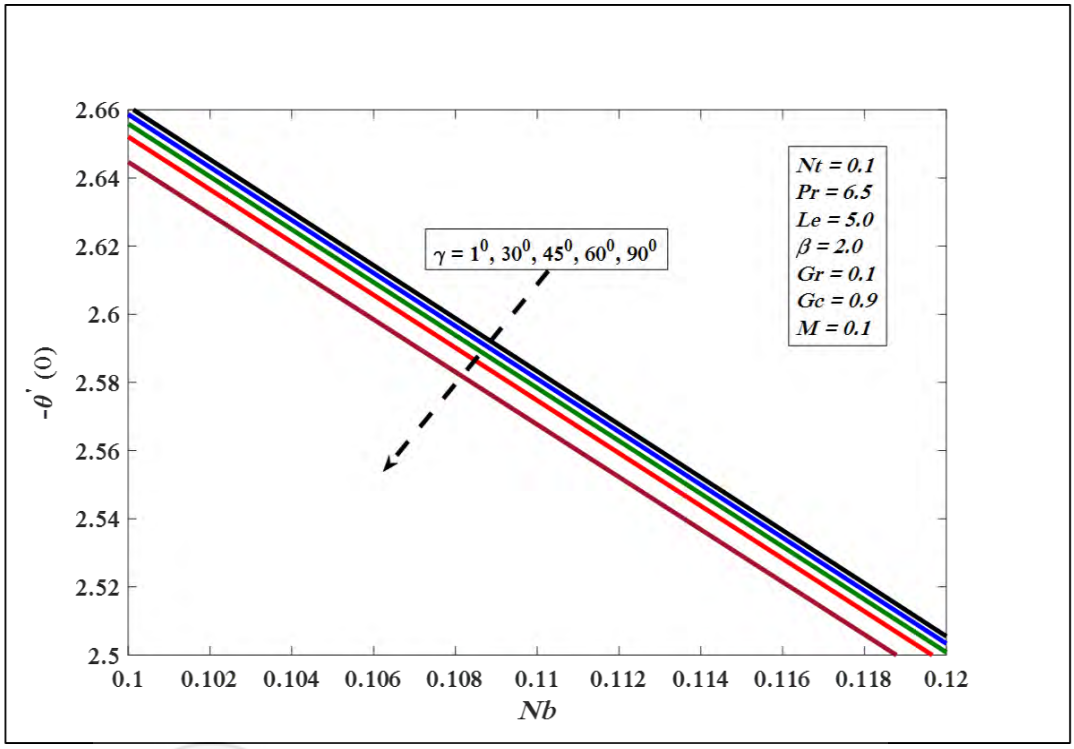

Figure 6.22. $-\theta'(0)$ against Nb for several values of γ.

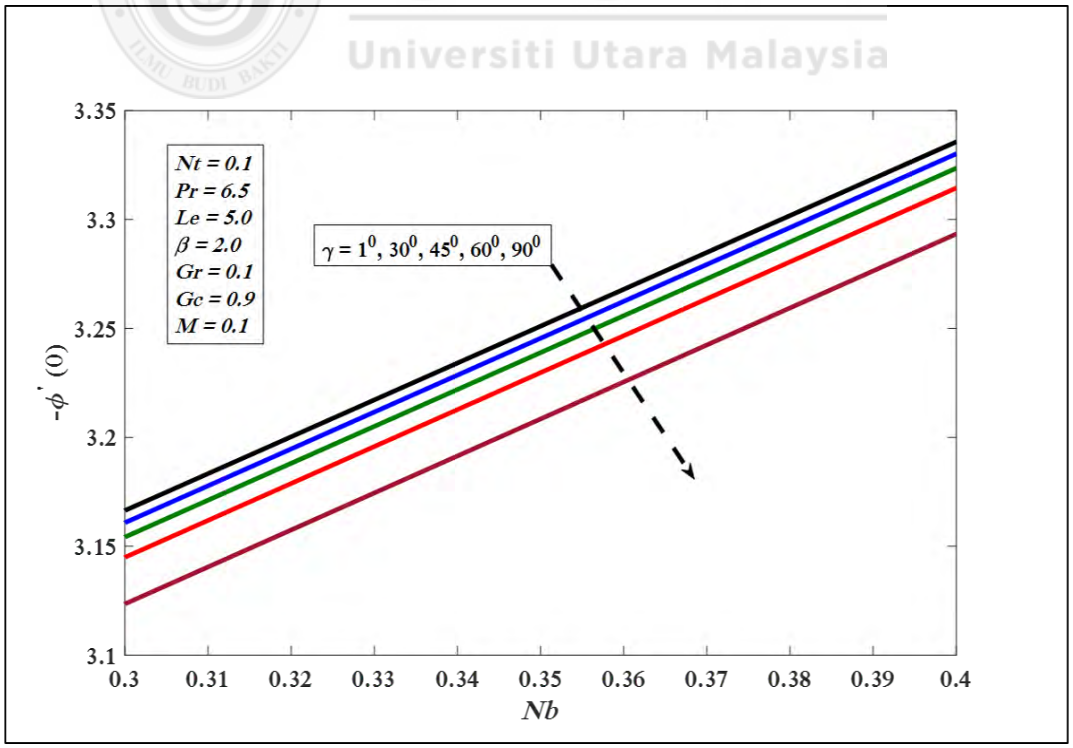

Figure 6.23. $-\phi'(0)$ against Nb for several values of γ.

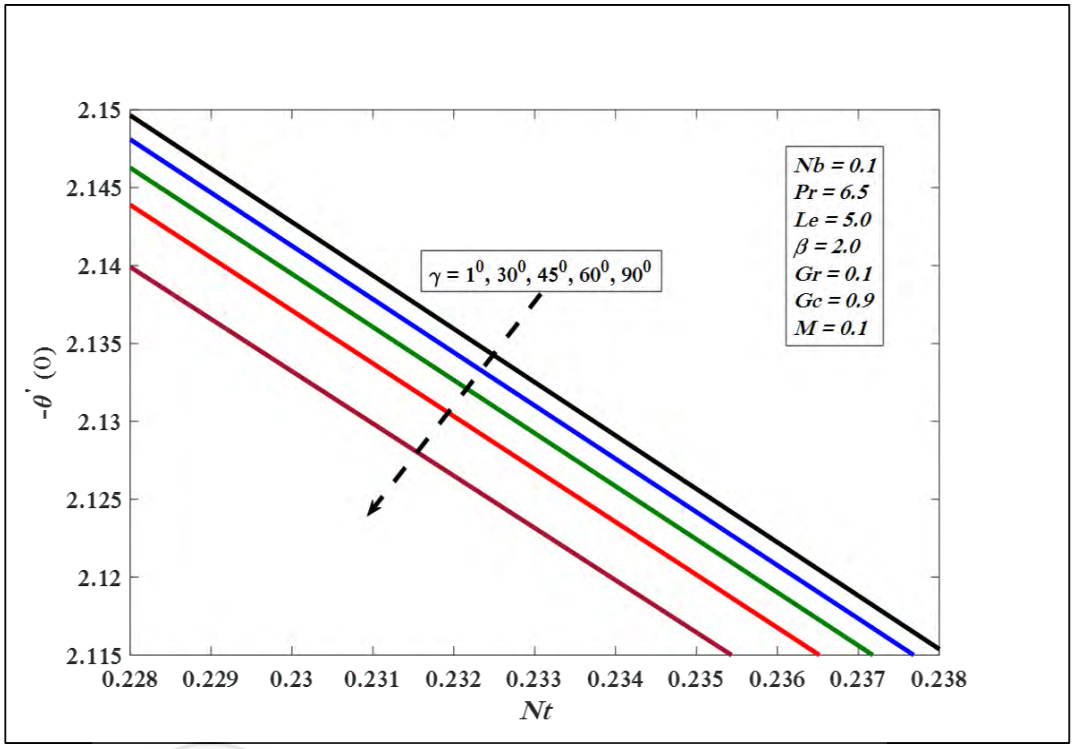

Figure 6.24. $-\theta'(0)$ against Nt for several values of γ.

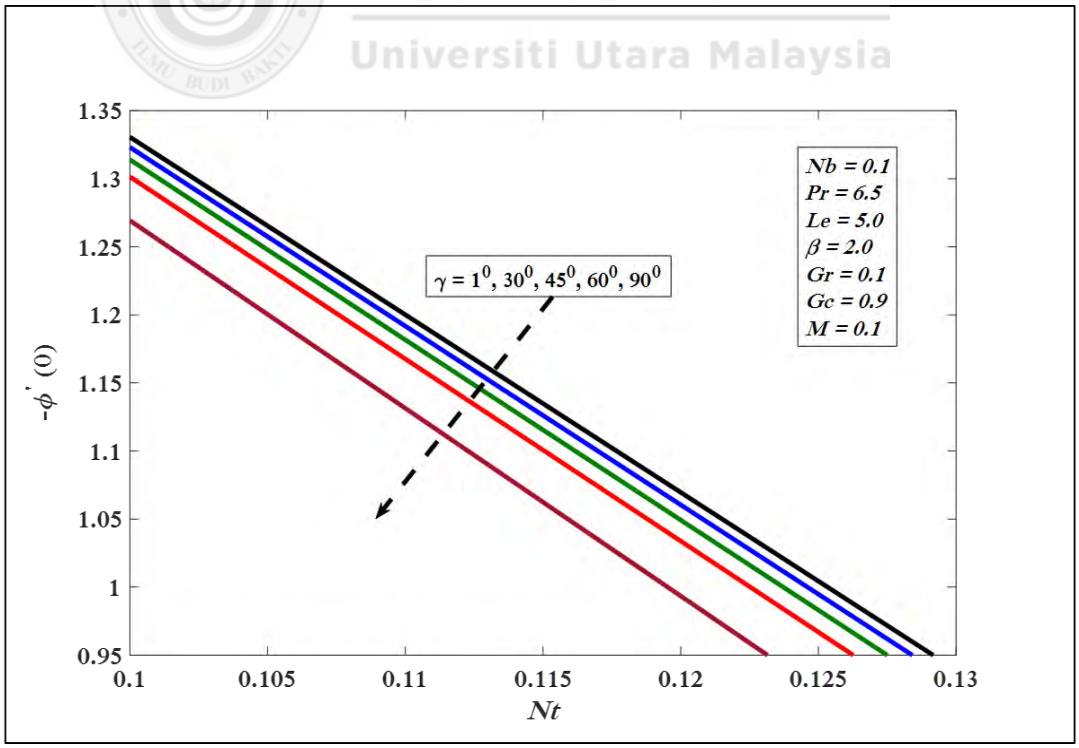

Figure 6.25. $-\phi'(0)$ against Nt for several values of γ.

6.4 Conclusions

This chapter is prepared for the boundary layer flow of Casson nanofluid flow over a linear inclined surface in the presence of magnetic effects. After the conversion of flow equations into ordinary differential equation we use well known numerical technique for solution named Keller box scheme. The influence of Casson parameter (β) on velocity profile discussed graphically. In the same vein, the numerical variation with respect to Casson parameter (β) is examined via table. The key conclusions of this problem presented by:

1. The Casson parameter retards the velocity of the fluid.
2. An increment in Casson factor enhance heat and mass transfer rates.
3. Skin friction reduces by increasing Casson parameter.

CHAPTER SEVEN

BOUNDARY LAYER FLOW OF CASSON NANOFLUID OVER A NONLINEAR INCLINED STRETCHING SURFACE

7.1 Introduction

In this chapter, problem on Casson nanofluid flow over a power law inclined stretching surface is explored by incorporating radiations impact. Using appropriate similarity transformations, the system of nonlinear partial differential equations is transformed to a system of nonlinear ordinary differential equations. To approve the numerical outcomes, the present outcomes are contrasted with previously published results in the lack of Hartmann number M, Gr (local Grashof number), Gc (modified local Grashof number), N (radiation factor) and Casson constraint β, with $\gamma = 90^0$ and found in good agreement.

7.2 Governing Equations

Suppose two dimensional incompressible Casson nanofluid flow over nonlinear inclined extending surface slant at γ, where $u_\infty(x) = 0$ represent free stream velocity and $u_w(x) = ax^m$ shows stretching velocity. Further $B(x) = B_0 x^{\frac{m-1}{2}}$ represents transverse magnetic field. The slanted surface stretched nonlinearly. Moreover, thermal radiation impacts are under consideration in this problem. The flow equations for the problem under examination are as follows (see Equations 3.59, 3.62 (when $Q_0 =$),

3.63 (when $R^* = 0$), and 3.100.

$$\frac{\partial u}{\partial x} + \frac{\partial v}{\partial y} = 0,$$

$$u\frac{\partial u}{\partial x} + v\frac{\partial u}{\partial y} = \left(1 + \frac{1}{\beta}\right)\nu\frac{\partial^2 u}{\partial y^2} + g\beta_t(T - T_\infty)\cos\gamma$$

$$+ g\beta_c(C - C_\infty)\cos\gamma - \left(\frac{\sigma B^2(x)}{\rho}\right)u,$$

$$u\frac{\partial T}{\partial x} + v\frac{\partial T}{\partial y} = \left(\alpha + \frac{16\sigma^* T_\infty^3}{3k^*(\rho c)_f}\right)\frac{\partial^2 T}{\partial y^2} + \tau\left[D_B\frac{\partial C}{\partial y}\frac{\partial T}{\partial y} + \frac{D_T}{T_\infty}\left(\frac{\partial T}{\partial y}\right)^2\right], \quad (7.1)$$

$$u\frac{\partial C}{\partial x} + v\frac{\partial C}{\partial y} = D_B\frac{\partial^2 C}{\partial y^2} + \frac{D_T}{T_\infty}\frac{\partial^2 T}{\partial y^2},$$

subject to the boundary conditions

$$u = u_w(x) = ax^m\,, v = 0\,, T = T_w\,, C = C_w \qquad at \qquad y = 0,$$

$$u \to u_\infty(x) = 0\,, v \to 0\,, T \to T_\infty\,, C \to C_\infty \qquad as \qquad y \to \infty. \quad (7.2)$$

7.2.1 Similarity Transformations

The stream function use for this procedure is given as

$$u = \frac{\partial \psi}{\partial y}\,, \quad v = -\frac{\partial \psi}{\partial x}, \quad (7.3)$$

where continuity equation in equation (7.1) is satisfied identically. The similarity transformations are characterized as

$$\psi = \sqrt{\frac{2\nu a x^{m+1}}{m+1}}f(\eta)\,, \eta = y\sqrt{\frac{(m+1)ax^{m-1}}{2\nu}},$$

$$\theta = \frac{T - T_\infty}{T_w - T_\infty}, \phi = \frac{C - C_\infty}{C_w - C_\infty}. \tag{7.4}$$

On substituting Equation (7.4), system of Equations (7.1) is converted to the following nonlinear ordinary differential equations:

$$\left(1 + \frac{1}{\beta}\right) f''' + ff'' - \left(\frac{2m}{m+1}\right) f'^2 + \left(\frac{2}{m+1}\right) (Gr_x \theta + Gc_x \phi) cos\gamma - \left(\frac{2M}{m+1}\right) f' = 0,$$

$$Pr_N \theta'' + f\theta' + Nb\theta'\phi' + Nt\theta'^2 = 0, \tag{7.5}$$

$$\phi'' + Lef\phi' + Nt_b\theta'' = 0.$$

Here, $Pr_N = \frac{1}{Pr}\left(1 + \frac{3}{4}N\right)$ where $N = \frac{4\sigma^* {T_\infty}^3}{\alpha k^*}$ is the radiation constraint (Anwar, 2013), the other involved parameters are defined same as in Chapter 3. Moreover, Gr and Gc are defined same as in Chapter 6.

The converted boundary conditions are

$$f(\eta) = 0,\ f'(\eta) = 1,\ \theta(\eta) = 1, \phi(\eta) = 1 \ at\ \eta = 0,$$

$$f'(\eta) \to 0, \theta(\eta) \to 0, \phi(\eta) \to 0 \ \ at \ \ \eta \to \infty. \tag{7.6}$$

The associated expressions of the skin friction coefficient $C_{fx}(0)$, the local Nusselt number $-\theta'(0)$ and the local Sherwood number $-\phi'(0)$ are defined in the same way as in Equation (6.10) other than the expression $q_w = -\left[k + \frac{4\sigma^* T_\infty^3}{3k^*}\right](\frac{\partial T}{\partial y})_{y=0}$ in the reduced Nusselt number. Using the expression of q_w, the reduced Nusselt number is

$$-\theta'(0) = \frac{Nu}{\left(1 + \frac{4}{3}N\right)\sqrt{\frac{m+1}{2}Re_x}}. \tag{7.7}$$

7.3 Results and Discussion

This section manages mathematical results of converted nonlinear ordinary differential equations (7.5) with boundary conditions (7.6) are elucidated via Keller-box method. For numerical result of physical parameters including Brownian motion denoted by Nb, thermophoresis given by Nt, magnetic factor M, local Grashof number Gr, local modified Grashof number Gc, inclination factor γ, Prandtl number Pr, Lewis number Le, radiation factor N, Casson parameter β, and nonlinear factor m, different figures are drawn. In the deficiency of Gr, Gc, M, N and with $m = 1$, $\gamma = 90^0$ and $\beta \to \infty$, the consequences of (reduced Nusselt number) $-\theta'(0)$ and (reduced Sherwood number) $-\phi'(0)$ are equated by the Khan and Pop (2010) (see Table 3.1) results. The consequences established good settlement. The effects on $-\theta'(0)$, $-\phi'(0)$ and skin friction measurement $C_{fx}(0)$ against several values of involved physical factors Nb, β, Nt, $M, N, Gr, Gc, \gamma, Pr, Le$ and m are exposed in Table 7.1. It is noted that $-\theta'(0)$ drops for the increasing values of $Nb, Nt, M, \beta, N, Le, m, \gamma$ and increased by enhancing numerical values of Gr, Gc and Pr. Moreover, it is perceived that $-\phi'(0)$ enhanced with the larger values of Nb, N, Le, Gr, Gc and drops for bigger values of m, M, β, γ, Pr and Nt. Further, $C_{fx}(0)$ rises with the growing values $Nb, Le, \beta, M, N, \gamma, m$ and drops versus Nt, Gr, Gc and Pr.

Table 7.1
Variations of local Nusselt number $-\theta'(0)$*, local Sherwood number* $-\phi'(0)$ *and skin-friction coefficient* $C_{fx}(0)$.

Nb	*Nt*	*Pr*	*Le*	*M*	*N*	*Gr*	*Gc*	β	*m*	γ	$-\theta'(0)$	$-\phi'(0)$	$C_{fx}(0)$
0.1	0.1	6.5	5.0	0.1	1.0	0.1	0.9	1.0	0.5	45^0	0.9180	1.3209	0.4857
0.5	0.1	6.5	5.0	0.1	1.0	0.1	0.9	1.0	0.5	45^0	0.4290	1.6634	0.5173
0.1	**0.5**	6.5	5.0	0.5	1.0	1.0	1.0	5.0	0.5	45^0	0.6301	1.0406	0.3634
0.1	0.1	**10.0**	5.0	0.1	1.0	0.1	0.9	1.0	0.5	45^0	1.0446	1.2633	0.4835
0.1	0.1	6.5	**10.0**	0.1	1.0	0.1	0.9	1.0	0.5	45^0	0.8737	2.1720	0.5374
0.1	0.1	6.5	5.0	**2.5**	1.0	0.1	0.9	1.0	0.5	45^0	0.8008	1.1334	1.2603
0.1	0.1	6.5	5.0	0.1	**5.0**	0.1	0.9	1.0	0.5	45^0	0.5458	1.4921	0.4882
0.1	0.1	6.5	5.0	0.1	1.0	**0.5**	0.9	1.0	0.5	45^0	0.9267	1.3339	0.4067
0.1	0.1	6.5	5.0	0.1	1.0	0.1	**3.0**	1.0	0.5	45^0	0.9553	1.3778	0.1101
0.1	0.1	6.5	5.0	0.1	1.0	0.1	0.9	**3.0**	0.5	45^0	0.9024	1.2947	0.5526
0.1	0.1	6.5	5.0	0.1	1.0	0.1	0.9	1.0	**1.5**	45^0	0.8973	1.2891	0.6641
0.1	0.1	6.5	5.0	0.1	1.0	0.1	0.9	1.0	0.5	$\mathbf{60}^0$	0.9116	1.3114	0.5412

Figures 7.1 to 7.7 show physical impacts of the concerned factors on the momentum, temperature and concentration profiles. It is clear from Figure 7.1 that the velocity field falls with the influence of nonlinear stretching factor *m*. It is clearly observed that nonlinear stretching rate declines the velocity of the fluid while it enhances $\theta(\eta)$ and $\phi(\eta)$ (see Figures 7.2 and 7.3). Moreover, in Figure 7.4, the magnetic effect decreases the velocity of the fluid due to Lorentz force which built resistance in the flow path.

Whereas, Figures 7.5 and 7.6 present $\theta(\eta)$ and $\phi(\eta)$ that increase with the improvement of magnetic factor. In addition, the radiation effect shows direct correspondence with $\theta(\eta)$ as shown in Figure 7.7. Figures 7.8 and 7.9 show variations in $-\theta'(0)$ and $-\phi'(0)$ versus *Nb* with altered magnitudes of γ. It is clearly observed that $-\theta'(0)$ and $-\phi'(0)$ decrease on enhancing the inclination factor. Further, Figures 7.10 and 7.11 exhibit similar impact on $-\theta'(0)$ and $-\phi'(0)$ with the growth of *Nt* and γ. Moreover, $-\theta'(0)$ increases with the increasing factors *N* and *Pr*. Whereas, $-\phi'(0)$ declines on the improvement of *Pr* and *N*.

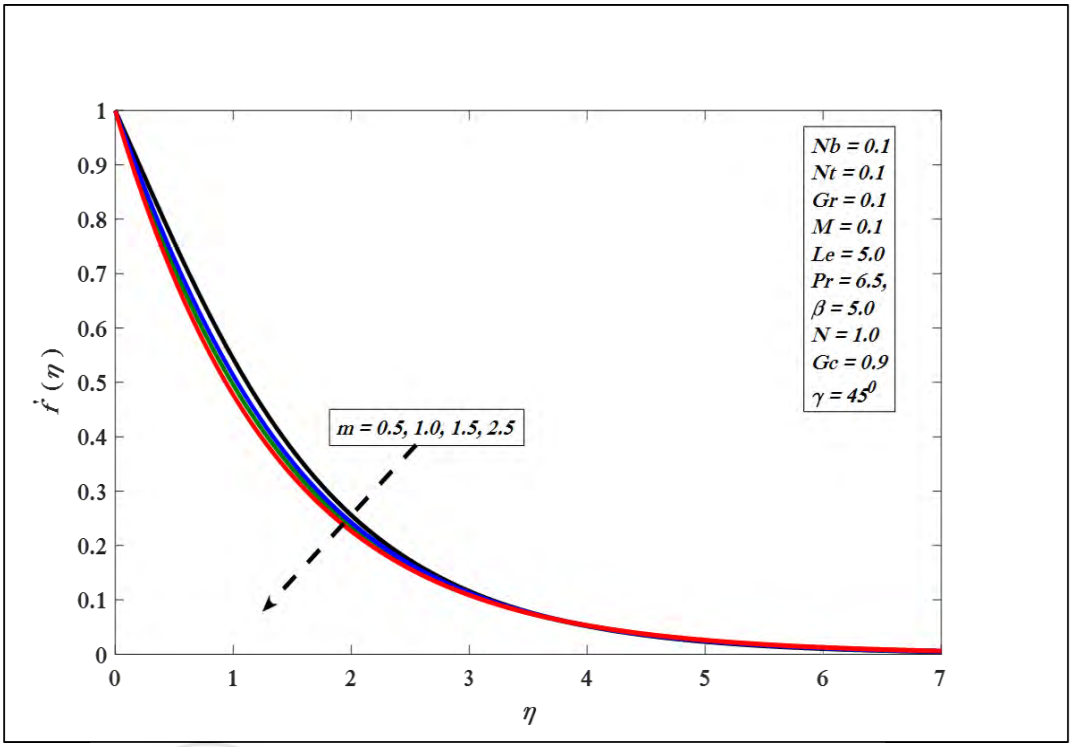

Figure 7.1. Variations in velocity profile for several values of m.

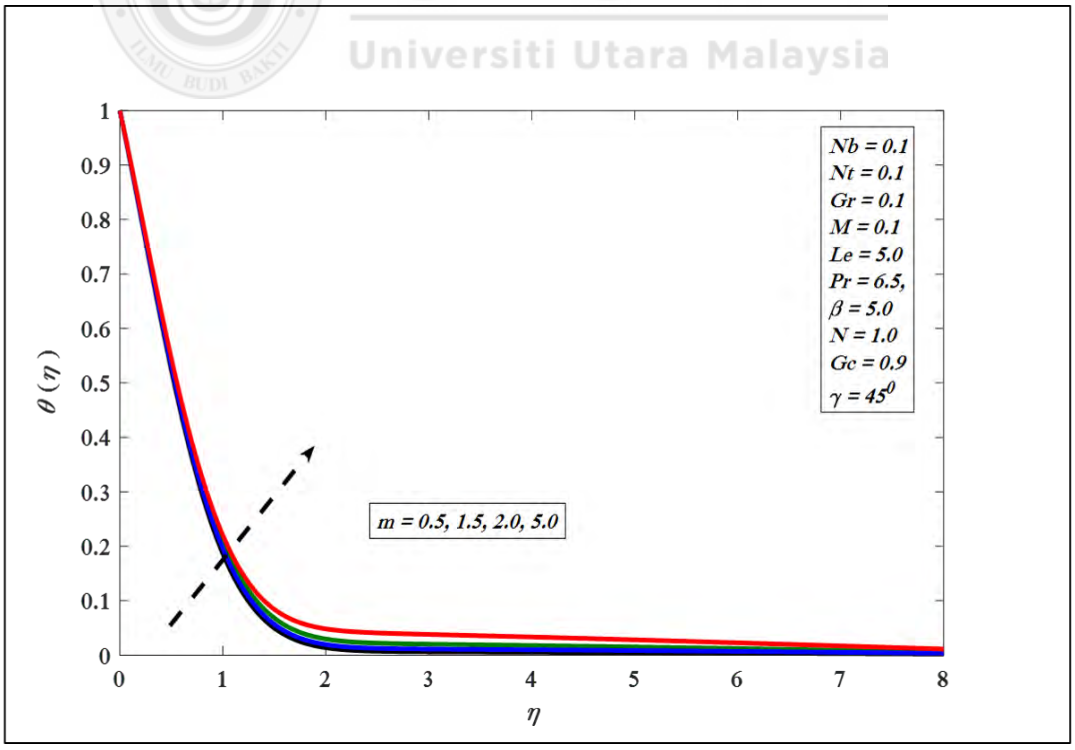

Figure 7.2. Variations in temperature profile for several values of m.

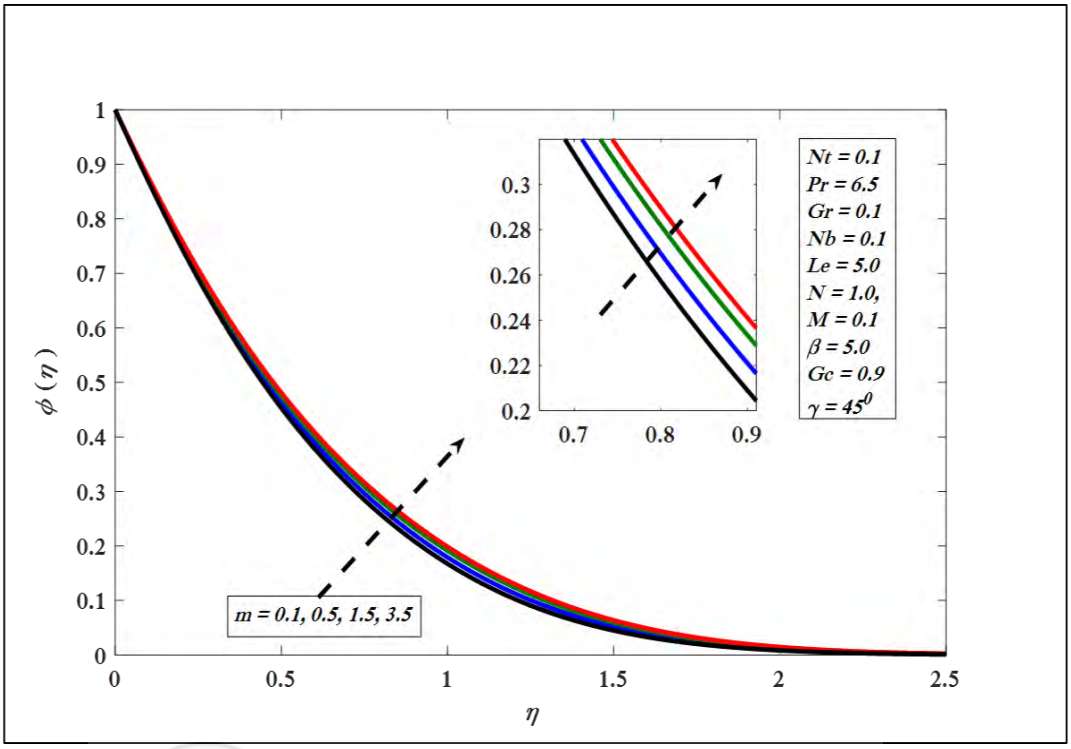

Figure 7.3. Variations in concentration profile for several values of m.

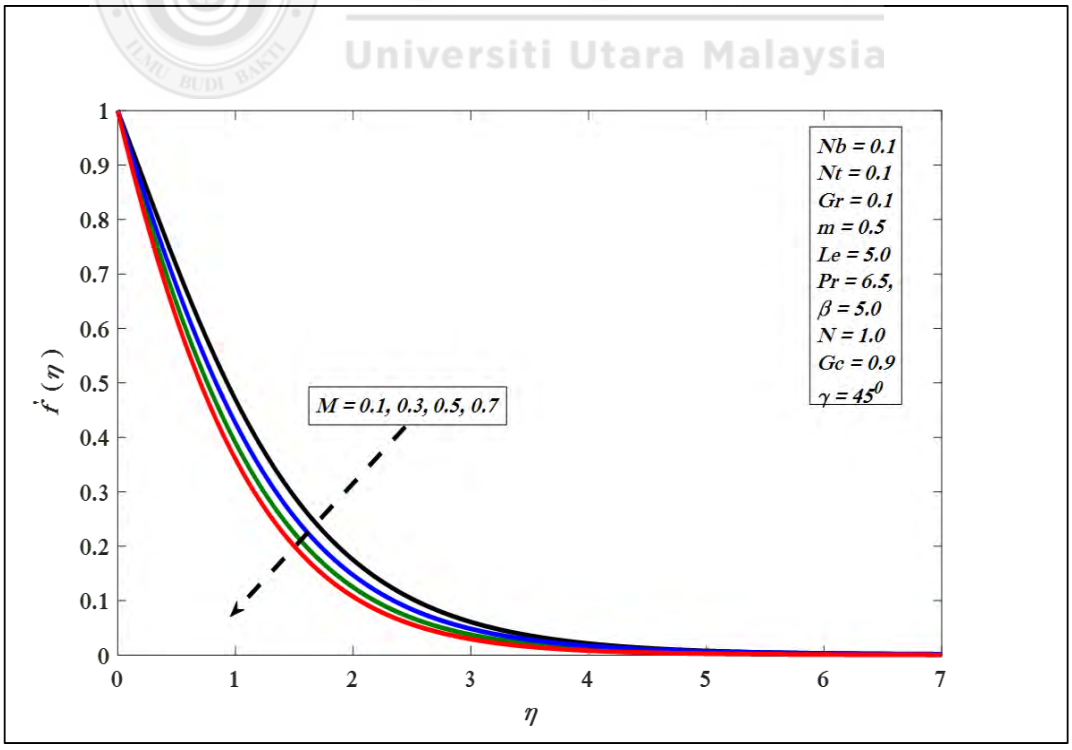

Figure 7.4. Variations in velocity profile for several values of M.

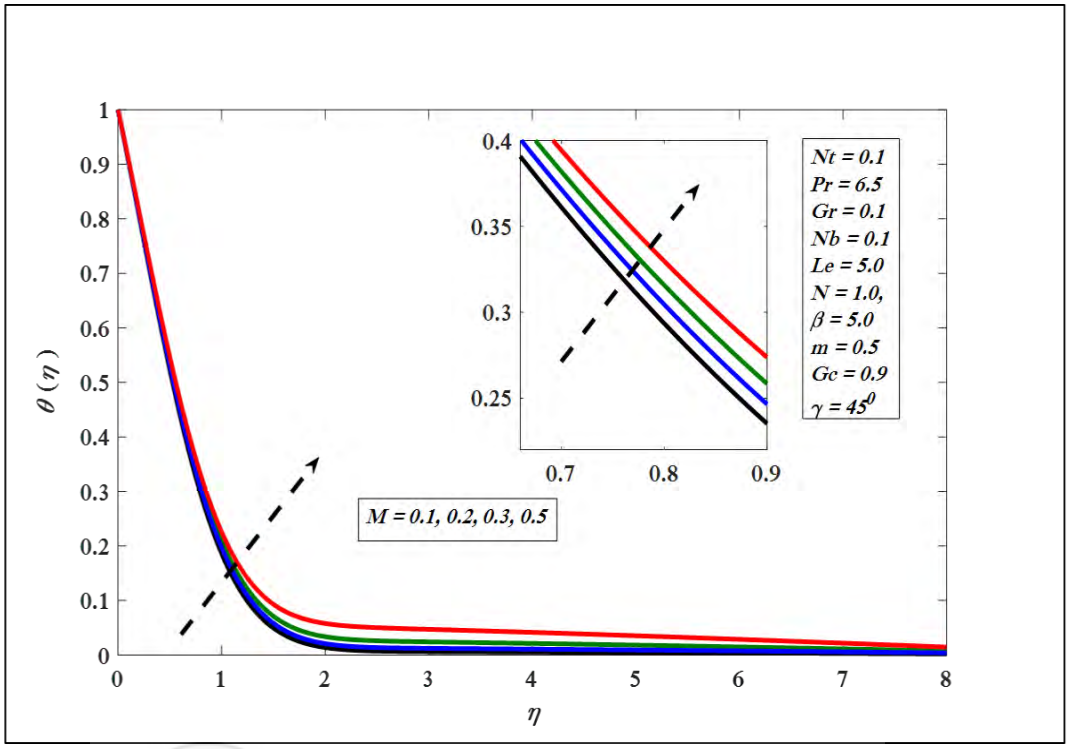

Figure 7.5. Variations in temperature profile for several values of M.

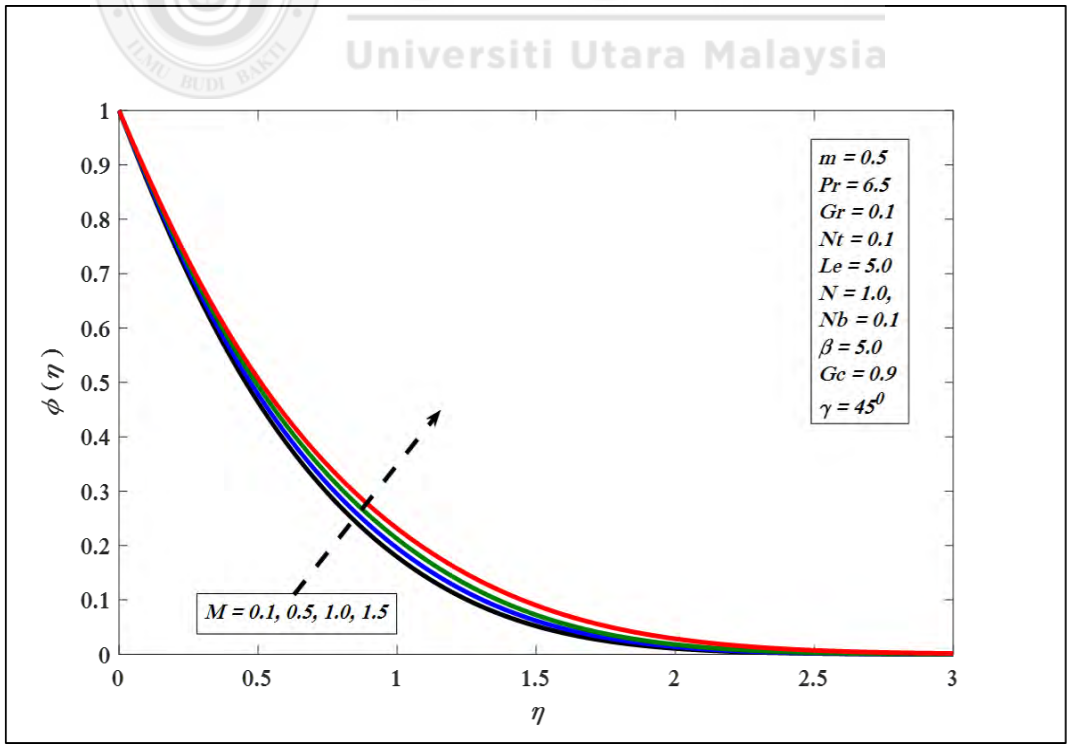

Figure 7.6. Variations in concentration profile for several values of M.

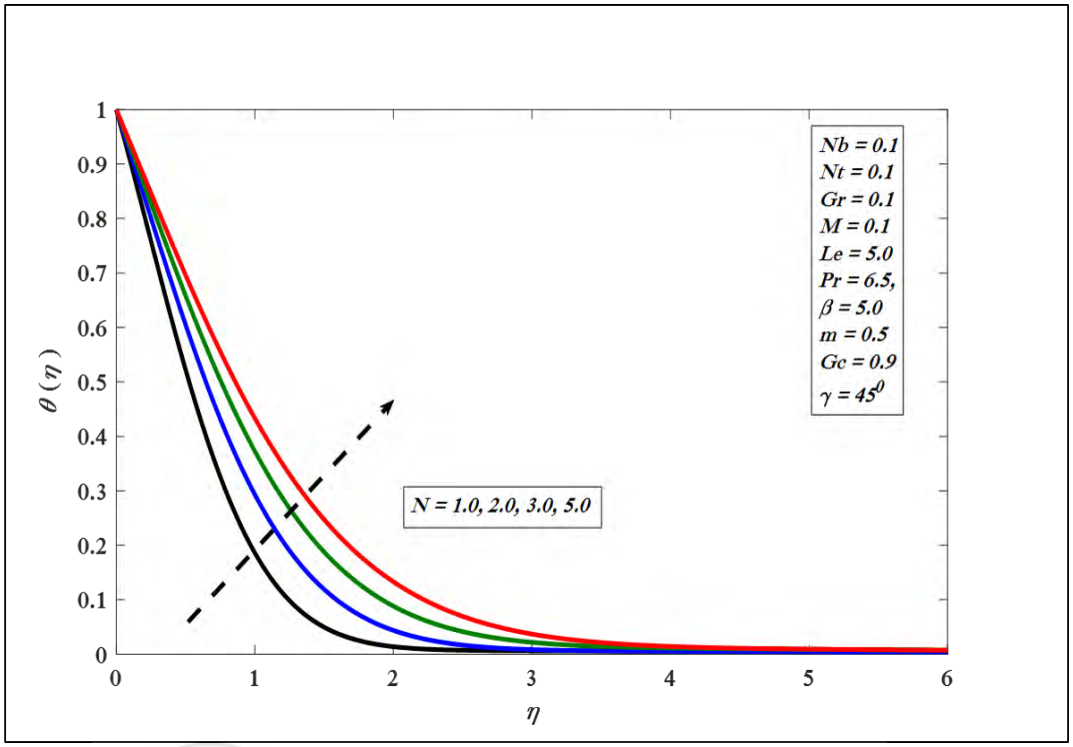

Figure 7.7. Variations in temperature profile for several values of N.

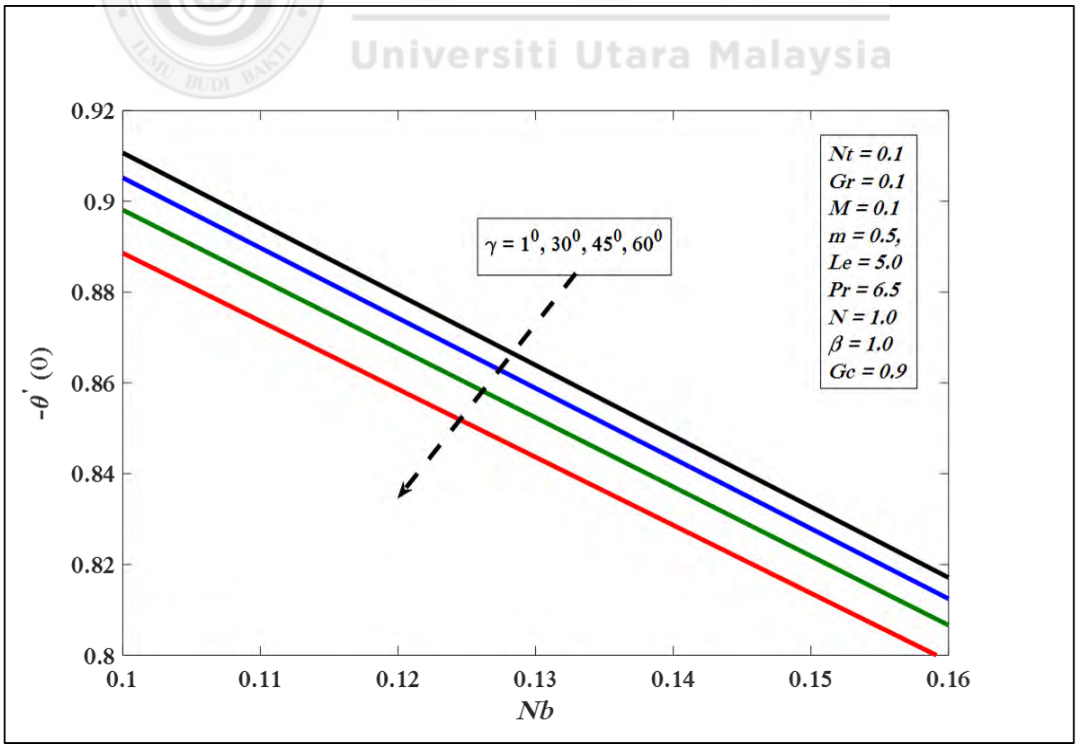

Figure 7.8. $-\theta'(0)$ against Nb for several values of γ.

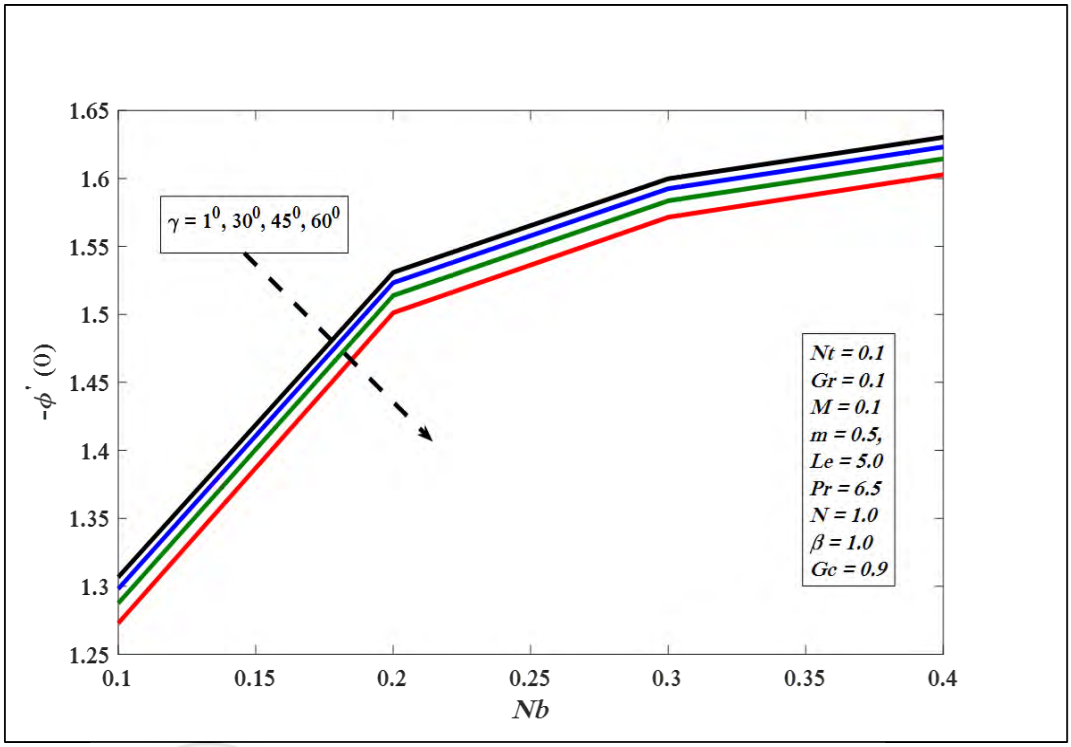

Figure 7.9. $-\phi'(0)$ against Nb for several values of γ.

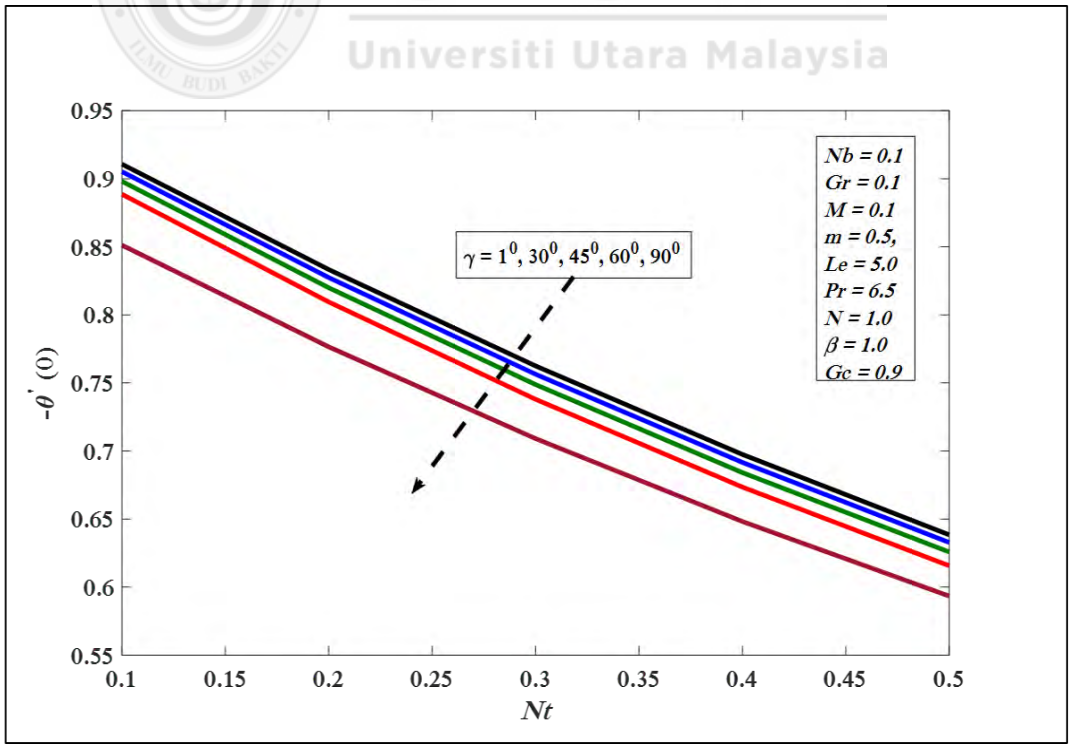

Figure 7.10. $-\theta'(0)$ against Nt for several values of γ.

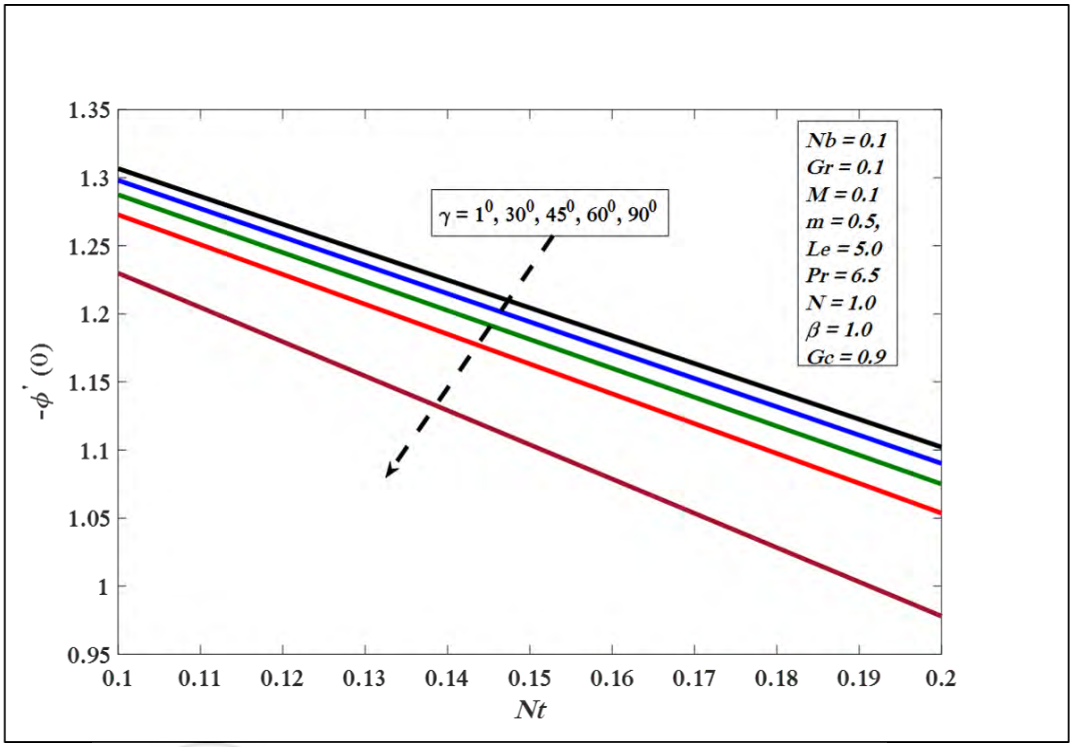

Figure 7.11. $-\phi'(0)$ against Nt for several values of γ.

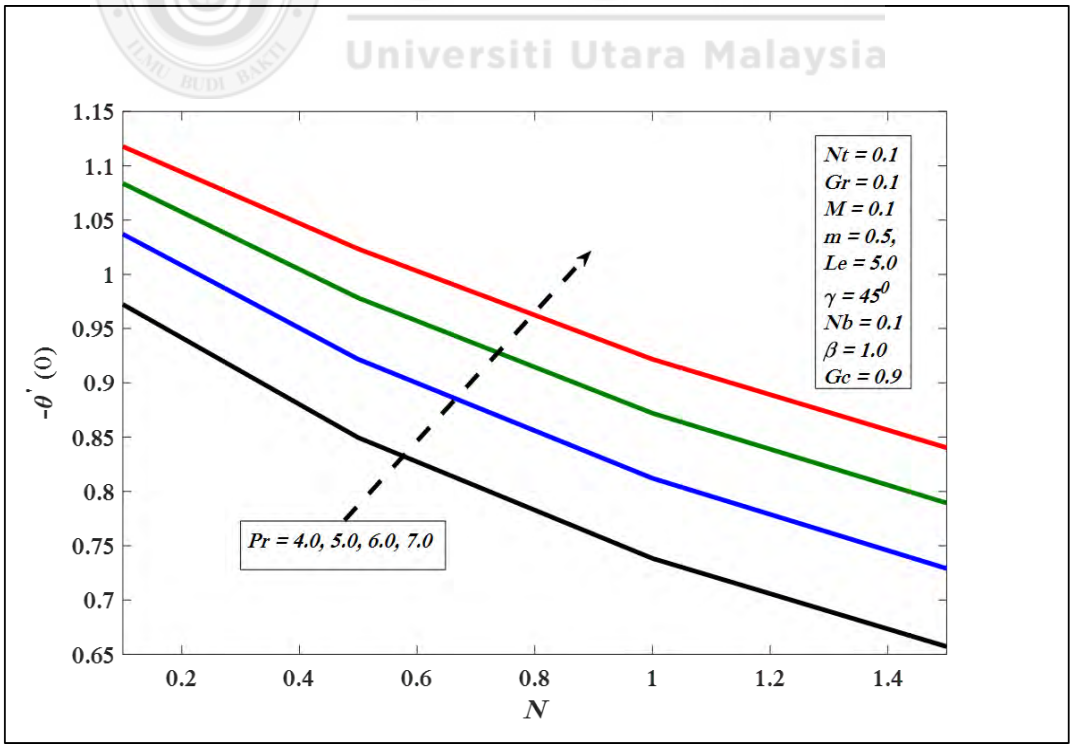

Figure 7.12. $-\theta'(0)$ against N for several values of Pr.

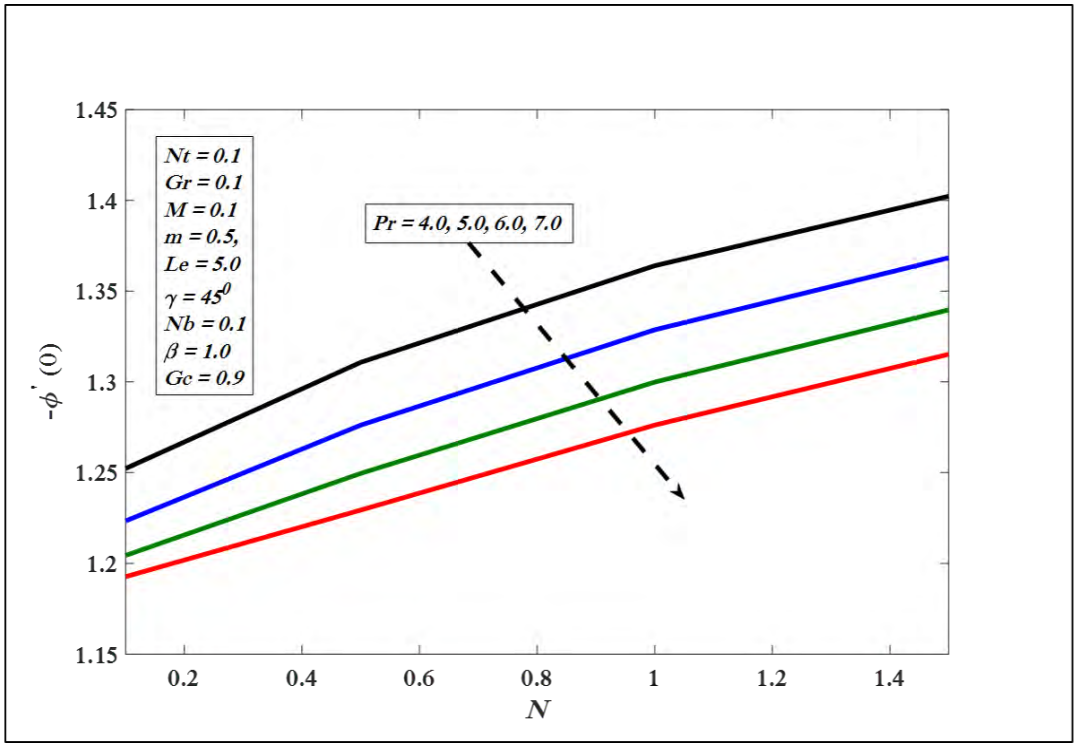

Figure 7.13. $-\phi'(0)$ against N for several values of Pr.

7.4 Conclusions

Heat and species transfer of Casson nanofluid flow towards nonlinear slanted stretching surface is under consideration in this problem. In addition MHD along with thermal radiations effects are investigated numerically. For numerical solution first momentum, energy and mass equations are converted into ordinary differential equations form by utilizing suitable transformations then apply Keller box scheme and recovered numerical outcomes. In this problem we examined the Prandtl number along with thermal radiations influence on our concern physical quantities such as Nusselt number, Sherwood number through graphs. The main conclusions of this problem are given as:

1. Heat transfer rate increases against higher values of Prandtl number and thermal radiations while mass transfer rate reduces.

2. $-\phi'(0)$ and $-\theta'(0)$ decrease with increase in inclination and thermophoretic effects.

3. $-\phi'(0)$ and $-\theta'(0)$ decline against higher values of nonlinear stretching parameter.

CHAPTER EIGHT

CONCLUSION AND AREA OF FUTURE WORK

8.1 Summary of Research

In Chapter 1, background of research, problem statements, objectives and scope of study, significance of study and thesis outline were presented while in Chapter 2, literature review of the problems were revealed. In this thesis, 5 different problems concerning energy and mass transport of magnetohydrodynamic (MHD) boundary layer flow of non-Newtonian nanofluid over an inclined stretching surface were discussed. The first problem focused on MHD boundary layer flow of micropolar nanofluid flow over a linear inclined streching surface. In the second problem, heat generation or absorption with chemical reaction effects were considered over a permeable linear inclined stretching surface which was the extension of the first problem. Moreover, third problem presented micropolar nanofluid flow for power law stretching inclined surface. Problem four was considered for Casson nanofluid flow along linear slanted geometry. In the same vein, the last problem explained radiation effects over Casson nanofluid for the power law inclined stretching surface.

For numerical simulation of all above stated problems, a very efficient numerical technique known as the Keller box scheme were utilized. In all these problems of micropolar nanofluid and Casson nanofluid flow, velocity, temperature, concentration and micro-rotation profiles along with skin friction coefficient and Sherwood number for wide range of flow factors were studied. The model under consideration for first problem consists on the effects of Nb, Nt, $K, Pr, Le, Gr_x, Gc_x, \gamma$, and M. By considering $Gr, Gc, M, K = 0$ with $\gamma = 90^0$ and $Pr = Le = 10$, the current

outcomes matched with already published results (see Table 3.1). It is eminent that $C_{fx}(0)$ upsurges with the improved magnitudes of Le, M, Nb, K, γ and reduces with the increment in Gr, Gc, Pr, Nt. Results with the growth of $Nt, Gr, Gc, Le, K, Nb, Pr$ presented that $-\phi^{'}(0)$ increases while decreases with the increase in γ, M. Whereas, $-\theta^{'}(0)$ increases against the upsurge magnitudes of Pr, Gr, K, Gc and declines by enhancing γ, M, Nb, Le, Nt. Moreover, $-\theta^{'}(0)$ and $-\phi^{'}(0)$ versus Nb and Nt decreases on improving the inclination factor shown in Figures 3.23 to 3.26. Whereas, $-\theta^{'}(0)$ and $-\phi^{'}(0)$ versus Nb and Nt increases on the increments in K (see Figures 3.27 to 3.30).

The second problem discussed in the Chapter 4, which focused on permeable inclined stretching surface, where suction or injection effect were taken into account. In this problem, the current results reduced to Khan and Pop (2010) taking $Gr, Gc, M, K, \lambda_1, R = 0$ with $\gamma = 90^0$ and $Pr = Le = 10$. Table 4.1 exhibits that $C_{fx}(0)$ reveals quite opposite outcomes for $S > 0$ and for $S < 0$. Further, $C_{fx}(0)$ increases for the increasing magnitudes of λ_1 and R. Whereas, $-\theta^{'}(0)$ increases against $S > 0$ and declines verses $S < 0$. On the other hand, $-\theta^{'}(0)$ shows decrease for the increment in R and λ_1. Besides, $-\phi^{'}(0)$ improves by improving R and λ_1 numerically. In Figures 4.7 and 4.8, $-\theta^{'}(0)$ and $-\phi^{'}(0)$ versus M upturns with the increment in S. Whereas, Figures 4.11 and 4.12 show opposite results for $-\theta^{'}(0)$ and $-\phi^{'}(0)$ versus R with the growth of Nb and Nt.

The problem examined in Chapter 5 focuses on an incompressible flow of micropolar nanofluid over a power law slanted extending surface. In this problem an additional effect of nonlinear stretching parameter m was considered. The results shown in Table 5.1 exhibit that $-\phi^{'}(0)$ shows an inverse relation with m, M and γ. Whereas, $C_{fx}(0)$ presents a direct relation with m. Moreover, it is found that enhancement in

m means reduction in $-\theta^{'}(0)$. On the other hand, the enhancement in factor m slows down the velocity of the fluid (see Figure 5.8) and upturns $\theta(\eta)$ and $\phi(\eta)$ shown in Figures 5.9 and 5.10. Further,in Chapter 5 thermal radiations and convective boundary conditions are investigated over power law inclined stretching surface. By Putting $N = 0$ and $\gamma_1 \to \infty$, the problem under concern reduces to the problem discussed in the previous Section 5.2. Table 5.2 shows that $-\theta^{'}(0)$ decreases on increasing factors γ_1 and N and $-\phi^{'}(0)$ increases with the increase in N and γ_1. Whereas, in the case of $C_{fx}(0)$, the enhancement in γ_1 shows direct correspondence with $C_{fx}(0)$ and the increase in N shows inverse relation with $C_{fx}(0)$. Further, $\theta(\eta)$ and $\phi(\eta)$ upturns with the enhancement in γ_1 and N. Whereas, $-\theta^{'}(0)$ increases versus N for the higher magnitudes of γ_1 and $-\phi^{'}(0)$ decreases on the improvement of γ_1 and N as shown in Figures 5.33 and 5.34. Similarly, in Figure 5.35 $-\theta^{'}(0)$ decreases against the increment in Nb and γ_1 while $-\phi^{'}(0)$ increases in Figure 5.36.

Table 8.1
Summary of results in problems 1, 2 and 3 for the local Nusselt number $-\theta'(0)$, the local Sherwood number $-\phi'(0)$ and Skin-friction coefficient $C_{fx}(0)$.

Problems	Parameters	$-\theta'(0)$	$-\phi'(0)$	$C_{fx}(0)$
	Nb	$\downarrow$	$\uparrow$	$\uparrow$
	Nt	$\downarrow$	$\uparrow$	$\downarrow$
	Pr	$\uparrow$	$\uparrow$	$\downarrow$
	Le	$\downarrow$	$\uparrow$	$\uparrow$
1	M	$\downarrow$	$\downarrow$	$\uparrow$
	K	$\uparrow$	$\uparrow$	$\uparrow$
	Gr	$\uparrow$	$\uparrow$	$\downarrow$
	Gc	$\uparrow$	$\uparrow$	$\downarrow$
	γ	$\downarrow$	$\downarrow$	$\uparrow$
	λ_1	$\downarrow$	$\uparrow$	$\uparrow$
	$S > 0$	$\uparrow$	$\uparrow$	$\uparrow$
2	$S < 0$	$\downarrow$	$\downarrow$	$\downarrow$
	R	$\downarrow$	$\uparrow$	$\uparrow$
	γ	$\downarrow$	$\downarrow$	$\uparrow$
	Nb	$\downarrow$	$\uparrow$	$\downarrow$
3	Pr	$\uparrow$	$\uparrow$	$\uparrow$
	m	$\downarrow$	$\downarrow$	$\uparrow$

The Casson nanofluid flow over an inclined stretching surface is discussed in Chapter 6. For the accuracy of results, by considering $M, Gr, Gc = 0$, with $\beta \to \infty$, $Le = Pr = 10$ and $\gamma = 90^0$, matched our outcomes with Khan and Pop (2010) which shows good agreement. From Table 6.1 it is observed that $-\theta^{'}(0)$ and $-\phi^{'}(0)$ enhances by enhancing β. Moreover, $C_{fx}(0)$ diminishes because of the increase in β. Whereas, due to the growing magnitudes of γ, $-\theta^{'}(0)$ and $-\phi^{'}(0)$ were reduced. From Figure 6.4 it is clearly seen $f^{'}(\eta)$ falls while $\theta(\eta)$ and $\phi(\eta)$ upturn against different numeric of β. In addition, $-\theta^{'}(0)$ and $-\phi^{'}(0)$ versus Nb drop for the enhancement in γ (see Figures 6.22 and 6.23). The similar effect can be seen in Figures 6.24 and 6.25 for $-\theta^{'}(0)$ and $-\phi^{'}(0)$ versus Nt on improving γ. In Chapter 7, final problem is probed for power law inclined extending surface with the addition of radiations effect. The numerical outcomes of this problem for M, Gr, Gc and $N = 0$, with $\beta \to \infty$, $Le = Pr = 10$ and $m = 1$, $\gamma = 90^0$ where compared with available literature found a decent settlement. Moreover, $-\theta^{'}(0)$ and $-\phi^{'}(0)$ diminish against altered magnitudes of m while $C_{fx}(0)$ increases exhibited in Table 7.1. Further, $-\theta^{'}(0)$ decreases with the increase in N. Besides, $-\phi^{'}(0)$ and $C_{fx}(0)$ increases by increasing N. Moreover, $f^{'}(\eta)$ drops while $\theta(\eta)$ and $\phi(\eta)$ upsurge versus m (see Figures 7.1 to 7.3). Further, $\theta(\eta)$ boosts due to the increase in N shown in Figure 7.7. In Figure 7.12, $-\theta^{'}(0)$ shows a direct relation with Pr and N. Whereas, $-\phi^{'}(0)$ shows an inverse relation with N and Pr in Figure 7.13.

Table 8.2
Summary of results in problems 4 and 5 for the local Nusselt number $-\theta'(0)$, the local Sherwood number $-\phi'(0)$ and Skin-friction coefficient $C_{fx}(0)$.

Problems	Parameters	$-\theta'(0)$	$-\phi'(0)$	$C_{fx}(0)$
	Gr	$\downarrow$	$\downarrow$	$\uparrow$
4	β	$\uparrow$	$\uparrow$	$\downarrow$
	Nt	$\downarrow$	$\downarrow$	$\downarrow$
	Pr	$\uparrow$	$\downarrow$	$\downarrow$
5	N	$\downarrow$	$\uparrow$	$\uparrow$
	β	$\downarrow$	$\downarrow$	$\uparrow$
	m	$\downarrow$	$\downarrow$	$\uparrow$

8.2 Suggestions for Future Work

The field with energy and mass transport can be unsteady due to sudden stretching of the sheet or by a step change of heat flux or temperature. Moreover, an inviscid flow is developed instantaneously, if the surface is impulsively stretched with certain velocity. However, the flow in the viscous layer near the sheet develop slowly, and it becomes fully developed steady flow after a certain amount of time (Sharidan et al., 2006). Madhu et al. (2017) discussed the radiations effect on the unsteady flow of Maxwell nanofluid with energy and mass exchange over a stretching surface. Mabood and Shateyi (2019) examined the heat and mass exchange of unsteady flow with radiation and magnetic effect over a stretching surface. Further, the boundary layer flow for slanted stretching surface play a significant role in the field of engineering and industry. Therefore, studied problems can be extended for different geometries. Recently, Khan et al. (2017) investigated Carreau nanofluid flow over a slanted stretching cylinder by incorporating convective boundary conditions. Saeed et al. (2019) discussed the Casson nanofluid flow over a slanted disk. In view of the above stated literature, the studied problems can be extended for unsteady nanofluid problems and for stretching inclined sphere, cylinder, and disk. Therefor for future research there are a few cases which can be considered which are:

1. Boundary layer flow of unsteady nanofluid for inclined geometry and porous medium.

2. Tewari and Das model for inclined stretching/shrinking surface.

3. Using Keller box scheme for non-similarity partial differential equations for all problems considered in this thesis.

4. All studied problems can be extended for stretching inclined cylinder, disk and sphere.

5. Boundary layer flow for stretching/shrinking inclined surface in different types of

fluids for instance Maxwell nanofluid and Carreau nanofluid.

REFERENCES

Abbas, Z. (2009). *Numerical and series solutions for flows of non-linear fluids*. PhD thesis, Quaid-I-Azam University Islamabad.

Abbas, Z. and Hayat, T. (2011). Stagnation slip flow and heat transfer over a nonlinear stretching sheet. *Numerical Methods for Partial Differential Equations*, 27(2):302–314.

Afify, A. A. (2009). Similarity solution in mhd: effects of thermal diffusion and diffusion thermo on free convective heat and mass transfer over a stretching surface considering suction or injection. *Communications in Nonlinear Science and Numerical Simulation*, 14(5):2202–2214.

Afridi, M. I., Qasim, M., Khan, I., Shafie, S., and Alshomrani, A. S. (2017). Entropy generation in magnetohydrodynamic mixed convection flow over an inclined stretching sheet. *Entropy*, 19(1):10.

Ajayi, T., Omowaye, A., and Animasaun, I. (2017). Viscous dissipation effects on the motion of casson fluid over an upper horizontal thermally stratified melting surface of a paraboloid of revolution: Boundary layer analysis. *Journal of Applied Mathematics*, 2017.

Alam, M., Rahman, M., and Sattar, M. (2008). Effects of variable suction and thermophoresis on steady mhd combined free-forced convective heat and mass transfer flow over a semi-infinite permeable inclined plate in the presence of thermal radiation. *International Journal of Thermal Sciences*, 47(6):758–765.

Anderson Jr, J. D. (2010). *Fundamentals of aerodynamics*. Tata McGraw-Hill Education.

Animasaun, I. (2015). Effects of thermophoresis, variable viscosity and thermal conductivity on free convective heat and mass transfer of non-darcian mhd dissipative

casson fluid flow with suction and nth order of chemical reaction. *Journal of the Nigerian Mathematical Society*, 34(1):11–31.

Animasaun, I., Adebile, E., and Fagbade, A. (2016). Casson fluid flow with variable thermo-physical property along exponentially stretching sheet with suction and exponentially decaying internal heat generation using the homotopy analysis method. *Journal of the Nigerian Mathematical Society*, 35(1):1–17.

Anjali Devi, S. and Suriyakumar, P. (2017). Effect of magnetic field on blasius and sakiadis flow of nanofluids past an inclined plate. *Journal of Taibah University for Science*, 11(6):1275–1288.

Anwar, M., Shafie, S., Hayat, T., Shehzad, S., and Salleh, M. (2017). Numerical study for mhd stagnation-point flow of a micropolar nanofluid towards a stretching sheet. *Journal of the Brazilian Society of Mechanical Sciences and Engineering*, 39(1):89–100.

Anwar, M. I. (2013). *Heat and Mass Transfer of Magnetohydrodynamic Boundary Layer Stagnation Point Flow of Nanofluid over a Stretching Surface*. PhD thesis, Universiti Teknologi Malalaysia.

Arifin, N. M., Nazar, R., and Pop, I. (2011). Viscous flow due to a permeable stretching/shrinking sheet in a nanofluid. *Sains Malaysiana*, 40(12):1359–1367.

Ashraf, M. B., Hayat, T., Shehzad, S., and Alsaedi, A. (2015). Mixed convection radiative flow of three dimensional maxwell fluid over an inclined stretching sheet in presence of thermophoresis and convective condition. *AIP advances*, 5(2):027134.

Babu, S. R., Babu, P. R., and Rambabu, V. (2013). Effects of some parameters on thermal conductivity of nanofluids and mechanisms of heat transfer improvement. *International Journal of Engineering Research and Applications*, 3(4):2136–2140.

Barnes, H. A., Hutton, J. F., and Walters, K. (1989). *An introduction to rheology*, volume 3. Elsevier.

Bejan, A. (2013). *Convection heat transfer*. John wiley & sons.

Bergman, T. L., Incropera, F. P., DeWitt, D. P., and Lavine, A. S. (2011). *Fundamentals of heat and mass transfer*. John Wiley & Sons.

Bohra, S. and Jain, S. (2017). Heat and mass transfer over a three-dimensional inclined non-linear stretching sheet with convective boundary conditions. *Indian Journal of Pure & Applied Physics (IJPAP)*, 55(12):847–856.

Buongiorno, J. (2006). Convective transport in nanofluids. *Journal of heat transfer*, 128(3):240–250.

Cebeci, T. and Bradshaw, P. (2012). *Physical and computational aspects of convective heat transfer*. Springer Science & Business Media.

Chamkha, A. J. (2000). Transient hydromagnetic three-dimensional natural convection from an inclined stretching permeable surface. *Chemical Engineering Journal*, 76(2):159–168.

Chamkha, A. J. and Khaled, A.-R. A. (2001). Similarity solutions for hydromagnetic simultaneous heat and mass transfer by natural convection from an inclined plate with internal heat generation or absorption. *Heat and Mass Transfer*, 37(2):117–123.

Chandrasekar, M. and Suresh, S. (2009). A review on the mechanisms of heat transport in nanofluids. *Heat Transfer Engineering*, 30(14):1136–1150.

Chen, C.-H. (2004). Heat and mass transfer in mhd flow by natural convection from a permeable, inclined surface with variable wall temperature and concentration. *Acta Mechanica*, 172(3):219–235.

Chen, C.-H. (2008). Effects of magnetic field and suction/injection on convection heat transfer of non-newtonian power-law fluids past a power-law stretched sheet with surface heat flux. *International Journal of Thermal Sciences*, 47(7):954–961.

Chen, T., Tien, H.-C., and Armaly, B. F. (1986). Natural convection on horizontal, inclined, and vertical plates with variable surface temperature or heat flux. *International Journal of Heat and Mass Transfer*, 29(10):1465–1478.

Chiam, T. (1995). Hydromagnetic flow over a surface stretching with a power-law velocity. *International Journal of Engineering Science*, 33(3):429–435.

Choi, S. and Eastman, J. (1995). Asme international mechanical engineering congress and exposition. *San Francisco, CA*, pages 12–17.

Chon, C. and Kihm, K. (2005). Thermal conductivity enhancement of nanofluids by brownian motion. *Journal of Heat Transfer*, 127(8):810–810.

Chopkar, M., Das, P. K., and Manna, I. (2006). Synthesis and characterization of nanofluid for advanced heat transfer applications. *Scripta Materialia*, 55(6):549–552.

Cortell, R. (2007). Viscous flow and heat transfer over a nonlinearly stretching sheet. *Applied Mathematics and Computation*, 184(2):864–873.

Crane, L. J. (1970). Flow past a stretching plate. *Zeitschrift für angewandte Mathematik und Physik ZAMP*, 21(4):645–647.

Currie, R. G. (1974). Period and qw of the chandler wobble. *Geophysical Journal International*, 38(1):179–185.

Das, S., Jana, R., and Makinde, O. (2015). Magnetohydrodynamic mixed convective slip flow over an inclined porous plate with viscous dissipation and joule heating. *Alexandria Engineering Journal*, 54(2):251–261.

Das, S. K., Choi, S. U., Yu, W., and Pradeep, T. (2007). *Nanofluids: science and technology*. John Wiley & Sons.

Demuren, A. and Grotjans, H. (2009). Buoyancy-driven flows—beyond the boussinesq approximation. *Numerical Heat Transfer, Part B: Fundamentals*, 56(1):1–22.

Deswita, L., Nazar, R., Ishak, A., Ahmad, R., and Pop, I. (2010). Mixed convection boundary layer flow past a wedge with permeable walls. *Heat and Mass Transfer*, 46(8-9):1013–1018.

Devanathan, R. and Parvathamma, S. (1983). Flow of micropolar fluid through a tube with stenosis. *Medical and Biological Engineering and Computing*, 21(4):438–445.

Eastman, J., Choi, U., Li, S., Thompson, L., and Lee, S. (1996). Enhanced thermal conductivity through the development of nanofluids. In *MRS proceedings*, volume 457, page 3. Cambridge Univ Press.

Eringen, A. C. (1964). Simple microfluids. *International Journal of Engineering Science*, 2(2):205–217.

Eringen, A. C. (1966). Theory of micropolar fluids. *Journal of Mathematics and Mechanics*, pages 1–18.

Fatunmbi, E. O. and Okoya, S. S. (2020). Heat transfer in boundary layer magneto-micropolar fluids with temperature-dependent material properties over a stretching sheet. *Advances in Materials Science and Engineering*, 2020.

Fox, R. W. and McDonald, A. T. (1994). *Introduction to fluid mechanics*. John Wiley.

Ghadikolaei, S., Hosseinzadeh, K., Ganji, D., and Jafari, B. (2018). Nonlinear thermal radiation effect on magneto casson nanofluid flow with joule heating effect over an inclined porous stretching sheet. *Case Studies in Thermal Engineering*, 12:176–187.

Guohua, L. (1999). *The Microchannel Flow of a Micropolar Fluid*. PhD thesis, Louisiana Tech University.

Ibrahim, W. and Gamachu, D. (2020). Dusty nanofluid past a centrifugally stretching surface. *Mathematical Problems in Engineering*, 2020.

Ilias, M. R., Rawi, N. A., and Shafie, S. (2016). Mhd free convection flow and heat transfer of ferrofluids over a vertical flat plate with aligned and transverse magnetic field. *Indian Journal of Science and Technology*, 9:36.

Imtiaz, M., Nazar, H., Hayat, T., and Alsaedi, A. (2020). Soret and dufour effects in the flow of viscous fluid by a curved stretching surface. *Pramana*, 94(1):1–11.

Ishak, A., Nazar, R., and Pop, I. (2008). Uniform suction/blowing effect on flow and heat transfer due to a stretching cylinder. *Applied Mathematical Modelling*, 32(10):2059–2066.

Ishak, A., Yacob, N. A., and Bachok, N. (2011). Radiation effects on the thermal boundary layer flow over a moving plate with convective boundary condition. *Meccanica*, 46(4):795–801.

Jain, P. and Chaudhary, R. (2013). Closed form solution of heat and mass transfer past an inclined oscillating surface with newtonian heating under the effect of thermal radiation and mass diffusion. *Adv Appl Sci Res*, 4(6):285–306.

Jaluria, Y. (1980). Natural convection, heat and mass transfer. In *Unknown Host Publication Title*. Pergamon Press.

Jamaludin, A., Nazar, R., and Pop, I. (2018). Three-dimensional magnetohydrodynamic mixed convection flow of nanofluids over a nonlinearly permeable stretching/shrinking sheet with velocity and thermal slip. *Applied Sciences*, 8(7):1128.

Jang, S. P. and Choi, S. U. (2004). Role of brownian motion in the enhanced thermal conductivity of nanofluids. *Applied Physics Letters*, 84(21):4316–4318.

Jena, S. K. and Mathur, M. (1981). Similarity solutions for laminar free convection flow of a thermomicropolar fluid past a non-isothermal vertical flat plate. *International Journal of Engineering Science*, 19(11):1431–1439.

Kebede, T., Haile, E., Awgichew, G., and Walelign, T. (2020). Heat and mass transfer in unsteady boundary layer flow of williamson nanofluids. *Journal of Applied Mathematics*, 2020.

Keblinski, P., Eastman, J. A., and Cahill, D. G. (2005). Nanofluids for thermal transport. *Materials Today*, 8(6):36–44.

Keller, H. B. and Cebeci, T. (1972). Accurate numerical methods for boundary-layer flows. ii: Two dimensional turbulent flows. *AIAA Journal*, 10(9):1193–1199.

Khan, I., Malik, M., Hussain, A., Khan, M., et al. (2017). Magnetohydrodynamics carreau nanofluid flow over an inclined convective heated stretching cylinder with joule heating. *Results in Physics*, 7:4001–4012.

Khan, M., Sardar, H., Gulzar, M. M., and Alshomrani, A. S. (2018). On multiple solutions of non-newtonian carreau fluid flow over an inclined shrinking sheet. *Results in Physics*, 8:926–932.

Khan, N. S., Shah, Q., Bhaumik, A., Kumam, P., Thounthong, P., and Amiri, I. (2020). Entropy generation in bioconvection nanofluid flow between two stretchable rotating disks. *Scientific Reports*, 10(1):1–26.

Khan, W. and Pop, I. (2010). Boundary-layer flow of a nanofluid past a stretching sheet. *International Journal of Heat and Mass Transfer*, 53(11-12):2477–2483.

Koriko, O. K., Oreyeni, T., Omowaye, A. J., and Animasaun, I. L. (2016). Homotopy analysis of mhd free convective micropolar fluid flow along a vertical surface embedded in non-darcian thermally-stratified medium. *Open Journal of Fluid Dynamics*, 6(3):198–221.

Kumar, M. S., Sandeep, N., Kumar, B. R., and Saleem, S. (2017). A comparative study of chemically reacting 2d flow of casson and maxwell fluids. *Alexandria Engineering Journal*.

Leal, L. G. (1992). *Laminar flow and convective transport processes*, volume 251. Elsevier.

Lee, H.-R., Chen, T., and Armaly, B. F. (1992). Non-parallel thermal instability of natural convection flow on non-isothermal inclined flat plates. *International Journal of Heat and Mass Transfer*, 35(1):207–220.

Lok, Y. Y. (2008). *Mathematical modelling of a micropolar fluid boundary layer near a stagnation-point*. PhD thesis, Universiti Teknologi Malalaysia.

Lukaszewicz, G. (1999). *Micropolar fluids: theory and applications*. Springer Science & Business Media.

Mabood, F. and Shateyi, S. (2019). Multiple slip effects on mhd unsteady flow heat and mass transfer impinging on permeable stretching sheet with radiation. *Modelling and Simulation in Engineering*, 2019.

Madhu, M., Kishan, N., and Chamkha, A. J. (2017). Unsteady flow of a maxwell nanofluid over a stretching surface in the presence of magnetohydrodynamic and thermal radiation effects. *Propulsion and Power research*, 6(1):31–40.

Majid, N. A., Mohammad, N. F., Kasim, A. R. M., Ilias, M. R., and Shafie, S. (2019). Effect of constant heat flux on force convective miropolar fluid flow over a surface of another quiescent fluid. *Universal Journal of Mechanical Engineering*, 7(4):198–205.

Makinde, O. D. and Olanrewaju, P. (2010). Buoyancy effects on thermal boundary layer over a vertical plate with a convective surface boundary condition. *Journal of Fluids Engineering*, 132(4):044502.

Michaelides, E. E. (2015). Brownian movement and thermophoresis of nanoparticles in liquids. *International Journal of Heat and Mass Transfer*, 81:179–187.

Mishra, S., Baag, S., and Mohapatra, D. (2016). Chemical reaction and soret effects on hydromagnetic micropolar fluid along a stretching sheet. *Engineering Science and Technology, an International Journal*, 19(4):1919–1928.

Mondal, S. K. and Pal, D. (2020). Computational analysis of bioconvective flow of nanofluid containing gyrotactic microorganisms over a nonlinear stretching sheet with variable viscosity using ham. *Journal of Computational Design and Engineering*, 7(2):251–267.

Mucoglu, A. and Chen, T. (1979). Mixed convection on inclined surfaces. *Journal of Heat Transfer*, 101(3):422–426.

Nakamura, M. and Sawada, T. (1988). Numerical study on the flow of a non-newtonian fluid through an axisymmetric stenosis. *Journal of Biomechanical Engineering*, 110(2):137–143.

Nazar, R. M. (2004). *Mathematical models for free and mixed convection boundary layer flows of micropolar fluids*. PhD thesis, Universiti Teknologi Malaysia.

Olanrewaju, P. and Hayat, T. (2014). The effects of buoyancy and transpiration on the flow and heat transfer over a moving permeable surface in a parallel stream in the presence of radiation. *International Journal for Computational Methods in Engineering Science and Mechanics*, 15(4):330–336.

Palani, G. (2001). Free convection effects on inclined plate.

Peng, Y., Alsagri, A. S., Afrand, M., and Moradi, R. (2019). A numerical simulation for magnetohydrodynamic nanofluid flow and heat transfer in rotating horizontal annulus with thermal radiation. *RSC advances*, 9(39):22185–22197.

Pfautsch, E. (2008). *Forced convection in nanofluids over a flat plate*. University of Missouri-Columbia.

Rahman, M. M., Aziz, A., and Al-Lawatia, M. A. (2010). Heat transfer in micropolar fluid along an inclined permeable plate with variable fluid properties. *International Journal of Thermal Sciences*, 49(6):993–1002.

Ramesh, G., Chamkha, A., and Gireesha, B. (2016). Boundary layer flow past an inclined stationary/moving flat plate with convective boundary condition. *Afrika Matematika*, 27(1-2):87–95.

Ramesh, G., Gireesha, B., and Bagewadi, C. (2012). Heat transfer in mhd dusty boundary layer flow over an inclined stretching sheet with non-uniform heat source/sink. *Advances in Mathematical Physics*, 2012.

Rashad, A. M. (2017). Unsteady nanofluid flow over an inclined stretching surface with convective boundary condition and anisotropic slip impact. *International Journal of Heat and Technology*, 35(1):82–90.

Rawi, N. A. (2018). *g-jitter induced mixed convection flow of Newtonian and non-Newtonian nanofluid past an inclined stretching sheet*. PhD thesis, Universiti Teknologi Malalaysia.

Rawi, N. A., Kasim, M., Rahman, A., Mat Isa, Z., Mangi, A., and Shafie, S. (2017). G-jitter effects on the mixed convection flow of nanofluid past an inclined stretching sheet. *Frontiers in Heat and Mass Transfer (FHMT)*, 8.

Reddy, M. G. and Ferdows, M. (2020). Species and thermal radiation on micropolar hydromagnetic dusty fluid flow across a paraboloid revolution. *Journal of Thermal Analysis and Calorimetry*, pages 1–19.

Reddy, P. B. A. (2016). Magnetohydrodynamic flow of a casson fluid over an exponentially inclined permeable stretching surface with thermal radiation and chemical reaction. *Ain Shams Engineering Journal*, 7(2):593–602.

Reddy, P. S., Chamkha, A. J., and Al-Mudhaf, A. (2017). Mhd heat and mass transfer flow of a nanofluid over an inclined vertical porous plate with radiation and heat generation/absorption. *Advanced Powder Technology*, 28(3):1008–1017.

Rohsenow, W. M., Hartnett, J. P., Cho, Y. I., et al. (1998). *Handbook of heat transfer*, volume 3. McGraw-Hill New York.

Rosca, N. C., Grosan, T., and Pop, I. (2012). Stagnation-point flow and mass transfer with chemical reaction past a permeable stretching/shrinking sheet in a nanofluid. *Sains Malaysiana*, 41(10):1271–1279.

Roy, G., Nguyen, C. T., and Lajoie, P.-R. (2004). Numerical investigation of laminar flow and heat transfer in a radial flow cooling system with the use of nanofluids. *Superlattices and Microstructures*, 35(3):497–511.

Saeed, A., Shah, Z., Islam, S., Jawad, M., Ullah, A., Gul, T., and Kumam, P. (2019). Three-dimensional casson nanofluid thin film flow over an inclined rotating disk with the impact of heat generation/consumption and thermal radiation. *Coatings*, 9(4):248.

Sakiadis, B. (1961). Boundary-layer behavior on continuous solid surfaces: I. boundary-layer equations for two-dimensional and axisymmetric flow. *AIChE Journal*, 7(1):26–28.

Sandeep, N. and Kumar, M. J. (2016). Heat and mass transfer in nanofluid flow over an inclined stretching sheet with volume fraction of dust and nanoparticles. *Journal of Applied Fluid Mechanics*, 9(5):2205–2215.

Schlichting, H., Gersten, K., Krause, E., Oertel, H., and Mayes, K. (1960). *Boundary-layer theory*, volume 7. Springer.

Seth, G., Mishra, M., and Chamkha, A. (2016). Hydromagnetic convective flow of viscoelastic nanofluid with convective boundary condition over an inclined stretching sheet. *Journal of Nanofluids*, 5(4):511–521.

Shah, Z., Kumam, P., and Deebani, W. (2020). Radiative mhd casson nanofluid flow with activation energy and chemical reaction over past nonlinearly stretching surface through entropy generation. *Scientific Reports*, 10(1):1–14.

Shamshuddin, M. and Thumma, T. (2019). Numerical study of a dissipative micropolar fluid flow past an inclined porous plate with heat source/sink. *Propulsion and Power Research*, 8(1):56–68.

Sharidan, S., Mahmood, M., and Pop, I. (2006). Similarity solutions for the unsteady boundary layer flow and heat transfer due to a stretching sheet. *Applied Mechanics and Engineering*, 11(3):647.

Sharma, A. K., Tiwari, A. K., and Dixit, A. R. (2016). Rheological behaviour of nanofluids: a review. *Renewable and Sustainable Energy Reviews*, 53:779–791.

Sharma, S. and Deka, R. K. (2012). Chemical reaction effects on mhd mixed convection flow of water at maximum density past a vertical plate under variable temperature. *IOSR Journal of Applied Physics*, 1(2):1–7.

Shehzad, S., Hayat, T., Qasim, M., and Asghar, S. (2013). Effects of mass transfer on mhd flow of casson fluid with chemical reaction and suction. *Brazilian Journal of Chemical Engineering*, 30(1):187–195.

Shit, G. and Majee, S. (2014). Hydromagnetic flow over an inclined non-linear stretching sheet with variable viscosity in the presence of thermal radiation and chemical reaction. *Journal of Applied Fluid Mechanics*, 7(2):239–247.

Singh, G. and Makinde, O. D. (2012). Computational dynamics of mhd free convection flow along an inclined plate with newtonian heating in the presence of volumetric heat generation. *Chemical Engineering Communications*, 199(9):1144–1154.

Sudarsana Reddy, P. and Sreedevi, P. (2020). Impact of chemical reaction and double stratification on heat and mass transfer characteristics of nanofluid flow over porous stretching sheet with thermal radiation. *International Journal of Ambient Energy*, pages 1–11.

Suriyakumar, P. and Devi, S. A. (2015). Effects of suction and internal heat generation on hydromagnetic mixed convective nanofluid flow over an inclined stretching plate. *European Journal of Advances in Engineering and Technology*, 2(3):51–58.

Tlili, I. (2019). Effects mhd and heat generation on mixed convection flow of jeffrey fluid in microgravity environment over an inclined stretching sheet. *Symmetry*, 11(3):438.

Tyndall, J. (1870). On haze and dust. *Nature*, 1(13):339–42.

Uddin, M. J. (2011). Convective flow of micropolar fluids along an inclined flat plate with variable electric conductivity and uniform surface heat flux. *Daffodil International University Journal of Science and Technology*, 6(1):69–79.

Ullah, I., Nisar, K. S., Shafie, S., Khan, I., Qasim, M., and Khan, A. (2019). Unsteady free convection flow of casson nanofluid over a nonlinear stretching sheet. *IEEE Access*, 7:93076–93087.

Usman, M., Soomro, F. A., Haq, R. U., Wang, W., and Defterli, O. (2018). Thermal and velocity slip effects on casson nanofluid flow over an inclined permeable stretching cylinder via collocation method. *International Journal of Heat and Mass Transfer*, 122:1255–1263.

Vajravelu, K. (2001). Viscous flow over a nonlinearly stretching sheet. *Applied Mathematics and Computation*, 124(3):281–288.

Venkatesan, J., Sankar, D., Hemalatha, K., and Yatim, Y. (2013). Mathematical analysis of casson fluid model for blood rheology in stenosed narrow arteries. *Journal of Applied Mathematics*, 2013.

Yu, W.-S. and Lin, H.-T. (1988). Free convection heat transfer from an isothermal plate with arbitrary inclination. *Wärme-und Stoffübertragung*, 23(4):203–211.

Zaimi, K., Ishak, A., and Pop, I. (2014). Boundary layer flow and heat transfer over a nonlinearly permeable stretching/shrinking sheet in a nanofluid. *Scientific Reports*, 4:4404.

APPENDIX A

THE KELLER-BOX SCHEME AND MATLAB PROGRAM FOR THE SOLUTION OF MHD BOUNDARY LAYER MICROPOLAR NANOFLUID FLOW OVER AN INCLINED STRETCHING SURFACE

A.1 The Finite Difference Method

Equations in (3.105) subject to the boundary conditions (3.109) are written in a system of first order differential equations. For this purpose, new dependent variables are introduced for $f(\eta)$, $u(\eta)$, $v(\eta)$, $t(\eta)$, $l(\eta)$, $g(\eta)$, $p(\eta)$, $q(\eta)$, and $s(\eta)$. Also, $h(\eta)$, $\theta(\eta)$ and $\phi(\eta)$ are replaced with $t(\eta)$, $g(\eta)$ and $q(\eta)$, respectively that represent the microrotation, fluid temperature and concentration, respectively. Therefore, the following first-order equations are

$$f'(\eta) = u(\eta),$$

$$u'(\eta) = v(\eta),$$

$$t'(\eta) = l(\eta),$$

$$g'(\eta) = p(\eta),$$

$$q'(\eta) = s(\eta), \tag{A.1}$$

$$(1+K)v' + f v - u^2 + K l + ((Gr)g + (Gc)q)cos\gamma - \Big(M\Big)u = 0,$$

$$\left(1+\frac{K}{2}\right) l' + f\, l - u\, t - K(2t+v) = 0,$$

$$\left(\frac{1}{\mathrm{Pr}}\right) p' + f\, p + Nb\, s\, p + Nt\, p^2 = 0,$$

$$s' + Le\, f\, s + Nt_b\, p' = 0.$$

The boundary conditions in terms of new dependent variable η becomes

$$f(\eta) = 0,\ u(\eta) = 1,\ t(\eta) = 0,\ g(\eta) = 1,\ q(\eta) = 1\ at\ \eta = 0,$$

$$u(\eta) \to 0,\ t(\eta) \to 0,\ g(\eta) \to 0,\ q(\eta) \to 0\ at\ \eta \to \infty. \tag{A.2}$$

The net rectangle is considered in the $x-\eta$ plane as shown in Figure A.1 and the net points are defined as below:

$$x^0 = 0,\ x^i = x^{i-1} + k_i,\ i = 1,2,3,.....I, \tag{A.3}$$

$$\eta^0 = 0, \eta_j = \eta_{j-1} + h_j,\ j = 1,2,3,.....J, \eta_J = \eta_\infty, \tag{A.4}$$

where k_i is the $\Delta x-$spacing and h_j is the $\Delta\eta-$spacing. Here i and j are just sequence of numbers that indicate the coordinate location, not tensor indices or exponents.

The derivatives in the x-direction are given by finite difference, for example

$$\frac{\partial u}{\partial x} = \frac{u^i - u^{i-1}}{k_i}, \tag{A.5}$$

while the derivatives in the η-direction are replaced by finite difference, for example

$$v' = \frac{\partial v}{\partial \eta} = \frac{v_j - v_{j-1}}{h_j}, \tag{A.6}$$

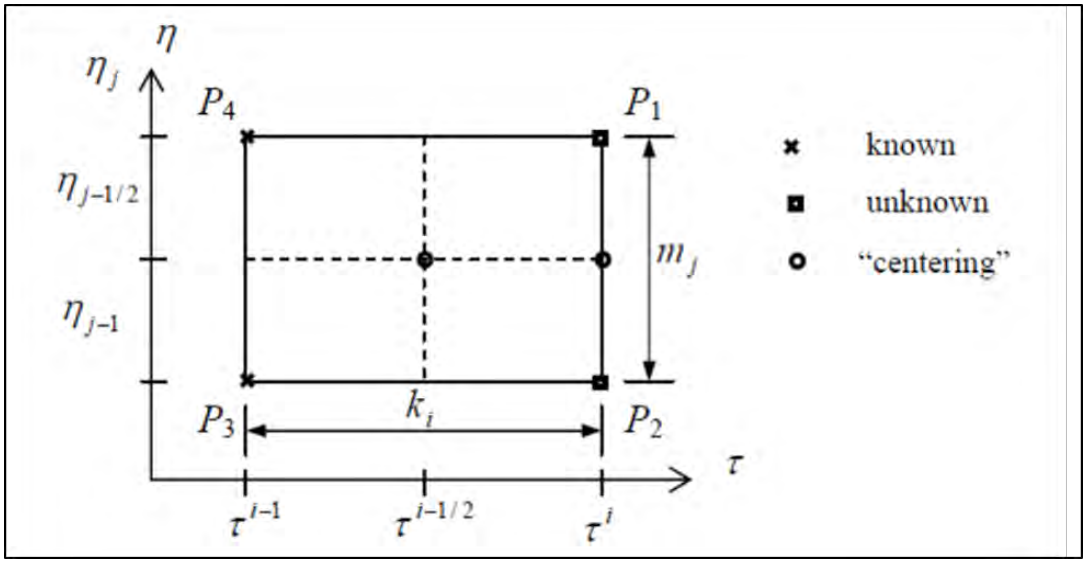

Figure A.1. Net rectangle for difference approximations.

for any points:

$$()_j^{i-1/2} = \frac{1}{2}\left[()_j^i + ()_j^{i-1}\right] \tag{A.7}$$

and

$$()_{j-1/2}^i = \frac{1}{2}\left[()_j^i + ()_{j-1}^i\right]. \tag{A.8}$$

The difference equations, which are to approximate Equations (A.1) are written by considering one mesh rectangle as shown in Figure A.1. Using centered-difference derivatives, the finite difference approximations of the ordinary differential Equations (A.1) are written for the midpoint $(\eta_{j-1/2})$ of the segment P_1P_2. This process is called centering about $(\eta_{j-1/2})$ written as

$$\frac{\left(f_j^i - f_{j-1}^i\right)}{h_j} = \frac{1}{2}\left(u_j^i + u_{j-1}^i\right) = u_{j-1/2}^i,$$

$$\frac{\left(u_j^i - u_{j-1}^i\right)}{h_j} = \frac{1}{2}\left(v_j^i + v_{j-1}^i\right) = v_{j-1/2}^i,$$

$$\frac{\left(t_j^i - t_{j-1}^i\right)}{h_j} = \frac{1}{2}\left(l_j^i + l_{j-1}^i\right) = l_{j-1/2}^i,$$

$$\frac{\left(g_j^i - g_{j-1}^i\right)}{h_j} = \frac{1}{2}\left(p_j^i + p_{j-1}^i\right) = p_{j-1/2}^i,$$

$$\frac{\left(q_j^i - q_{j-1}^i\right)}{h_j} = \frac{1}{2}\left(s_j^i + s_{j-1}^i\right) = s_{j-1/2}^i \tag{A.9}$$

$$(1+K)\frac{\left(v_j^i - v_j^i - 1\right)}{h_j} + \left[\left(\frac{f_j^i + f_{j-1}^i}{2}\right)\left(\frac{v_j^i + v_{j-1}^i}{2}\right)\right] -$$

$$\left[\left(\frac{u_j^i + u_{j-1}^i}{2}\right)^2\right] + K\left(\frac{l_j^i + l_{j-1}^i}{2}\right) + Gr\left(\frac{g_j^i + g_{j-1}^i}{2}\right)cos(\gamma) +$$

$$Gc\left(\frac{q_j^i + q_{j-1}^i}{2}\right)cos(\gamma) - \left(M\right)\left(\frac{u_j^i + u_{j-1}^i}{2}\right) = 0,$$

$$(1+\frac{K}{2})\frac{\left(l_j^i - l_{j-1}^i\right)}{h_j} + \left[\left(\frac{f_j^i + f_{j-1}^i}{2}\right)\left(\frac{l_j^i + l_{j-1}^i}{2}\right)\right] -$$

$$\left[\left(\frac{u_j^i + u_{j-1}^i}{2}\right)\left(\frac{t_j^i + t_{j-1}^i}{2}\right)\right] - K\left[2\left(\frac{t_j^i + t_{j-1}^i}{2}\right) + \left(\frac{v_j^i + v_{j+1}^i}{2}\right)\right] = 0,$$

$$\left(\frac{1}{\mathrm{Pr}}\right)\frac{\left(p_j^i - p_j^i - 1\right)}{h_j} + \left[\left(\frac{f_j^i + f_{j-1}^i}{2}\right)\left(\frac{p_j^i + p_{j-1}^i}{2}\right)\right] +$$

$$Nb\left[\left(\frac{s_j^i + s_{j-1}^i}{2}\right)\left(\frac{p_j^i + p_{j-1}^i}{2}\right)\right] + Nt\left[\left(\frac{p_j^i + p_{j+1}^i}{2}\right)^2\right] = 0,$$

$$\frac{\left(s_j^i - s_{j-1}^i\right)}{h_j} + Le\left[\left(\frac{f_j^i + f_{j-1}^i}{2}\right)\left(\frac{s_j^i + s_{j-1}^i}{2}\right)\right] +$$

$$Nt_b\left[\left(\frac{p_j^i - p_{j+1}^i}{h_j}\right)\right] = 0.$$

At $x = x^i$, the subjected boundary conditions (A.2) in terms of the dependent variable

(η) become

$$f_0^i = 0,\ u_0^i = 1,\ h_0^i = 0,\ g_0^i = 1,\ q_0^i = 1, \tag{A.10}$$

$$u_J^i = 0,\ h_J^i = 0,\ g_J^i = 0,\ q_J^i = 0.$$

A.1.1 Newton's Method

If $\left(f_j^{i-1},\ u_j^{i-1},\ v_j^{i-1},\ t_j^{i-1},\ l_j^{i-1},\ g_j^{i-1},\ p_j^{i-1},\ q_j^{i-1},\ s_j^{i-1} \right)$ are assumed to be known for $0 \leq\ j \leq\ J$, then the solution of the unknown $\left(f_j^i,\ u_j^i,\ v_j^i,\ t_j^i,\ l_j^i,\ g_j^i,\ p_j^i,\ q_j^i,\ s_j^i \right)$ $0 \leq\ j \leq\ J$ have to be obtained. For simplicity of notations, unknown at $x = x^i$, $\left(f_j^i,\ u_j^i,\ v_j^i,\ t_j^i,\ l_j^i,\ g_j^i,\ p_j^i,\ q_j^i,\ s_j^i \right)$ are written as$\left(f_j,\ u_j,\ v_j,\ t_j,\ l_j,\ g_j,\ p_j,\ q_j,\ s_j \right)$. After multiplying with h_j, the system of equation (A.9) can be written as

$$f_j - f_{j-1} - \frac{h_j}{2}\left(u_j + u_{j-1} \right) = 0,$$

$$u_j - u_{j-1} - \frac{h_j}{2}\left(v_j + v_{j-1} \right) = 0,$$

$$t_j - t_{j-1} - \frac{h_j}{2}\left(l_j + l_{j-1} \right) = 0,$$

$$g_j - g_{j-1} - \frac{h_j}{2}\left(p_j + p_{j-1} \right) = 0,$$

$$q_j - q_{j-1} - \frac{h_j}{2}\left(s_j + s_{j-1} \right) = 0, \tag{A.11}$$

$$(1+K)\left(v_j - v_{j-1} \right) + h_j \left[\left(\frac{f_j + f_{j-1}}{2} \right) \left(\frac{v_j + v_{j-1}}{2} \right) \right] -$$

$$h_j \left[\left(\frac{u_j + u_{j-1}}{2} \right)^2 \right] + K h_j \left(\frac{l_j + l_{j-1}}{2} \right) + Gr \left(\frac{g_j + g_{j-1}}{2} \right) cos(\gamma) +$$

$$Gc\left(\frac{q_j+q_{j-1}}{2}\right)cos(\gamma)-\left(M\right)\left(\frac{u_j+u_{j-1}}{2}\right)=0,$$

$$(1+\frac{K}{2})\,(\,l_j-\,l_{j-1})+\,h_j\left[\left(\frac{f_j+f_{j-1}}{2}\right)\left(\frac{l_j+l_{j-1}}{2}\right)\right]-$$

$$h_j\left[\left(\frac{u_j+u_{j-1}}{2}\right)\left(\frac{t_j+t_{j-1}}{2}\right)\right]-$$

$$K\,h_j\left[2\left(\frac{t_j+t_{j-1}}{2}\right)+\left(\frac{v_j+v_{j+1}}{2}\right)\right]=0,$$

$$\left(\frac{1}{\mathrm{Pr}}\right)(\,p_j-\,p_{j-1})+\,h_j\left[\left(\frac{f_j+f_{j-1}}{2}\right)\left(\frac{p_j+p_{j-1}}{2}\right)\right]+$$

$$h_j\,Nb\left[\left(\frac{s_j+s_{j-1}}{2}\right)\left(\frac{p_j+pj-1}{2}\right)\right]+\,h_j\,Nt\left[\left(\frac{p_j+p_{j+1}}{2}\right)^2\right]=0,$$

$$(\,s_j-\,s_{j-1})+\,h_j\,Le\left[\left(\frac{f_j+f_{j-1}}{2}\right)\left(\frac{s_j+s_{j-1}}{2}\right)\right]+Nt_b\left[(\,p_j-\,p_{j-1})\right]=0.$$

For the Newton's method, the following iterates are introduced to linearize the non-linear system of equations (A.11).

$$\begin{aligned}
&f_j^{(k+1)}=\,f_j^k+\delta\,f_j^k,\;u_j^{(k+1)}=\,u_j^k+\delta\,u_j^k,\\
&t_j^{(k+1)}=\,t_j^k+\delta\,t_j^k,\;\;g_j^{(k+1)}=\,g_j^k+\delta\,g_j^k,\\
&p_j^{(k+1)}=\,p_j^k+\delta\,p_j^k\;,\;q_j^{(k+1)}=\,q_j^k+\delta\,q_j^k,\\
&s_j^{(k+1)}=\,s_j^k+\delta\,s_j^k.
\end{aligned}\tag{A.12}$$

Substituting these expressions (A.12) into Equation (A.11), and after dropping the quadratic and higher-order terms in $\delta\,f_j^{(k)}$,$\delta\,u_j^{(k)}$, $\delta\,v_j^{(k)}$,$\delta\,l_j^{(k)}$, $\delta\,t_j^{(k)}$,$\delta\,g_j^{(k)}$, $\delta\,p_j^{(k)}$,$\delta\,q_j^{(k)}$ and $\delta\,s_j^{(k)}$ as well as the superscript i for simplicity, this procedure yields the following linear tridiagonal system.

$$\delta\,f_j-\delta\,f_{j-1}-\frac{h_j}{2}\left(\delta\,u_j+\delta\,u_{j-1}\right)=(\,r_1)_{j-1/2},$$

$$\delta\,u_j-\delta\,u_{j-1}-\frac{h_j}{2}\left(\delta\,v_j+\delta\,v_{j-1}\right)=(\,r_2)_{j-1/2},$$

$$\delta\, t_j - \delta\, t_{j-1} - \frac{h_j}{2}\left(\delta\, l_j + \delta\, l_{j-1}\right) = (\, r_3)_{j-1/2}\,,$$

$$\delta\, g_j - \delta\, g_{j-1} - \frac{h_j}{2}\left(\delta\, p_j + \delta\, p_{j-1}\right) = (\, r_4)_{j-1/2}\,,$$

$$\delta\, q_j - \delta\, q_{j-1} - \frac{h_j}{2}\left(\delta\, s_j + \delta\, s_{j-1}\right) = (\, r_5)_{j-1/2}\,, \tag{A.13}$$

$$(\, a_1)_j\, \delta\, v_j + (\, a_2)_j\, \delta\, v_{j-1} + (\, a_3)_j\, \delta\, f_j + (\, a_4)_j\, \delta\, f_{j-1} + (\, a_5)_j\, \delta\, u_j +$$

$$(\, a_6)_j\, \delta\, u_{j-1} + (\, a_7)_j\, \delta\, l_j + (\, a_8)_j\, \delta\, l_{j-1} + (\, a_9)_j\, \delta\, g_j + (\, a_{10})_j\, \delta\, g_{j-1} +$$

$$(\, a_{11})_j\, \delta\, q_j + (\, a_{12})_j\, \delta\, q_{j-1} = (\, r_6)_{j-1/2}\,,$$

$$(\, b_1)_j\, \delta\, l_j + (\, b_2)_j\, \delta\, l_{j-1} + (\, b_3)_j\, \delta\, f_j + (\, b_4)_j\, \delta\, f_{j-1} + (\, b_5)_j\, \delta\, u_j +$$

$$(\, b_6)_j\, \delta\, u_{j-1} + (\, b_7)_j\, \delta\, v_j + (\, b_8)_j\, \delta\, v_{j-1} +$$

$$(\, b_9)_j\, \delta\, t_j + (\, b_{10})_j\, \delta\, t_{j-1} = (\, r_7)_{j-1/2}\,,$$

$$(\, c_1)_j\, \delta\, p_j + (\, c_2)_j\, \delta\, p_{j-1} + (\, c_3)_j\, \delta\, f_j + (\, c_4)_j\, \delta\, f_{j-1} + (\, c_5)_j\, \delta\, s_j +$$

$$(\, c_6)_j\, \delta\, s_{j-1} = (\, r_8)_{j-1/2}\,,$$

$$(\, d_1)_j\, \delta\, s_j + (\, d_2)_j\, \delta\, s_{j-1} + (\, d_3)_j\, \delta\, f_j + (\, d_4)_j\, \delta\, f_{j-1} +$$

$$(\, d_5)_j\, \delta\, p_j + (\, d_6)_j\, \delta\, p_{j-1} = (\, r_9)_{j-1/2}$$

where,

$$(\, a_1)_j = 1 + K + \frac{h_j}{2}\, f_{j-1/2}, (\, a_2)_j = -1 - K + \frac{h_j}{2}\, f_{j-1/2},$$

$$(\, a_3)_j = \frac{h_j}{2}\, v_{j-1/2}, (\, a_4)_j = (\, a_3)_j\,,$$

$$(a_5)_j = -h_j\, u_{j-1/2}, (a_6)_j = (a_5)_j,$$

$$(a_7)_j = \frac{h_j\, K}{2}, (a_8)_j = (a_7)_j,$$

$$(a_9)_j = \frac{h_j}{2} Grcos(\gamma), (a_{10})_j = (a_9)_j,$$

$$(a_{11})_j = \frac{h_j}{2} Gccos(\gamma), (a_{12})_j = (a_{11})_j,$$

$$(b_1)_j = 1 + \frac{K}{2} + \frac{h_j}{2} f_{j-1/2}, (b_2)_j = -1 - \frac{K}{2} + \frac{h_j}{2} f_{j-1/2},$$

$$(b_3)_j = \frac{h_j}{2} l_{j-1/2}, (b_4)_j = (b_3)_j$$

$$(b_5)_j = -\frac{h_j}{2} t_{j-1/2}, (b_6)_j = (b_5)_j,$$

$$(b_7)_j = -\frac{h_j\, K}{2}, (b_8)_j = (b_7)_j,$$

$$(b_9)_j = \frac{-h_j}{2} u_{j-1/2} - h_j\, K, (b_{10})_j = (b_9)_j,$$

$$(c_1)_j = 1 + \frac{h_j \Pr}{2} f_{j-1/2} + \frac{h_j\, Nb \Pr}{2} s_{j-1/2} + h_j\, Nt \Pr p_{j-1/2},$$

$$(c_2)_j = (c_1)_j - 2,$$

$$(c_3)_j = \frac{h_j \Pr}{2} p_{j-1/2}, (c_4)_j = (c_3)_j,$$

$$(c_5)_j = \frac{h_j\, Nb \Pr}{2} p_{j-1/2}, (c_6)_j = (c_5)_j,$$

$$(d_1)_j = 1 + \frac{h_j\, Le}{2} f_{j-1/2}, (d_2)_j = (d_1)_j - 2,$$

$$(d_3)_j = \frac{h_j\, Le}{2} s_{j-1/2}, (d_4)_j = (d_3)_j,$$

$$(d_5)_j = Nt_b, (d_6)_j = -Nt_b,$$

$$(r_1)_j = f_{j-1} - f_j + h_j\, u_{j-1/2},$$

$$(r_2)_j = u_{j-1} - u_j + h_j\, v_{j-1/2},$$

$$(r_3)_j = t_{j-1} - t_j + h_j\, l_{j-1/2},$$

$$(r_4)_j = g_{j-1} - g_j + h_j\, p_{j-1/2},$$

$$(r_5)_j = q_{j-1} - q_j + h_j\, s_{j-1/2},$$

$$(r_6)_j = (1+K)\left(v_{j-1} - v_j\right) - h_j\, f_{j-1/2}\, v_{j-1/2} + h_j\, u^2_{j-1/2} - h_j\, K\, l_{j-1/2} -$$

$$h_j(Gr)g_{j-1/2} - h_j(Gc)q_{j-1/2} + h_j\left(M\right)u_{j-1/2},$$

$$(r_7)_j = \left(1+\frac{K}{2}\right)\left(l_{j-1} - l_j\right) - h_j\, f_{j-1/2}\, l_{j-1/2} + h_j\, u_{j-1/2}\, t_{j-1/2} +$$

$$2\, h_j\, K\, t_{j-1/2} + h_j\, K\, v_{j-1/2},$$

$$(r_8)_j = p_{j-1} - p_j - h_j\, \mathrm{Pr}\, f_{j-1/2}\, p_{j-1/2} - h_j\, Nt\, \mathrm{Pr}\, p^2_{j-1/2} -$$

$$h_j\, Nb\, \mathrm{Pr}\, s_{j-1/2}\, p_{j-1/2},$$

$$(r_9)_j = s_{j-1} - s_j - h_j\, Le\, f_{j-1/2}\, s_{j-1/2} + Nt_b\left(p_{j-1} - p_j\right).$$

To complete the system (A.13), the boundary conditions (A.10) are recalled that can be satisfied exactly with no iteration. So, the correct values in all the iterations are maintained by taking

$$\delta\, f_0 = 0, \delta\, u_0 = 0, \delta\, t_0 = 0, \delta\, g_0 = 0, \delta\, q_0 = 0,$$

$$\delta\, u_J = 0,\ \ \delta\, t_J = 0,\ \ \delta\, g_J = 0,\ \ \delta\, q_J = 0. \tag{A.14}$$

A.1.2 The Block-Elimination Method

The linearized differential equations of the system (A.13) have a block-tridiagonal structure. In vector-matrix form, it can be written as

$$[A][\delta] = [r] \tag{A.15}$$

where,

$$[A] = \begin{bmatrix} [A_1] & [C_1] & & & \\ [B_2] & [A_2] & [C_2] & & \\ & & \ddots & & \\ & & \ddots & & \\ & & [B_{J-1}] & [A_{J-1}] & [C_{J-1}] \\ & & & [B_J] & [A_J] \end{bmatrix}, \tag{A.16}$$

$$[\delta] = \begin{bmatrix} [\delta_1] \\ [\delta_2] \\ \vdots \\ [\delta_{J-1}] \\ [\delta_J] \end{bmatrix}, [r] = \begin{bmatrix} [r_1] \\ [r_2] \\ \vdots \\ [r_{J-1}] \\ [r_J] \end{bmatrix} \tag{A.17}$$

The block-tridiagonal structure are commonly consisting of variables or constants, but here, an interesting feature can be observed that is, for the Keller-Box method, it consists of block matrices. By taking $e_j = -\frac{h_j}{2}$, the elements of matrices are

defined as follows

$$[A_1] = \begin{bmatrix} 0 & 0 & 0 & 0 & 1 & 0 & 0 & 0 & 0 \\ e_1 & 0 & 0 & 0 & 0 & e_1 & 0 & 0 & 0 \\ 0 & e_1 & 0 & 0 & 0 & 0 & e_1 & 0 & 0 \\ 0 & 0 & e_1 & 0 & 0 & 0 & 0 & e_1 & 0 \\ 0 & 0 & 0 & e_1 & 0 & 0 & 0 & 0 & e_1 \\ (a_2)_1 & (a_8)_1 & 0 & 0 & (a_3)_1 & (a_1)_1 & (a_7)_1 & 0 & 0 \\ (b_8)_1 & (b_2)_1 & 0 & 0 & (b_3)_1 & (b_7)_1 & (b_1)_1 & 0 & 0 \\ 0 & 0 & (c_2)_1 & (c_6)_1 & (c_3)_1 & 0 & 0 & (c_1)_1 & (c_5)_1 \\ 0 & 0 & (d_6)_1 & (d_2)_1 & (d_3)_1 & 0 & 0 & (d_5)_1 & (d_1)_1 \end{bmatrix}, \tag{A.18}$$

$$[A_j] = \begin{bmatrix} e_j & 0 & 0 & 0 & 1 & 0 & 0 & 0 & 0 \\ -1 & 0 & 0 & 0 & 0 & e_j & 0 & 0 & 0 \\ 0 & -1 & 0 & 0 & 0 & 0 & e_j & 0 & 0 \\ 0 & 0 & -1 & 0 & 0 & 0 & 0 & e_j & 0 \\ 0 & 0 & 0 & -1 & 0 & 0 & 0 & 0 & e_j \\ (a_6)_j & 0 & (a_{10})_j & (a_{12})_j & (a_3)_j & (a_1)_j & (a_7)_j & 0 & 0 \\ (b_6)_j & (b_{10})_j & 0 & 0 & (b_3)_j & (b_7)_j & (b_1)_j & 0 & 0 \\ 0 & 0 & 0 & 0 & (c_3)_j & 0 & 0 & (c_1)_j & (c_5)_j \\ 0 & 0 & 0 & 0 & (d_3)_j & 0 & 0 & (d_5)_j & (d_1)_j \end{bmatrix}, 2 \leq j \leq J \tag{A.19}$$

$$[B_j] = \begin{bmatrix} 0 & 0 & 0 & 0 & -1 & 0 & 0 & 0 & 0 \\ 0 & 0 & 0 & 0 & 0 & e_j & 0 & 0 & 0 \\ 0 & 0 & 0 & 0 & 0 & 0 & e_j & 0 & 0 \\ 0 & 0 & 0 & 0 & 0 & 0 & 0 & e_j & 0 \\ 0 & 0 & 0 & 0 & 0 & 0 & 0 & 0 & e_j \\ 0 & 0 & 0 & 0 & (a_4)_j & (a_2)_j & (a_8)_j & 0 & 0 \\ 0 & 0 & 0 & 0 & (b_4)_j & (b_8)_j & (b_2)_j & 0 & 0 \\ 0 & 0 & 0 & 0 & (c_4)_j & 0 & 0 & (c_2)_j & (c_6)_j \\ 0 & 0 & 0 & 0 & (d_4)_j & 0 & 0 & (d_6)_j & (d_2)_j \end{bmatrix} \quad 2 \leq j \leq J \quad \text{(A.20)}$$

$$[C_j] = \begin{bmatrix} e_j & 0 & 0 & 0 & 1 & 0 & 0 & 0 & 0 \\ 1 & 0 & 0 & 0 & 0 & 0 & 0 & 0 & 0 \\ 0 & 1 & 0 & 0 & 0 & 0 & 0 & 0 & 0 \\ 0 & 0 & 1 & 0 & 0 & 0 & 0 & 0 & 0 \\ 0 & 0 & 0 & 1 & 0 & 0 & 0 & 0 & 0 \\ (a_5)_j & 0 & (a_9)_j & (a_{11})_j & 0 & 0 & 0 & 0 & 0 \\ (b_5)_j & (b_9)_j & 0 & 0 & 0 & 0 & 0 & 0 & 0 \\ 0 & 0 & 0 & 0 & 0 & 0 & 0 & 0 & 0 \\ 0 & 0 & 0 & 0 & 0 & 0 & 0 & 0 & 0 \end{bmatrix}, 1 \leq j \leq J-1 \quad \text{(A.21)}$$

$$[\delta]_1 = \begin{bmatrix} \delta\, v_0 \\ \delta\, l_0 \\ \delta\, p_0 \\ \delta\, s_0 \\ \delta\, f_1 \\ \delta\, v_1 \\ \delta\, l_1 \\ \delta\, p_1 \\ \delta\, s_1 \end{bmatrix}, [\delta]_j = \begin{bmatrix} \delta\, u_{j-1} \\ \delta\, t_{j-1} \\ \delta\, g_{j-1} \\ \delta\, q_{j-1} \\ \delta\, f_j \\ \delta\, v_j \\ \delta\, l_j \\ \delta\, p_j \\ \delta\, s_j \end{bmatrix}, 2 \leq\ j \leq\ J \tag{A.22}$$

and

$$[\, r_j] = \begin{bmatrix} (\, r_1)_{j-1/2} \\ (\, r_2)_{j-1/2} \\ (\, r_3)_{j-1/2} \\ (\, r_4)_{j-1/2} \\ (\, r_5)_{j-1/2} \\ (\, r_6)_{j-1/2} \\ (\, r_7)_{j-1/2} \\ (\, r_8)_{j-1/2} \\ (\, r_9)_{j-1/2} \end{bmatrix} 1 \leq\ j \leq\ J. \tag{A.23}$$

The coefficient matrix A is known as a tridiagonal matrix due to the fact that all elements $[A]$ are zero except those 3 along the diagonal. To solve Equation (A.15) $[A]$ is assumed to be non singular and can be factorized into

$$[A] = [L]\,[U] \tag{A.24}$$

where,

$$[L] = \begin{bmatrix} [I] & & & \\ [\Gamma_2] & [I] & & \\ & \ddots & & \\ & \ddots & & \\ & & [I] & \\ & & [\Gamma_J] & [I] \end{bmatrix} \tag{A.25}$$

and

$$[U] = \begin{bmatrix} [\alpha_1] & [C_1] & & \\ & [\alpha_2] & [C_2] & \\ & \ddots & & \\ & \ddots & & \\ & & [\alpha_{J-1}] & [C_{J-1}] \\ & & & [\alpha_J] \end{bmatrix}, \tag{A.26}$$

where $[I]$ is the identity matrix of order 9 and $[\alpha_i]$, $[\Gamma_i]$ are 9 x 9 matrices whose elements are determined by the following equations:

$$[\alpha_1] = [A_1], \tag{A.27}$$

$$[A_1][\Gamma_1] = [C_1], \tag{A.28}$$

$$[\alpha_j] = [A_j] - [B_j][\Gamma_{j-1}],\ j = 2,3,.....,J, \tag{A.29}$$

$$[\alpha_j][\Gamma_{j-1}] = [C_j],\ j = 2,3,.....,J. \tag{A.30}$$

Equation (A.24) can be substituted into Equation (A.15), which is

$$[L][U][\delta] = [\gamma] \tag{A.31}$$

$$[U][\delta] = [W], \tag{A.32}$$

then Equation (A.31) becomes

$$[L][W] = [\gamma] \tag{A.33}$$

where

$$[W] = \begin{bmatrix} [W_1] \\ [W_2] \\ \vdots \\ [W_{J-1}] \\ [W_J] \end{bmatrix}. \tag{A.34}$$

Here $[W_j]$ are 9 x 1 column matrices. The elements $[W]$ can be solved from Equation (A.33)

$$[\alpha_1][W_1] = [\gamma_1], \tag{A.35}$$

and

$$[\alpha_j][W_j] = [\gamma_j] - [B_j][W_{j-1}],\ 2 \leq j \leq J. \tag{A.36}$$

The step in which $[\Gamma_j]$, $[\alpha_j]$ and $[W_j]$ are calculated is usually referred to as the forward sweep. Once the elements of $[W_j]$ are found, Equation (A.33) then gives the solution $[\delta_j]$ in the so-called backward sweep, in which the elements are obtained by the following relations:

$$[\delta_J] = [W_J], \tag{A.37}$$

and

$$[\delta_j] = [W_j] - [\Gamma_j] - [\delta_{j-1}], 2 \leq j \leq J. \tag{A.38}$$

Once the elements of $[\delta_J]$ are found, Equations (A.11) can be used to find the $(k+1)th$ iteration in Equation (A.13).

A.1.3 Starting Conditions

The Keller Box scheme is the only one in which several spacing along x and y directions can be utilized (Nazar, 2004). For numerical simulation, a suitable value of boundary layer thickness (η_∞) must be established by starting from the small values, also a proper step size determined. In view of Cebeci and Bradshaw (2012) the transformed boundary layer thickness (η) mostly constant in some cases of laminar boundary layer flows and typically lies between 5 to 10. Whereas, according to Nazar (2004), for accurate numerical results, step size ($\triangle\eta$) of 0.02 to 0.04 is suitable. Moreover, Lok (2008) successfully utilized the step size of 0.1, but in this thesis we considered the step size 0.01. In addition, the numerical values recovered in the problems are independent of ($\triangle\eta$).

In order to start and proceed with numerical computation, it is necessary to make initial guesses for the functions f, u, v, t, l, g, p, q and s across boundary layer from $\eta = 0$ to $\eta \to \infty$. There are few checks on the selections of distribution curves that they must satisfy the boundary conditions in Equation (3.109). Different guesses of initial value profiles will give the same final results but the iteration count and computation time may be more or less. For the present problem, the following initial value profiles have been taken.

$$f = \eta - \left(\frac{\eta^2}{2\eta_\infty}\right), f' = u = 1 - \left(\frac{\eta}{\eta_\infty}\right), f'' = v = \left(\frac{1}{\eta_\infty}\right),$$

$$h = t = \frac{\eta}{\eta_\infty} - \frac{\eta^2}{{\eta_\infty}^2}, h' = l = \frac{1}{\eta_\infty} - \frac{2\eta}{{\eta_\infty}^2},$$

$$\theta = g = 1 - \frac{\eta}{\eta_\infty}, \theta' = p = \frac{1}{\eta_\infty},$$

$$\phi = q = 1 - \frac{\eta}{\eta_\infty}, \phi' = s = -\frac{1}{\eta_\infty}. \tag{A.39}$$

In laminar flow calculations, the wall shear stress parameter $v(\eta)$ is commonly used as the convergence criterion. This is probably because in boundary layer flow calculations, it is seen that usually the greatest error appears in the wall shear stress parameter. It is noted that throughout this study, this criterion of convergence is used for all the considered problems and iterations are repeated until the convergence is satisfied. Therefore, calculations are stopped when

$$\left|\delta v^{(i)}{}_0\right| < \varepsilon_1, \tag{A.40}$$

where ε_1 is a small prescribed value$(\varepsilon_1 = 0.00001)$ (Anwar, 2013). This shows the accuracy of most predicted quantities up to four decimal places (Cebeci and Bradshaw, 2012).

A.2 Matlab Program

```
%input the following values
Nb = input ('Input the values of Nb = ');
Nt = input ('Input the values of Nt = ');
Pr = input ('Input the values of Prandtle number = ');
Le = input ('Input the values of Lewis number = ');
Gr = input ('Input the values of local Grashof number = ');
Gc = input ('Input the values of local modified Grashof number = ');
M = input ('Input the values of Hartmann number = ');
γ = input ('Input the values of γ = ');
K = input ('Input the values of material factor K = ');
% Set initial values for iteration
stop = 1.0;
k = 1.0;
epselon = 0.0001;
while stop > epselon
eta(1,1) = 0.0;
for j = 2:np
eta(j,1) = eta(j-1,1) + deleta;
end
for j = 1:np
deta(j,k) = deleta;
% initial guess
f(j,1) = eta(j,1) − eta(j,1)^2/2 ∗ eta(np,1);
u(j,1) = 1 - (eta(j,1)/eta(np,1));
v(j,1) = (1/eta(np,1));
```

$t(j,1) = eta(j,1)/eta(np,1) - eta(j,1)^2/eta(np,1)^2;$

$L(j,1) = 1/eta(np,1) - 2 * eta(j,1)/eta(np,1);$

g(j,1) = 1 - etab;

p(j,1) = -etau15;

q(j,1) = 1 - etab;

s(j,1) = -etau1;

end

% Present station (centered-difference derivatives) for j = 2:np

fb(j,k) = 0.5 * (f(j,k) + f(j-1,k));

ub(j,k) = 0.5 * (u(j,k) + u(j-1,k));

vb(j,k) = 0.5 * (v(j,k) + v(j-1,k));

pb(j,k) = 0.5 * (p(j,k) + p(j-1,k));

qb(j,k) = 0.5 * (q(j,k) + q(j-1,k));

tb(j,k) = 0.5 * (t(j,k) + t(j-1,k));

Lb(j,k) = 0.5 * (L(j,k) + L(j-1,k));

fLb(j,k) = fb(j,k) * Lb(j,k);

utb(j,k) = ub(j,k) * tb(j,k);

fvb(j,k) = fb(j,k) * vb(j,k);

uub(j,k) = ub(j,k) * ub(j,k);

fpb(j,k) = fb(j,k) * pb(j,k);

ppb(j,k) = pb(j,k) * pb(j,k);

ugb(j,k) = ub(j,k) * gb(j,k); dervb(j,k) = (v(j,k) - v(j-1,k)) / deta(j,k);

derLb(j,k) = (L(j,k) - L(j-1,k)) / deta(j,k);

derpb(j,k) = (p(j,k) - p(j-1,k)) / deta(j,k);

% Coefficients of the difference momentum equation

a1(j,k) = 1 + KK + 0.5 * deta(j,k) * fb(j,k);

a2(j,k) = -1 - KK + 0.5 * deta(j,k) * fb(j,k);

```
a3(j,k) = 0.5 * deta(j,k) * vb(j,k);

a4(j,k) = a3(j,k);

a5(j,k) = - 0.5 * deta(j,k) * (MM )- deta(j,k) * ub(j,k);

a6(j,k) = a5(j,k);

a7(j,k) = 0.5 * deta(j,k) * KK;

a8(j,k) = a7(j,k);

a9(j,k) = 0.5 * deta(j,k) * Gr * cos (gamma);

a10(j,k) = a9(j,k);

a11(j,k) = 0.5 * deta(j,k) * Gc * cos (gamma);

a12(j,k) = a11(j,k);

% Coefficients of the difference micropolar equation

b1(j,k) = 1 + KK/2 + 0.5 * deta(j,k) * fb(j,k);

b2(j,k) = -1 - KK/2 + 0.5 * deta(j,k) * fb(j,k);

b3(j,k) = 0.5 * deta(j,k) * Lb(j,k);

b4(j,k) = b3(j,k);

b5(j,k) = -0.5 * deta(j,k) * tb(j,k);

b6(j,k) = b5(j,k);

b7(j,k) = -deta(j,k) * KK;

b8(j,k) = b7(j,k);

b9(j,k) = -0.5 * deta(j,k)* ub(j,k)-deta(j,k) * KK;

b10(j,k) = b9(j,k);

% Coefficients of the difference energy equation

c1(j,k) = 1 + 0.5 * deta(j,k) * Pr * fb(j,k) + Nb * 0.5 * deta(j,k) * Pr * sb(j,k) + Nt *

deta(j,k) * Pr * pb(j,k);

c2(j,k) = c1(j,k) - 2;

c3(j,k) = 0.5 * deta(j,k) * Pr * pb(j,k);

c4(j,k) = c3(j,k);
```

```
c5(j,k) = Nb * 0.5 * deta(j,k) * Pr * pb(j,k);

c6(j,k) = c5(j,k);

% Coefficients of the difference nanoparticle equation

d1(j,k) = 1 + Le * 0.5 * deta(j,k) * fb(j,k);

d2(j,k) = d1(j,k) - 2;

d3(j,k) = Le * 0.5 * deta(j,k) * sb(j,k);

d4(j,k) = d3(j,k);

d5(j,k) = Nt/Nb;

d6(j,k) = -d5(j,k);

% Expressions of rj-1/2

r1(j,k) = f(j-1,k) - f(j,k) + deta(j,k) * ub(j,k);

r2(j,k) = u(j-1,k) - u(j,k) + deta(j,k) * vb(j,k);

r3(j,k) = t(j-1,k) - t(j,k) + deta(j,k) * Lb(j,k);

r4(j,k) = g(j-1,k) - g(j,k) + deta(j,k) * pb(j,k);

r5(j,k) = q(j-1,k) - q(j,k) + deta(j,k) * sb(j,k);

r6(j,k) = (1+KK)*(v(j-1,k) - v(j,k)) - deta(j,k)* fvb(j,k)+ deta(j,k)* uub(j,k) - KK *
deta(j,k)* Lb(j,k) - deta(j,k)* Gr * cos(gamma)* gb(j,k)- deta(j,k)* Gc * cos(gamma)*
qb(j,k)+ deta(j,k)* (MM )* ub(j,k);

r7(j,k) = (1+KK/2)*(L(j-1,k) - L(j,k)) - deta(j,k)* fLb(j,k)+ deta(j,k)* utb(j,k) + 2 *
deta(j,k) * KK * tb(j,k)+ deta(j,k) * KK * vb(j,k);

r8(j,k) = p(j-1,k) - p(j,k)- deta(j,k) * Pr * fpb(j,k)- Nb * deta(j,k) * Pr * spb(j,k)- Nt *
deta(j,k) * Pr * ppb(j,k);

r9(j,k) = s(j-1,k)- s(j,k)- Le * deta(j,k) * fsb(j,k)+(Nt/Nb) * (p(j-1,k)-p(j,k));

end

% Obtain the matrices P1

aa2,k=[ 0 0 0 0 1 0 0 0 0;

-0.5*deta(2,k) 0 0 0 0 -0.5*deta(2,k) 0 0 0;
```

```
0 -0.5*deta(2,k) 0 0 0 0 -0.5*deta(2,k) 0 0;
0 0 -0.5*deta(2,k) 0 0 0 0 -0.5*deta(2,k) 0;
0 0 0 -0.5*deta(2,k) 0 0 0 0 -0.5*deta(2,k);
a2(2,k) a8(2,k) 0 0 a3(2,k) a1(2,k) a7(2,k) 0 0;
b8(2,k) b2(2,k) 0 0 b3(2,k) b7(2,k) b1(2,k) 0 0;
0 0 c2(2,k) c6(2,k) c3(2,k) 0 0 c1(2,k) c5(2,k);
0 0 d6(2,k) d2(2,k) d3(2,k) 0 0 d5(2,k) d1(2,k)];
for j = 3:np
aaj,k=[ -0.5*deta(j,k) 0 0 0 1 0 0 0 0;
-1 0 0 0 0 -0.5*deta(j,k) 0 0 0;
0 -1 0 0 0 0 -0.5*deta(j,k) 0 0;
0 0 -1 0 0 0 0 -0.5*deta(j,k) 0;
0 0 0 -1 0 0 0 0 -0.5*deta(j,k);
a6(j,k) 0 a10(j,k) a12(j,k) a3(j,k) a1(j,k) a7(j,k) 0 0;
b6(j,k) b10(j,k) 0 0 b3(j,k) b7(j,k) b1(j,k) 0 0;
0 0 0 0 c3(j,k) 0 0 c1(j,k) c5(j,k);
0 0 0 0 d3(j,k) 0 0 d5(j,k) d1(j,k)];
bbj,k=[ 0 0 0 0 -1 0 0 0 0;
0 0 0 0 0 -0.5*deta(j,k) 0 0 0;
0 0 0 0 0 0 -0.5*deta(j,k) 0 0;
0 0 0 0 0 0 0 -0.5*deta(j,k) 0;
0 0 0 0 0 0 0 0 -0.5*deta(j,k);
0 0 0 0 a4(j,k) a2(j,k) a8(j,k) 0 0;
0 0 0 0 b4(j,k) b8(j,k) b2(j,k) 0 0;
0 0 0 0 c4(j,k) 0 0 c2(j,k) c6(j,k);
0 0 0 0 d4(j,k) 0 0 d6(j,k) d2(j,k)];
end
```

```
for j = 2:np-1
ccj,k=[ -0.5*deta(j,k) 0 0 0 0 0 0 0 0;
1 0 0 0 0 0 0 0 0;
0 1 0 0 0 0 0 0 0;
0 0 1 0 0 0 0 0 0;
0 0 0 1 0 0 0 0 0;
a5(j,k) 0 a9(j,k) a11(j,k) 0 0 0 0 0;
b5(j,k) b9(j,k) 0 0 0 0 0 0 0;
0 0 0 0 0 0 0 0 0;
0 0 0 0 0 0 0 0 0 ];
end
% The recursion formulas for P1
% Forward sweep
alfa2,k = aa2,k;
for j = 3:np
gammaj,k = bbj,k * inv(alfaj-1,k);
alfaj,k = aaj,k - gammaj,k * ccj-1,k;
end
for j = 2:np
rrj,k = [ r1(j,k); r2(j,k); r3(j,k); r4(j,k);
r5(j,k);
r6(j,k); r7(j,k); r8(j,k); r9(j,k) ];
end
ww2,k = r2,k;
for j = 3:np
wwj,k = rrj,k - gammaj,k * wwj,k;
end
```

```
% Backward sweep in P1
delf(1,k) = 0.0; delu(1,k) = 0.0; delt(1,k) = 0.0; delg(1,k) = 0.0; delq(1,k) = 0.0;
delu(np,k) = 0.0; delt(np,k) = 0.0; delg(np,k) = 0.0; delq(np,k) = 0.0;
dellnp,k = inv(alfanp,k) * wwnp,k;
dellj,k = inv(alfaj,k) * (wwj,k - (ccj,k * dellj-1,k));
end
delv(1,k) = dell2,k(1,1);delL(1,k) = dell2,k(2,1);
delp(1,k) = dell2,k(3,1);
dels(1,k) = dell2,k(4,1);
delf(2,k) = dell2,k(5,1);
delv(2,k) = dell2,k(6,1);
delL(2,k) = dell2,k(7,1);
delp(2,k) = dell2,k(8,1);
dels(2,k) = dell2,k(9,1);
for j = np:-1:3
delu(j-1,k) = dellj,k(1,1);delt(j-1,k) = dellj,k(2,1);
delg(j-1,k) = dellj,k(3,1);
delq(j-1,k) = dellj,k(4,1);
delf(j,k) = dellj,k(5,1);
delv(j,k) = dellj,k(6,1);
delL(j,k) = dellj,k(7,1);
delp(j,k) = dellj,k(8,1);
dels(j,k) = dellj,k(9,1);
end
% Newton's method
for j = 1:np
f(j,k+1) = f(j,k) + delf(j,k);
```

```
u(j,k+1) = u(j,k) + delu(j,k);

v(j,k+1) = v(j,k) + delv(j,k);

t(j,k+1) = t(j,k) + delt(j,k);

L(j,k+1) = L(j,k) + delL(j,k);

g(j,k+1) = g(j,k) + delg(j,k);

p(j,k+1) = p(j,k) + delp(j,k);

q(j,k+1) = q(j,k) + delq(j,k);

s(j,k+1) = s(j,k) + dels(j,k);

end

kmax = k;

k = k+1;

end
```

APPENDIX B

LIST OF PUBLICATIONS

1. Rafique, K., Anwar, M. I., Misiran, M., Khan, I., Seikh, A. H., Sherif, E. S. M., & Nisar, K. S. (2019). Brownian Motion and Thermophoretic Diffusion Effects on Micropolar Type Nanofluid Flow with Soret and Dufour Impacts over an Inclined Sheet: Keller-Box Simulations. Energies, 12(21), 4191.

2. Rafique, K., Anwar, M. I., Misiran, M., Khan, I., Alharbi, S. O., Thounthong, P., & Nisar, K. S. (2019). Numerical Solution of Casson Nanofluid Flow Over a Non-linear Inclined Surface With Soret and Dufour Effects by Keller-Box Method. Front. Phys. 7: 139. doi: 10.3389/fphy.

3. Rafique, K., Imran Anwar, M., Misiran, M., Khan, I., Alharbi, S. O., Thounthong, P., & Nisar, K. S. (2019). Keller-Box Analysis of Buongiorno Model with Brownian and Thermophoretic Diffusion for Casson Nanofluid over an Inclined Surface. Symmetry, 11(11), 1370.

4. Rafique, K., Anwar, M. I., Misiran, M., Khan, I., Seikh, A. H., Sherif, E. S. M., & Nisar, K. S. (2019). Numerical Analysis with Keller-Box Scheme for Stagnation Point Effect on Flow of Micropolar Nanofluid over an Inclined Surface. Symmetry, 11(11), 1379.

5. Anwar, M. I., Rafique, K., Misiran, M., & Shehzad, S. A. Numerical study of hydrodynamic flow of a Casson nanomaterial past an inclined sheet under porous medium. Heat Transfer—Asian Research.

6. Rafique, K., Anwar, M. I., & Misiran, M. (2019). Numerical Study on Micropolar Nanofluid Flow over an Inclined Surface by Means of Keller-Box. Asian Journal of Probability and Statistics, 1-21.

7. Rafique, K., Anwar, M. I., & Misiran, M. (2019). Keller-box study on casson nano fluid flow over a slanted permeable surface with chemical reaction. Asian Research

Journal of Mathematics, 1-17.

8. Anwar, M. I., Ali, M., Rafique, K., & Shehzad, S. A. (2019). Soret–Dufour and radiative aspects in hydromagnetized nanofluid flow in stratified porous medium. SN Applied Sciences, 1(11), 1430.

9. Imran, M. A., Shah, N. A., Rafique, K., Sohail, A., & Ejaz, S. (2017). General solutions of convective flows of MHD Casson fluid with slip and radiative heat transfer at the boundary. Computational Thermal Sciences: An International Journal, 9(1).

10. Rafique, K., Anwar, M. I., Misiran, M., Khan, I., Seikh, A. H., Sherif, E. S. M., & Sooppy Nisar, K. (2019). Keller-Box Simulation for the Buongiorno Mathematical Model of Micropolar Nanofluid Flow over a Nonlinear Inclined Surface. Processes, 7(12), 926.

11. Rafique, K., Anwar, M. I., Misiran, M., Khan, I., & M Sherif, E. S. (2020). The Implicit Keller Box Scheme for Combined Heat and Mass Transfer of Brinkman-Type Micropolar Nanofluid with Brownian Motion and Thermophoretic Effect Over an Inclined Surface. Applied Sciences, 10(1), 280.

12. Rafique, K., Anwar, M.I., Misiran, M., Khan, I., Baleanu, D., Nisar, K.S., Sherif, E.-S., & Seikh, A.H. (2020) Hydromagnetic Flow of Micropolar Nanofluid. Symmetry, 12, 251.

13. Anwar, M. I., Rafique, K., Misiran, M., Shehzad, S. A., & Ramesh, G. K. (2020). Keller-box analysis of inclination flow of magnetized Williamson nanofluid. SN Applied Sciences, 2(3), 377.

Accepted Articles

1. "Energy and Mass transport of Micropolar Nanofluid Flow over an Inclined Surface with Keller box Simulation " Heat Transfer-Asian Research (2020).

Authors: Khuram Rafique, Muhammad Imran Anwar, Masnita Misiran, Muhammad Imran Asjad*